Intramural Stress and Inflammation in Arterial Branches:

A Histology-Based Approach

A Thesis
Presented to
The Academic Faculty

By

Peter H. Carnell

In Partial Fulfillment
of the Requirements for the Degree
Doctor of Philosophy in the
George W. Woodruff School of Mechanical Engineering

Georgia Institute of Technology
August 2004

Intramural Stress and Inflammation in Arterial Branches:

A Histology-Based Approach

Approved by:

Dr. Raymond P. Vito, Advisor

Dr. W. Robert Taylor

Dr. Don P. Giddens

Dr. Robert E. Guldberg

Dr. Marc E. Levenston

August 31, 2004

Cell and tissue, shell and bone, leaf and flower, are so many portions of matter, and it is in obedience to the laws of physics that their particles have been moved, molded and conformed… Their problems of form are in the first instance mathematical problems, their problems of growth are essentially physical problems, and the morphologist is, *ipso facto*, a student of physical science.

D'Arcy Wentworth Thompson
On Growth and Form, 1917

ACKNOWLEDGMENTS

I owe a deep debt of gratitude to Dr. Raymond Vito – professor, mentor, and friend - whose supervision and support steered me through the many challenges of this project. I am also deeply grateful to Dr. Robert Taylor, whose insights helped frame this research and whose enthusiasm propelled it forward. My thanks as well go to Dr. Don Giddens, Dr. Robert Guldberg, and Dr. Marc Levenston for generously giving their time and guidance whenever asked.

I am also grateful to: Dr. Oskar Skrinjar for his helpful recommendations regarding section alignment and distortion correction; to histologist Tracey Couse for her valuable assistance, cheerfully and unstintingly given; to John Kools, Derek Doran, and Daiana Weiss for their help with the animal studies, to Giji Joseph for her efforts with immunological techniques, to Allen Young for his practical engineering expertise and assistance; to Dr. David Frakes for his suggestions concerning reconstruction validation; and to Jonathan Morris, Shalin Shah, Ben Spivey, Martijn Cox, and Tom Schroder for their assistance with data collection and programming.

Thanks to my lab mates, including Brian Wayman, Lori Lowder, Melissa Dean, Karen Tisdale, James Warnock, and Senhu Li. I especially thank my office mate, Yu Shin Kim, for good company and sound research advice.

To my good friends Roger, David, Caroline, Linda, Carlos, Mimi, Becky, Lou and Vicki, thanks for reminding me of life beyond the dissertation.

Thank you to my parents, Corbin and Carol Carnell, my brothers, and the rest of my family for their encouragement throughout this process. To my dear wife, Nancy, thank you for your steadfast love and support. You have kept me going through the most difficult times.

I dedicate this work to the late Jeffery Scott O'Brien …for his commitment to family, for his courage in adversity, and above all for his trust in God's mercy and goodness.

TABLE OF CONTENTS

LIST OF TABLES

LIST OF FIGURES

SUMMARY

Hypertension is a major risk factor for coronary artery disease, stroke, and kidney disease. Many studies suggest that elevated intramural stresses caused by hypertension may stimulate inflammatory changes, but little has been done to ascertain whether inflammation and stress are spatially correlated. Such correlations are a first step in identifying the mechanisms that may relate intramural stress to disease so that more effective treatments may be developed.

Arterial branches exhibit large variations in stress and are focal points for the onset of disease. Hence branches are a logical place to examine whether high stresses spatially correlate with increased inflammation. This research seeks 1) to develop a method that uses histological data to reconstruct small arterial branches; 2) to use finite element analysis to evaluate intramural stresses where experimental testing is of limited use; 3) to quantify biological measures of inflammation; and 4) to visually and statistically compare the distribution of stress with the distribution of inflammation.

Hypertension was induced in Sprague-Dawley rats by implanting Angiotensin II pumps for 7 days or 21 days. Normotensive rats were used as controls. To preserve morphology, the mesentery was pressure-fixed *in situ*, harvested, processed and embedded in glycol methacrylate resin.

The small size of the mesenteric arteries (100-300 μm in diameter) makes it difficult to determine stresses experimentally and underscores the need for analytical methods. This is particularly true when considering branches, with their more complex geometry and less clearly defined mechanical characteristics. Because of these experimental challenges, the finite element method was used to approximate the stresses.

Finite element analysis was applied directly to three-dimensional reconstructions from histology. The reconstruction technique involved reconstituting the original geometry from serial sections. Distortions produced by sectioning were determined and eliminated from each section. Then an image similarity measure was used to align serial sections. The inner and outer boundaries of the vessel were identified using a semi-automated segmentation technique. The boundary data was assembled as a point cloud suitable for surface reconstruction. Finally the inner and outer surfaces were combined to obtain a variable-thickness model of the midplane surface. This approach minimized memory and computational requirements while taking full advantage of the high in-plane resolution afforded by microscopy.

The branch reconstructions revealed a complex and variable pattern of geometric characteristics. Within a given branch, curvature and wall thickness varied considerably, leading to patterns of intramural stress that only roughly corresponded to the results from idealized finite element models. Geometry also varied considerably from branch to branch. In addition to thickness and curvature differences, branch angles and mother-to-daughter vessel size also differed significantly for each branch.

The pattern of inflammation was characterized by measuring the local density of monocytes and macrophages. Cell density was expressed as a distribution on the branch

surface. This mapping of cell density to the surface simplified visualization and facilitated statistical comparisons with stress.

This research shows that intramural stress is generally greater near branches. This trend was evident for nearly all hypertensive cases despite a pattern of greater wall thickness near branches. The thickness pattern may reflect an adaptive response to reduce mechanical stresses. Regardless of its origin, increased wall thickness near branches reduces the intramural stresses and limits the strength of the correlation between intramural stress and branch proximity.

Inflammation, as measured by monocyte/macrophage density, was greater near branches. The trend was stronger for the hypertensive cases than for the normotensive cases. One might infer that the difference arose from increased intramural stresses produced during hypertension. In most cases, however, high stresses and high cell density were not spatially collocated.

Wall thickness was negatively correlated to cell density for most cases. Increased inflammation in the adventitia adjacent to locations where the wall is thin is consistent with an adaptive response to elevated intramural stress.

Maximal wall tension was considered as an alternative mechanical correlate to von Mises stress and it represents the maximum midplane stress multiplied by the wall thickness. In hypertensive branches wall tension was generally strongly correlated both with branch proximity and with cell density. These trends were less well defined in the normotensive branches.

Wall thickness tended to be high where a constant thickness model would have predicted large stresses. This suggests the mechanical environment may locally control

the adaptive response within branches. But because wall thickness is related to both stress and inflammation, it is difficult to decouple the stress as a stimulus from inflammation as a response. The onset of hypertension is probably accompanied by an adaptive response that reduces the strength of correlations between stress and inflammation.

CHAPTER 1:

INTRODUCTION AND BACKGROUND

This chapter provides a context for understanding this research by reviewing the literature and discussing what is presently understood about the structure and function of arteries, along with pertinent information concerning three-dimensional reconstruction and analytical models. First the general structure and function of arteries is reviewed. Then, inflammation is described with observations suggesting hypertension stimulates inflammation and a description of possible mechanistic linkages. Next, three-dimensional reconstruction techniques are discussed that are suitable for small vessel branches. The review concludes with a survey of pertinent mechanical models, ranging from simple algebraic relations to finite element models.

Arterial Structure and Function

Some insights into how arteries function may be gained by a brief discussion of vessel structure. Arteries have a multilayered structure consisting of the intima, media and adventitia, with elastic laminae separating these layers.

The intima, the thin innermost layer, is composed of endothelial cells embedded in extracellular matrix (ECM) and attached to a basement membrane. Because the intima is antithrombotic and has a low permeability, it is well suited for contact with blood. The endothelial cells sense and respond to changes in the flow environment (changes from

homeostasis). For example, endothelial cells help control vascular tone by releasing vasoconstrictors or vasodilators to regulate pressure and flow (Ku 1997). Typically the intima is thin and can be neglected when considering the bulk stiffness of the vessel wall, but under certain circumstances the intima can thicken and may affect the stresses and strains produced by pressure loading. Separating the intima from the media is a membrane composed of elastin fibers called the internal elastic lamina. Microscopic holes in the internal elastic lamina may facilitate permeability control.

The media is a heterogeneous material consisting of smooth muscle cells, elastin and collagen and usually accounts for most of the thickness of the artery wall. During the 1960's, Glagov introduced the concept of a lamellar unit that is made up of elastin, collagen and smooth muscle cells (Wolinsky and Glagov 1964; Clark and Glagov 1985). Lamellar units have been proposed as the microstructural building blocks that characterize both the structure and function of the media. The lamellar unit helps explain how the various components of the media contribute to the overall mechanical characteristics of the blood vessel. At low pressures the elastin network bears most of the resulting stress and largely determines the wall properties. Elastin permits significant compliance and allows energy return over a wide range of deformations. As pressure increases more collagen fibers are brought into tension, accounting for the significant increase in wall stiffness. Smooth muscle cells provide active tension control (i.e. vascular tone) permitting rapid response to a variety of stimuli. In the small arteries that are the subject of the current study, smooth muscle cells can account for over 70% of the tissue volume (Mathieu-Costello and Fronek 1985). The external elastic lamina is a membrane that separates the media from the adventitia. This membrane is similar in

structure to the internal elastic lamina, but tends to have more microscopic holes (Gray 1973).

The adventitia is the outermost layer and its mechanical function is less well defined. In large vessels the adventitia often contains microvessels to improve nutrient and waste transport to and from the media (*vasa vasorum*). The media can be innervated from the adventitia to facilitate systemic signaling. In small vessels, like the mesenteric arteries in the present study, the adventitia is thinner than the media. Whether the vessels are large or small the adventitia contains a greater percentage of collagen fibers and less uniformity in structure than the media. The adventitia bears little of the pressure load until the internal pressure is large. At very high pressure the adventitia serves to reinforce the arterial wall and protects the artery from excessive stretch (Ogden and Schulze-Bauer 2000). The adventitia also tethers blood vessels to surrounding structures and helps distribute the axial loads that are exerted on vessels *in vivo*. After the onset of hypertension or atherosclerosis, the adventitia can significantly change. Initially there can be an increase in the number of fibroblasts followed by an increase in the amount of ECM (mostly collagen type I) (Xu, Zarins et al. 2000). In the late stages of disease the adventitia may be lost altogether, presumably because it has been stripped of its blood supply.

There is considerable interest in the development of microstructural models where the macroscopic behavior of the tissue is characterized by modeling the interactions of extracellular matrix components and cells. Such models hold promise for a greater understanding of how ECM components interact and may be adapted to changes in the mechanical environment. In addition, models that consider the role of cells in this

framework may provide insight into how cellular responses are mechanistically linked to gross changes in loading. Such models have great promise for the future, but require a more extensive understanding of the behavior and interaction of the building blocks on successive levels (Fung 1987). Since the interactions between microstructural components are not well understood and particularly difficult to quantify at branches, such models are beyond the scope of this research effort.

Under physiological conditions, arteries experience spatial and temporal changes in pressure and flow that affect the state of stress on the vessel surface and within the wall. Such stresses also vary due to the complex interactions of pressure and flow on the local geometry. Within limits, arteries can adapt to changes in pressure and flow, but beyond these limits the physiological response can be maladaptive. While the adaptive and maladaptive responses of arteries to the mechanical environment are not understood in detail, some general trends have been observed. For instance, arteries respond to increased flow by dilating until shear stress returns to a baseline level of about 15 to 20 dynes/cm^2. Regions of low fluid shear stress have been shown to stimulate intimal hyperplasia (Salam, Lumsden et al. 1996). Another example can be seen in how elevated circumferential stresses stimulate medial thickening. After the sudden onset of hypertension, there is a rapid increase in wall thickness helping reduce the levels of circumferential stress (Masuda, Bassiouny et al. 1989; Glagov, Bassiouny et al. 1997). While these examples help illustrate a relationship exists between form and mechanical function, they focus on tubular cross sections. Few studies have examined how changes in the mechanical environment affect branch morphology. This lack of research

represents a significant void, since the stresses vary greatly where arteries branch and these locations are common sites of atherosclerotic lesions.

Hypertension, Inflammation and Mechanical Forces

Hypertension and Atherogenesis

This section outlines evidence suggesting that hypertension and atherogenesis are interrelated pathologies. Subsequent sections describe the inflammatory process, discuss apparent correlations between mechanical forces and inflammation, and identify mechanisms by which intramural mechanical forces or deformations may be mechanistically linked to the onset and progression of the inflammatory changes.

While the focus of this research is to identify possible relationships between mechanical stress and hypertensive vascular disease, it is important to note that these investigations may also provide insight into the onset and progression of atherosclerosis. In fact, hypertension and atherosclerosis appear to be strongly interrelated pathologies.

Like atherosclerosis, hypertension is a major risk factor for coronary artery disease, stroke, and kidney disease (Wilson 1994). Individuals with high cholesterol are more likely to have high blood pressure. Large epidemiological studies (Framingham Study and the Multiple Risk Factor Intervention Trial, MRFIT) demonstrate that hypertension significantly increases the chances of atherogenesis and accelerates the development of atherosclerotic plaques.

Hypertensive vascular disease and atherosclerosis also share some common physiological and biochemical features. During both pathologies, there are functional changes in endothelial cells and smooth muscle cells. Endothelial cells lose their ability to regulate smooth muscle cell (SMC) tone and growth. Cell culture studies of smooth

muscle cells that are exposed to axial stretch tend to lose their contractile phenotype and tend to grow, proliferate and can migrate from the media to the intima (Griendling and Alexander 1998). Another common characteristic is the inflammatory response, which includes the recruitment of monocytes into the arterial wall and the activation of proinflammatory mechanisms within the tissue. Additional connective tissue is deposited in the adventitia and media. This structural remodeling often permanently alters vascular function. Since hypertension and atherosclerosis are interrelated, it is reasonable to hypothesize that elevated intramural stresses may play an important role in the onset of atherosclerosis. While the role of intramural stresses in atherosclerosis is not studied per se, the possibility of such a cause-effect relationship further underscores the significance of the current research.

ApoE-deficient mice lack the gene to synthesize apolipoprotein E, a glycoprotein that helps cells clear lipoproteins from the bloodstream (Piedrahita, Zhang et al. 1992). Consequently these mice develop high cholesterol and atherosclerotic lesions and serve as a good animal model for atherosclerosis (Zhang, Reddick et al. 1992; Breslow 1996). Hypertension has recently been shown to accelerate the development of atherosclerosis in apoE-deficient mice (Weiss, Kools et al. 2001A). These researchers showed norepinephrine-induced hypertension accelerates atherosclerosis even in the absence of any increase in Angiotensin II, thus highlighting the direct role that elevated pressure plays in atherogenesis.

Description of Inflammatory Response

Inflammation is primarily characterized by the recruitment of leukocytes from the blood stream to the extravascular tissue. Endothelial cells play an important role in the

recruitment by secreting chemotactic molecules and expressing adhesion molecules that interact with surface proteins on leukocytes (Griendling and Alexander 1998). Chronic inflammation involves the recruitment of monocytes from the blood stream and the differentiation of these monocytes into macrophages, which are actively phagocytic. Chemoattractants, such as monocyte chemoattractant protein–1 (MCP-1), are released and specific adhesion molecules are expressed to facilitate monocyte recruitment and differentiation. Selective responses of different leukocyte classes to inflammatory agents can largely be explained by their receptivity to distinct combinations of molecular signals from the vascular endothelium (Springer 1994).

Inflammatory responses not only protect the body from infection, but also allow for the removal of cell debris and damaged components of the extracellular matrix. This function is necessary after ischemia or trauma and may be important during remodeling. For example, patients suffering from leukocyte adhesion deficiency type I not only show compromised leukocyte recruitment due to the absence of β_2-integrins, but also show impaired wound healing (Walzog and Gaehtgens 2000). Such findings tend to support the thought that inflammation plays an important role in tissue repair and, possibly, in tissue remodeling.

Mechanical Forces and Inflammation

Without focusing on possible mechanistic links between intramural stresses and inflammation, a variety of experiments suggest the two may be correlated. Howard and his fellow researchers observed that cyclic stretch induced an oxidative stress within endothelial cell monolayers as measured by lipid peroxidation products and superoxide release (Howard, Alexander et al. 1997). They identified a nonphagocytic nicotinamide

adenine dinucleotide phosphate (NADPH) oxidase as a source for superoxide generation and concluded that mechanical deformation of endothelial cells may play a critical role in the creation of an oxidative stress in the vessel wall. In addition, Howard et al. concluded the pulsatile component of cyclic strain plays a critical role in the generation of oxidative stress. Further, they observed that oxidative stress persisted for 24 hours even after only 2 hours of cyclic strain; suggesting cyclic strain may trigger the onset of inflammatory changes but may not be needed for the response to continue.

Aortic coarctation has been used in an attempt to separate the effects of mechanical and humoral factors (Ollerenshaw, Heagerty et al. 1988). Ollerenshaw and colleagues studied the effects of pressure by considering segments of the aorta immediately above and below the site of coarctation. Above the ligature, medial area and thickness increased, hypertrophy occurred, but not hyperplasia. Below the ligature the structural changes were small and indicated a limited amount of atrophy. Time course data for 3, 9, and 20 days revealed the changes became statistically significant by day 9. The lack of hypertrophy or other structural changes below the site of coarctation suggests that downstream humoral factors did not significantly affect morphology. A rise in inositol phosphate production (involved in cell proliferation) was seen above the ligature, but no such increase was seen below, despite an increase in renin levels. Increased pressure appears to stimulate the growth changes. However the role of some humoral factors, such as Angiotensin II, cannot be entirely excluded.

More detailed studies of the mechanics of branch points suggest elevated stresses produced by hypertension are locally correlated with atherosclerosis. Salazar and his fellow researchers developed finite element models to determine the intramural stress

distribution in the carotid bifurcation (Salazar, Thubrikar et al. 1995). They found highly localized stress concentrations exist in regions that are susceptible to atherosclerotic lesions. A more detailed review of finite element models is presented later. Comparing results from a variety of experiments to the stress distribution suggest there is a phenomenological relationship between the location of elevated mechanical stresses and pathological changes such as medial thickening and plaque formation.

Monocyte chemoattractant protein-1 (MCP-1) is upregulated during Angiotensin II-induced hypertension in Sprague-Dawley rats (Capers, Alexander et al. 1997). MCP-1 is a potent chemoattractant for macrophage recruitment and is synthesized by vascular smooth muscle cells, endothelial cells, and macrophages. When hydralazine was used to normalize blood pressure there was a significant, but not complete inhibition of MCP-1 expression (Capers, Alexander et al. 1997). Capers et al. also exposed vascular smooth muscle cells plated onto a flexible membrane to 20 percent cyclic strains and found a significant increase in MCP-1 expression. By contrast, a constant strain of 20% produced no significant increase in MCP-1 expression. This finding suggests the oscillatory character of the loading is needed to amplify MCP-1 expression. Taken together, in vitro experiments, *in vivo* experiments, and analytical models all point to a phenomenological connection between mechanical forces and inflammation.

Possible Linkages between Mechanical Forces and Inflammation

The previous section discussed how changes in mechanical forces are correlated with an increase in inflammation, but does not elaborate on the specific mechanisms that might link the two phenomena. Recent studies indicate Angiotensin II may help stimulate the production of oxidative stress from a number of sources. In vascular cells,

Angiotensin II produces inflammatory changes and stimulates the generation of reactive oxygen species through multiple pathways. The oxidative stress produced by Angiotensin II upregulates the expression of many redox-sensitive cytokines (e.g. VCAM-1 facilitates monocyte adhesion), chemokines (e.g. MCP-1 induces migration of undifferentiated monocytes), and growth factors (e.g. IGF-1 in SMC hypertrophy) that have been implicated in hypertensive vascular disease and atherosclerosis. Acute release of Angiotensin II produces vasoconstriction, increases blood volume and can help modulate the systemic flow patterns. But chronic exposure to Angiotensin II produces proinflammatory changes. Recent studies with apolipoprotein E deficient mice indicate that when hypertension is induced using norepinephrine rather than Angiotensin II the atherosclerotic changes are less pronounced. This suggests that Angiotensin II plays an important role in linking the elevated forces with the onset and progression of inflammation. So when studying mechanical phenomena that stimulate hypertension it is important to consider that mechanical changes may also be enhanced by other phenomena, such as humoral and fluid mechanical changes. While this research might yield hypotheses about how intramural stresses are mechanistically linked to hypertension, rigorous testing of such hypotheses is not anticipated.

Three-Dimensional Reconstruction

Methods to Align Serial Sections

Three-dimensional reconstruction of serial sections can facilitate the full geometric description of complex structures and can be used to define the geometry for finite element analysis. In the case of small branching blood vessels, reconstruction of serial sections can accurately couple histology with the three-dimensional geometry. Advanced medical imaging techniques may not have adequate resolution to accurately

reconstruct the geometry of such small vessels, particularly since contrast enhancement can interfere with subsequent histology. Further, traditional imaging techniques cannot characterize the biology to the same extent as histological techniques. It is also difficult with small vessels to overlay the geometry from nonintrusive scanning techniques with the results from subsequent histological studies.

Because of the difficulties described above, it is desirable to reconstruct the three-dimensional geometry from serial histological sections. But distortions are introduced during various stages of tissue processing and are discussed in some detail in the following section. While the tissue processing and embedding protocol was designed to minimize distortions, such distortions remain and make it difficult to determine the original shape and alignment of serial sections. A registration technique is employed to help align serial sections and correct for the distortions.

The need for 3D reconstruction and the problems associated with serial section alignment have been recognized for over a century. The earliest methods used morphological characteristics such as symmetry to coarsely align sections. In addition, marks or notches made at the edges in the embedding medium have long been used to improve section alignment. Heard was among the first to introduce fiduciary marks within the block (Heard 1953; Jones, Milthorpe et al. 1994). Other researchers drilled holes perpendicular to the cutting surface of paraffin blocks (Dixon and Howarth 1957). More recently a method was presented that integrated registration and sectioning by drilling holes in a block after it is positioned in a microtome (Jones, Milthorpe et al. 1994). But difficulties associated with drilling include damage to the tissue and the tendency of the drill bit to drift as it cuts through the material. The latter problem is more

pronounced with small diameter drill bits and a more rigid embedding medium. In addition, these methods rely on the holes being placed in the tissue, since subsequent processing eliminates the paraffin and makes it impossible to identify holes that are not drilled through tissue.

Some of the early researchers inserted foreign objects such as nerve fibers or cactus spines so that the holes might be more easily identified. In the case of nerve fibers, holes were pre-drilled before the fibers were inserted (Burston and Thurley 1957). In the case of cactus spines, the researchers used an apparatus to advance the spines into the tissue *before* embedding (Deverell, Bailey et al. 1989A; Deverell and Whimster 1989B). The cactus spines were roughly positioned at regular intervals and perpendicular to the eventual cutting plane. The birefringence of the cactus spines made it easy to identify them during microscopy. This approach did not permit the placement of landmarks beyond the periphery of the tissue. In addition, embedded objects like cactus spines can be significantly stiffer than the surrounding embedding medium and can result in local distortions near the fiduciary marks that are not representative of the distortion pattern elsewhere in the section.

More recently, researchers have used a laser to produce registration holes (Yaegashi, Takahashi et al. 1987; Yaegashi, Zhang et al. 2000). Tissue was embedded in paraffin and then holes were created in the marginal areas of the tissue. However, like the drilling techniques, laser generated holes are lost in paraffin sections if they are located beyond the periphery of the tissue. An embedding medium that remains intact after staining helps eliminate the requirement that the holes be present within the tissue. Since an array of holes can be added after the tissue is embedded, the use of a laser

avoids some of the difficulties associated with embedding objects. However, preliminary attempts to use a laser with resin produced inconsistent results with variability in the size of the holes and peripheral damage to the resin near the holes.

Another approach to section alignment is to use an image similarity measure (ISM). ISMs can be used to make pixel-by-pixel comparisons of intensities between two images. A relatively simple image similarity measure is the Mean Square Difference (MSD) between images (Studholme, Hill et al. 1997).

$$MSD = \frac{1}{N}\sum_{x \in X}\left[I_2(x) - I_1(x)\right]^2 \qquad \text{Equation 1.1}$$

In this equation N represents the number of pixels over coordinate space x, while I_1 and I_2 represent serial images. The result of an ISM is a scalar measure of the degree of similarity existing between two images. In the case of the mean square difference, the image similarity measure is minimized during alignment, but other similarity measures seek to maximize the scalar result (e.g. Normalized Mutual Information and Pattern Intensity (PI)). In general, a gradient descent method can be used to align one section over another and this will be further discussed in Chapter 3.

Such techniques have been used to align patient brain MRI with a database of brain data (Holden, Hill et al. 2000) and to align and overlay images generated from different imaging modalities (Studholme, Hill et al. 1997). For larger vessels, an ISM might even be used to correct for deformations due to embedding and sectioning if one imaging modality (MRI or microCT) represents the undeformed geometry. Image similarity measures may also be used to align serial sections when there is no common frame of reference provided the sections are close to one another and share a common set of features.

Methods to Correct for Section Deformations

As mentioned earlier, various stages of tissue preparation can introduce distortions that affect how accurately the sections represent the *in vivo* geometry. Distortions can be produced during sectioning and staining, but can also be produced by sample preparation steps before embedding. The magnitude of the distortions can vary significantly depending on the type of tissue as well as how the tissue is processed (Bancroft and Stevens 1996). Formalin fixation and temperature decrease from *in vivo* to *ex vivo* conditions are two possible sources of distortion before the tissue is embedded. One study found that Formalin fixation increases the size of diseased carotid arteries by 2%-3%, while the decrease from body temperature to room temperature (37 ^{o}C to 23 ^{o}C) caused a 4%-7% expansion (Dalager-Pedersen, Falk et al. 1999). Another study found that Formalin fixation of porcine aortas at zero transmural pressure resulted in, on average, a 25% swelling of the arterial wall, but that Formalin fixation at physiological pressure resulted in no significant dimensional changes (Wilhjelm, Vogt et al. 1997). Variability in Formalin fixed sections is caused by delay of fixation and variations in the duration of the fixation. Starting fixation soon (<30 min) after removal of the tissue and avoiding over-fixation (>24-48 hours) can help reduce the distortions and variability associated with Formalin fixation (Werner, Chott et al. 2000). An examination of various immersion fixatives and embedding media found high quality sections were produced by using glycol methacrylate resin as the support medium for the sectioning of Formalin-fixed tissue (Chapin, Ross et al. 1984). If the distortions *before* embedding are determined to be significant, a global correction might be applied to scale the entire geometry or the wall thickness.

While the deformations are introduced during various stages of sample preparation, the most significant deformations appear to be introduced during the sectioning process. Compression in the cutting direction and surface tension on the water bath are two prominent sources of deformation. One early method to correct for such deformations involved photographing the face of the block and then comparing these images to the images of sections to rectify the distortion (Heard 1953). The magnitude of the deformations can vary significantly among soft tissues. For instance, one study showed the mean dimensional changes in the cutting direction to be 10.5% for lung, and 20.3% for skeletal muscle (Jones, Milthorpe et al. 1994). Researchers have recognized that tissue distortion will significantly affect the size and shape of the 3D reconstruction, and that accurate reconstruction requires correction for these deformations and standardization of all aspects of tissue preparation (Deverell, Bailey et al. 1989A).

Resolution Sciences, Inc. has developed specialized and proprietary methods to stain tissue before embedding. Fluorescent imaging of the block face is used to generate a stack of aligned images. This unique method has two advantages over traditional methods: It captures geometry before the tissue is sectioned and it simultaneously captures geometric and histological data. But the method currently has limitations: 1) sections are destroyed, 2) the method can only be applied to very small samples (less than 5x5x5 mm) with the resolution decreasing as sample size increases, and 3) a comparatively small variety of histological data may be collected. So while this method has significant advantages, the current limitations make it unsuitable for this research.

Mechanical Characteristics of Arteries and the Need for Analytical Studies

Earlier the structure and function of arteries was discussed. The layered, heterogeneous microstructure of arteries gives them their unique mechanical characteristics. Arteries exhibit nonlinear, anisotropic and viscoelastic material behavior. Under physiological pressures, these blood vessels experience large deformations, stress relaxation and creep (Fung 1993B). For simplicity, the stress strain behavior of blood vessels is often modeled as bilinear, being compliant at low pressures and very stiff at high pressures. Interestingly, the transition from compliant to stiff behavior tends to occur in the range of physiological pressures, suggesting that this bilinear behavior serves a functional purpose (Wolinsky and Glagov 1964). The bilinear behavior is connected to the heterogeneous microstructure of arteries. At low pressures elastin bears most of the strain induced by pressure. This elastic compliance reduces pressure peaks, and facilitates efficient distribution of blood downstream.

On a microscopic scale, arteries are highly heterogeneous. The bulk mechanical behavior depends on the properties of the various microstructural components, the proportions of the components, and the manner in which they are coupled (Gaballa, Raya et al. 1992). There is a great deal of interest in how stresses and strains are locally distributed between the cells and the extracellular matrix components. A more detailed understanding of stress and strain distribution could provide insights into how cells respond to the mechanical environment, what adaptive changes are made in the ECM, and how these responses and adaptations might lead to pathology.

There are numerous experimental methods that have been used to determine mechanical properties of arteries (Hayashi 1993). Most strain measurements are made

using surface particle tracking and it is important to consider to what extent the surface strains are representative of the strains through the wall. While it may be reasonable to assume constant strain through the thickness under some circumstances, it is probably not a good assumption proximity to a vessel bifurcation where high intramural stress gradients are present. This shortcoming of mechanical tests is part of the motivation for studying the local changes in stress and strain with analytical models, but the small size of the subject vessels provides another reason.

The mesenteric arteries studied in this research are only a few hundred micrometers in diameter. This small size precludes detailed mechanical testing, especially because of the interest in the variations of stress where vessels branch. Based on finite element studies and a limited number of experimental studies of larger vessels, intramural stresses appear to vary significantly in proximity to branches (Thubrikar, Roskelley et al. 1990; Fung and Liu 1992; Delfino, Stergiopulos et al. 1997). Studies have also shown that adventitial collagen is more highly organized at the apical or saddle region (Finlay, Whittaker et al. 1998), a structural adaptation that is consistent with a higher stress region. In addition, Liu and Fung (Liu 1998; Liu and Fung 1998) observed localized differences in the alignment of SMC actin filaments from the predominantly circumferential orientation seen elsewhere in mesenteric veins and arteries. But to capture the local variation of stresses in the presence of such large gradients is beyond current experimental capabilities. Given this limitation, experimental studies must be supplemented with analytical studies to more fully characterize the local state of stress and strain.

Analytical Methods to Study Mechanical Behavior

Elementary Mechanical Models

Various researchers have discussed sources of stress concentration in branching blood vessels (Willis 1954; Thubrikar and Robicsek 1995; Fung 1997). Stress concentrations can be produced with increased radius of curvature or in situations where one of principal radii of curvature is outside the wall. This phenomenon will be described in greater detail later in this section. Both of these conditions can produce local flattening necessitating greater wall stresses to resist the internal pressure. When a daughter vessel branches from a main vessel, the ostium produces a stress concentration analogous to an elliptical hole in a plate. Another source of elevated stress is bending stresses that can be produced in the transition region where vessels branch. These bending effects tend to be large at the junction of two vessels and are likely to be amplified by hypertension and longitudinal strains.

The following paragraphs will elaborate on some of these mechanisms using elementary mechanical models. The *in vivo* production of elevated stress at branch points is a complex phenomenon that cannot be captured by simplified models. While elementary models of blood vessels have many limitations, they can provide some insight into how geometry and pressure can produce large intramural stresses. Because the mesenteric arteries used in this study have a radius-to-thickness ratio of about 5:1, the circumferential stress varies significantly through the thickness. Thick-walled vessels can exhibit significant bending rigidity in response to internal pressure. Equation 1.2 represents a thick-walled model for a linear elastic cylindrical tube. This equation

describes how internal pressure (P) produces circumferential stress (σ_{circ}) and how this stress varies in the radial direction:

$$\sigma_{circ}(r) = \frac{r_{in}^2}{r_{out}^2 - r_{in}^2}\left[1 + \frac{r_{out}^2}{r^2}\right]P \qquad \text{Equation 1. 2}$$

In this equation, r represents the radial location where the stress is calculated, r_{out} is the outer radius of the wall, and r_{in} is the inner radius of the wall. This thick-walled model illustrates the variation of circumferential stress through the thickness of a vessel. When residual stresses are considered, the circumferential stress in proximity to the endothelium may actually move from tension to compression with decreasing intramural pressure. Another benefit of considering the thick-walled model it helps confirm that a finite element model captures the fundamental mechanical response of cylindrical cross sections away from the transition geometry. If a linear stress-strain relationship is used in the finite element model, Equation 1.2 might be used to help evaluate convergence and the magnitude of artifacts introduced by boundary conditions.

Unfortunately, there is no closed-form solution for the stress distribution where a daughter vessel branches from a main vessel. Despite this limitation, there is more to be learned from elementary models by considering how curvature can influence the state of stress. Neglecting the variation of stress through the thickness permits the application of membrane (thin-walled) theory. Laplace's Law describes the state of equilibrium of a curved membrane subjected to pressure. The membrane stress ($\sigma_{membrane}$) can be described as follows:

$$\sigma_{membrane} = \frac{P/h}{\left(\frac{1}{R_1} + \frac{1}{R_2}\right)} \qquad \text{Equation 1. 3}$$

In Equation 1.3, P represents the internal pressure, h is the membrane thickness, and R_1 and R_2 are the principal radii of curvature. This equation neglects external pressure and assumes that the membrane stress is independent of direction. For the case of a straight tube, $R_1 = R$, and $R_2 \Rightarrow \infty$, and the Law of Laplace yields the mean circumferential stress:

$$\overline{\sigma}_{circ} = \frac{PR}{h} \qquad \text{Equation 1. 4}$$

But if the tube is not straight and the radius of curvature of the bend is within an order of magnitude of the tube radius, both radii in Equation 1.3 must be considered. Such a condition is depicted in Figure 1-1 and the state of stress can differ significantly from the inner curve to the outer curve.

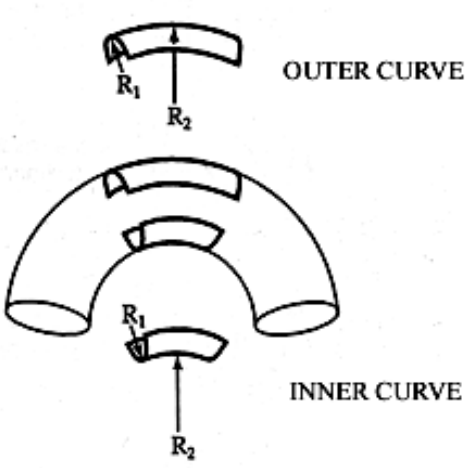

Figure 1-1: Schematic of the principal curvatures of a curved tube (Thubrikar and Robicsek 1995).

The Law of Laplace yields the following equations for the inner and outer curves:

$$\sigma_{outer\ curve} = \frac{P/h}{\left(\frac{1}{R_1} + \frac{1}{R_2}\right)} \qquad where \quad \sigma_{outer\ curve} < \overline{\sigma}_{circ} \qquad \text{Equation 1. 5}$$

$$\sigma_{inner\ curve} = \frac{P/h}{\left(\frac{1}{R_1} - \frac{1}{R_2}\right)} \qquad where \quad \overline{\sigma}_{circ} < \sigma_{inner\ \ curve} < \infty \qquad \text{Equation 1. 6}$$

As illustrated by Figure 1-1 and Equations 1.5 and 1.6, the stress on the inner curve can be significantly greater than the stress on the outer curve, assuming the wall thickness remains constant. On the inner curve the two principal radii of curvature have origins on opposite sides of the vessel wall. These opposing curvatures produce opposing wall tensions in a force balance and, therefore, have opposite signs in Laplace's equation (Willis 1954). When the two radii of curvature are approximately equal, the wall tensions in the principal directions are nearly equal and opposite, requiring a high membrane stress to resist the force due to pressure. This is physically represented a local region where the membrane wall is nearly flat and the stress must be very large to resist the internal pressure. In the limit where the curvatures are equal and opposite the membrane stress theoretically is infinite. This phenomenon is the three-dimensional analog to a taut horizontal cable bearing a vertical load.

The consequences of Laplace's Law are reflected in the variation of thickness where vessels are curved. The wall is thicker along the inner curve as compared to the outer curve in Figure 1-1 so that the tangential wall stresses remain relatively uniform. For example, the carotid siphon follows a curved path and the wall thickness along the inner curve is substantially greater than the thickness along the outer curve (Wolf and Werthessen 1976). Researchers have observed that the inner curves of the abdominal

aorta and the carotid sinus are common sites of atherosclerotic plaques (Thubrikar and Robicsek 1995).

The pattern of opposing curvatures is also present where vessels branch. Therefore elevated intramural stresses may help explain why locations such as the carotid bifurcation and coronary branches are common sites of atherogenesis. However, applying the Law of Laplace clearly has some limitations. This method does not permit variation in wall thickness, more complex variation in curvature, nor does it capture stress variations associated with localized bending. Arteries not only exhibit these complexities but also exhibit material nonlinearity, orthotropy, heterogeneity, and large deformations.

The simplifying assumptions necessary to obtain any of the closed-form analytical solutions previously discussed stand in contrast to the inherent complexity of branching arteries. This contrast underscores the need for a more sophisticated approach for modeling the mechanical behavior of branches. The finite element method permits the researcher to address such complexities and has been used extensively to study blood vessels.

Finite Element Models

Finite element analysis permits a given domain to be divided into subdomains, called finite elements, in which an approximate solution can be determined. The ability to discretize the domain into elements has three major advantages: 1), it allows the accurate representation of complex geometry; 2), it permits the inclusion of dissimilar materials; and 3), it enables the accurate representation of the solution within each element to bring out local effects (e.g. large gradients within the solution).

Because of its flexibility and power, the finite element method has been used to produce a variety of vascular models. The model characteristics have varied greatly, depending on the emphasis of the research effort. This review focuses on previous efforts to model solid-fluid interactions and branch geometry.

Thubrikar and colleagues have developed orthotropic shell element models of a coronary artery branch (Thubrikar, Roskelley et al. 1990) and the carotid bifurcation (Salazar, Thubrikar et al. 1995). In both cases they found the stress concentrations were collocated with known sites of atherogenesis. They hypothesized that the elevated stresses could injure the artery and make it susceptible to atherosclerosis. Stress concentration at branches and wall fatigue due to pulsatile blood pressure were considered to be relevant to atherosclerosis (Thubrikar and Robicsek 1995).

Poroelastic and biphasic models (Kwan, Lai et al. 1990; Prendergast, Driel et al. 1996; Simon, Kaufmann et al. 1998B) consider fluid-solid interactions within soft tissues like blood vessels. It has been demonstrated that the primary fields in the poroelastic and biphasic mixture theories are related by a change in kinematic variables so the two formulations produce equivalent results (Simon 1992). Much of the early modeling focused on cartilage and helped explain the high compressive stiffness during rapid compression, as well as the creep and stress relaxation characteristics (Mow, Ratcliffe et al. 1992). But compression may be present in blood vessels, particularly where vessels branch. A poroelastic or biphasic model could help explain how arteries support compressive loads and how compression might affect fluid and species transport related to leukocyte recruitment.

Holzapfel and colleagues (Holzapfel, Gasser et al. 2000; Holzapfel, Stadler et al. 2002) considered the three-dimensional geometric changes in straight segments of arteries produced by balloon angioplasty. The *in vitro* studies were conducted on aged human external iliac arteries within 24 hours of death. Uniaxial stretch experiments were conducted on axial and circumferential strips of intima, media and adventitia. The tissue was further classified by disease state. Histological studies were used to correlate MRI data with tissue type. This multimode approach to tissue characterization has great value, particularly when atherosclerotic legions are present. But such an approach is not possible for the small mesenteric branches that are the subject of this research.

The effect of fluid shear will not be considered in the present study. To examine the effect of fluid shear on the lumen would require coupling the finite element model of the vessel wall with a finite difference model of the blood flow. Ultimately, the convergence of solid and fluid models into one unifying mathematical model will be important, but this is beyond the scope of this research. This research compares hypertensive and normotensive states of stress where cardiac output remains approximately the same, so the changes in fluid shear are not pronounced. Also, the magnitude of fluid shear stresses is small compared to the magnitude of intramural stresses. For these reasons it is believed that the direct effect of fluid mechanics on the intramural state of stress is small. Yet it is possible that a synergy exists between the fluid and solid mechanical signaling pathways. Consideration of solid mechanical deformations of the vessel wall could also improve the accuracy of fluid mechanical models.

Residual stresses exist in the wall when a vessel is removed from its physiological loading environment. These residual stresses are most graphically demonstrated with excised rings of vascular tissue. When an artery is transversely cut into rings and then cut radially, these rings open up and the angle of the opening is a measure of the bending stresses that exist in the vessel when there is no internal pressure (Han and Fung 1991; Matsumoto and Hayashi 1993). As indicated by a recent study of coronary arteries, the opening angle and residual stresses tend to increase as one descends the arterial tree(Guo and Kassab 2004). To account for residual stresses where a vessel branches, researchers have measured opening angles in the carotid bifurcation and produced a finite element model accounting for these residual stresses (Delfino, Stergiopulos et al. 1997). Delfino and his collaborators found that the inclusion of residual stresses produced a much more uniform circumferential stress distribution within the carotid bifurcation. Other researchers have also found residual stresses tend to reduce circumferential stresses and stress gradients at *in vivo* pressures (Chaudhry, Bukiet et al. 1997).

Residual stresses are also present in the longitudinal direction. This is evidenced by the fact that arteries retract from their *in vivo* length when they are excised (Han and Fung 1995). Researchers have analytically and experimentally considered the role of extension in the mechanical behavior of straight vascular sections (Ogden and Schulze-Bauer 2000). Increased axial loads tend to reduce the circumferential stretch produced by blood pressure. However past studies of branch mechanics have neglected the role of axial loads on the local state of stress.

CHAPTER 2:

HYPOTHESES AND OBJECTIVES

The previous chapter outlined what is understood about the structure and function of arteries during the onset of hypertension and inflammation. Challenges exist in determining the geometry, evaluating the stress distribution, and quantifying the inflammatory state of small arterial branches. It is important to keep in mind that the goal in addressing these challenges is to help investigate a broader scientific question: Do intramural stresses associated with hypertension help stimulate inflammatory responses? In this context, more focused hypotheses were framed, leading to the following specific aims and research objectives:

Specific Aim 1: *Determine if intramural stresses and/or wall tension are locally elevated near branch points.*

The working hypothesis is that mechanical loads in the vessel wall peak where vessels branch. More specifically, the focus is on comparing the magnitude of midplane stresses near to and distant from the branch point. In addition to midplane stresses, wall tension is also considered. Wall tension is an alternative mechanical correlate to stress that readily can be expressed at the midplane of the geometry.

Specific Aim 2: *Determine if inflammation, as measured by the density of monocytes and macrophages, is more concentrated near the branch.*

It is hypothesized that vascular inflammation is more concentrated in proximity to arterial branches than at locations farther away from the branch. A localized measure of monocyte and macrophage cell density has been developed to help prove or disprove this hypothesis.

Specific Aim 3: *Determine if there is a spatial correlation between the regions of high intramural stress and measures of inflammation.*

The working hypothesis is that intramural loads such as stress and wall tension are locally greater where inflammation is greater. As previously mentioned, monocyte and macrophage density is the primary measure of inflammation. Wall thickness is also considered a measure of the inflammatory response, but since wall thickness affects the level of intramural stress it is also coupled to stimulus in the hypothesized paradigm. For this reason the distribution of wall thickness is not relied on as a primary measure of inflammation.

The following research objectives identify specific tasks that must be accomplished to quantify the problem. These research objectives represent landmarks in the larger research effort and flow directly from the specific aims:

Objective 1: *Develop a histology-based reconstruction technique for small arterial branches that corrects for deformations caused by histology and aligns serial sections.*

Objective 2: *Develop a generalized approach for creating finite element models from the three-dimensional reconstructions.*

Objective 3: *Identify markers of inflammation and characterize the three dimensional distribution of inflammation in a manner that facilitates comparison with finite element results.*

Objective 4: *Visually compare the spatial distribution of intramural stress to the distribution of inflammation.*

Objective 5: *Statistically compare the spatial distribution of intramural stress to the distribution of inflammation.*

These five objectives provide a framework for describing the materials and methods in the next chapter.

CHAPTER 3:

MATERIALS AND METHODS

This chapter describes the materials and methods used in this research. Because a considerable amount of development and validation work was done, this chapter also contains these supporting details. This organization keeps methods, development work and validation grouped together by subject, rather than creating separate chapters for each process (e.g. Methods Development, Validation, etc…). For convenience, a methods overview section precedes the more detailed descriptions.

Methods Overview

The methods developed and used in this research can be categorized broadly into data collection, consolidation, and comparison. Data collection steps include animal preparation, tissue processing, embedding, sectioning, staining, and microscopy. Data consolidation includes three-dimensional reconstruction, characterization of the stress distribution, and quantification of the distribution of inflammation. Data comparison involves visualization of data, spatial comparisons within a given branch, comparisons between branches from different animals, and comparisons between stress and inflammation data that are spatially collocated.

Figure 3-1 is a flowchart that summarizes the major steps involved in accomplishing this work. This flowchart illustrates how the different demands of

characterizing inflammation and stress lead to a bifurcation in the approach. The primary reason for this bifurcation is that a much higher in-plane image resolution is needed to identify inflammatory cells than to identify vascular structures for reconstruction. The reasons for the difference in resolution will be further discussed over the course of this chapter.

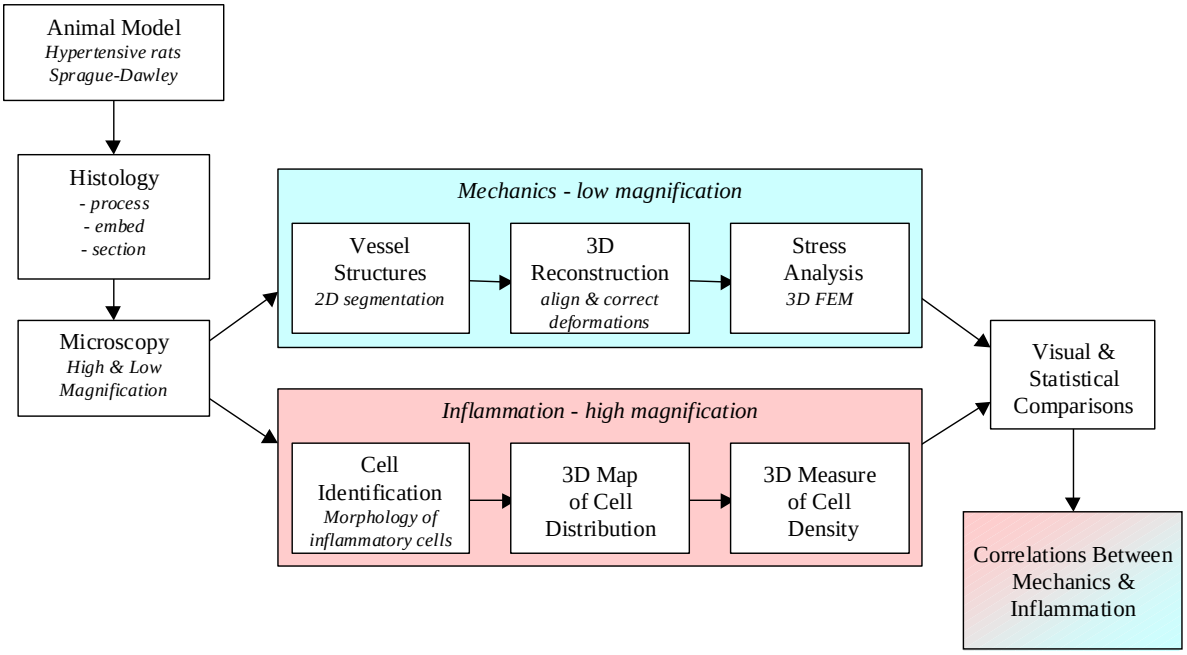

Figure 3-1: Flowchart of research.

Angiotensin II was used to induce hypertension in Sprague-Dawley rats. The mesentery of seven rats was harvested, embedded and sectioned. This included four 7-day hypertensive rats, one 21-day hypertensive rat and two normotensive rats. Arterial branches from each rat were identified and reconstructed. The goal was to quantify the distribution of stress and the distribution of inflammation in a branch and to determine whether visual similarities or statistical correlations existed.

The mesenteric tissue was pressure fixed and embedded in a glycol methacrylate (GMA) resin that is designed to preserve morphology while permitting immunological identification of inflammatory markers. However, the use of immunological techniques on GMA sections proved difficult and yielded inconsistent results. Morphological identification of monocytes and macrophages at high magnification reduced the section-to-section variability and produced more consistent results. The consistency was particularly important since the goal was to characterize the three-dimensional pattern of inflammation in branches.

Pins were embedded and then removed from the resin before sectioning. The resulting holes in each section were used to correct for section deformations. Because of the small size of the branches (100-300 μm) the pins did not prove to be an accurate way to align sections. Instead of using the pins for alignment, an image similarity measure was used. For an image similarity measure to more accurately drive histological alignment, the serial images must be sufficiently close to one another so that they share common features like cellular structures. In the mesentery tissue a distance of 10 μm provided adequate overlap of small features for alignment.

To identify the inner and outer boundaries of the vessel wall, anisotropic diffusion was used to preferentially blur features that were not near strongly delineated boundaries (Perona and Malik 1990). This was accomplished by spatially and directionally varying the diffusion coefficient based on the local gradient magnitude. This technique holds great promise, but still required sample-to-sample adjustments and manual identification of some boundaries.

After correcting for section deformations, aligning sections and identifying boundaries, the inner and outer boundaries were separately assembled into point clouds. These point clouds were then used to reconstruct the inner and outer branch surfaces. For purposes of finite element analysis, the branch must be represented as a midplane surface that includes discrete wall thickness measurements at each point on the surface.

A ray-tracing algorithm was utilized to identify the midplane points and local wall thickness measurements between the inner and outer surfaces. The resulting midplane surface was used as the basis for a variable thickness shell element model within Ansys.

Since the branches were pressure fixed at 80 mmHg, the pressure applied to the finite element models is the incremental pressure increase above 80 mmHg. Therefore, the stress results represent incremental stress changes from the pressure fixed geometry. A variety of stress correlates were considered with von Mises stress and maximal wall tension being most extensively used.

The raw data describing inflammation was a three-dimensional point cloud of inflammatory cells (monocytes and macrophages) that was aligned with the branch geometry. The cell distribution in a branch was expressed as a series of local cell density measurements. A sphere with a 150-μm radius was used for the local cell density calculations. The volume of lumen within each sphere must be excluded from consideration since no inflammatory cells are present in this region. When the spherical subvolumes are centered on each point of the luminal surface, a color-coded map of cell density can be produced. Using this approach the cells themselves do not need to be visualized to describe cell density with respect to the branch geometry. Expressing cell

density on the branch surface also facilitates comparisons between cell density and mechanical stresses since both are now quantified at the same spatial location.

To better understand the distribution of branch characteristics, a measure of branch proximity was created. The minimum distance between each surface point and the nearest branch was defined as a separate branch characteristic that is inversely proportional to branch proximity. Defining such a characteristic permitted a more rigorous analysis of whether other characteristics were elevated in proximity to a branch. In the end, the core branch characteristics that were studied in detail were von Mises stress, maximal wall tension, cell density, wall thickness and branch proximity (as indicated by minimum distance from a branch).

Branch characteristics were compared using two different approaches. First the color-coded distributions of branch characteristics (e.g. stress and cell density) can be visually compared side-by-side, but any two characteristics can also be statistically compared if they are treated as paired observations. The statistical analysis was further subdivided into Spearman rank correlations and a Wilcoxon rank sum test. The Spearman rank correlations were performed on the full range of data. The Wilcoxon rank sum test was performed by comparing subgroups of data and evaluating whether some threshold value might be associated with the proposed stimulus and response. Given this overview, a more detailed description of the methods will now be provided.

Animal Preparation

Male Harlan Sprague Dawley rats, aged 7 to 9 weeks received Angiotensin II (0.75 mg/kg/d) infusions from implanted osmotic pumps. The rats were euthanized by CO_2 narcosis after 7 days for the baseline experiments. Before the mesentery was

excised, the heart and downstream vasculature were pressure-perfused with 0.9% sodium chloride solution and then pressure-fixed at 80 mmHg with a 4% formaldehyde solution. The pressure fixation was continued for 1 hour, and then the mesentery tissue was excised. Because data suggests that macrophage migration, MCP-1 expression, and SMC hypertrophy were manifest by day 7 (Fukui, Ishizaka et al. 1997), a 7-day exposure was selected. A second, longer exposure time was considered for evaluating structural changes, since such changes tend to be more fully expressed by day 21.

Table 3-1: Summary of Sprague-Dawley rat experiments that yielded intact branches suitable for analysis. The original rat designation is shown in the right-most column.

Sample Name	Pressure State	Drug Treatment	Rat Identifier
H7A	Hypertensive	7-day exposure to Angiotensin II	R5
H7B	Hypertensive	7-day exposure to Angiotensin II	R8
H7C	Hypertensive	7-day exposure to Angiotensin II	R1D
H7D	Hypertensive	7-day exposure to Angiotensin II	R4
H21A	Hypertensive	21-day exposure to Angiotensin II	R10B
NA	Normotensive	none	R2
NB	Normotensive	none	R3

Table 3-1 summarizes the samples that ultimately produced intact branches that were suitable for finite element analysis. Several branches were truncated by how the tissue was embedded or were not fully contained in the 1 to 2 mm window of histological sections. A few additional branches were excluded based on unusual geometry features consistent with deformations during processing or embedding. The naming convention indicates 1) whether the sample was hypertensive or normotensive (H or N), 2) the nominal duration of hypertension (7 or 21 days, if applicable), and 3) a letter designation

that uniquely identifies the sample within the group. The rat identification number is included in the right-most column. This designation is not used in the text but may be helpful when referring to the raw data or the programs in the appendices.

The primary focus was on possible correlations between stress and inflammation during the onset of hypertension, and therefore, the majority of animals were studied after a 7-day exposure to Angiotensin II. One of the challenges in the experimental design was that a branch of interest could not be pre-selected; thus, a considerable variety in branch geometry can be seen from animal to animal. The geometric variations created a significant challenge when comparing data from different animals. For this reason greater emphasis was placed on comparisons between vessel characteristics for a given branch than on comparisons between branches. Nonetheless, two control animals were harvested where the pressure was normotensive. In addition, one 21-day study was performed to compare and contrast with the four 7-day studies. In total, 10 animals and 17 samples were processed, but there was attrition during processing. Some harvests did not yield rich beds of mesentery and no branches in the size range of interest were present over the interval of block that was cut. In other cases the tissue was damaged during processing and embedding. See Appendix C for more information about the animal studies.

Tissue Processing and Embedding Procedures

A glycol methacrylate (GMA) resin was chosen as the embedding medium (see Appendix D for complete embedding protocol). The particular GMA resin used is produced by Polysciences (Immuno-Bed™ Kit, Catalog Number 17324) and is designed for light microscopy and immunohistochemistry. Polysciences' GMA resin resembles

JB-4 medium in tissue infiltrations, embedding, and cutting procedures. This resin has greater rigidity than the paraffin at room temperature and is less likely to exhibit significant deformations when mounted on slides. The use of GMA also permits the placement of registration holes outside the embedded tissue. Such holes would be lost in paraffin sections, since the paraffin must be removed prior to staining. To create the holes, a registration fixture was designed to hold pins in place in the resin. After polymerization the fixture and pins were removed leaving an array of holes. The use of the registration fixture will be discussed later in this chapter.

Preliminary efforts to section the mesenteric tissue revealed that embedding a rolled sample of the mesentery in paraffin did not adequately preserve vessel geometry. The tissue was rolled to provide better gross stability for sectioning, but this process also introduced additional deformations. The magnitude and pattern of the deformations varied with sectioning procedures. Specifically, changes in embedding medium, embedding procedures, blade sharpness (more of a problem with paraffin than resin), blade temperature, bath temperature, length of time in bath, and bath surface tension all affected the ultimate shape of the cross sections. Further investigation revealed the paraffin embedding produced larger deformations and also a less uniform deformation pattern. The fact that the mesentery has little inherent rigidity may explain why paraffin is a less suitable embedding medium for preserving the geometry. The reader should bear in mind that tissue sample registration and preservation of tissue geometry are of critical importance in this research.

GMA provided adequate structural stability with free-floating samples; therefore, a problematic practice of rolling the tissue could be avoided. Methyl methacrylate

(MMA) resin was another possible choice for embedding media, but like paraffin the MMA is removed prior to staining causing fiduciary marks to be lost.

A disadvantage of resin sections is that they are more susceptible to folding and splitting. These problems can be overcome because they tend to be more prevalent around the periphery of the tissue causing gross distortions that are easily identified. During the course of this research, the embedding and sectioning methods were further optimized to limit such section damage. Even in the case of damaged sections, all or part of a section can be eliminated from consideration during subsequent histology. While some resin sections must be rejected because of obvious damage, the overall quality of the 3D reconstruction is improved because the damaged sections are much easier to identify and eliminate from consideration. The GMA sections that have no obvious folds or splits have greater uniformity than paraffin sections. Also, because GMA can be more readily sliced into thinner sections (2-5 micrometers) than paraffin, more data is available for reconstruction. There are numerous branches in the mesentery and several blocks can be cast from a single animal. Therefore obtaining a series of sections necessary to complete a reconstruction was possible, even when the location of a specific branch could not be identified until after staining. The reconstruction technique used was in part selected for its ability to readily accommodate lost or damaged sections provided sequential sections were not lost.

Sectioning and Staining Procedures

After polymerization the registration fixture and pins were removed, the embedded specimen was sanded and glued to a rectangular Lexan block that could be more rigidly held by a standard specimen clamp in a Microm HM 355S Rotary

Microtome. This microtome has a motorized cutting movement with retraction and a tungsten carbide blade was used (Delaware Diamond Knives). These microtome features help assure consistency and uniformity in the sectioning process. The embedded block was oriented so its long axis was approximately parallel to the edge of the blade. The clearance angle between the blade and the specimen face was set to seven degrees. The cutting speed was approximately 40 mm/s, but the speed was often varied from specimen to specimen to prevent section curling or incomplete sectioning. The sections were individually removed and floated out on a deionized water bath at room temperature. The sections were left on the water bath for approximately 1 minute to allow the sections to fully unfold and to generally reduce localized distortions caused by sectioning. When a GMA section is placed on the water bath, it rapidly moves around on the surface as it unfolds. This movement is driven by the surface tension being broken where the edges of the section are unfolding.

The sections were removed after the movement stopped and the sections achieved a uniform appearance. Early examination of this effect indicated that extending the time that the section remained on the water bath did not continue to stretch the section to any significant degree. A small quantity of detergent (Triton X-100) had been added to the water bath to observe what effect this had. The addition of the detergent substantially reduced the surface tension, decreased the section movement on the water bath and limited the net expansion that was induced in the section. One drop of Triton X per liter of water produced about a four percent expansion as opposed to about a ten percent expansion with no detergent. It was not determined if the reduced surface tension also reduced how well the section flattened out on the water bath, but one might expect

section-to-section differences in distortion to be larger with a lower surface tension. Sections did not stay on the slides as well with the addition of Triton X.

To identify vessel structures and inflammatory cells, the sections were stained using a modified haematoxylin and eosin (H&E) stain (see Appendix D for protocol). Early efforts to stain GMA sections revealed that the integrity of the resin was affected by exposure to mixtures of water and alcohol and also by transitions from water to alcohol. Therefore, an aqueous eosin solution was used and the alcohol exposure was limited to a three-second dip in an acid alcohol solution to help differentiate the haematoxylin stain. The resulting stain provided adequate detail to identify monocytes/macrophages at high magnification. This method produced less section-to-section variability than immunological methods but did not provide information about cell activity.

Microscopy

Figure 3-2 illustrates the relative size of features on a cross section. A typical area of interest is shown of an arterial branch. Three rectangular regions show the relative fields of view for a 4x, 20x, and 40x objective.

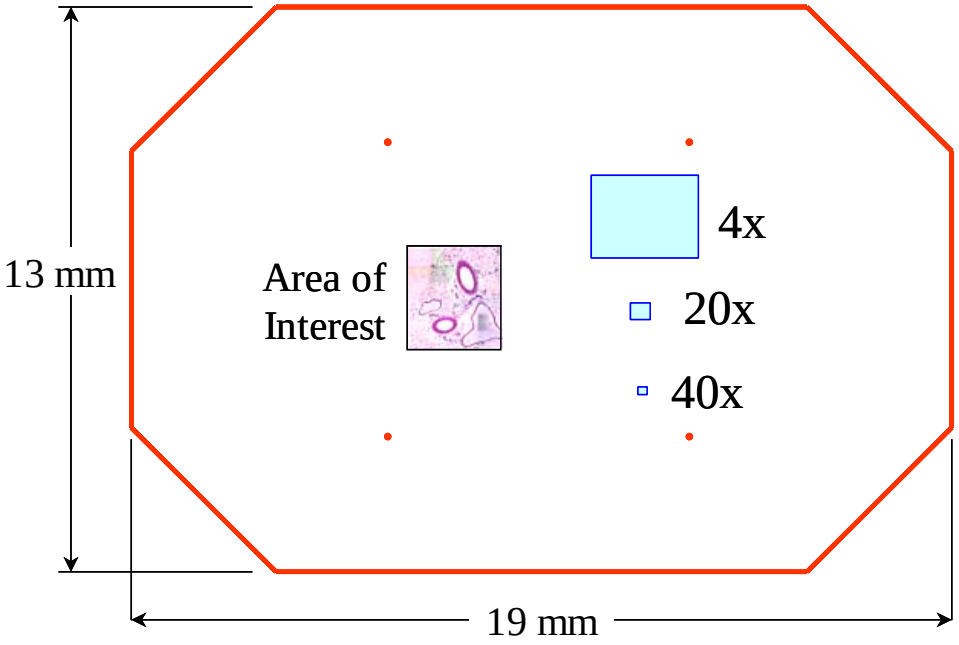

Figure 3-2: Schematic of a cross section showing relative scales of area of interest and fields of view with 4x, 20x, and 40x objectives.

Branches were identified by inspecting serial sections at low magnification (4x objective - Nikon CFI Plan Apo 4X/0.20) on a Nikon Eclipse E800 Microscope. A linearly encoded motorized Ludl stage facilitated the creation of montages to cover the complete area of the vessel section with relevant surrounding tissue. The initial montages were at 40x (Nikon CFI Plan Apo 40X/0.90) with a high sensitivity grayscale camera with a mechanical filter wheel (Photometrics Quantix KAF1401E, 1317x1035 well array). But a color CCD camera (Q-Imaging Micropublisher 5459, 2560x1920) improved the effective resolution to the point where a 20x objective (Nikon CFI Plan Apo 20X/0.75) could be used to capture the necessary detail. Table 3-2 indicates the effective resolution of various camera and objective combinations. The larger array and smaller well size of the Micropublisher camera more than doubles the image resolution

for a given objective. This improvement explains why the 20x objective rather than the 40x objective can be used with the Micropublisher camera to identify cells.

Table 3-2: Effective image resolution of various camera and objective combinations. This table shows that the Micropublisher camera reduces the objective magnification needed to identify cells.

Camera Specification (make/model)	Objective Specification	Image Resolution (μm/pixel)
Photometrics Quantix KAF1401E	Nikon CFI Plan Apo 4X/0.20	1.7226
Photometrics Quantix KAF1401E	Nikon CFI Plan Apo 20X/0.75	0.3428
Photometrics Quantix KAF1401E	Nikon CFI Plan Apo 40X/0.65	0.1710
Q-Imaging Micropublisher 5459	Nikon CFI Plan Apo 4X/0.20	0.8403
Q-Imaging Micropublisher 5459	Nikon CFI Plan Apo 20X/0.75	0.1667
Q-Imaging Micropublisher 5459	Nikon CFI Plan Apo 40X/0.65	0.0831

Resolution needed to identify cells

The CCD array has a Bayer filter array incorporated where alternating wells capture red, green and blue filtered signals. A Bayer filter consists of a row of alternating red and green filters, followed by a row of alternating green and blue filters. This pattern is repeated over the CCD array, so that cumulatively 25 percent of the array is filtered with red, 50 percent with green, and 25 percent with blue. A greater percentage of filters are green because the human eye is more receptive to green than red or blue and this arrangement is less sensitive to aliasing than other regular arrangements of filters. A demosaicing/interpolation algorithm is used to generate RGB data for each well. Simple PCI (C-Imaging Systems by Compix, Inc.) was used for the image captures since it provides superior interactive control of the camera and stage compared to Image Pro Plus and Stage Pro (Media Cybernetics, Inc.).

The size of the montages posed a significant challenge since some of the composite images consisted of as many as 28 individual image fields. With a single

frame size of 2560x1920 pixels, a RGB montage required over 400 MB as an uncompressed tiff and over 12 MB as a jpeg with moderate compression. As indicated in Table 3-2, the spatial resolution of the Micropublisher camera with the 20x objective was 0.1667 μm/pixel. It should be noted that the image detail needed to identify structures was considerably lower than what was needed to identify inflammatory cells. Therefore for better image uniformity a separate set of images was captured using a 4x objective. In general, the 4x objective was sufficient to capture all the structural information in a single frame with a spatial resolution of 0.8403 μm/pixels. The red channel was saved as a grayscale image since it provided the best contrast between the vessel wall and background.

Segmentation

The goal with segmentation is to identify and mark features of interest in an image. The result is often a binary mask that can replace the original image or be overlaid on top of the original image. Ideally segmentation is automated or semi-automated, since automation saves time and can help assure objectivity and consistency in feature identification. In this research, the features of interest are the inner and outer boundaries of the vessel wall. Gradient detection methods were primarily used to identify vessel boundaries on each image, but some manual segmentation was also necessary.

Understanding how to detect edges on an image requires a brief discussion of general image processing techniques. Important tools for detecting edges are the Gaussian kernel, the gradient magnitude kernel and the Laplacian kernel.

Discretizing the following equation in matrix form creates a two-dimensional Gaussian kernel:

$$G_{2D}(x, y, \sigma) = \frac{1}{2\pi\sigma^2} \cdot e^{\frac{-(x^2+y^2)}{2\sigma^2}} \qquad \text{Equation 3.1}$$

Where x and y are the spatial coordinates and σ is the standard deviation which determines the width of the kernel. This kernel can be convolved with an image to produce a weighted average of that image at every pixel:

$$I_{average}(x, y) = G_{2D}(x, y, \sigma) * I_{original}(x, y) \qquad \text{Equation 3.2}$$

Note that the amount of averaging is dependent on the size of σ. The power of using a Gaussian kernel is that it is a relatively simple matter to calculate derivatives of this kernel and convolve the image with these new kernels.

The first partial derivative of the Gaussian kernel with respect to x and y is called the gradient magnitude.

$$Gradient\ Magnitude = \sqrt{\left(\frac{dG}{dx}\right)^2 + \left(\frac{dG}{dy}\right)^2} \qquad \text{Equation 3.3}$$

When the gradient magnitude is convolved with an image the resulting image shows the spatial distribution of intensity gradients from the original image. In edge detection high gradients tend to indicate feature boundaries within the original image.

The second partial derivative of the Gaussian kernel with respect to x and y is called the Laplacian:

$$Laplacian = \sqrt{\left(\frac{d^2G}{dx^2}\right)^2 + \left(\frac{d\ G}{dy^2}\right)^2} \qquad \text{Equation 3.4}$$

And similarly, when the Laplacian kernel is convolved with an image the result indicates where the gradient is changing rapidly. The Laplacian is greatest when there is a change in sign of the gradient (referred to as a zero crossing). Using the Gaussian, Gradient Magnitude, and the Laplacian it is possible to identify a variety of features on an image.

Canny edge detection (Canny 1986) is a commonly used method to identify boundaries in images, and it works by taking the second partial derivative of image intensity with respect to x and y. The result can be represented as an image where the zero crossings have been demarcated. In Canny edge detection, two thresholds may be set to identify a range of *gradient magnitudes* where relevant boundary crossings occur. For example, a distinct boundary exists between cell nuclei and their surrounding environment, but these boundaries are associated with a different range of intensities than the transition from lumen to vessel wall. By including an intensity range criteria, the inner wall boundary can be distinguished from other features that have edges. However, Canny edge detection proved to be ineffective in distinguishing the outer boundary, even when the images were preprocessed with a Gaussian filter to average or blur small features. Another drawback of using Canny edge detection is that blurring steps tend to spread intensities and therefore displace boundaries.

The shortcomings of Canny edge detection were largely overcome by applying the method of Perona and Malik (Perona and Malik 1990). Convolution of an image with a Gaussian kernel can be seen as solving the isotropic form of the diffusion equation:

$$\frac{\partial I}{\partial t} = \nabla \cdot (\nabla f) = \frac{d^2 I}{dx^2} + \frac{d^2 I}{dy^2} \qquad \text{Equation 3.5}$$

In Equation 3.5 I represents the image and t is the width of the Gaussian kernel. This can be extended to anisotropic diffusion:

$$\frac{\partial I}{\partial t} = \nabla \cdot \left(c(x, y, t) \nabla f \right) \qquad \text{Equation 3.6}$$

The diffusion coefficient can be chosen so that smoothing occurs within a region but not across boundaries, in order to blur unimportant features while keeping edges sharp. Perona and Malik (Perona and Malik 1990) proposed the following equation for the diffusion constant:

$$c\left(\nabla f\right) = \frac{1}{1 + \frac{\left\| \nabla f \right\|^2}{k^2}} \qquad \text{Equation 3.7}$$

Where k is an arbitrary constant referred to as the "noise estimator" by Canny (Canny 1986). The method of Perona and Malik will not be numerically described in detail, but a finite difference approximation of the image (f) is made based on the values of f at the four nearest neighbors and the diffusion coefficients are updated after each diffusion time step. The noise estimator, k, was only calculated once based on the original image. A histogram of the gradient magnitude was computed and integrated. The value of k is 90 percent of this integral.

For segmentation, the red channel was used as a grayscale image. The red channel provided the greatest contrast between the vessel wall and other structures in the stained sections.

In practice, identifying the inner boundary was relatively easy, but the identifying the outer boundary was more challenging. The outer boundary was chosen to be the external elastic lamina. For transversely sectioned arteries, the outer boundary was

relatively easy to identify. Difficulties that make it challenging to automate include unevenness in staining within an image and variations in staining and microscopy from section-to-section. In addition morphological details, cells, ECM structures like collagen bands can interfere with the detection of more macroscopic features. Use of anisotropic diffusion to blur features away from distinct boundaries holds promise, but the process had to be optimized for each case. Even with adjustments, the manual selection of some boundaries was necessary to assure accurate segmentation. Appendix G includes sample Matlab programs used for segmentation and edge detection.

Cell Identification

Monocytes/macrophages were identified by their gross morphological appearance. While immunostaining or in-situ hybridization would have been desirable, these were not technically feasible. The gross characteristics of monocytes and macrophages are quite distinct. Simple staining is typically used to identify these cells in diagnostic clinical settings. A single observer blinded to the treatment used counted all macrophages. In addition, the nature of the sectioning prevented the observer from determining the position of any given section relative to a branch point in the vessel under study.

Histologic characteristics used to identify monocytes/macrophages were: the very large size of these cells, typically 10-17 μm in diameter, the characteristic U-shaped or kidney shaped nucleus, and the very characteristic blue cytoplasm. Mature macrophages contain secretory granules and a less characteristic nuclear shape. These cells also tend to be somewhat larger. Note that the other cell types present in these sections (fibroblast,

adipocytes, vascular smooth muscle cells, endothelial cells and lymphocytes etc.) are quite structurally distinct. Figure 3-3 shows representative examples of these cell types.

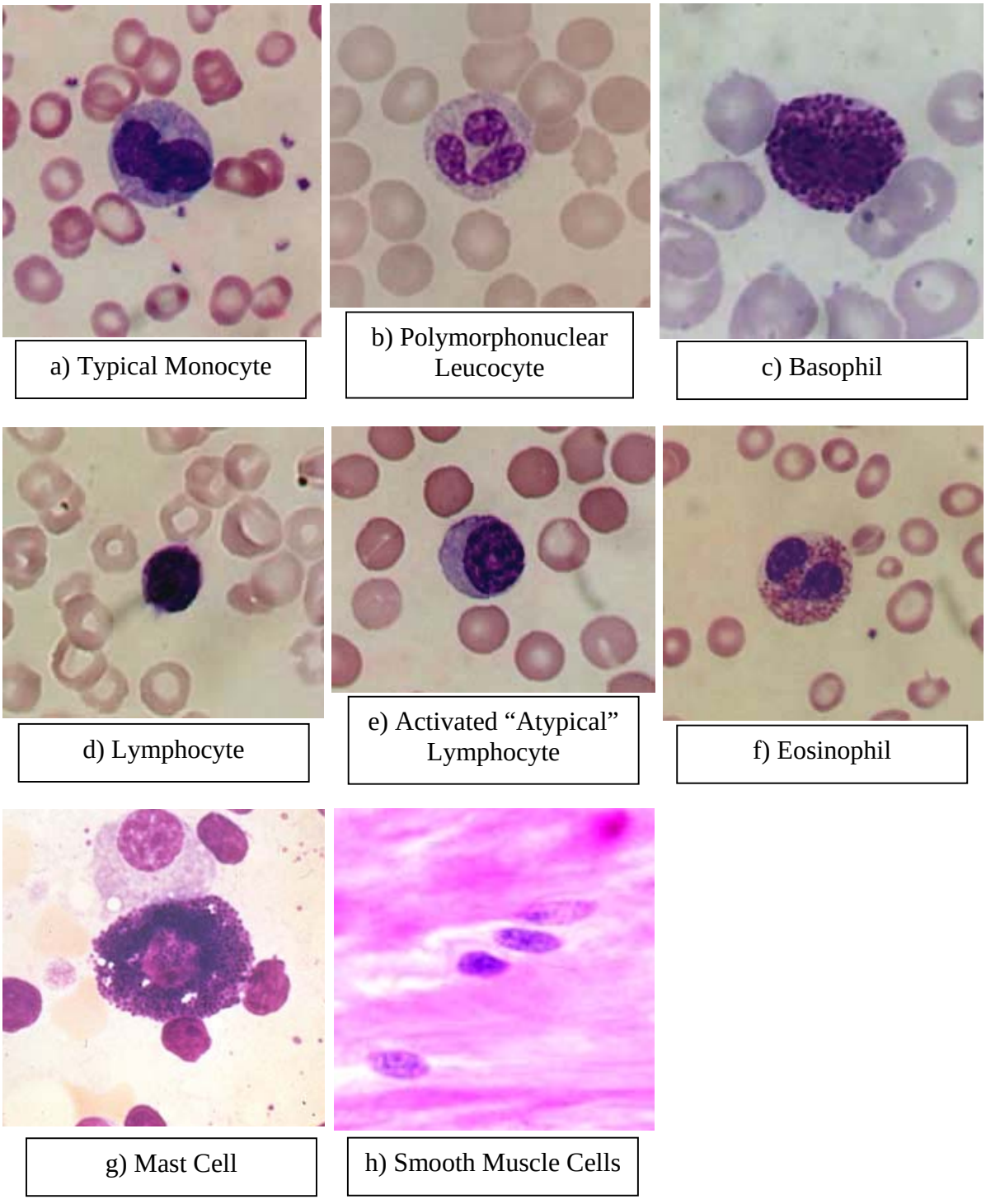

Figure 3-3: Various cell types and their morphological characteristics.

To facilitate the identification of monocytes and macrophages a graphic user interface (GUI) was designed in Matlab 7.0 (MathWorks Inc.). This GUI allowed an observer to zoom in and scroll through the montages and identify up to six different cell types based on morphology.

Preliminary results suggested that macrophages could be identified using radioisotopic *in situ* hybridization (ISH) (Capers, Alexander et al. 1997). The appeal of this approach was that it produced silver grains that are discrete indicators of inflammation. The distribution of silver grains might have been automated, which would have eliminated the need to individually identify the macrophages. Unfortunately *in situ* hybridization yielded inconsistent results with the GMA resin. The reasons for this were unclear since the Polysciences ImmunoBed Kit was designed and advertised for such immunological techniques. Pure GMA resin is too dense to be effectively penetrated by immunological stains. Manufacturers of kits introduce impurities that limit the degree of polymerization that occurs in the GMA to make it more porous. While Polysciences does not explain precisely what has been added to achieve this greater porosity, they advertised their kit for immunological stains. During the course of this research, Polysciences gradually revised their recommendations until they stopped recommending the ImmunoBed Kit for immunological work altogether. Polysciences has recognized the difficulties associated with section penetration, and they now have concluded that the impurity that was added did not produce a stable configuration. The ImmunoBed GMA would continue to polymerize, days, weeks and even months after embedding, making it very difficult to obtain repeatable results on older sections. This is not to suggest that immunohistochemistry (IHC) is not possible with Polysciences ImmunoBed Kit. In fact,

a number of studies have reported positive staining with this kit. But a pattern seems to be present where initial pilot studies are done with some antigen that is very highly expressed, but the follow up studies with less strongly expressed antigens are uncommon. This is consistent with the idea that there is generally a barrier to penetration and that the signal that is being seen is largely surface expression.

In summary, while GMA may be ideal for preserving soft tissue morphology, it presents significant challenges to immunological work, especially when the goal is to develop a quantitative, repeatable approach to ISH or IHC. It was in this context that a morphological identification methodology was implemented. Such a methodology, while time-consuming, avoids the problems with consistency and repeatability associated with immunological stains.

The disadvantages of *in situ* hybridization are that it is harder to process the sections and the process is more time-consuming than staining. Immunostains are relatively easy to process and can be completed in three hours, but they do not produce discrete markers like the silver grains from *in situ* hybridization. Immunohistochemistry (IHC) with a macrophage-specific antibody (Weiss, Kools et al. 2001A) was also considered, but general difficulties in stain consistency from section to section made it difficult to extend this technique to the three-dimensional problem at hand.

Three-Dimensional Reconstruction

Creating an Array of Fiduciary Marks

Various stages of tissue preparation can introduce distortion, but data suggest that pressure fixation with Formalin and embedding in GMA resin tend to reduce the

magnitude of these distortions (Wilhjelm, Vogt et al. 1997). The distortions that occur after embedding were addressed by introducing fiduciary marks.

A method was developed to generate an array of registration holes that can be used to help align serial sections and correct for the deformations that occur during preparation of slides for microscopy. As mentioned earlier, one of the benefits of using a GMA resin instead of paraffin or MMA is that fiduciary marks are still evident even in regions where no tissue is present.

An array of four stainless steel pins (Fine Science Tools No. 26002-20, diameter of 0.18 mm, length of 10 mm), are positioned in the mold before the resin is poured. After the resin has solidified the pins are pulled out. A thin coating of paraffin is used as a release agent to facilitate pin removal. The resulting holes serve as fiduciary marks and can be detected using bright field microscopy on H&E stained sections. The use of pins in this manner helps minimize the local distortions in the tissue and produces identifiable holes regardless of whether the pins are embedded in the tissue or in the surrounding resin. To align the array of four pins, a fixture was used and this fixture will be described shortly.

Since deformations are produced when the tissue is processed (sectioned, floated out on a water bath, mounted on a slide and stained), an effort was made to better understand the general characteristics and the magnitude of these deformations. An array of fiduciary marks was created within the block. These fiduciary marks help characterize the deformations of the individual sections and help align the serial sections for three-dimensional reconstruction. Developing a technique that produces holes but does not introduce additional objects to be sectioned is desirable since these objects can locally

affect the distortion pattern. Holes were generated by drilling, by poking, and by embedding objects in the block, and this preliminary work will be discussed in greater detail in the following paragraphs.

To help assure that the sections are not affected by the introduction of the holes, the holes should be small relative to the size of the section, and the embedding medium should help maintain section shape even in regions of the block where tissue is not present. Several methods were tried in an effort to produce the best overall results (drilling holes, poking holes, and embedding objects that are removed before sectioning). Preliminary work involved the use of a milling machine to drill an array of holes in the block, but drilling posed some problems because small diameter bits can move laterally as they cut into the block. The rotating bit can also snag on the tissue and produce damage to the area surrounding the holes, particularly in paraffin blocks. When resin was used as an alternative embedding medium, drilling often caused microscopic cracks in the block. These cracks interfered with sectioning, even in cases where the damage is not readily apparent. Using a milling machine to poke a small diameter pin worked in paraffin, but the resin was too stiff and tended to damage the block or bend the pin.

Because of the problems associated with drilling or poking holes, a method was developed for embedding and removing an array of small pins in a resin block. As previously mentioned, stainless steel pins were positioned in the mold, the resin was poured, and after the resin solidified the pins were removed. This approach appeared to cause the least amount of section distortion and produced identifiable holes even when the pins were embedded beyond the periphery of the tissue.

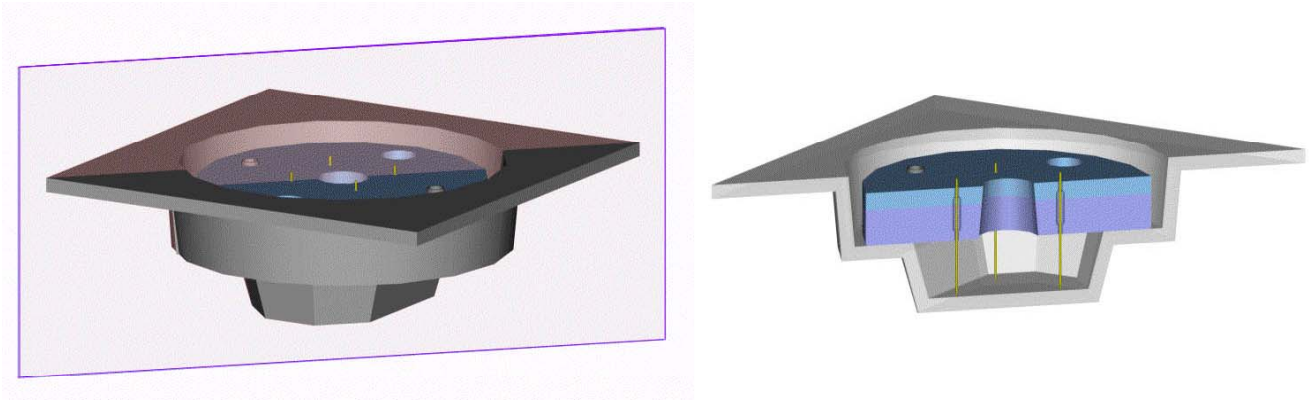

Figure 3-4: Isometric and sectional view of pin registration fixture. Fixture has a diameter of 26 mm.

As depicted in Figure 3-4, a fixture was created to improve the alignment of the registration pins within the block. For engineering drawings and more rendered views of the fixture, the reader should refer to Appendix E. This fixture was designed to rest on top of the mold and hold a square array of four pins in a cantilevered manner until the resin cured. A trade-off was found between the size of the pins and the accuracy of the alignment. Increasing the pin diameter increases the uncertainty in estimating the center of the hole. For this reason and to reduce section deformations, as discussed earlier, small pins were used (approximately 0.18 mm in diameter). The use of such small pins required special consideration in designing a fixture for alignment. Drilling small holes for long distances reduces the straightness of the hole. Therefore, the fixture was made from two pieces of 6061-T6 aluminum alloy. This fixture was designed for a specific Polysciences mold (Polyethylene Molding Cup Trays, Cat. #17177C, 13x19x5 mm) but works with any Polysciences mold in this series. To improve the precision of the alignment, the two halves were machined on a jig bore. The pilot holes were drilled through most of the thickness using a 0.03-inch diameter drill (about 0.76 mm), and through holes were created from the outside with a smaller diameter bit (about 0.008

inches or 0.20 mm). This approach minimized the drift that can occur when small bits are used and improved the angular alignment of the pins.

Correcting for Section Deformations

The positions of the holes on the face of the block after sectioning were measured by mounting the block on a light microscope with an encoded motorized stage. The relative positions of the holes were measured using the following convention. An image was captured of each hole, and the global coordinates of the corners of the image were recorded. The centroid of each hole was determined, and then interpolation was used to relate the pixel coordinates to the global physical coordinate system. The holes were captured starting at the lower left hole and moving counterclockwise. Earlier work demonstrated that the pinholes were approximately straight and also approximately parallel to each other. Under these conditions the distance between the pin holes should not vary significantly in the depth direction, especially over the relatively short distances that were sectioned (about 1 to 2 mm). For this reason, the hole locations on the block face were only captured *after* sectioning.

A similar procedure was followed for capturing the holes on individual sections, but for this work the stage movement and image capture were automated after the first hole was centered in the view field. The long axis of the sections only needed to be coarsely aligned with the x-axis of the stage for the automated stage control and image capture routine to work. Because the GMA tended to take up some eosin during staining, the holes appeared white on a light pink background. The background staining provided sufficient contrast to distinguish the hole from the GMA, and a thresholding procedure was used to identify the hole on the captured image.

The distortions associated with sectioning were determined by comparing the locations of the holes before and after sectioning for each section. To correct for deformations, an affine transformation was used to relate the hole positions before and after sectioning. This means that the array coordinates before and after sectioning can be related by a transformation matrix that includes in-plane rotation, translation, and constant normal and shear strains. In the simplest form the transformation can be expressed by the following equation:

$$\begin{Bmatrix} x' \\ y' \end{Bmatrix} = \begin{bmatrix} c_1 & c_2 \\ c_4 & c_5 \end{bmatrix} \begin{Bmatrix} x \\ y \end{Bmatrix} + \begin{Bmatrix} c_3 \\ c_6 \end{Bmatrix}$$

Equation 3.8

In this equation, x and y represent the undeformed coordinates, x' and y' represent the deformed coordinates, and the c_1 through c_6 represent the six coefficients of the transformation. Because Equation 3.8 includes six unknowns, three x-y pairs are the minimum number needed to obtain a solution. Because four holes produce redundant data, a least squares approach was taken to minimize the error associated with any one measurement. The matrix representation of the transformation takes the following form:

$$\begin{bmatrix} x_1 & y_1 & 1 & 0 & 0 & 0 \\ 0 & 0 & 0 & x_1 & y_1 & 1 \\ x_2 & y_2 & 1 & 0 & 0 & 0 \\ 0 & 0 & 0 & x_2 & y_2 & 1 \\ x_3 & y_3 & 1 & 0 & 0 & 0 \\ 0 & 0 & 0 & x_3 & y_3 & 1 \\ x_4 & y_4 & 1 & 0 & 0 & 0 \\ 0 & 0 & 0 & x_4 & y_4 & 1 \end{bmatrix} \begin{Bmatrix} c_1 \\ c_2 \\ c_3 \\ c_4 \\ c_5 \\ c_6 \end{Bmatrix} = \begin{Bmatrix} x_1' \\ y_1' \\ x_2' \\ y_2' \\ x_3' \\ y_3' \\ x_4' \\ y_4' \end{Bmatrix}$$

Equation 3.9

This arrangement permits any number of x-y pairs to be used, in excess of the minimum of three pairs. A minimum of four x-y pairs are needed for a least squares solution. This might be expressed more simply as:

$$A \cdot C = X_p \qquad \text{Equation 3.10}$$

In Equation 3.10 A is the undeformed coordinate matrix, C is the coefficient vector, and X_p is the deformed coordinate vector. Solving for C yields:

$$C = (A^T \cdot A)^{-1} \cdot A^T \cdot X_p \qquad \text{Equation 3.11}$$

This represents the least squares solution for C, the solution that minimizes the difference in residuals between the actual hole locations and the estimated hole locations. Provided the strains are not large, the Cauchy strains can be calculated:

$$\varepsilon_x \cong c_1 - 1 \qquad \text{Equation 3.12}$$

$$\varepsilon_y \cong c_5 - 1 \qquad \text{Equation 3.13}$$

$$\varepsilon_{xy} \cong \frac{c_2 + c_4}{2} \qquad \text{Equation 3.14}$$

These strains are approximate, recognizing that some error is associated with the coordinate measurements. For example, the holes were not perfectly circular on the cross sections and exhibited some variability in shape for section to section.

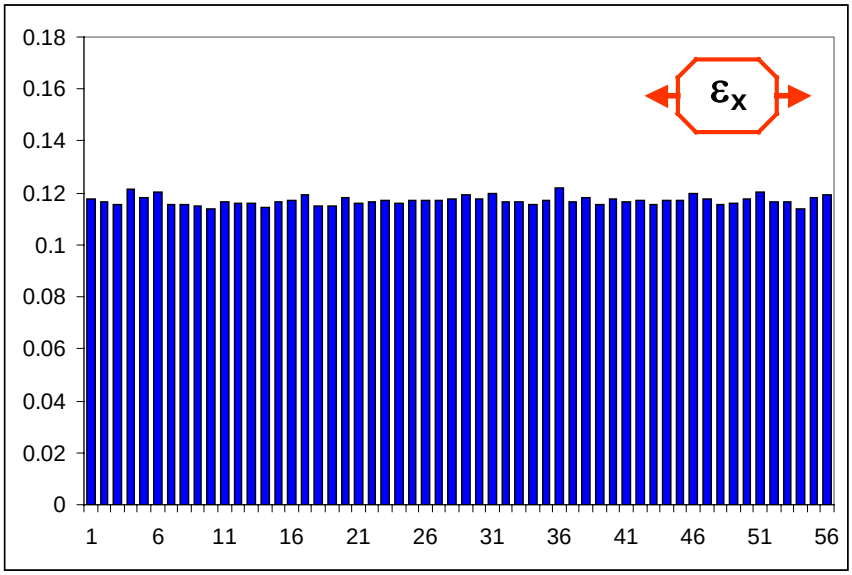

Figure 3-5: Normal strain in x-direction for each of 56 sections for branch H7C (mean = 0.1171, standard deviation = 0.0017).

Based on an affine transformation the plane strains may be determined and Figure 3-5 through Figure 3-8 show representative results from the 56 sections analyzed for branch H7C. Figure 3-5 shows the normal strains in the x-direction and indicates a mean strain of 0.1171 with a standard deviation of 0.0017. Figure 3-6 shows the normal strains in the y-direction and indicates a mean strain of 0.1291 with a standard deviation of 0.0024. Together, these results indicate a high degree of consistency in the deformation pattern from section to section. Note that the y-direction approximately corresponds with the cutting direction and produces somewhat larger strains, a pattern that was seen throughout the registration hole data. This is interesting since the sections are grossly compressed in the cutting direction before they are placed on the water bath. The deformations produced during cutting are theorized to make the sections preferentially more compliant in this direction. Consequently, when the sections are floated out on a water bath, they expand slightly more in this direction.

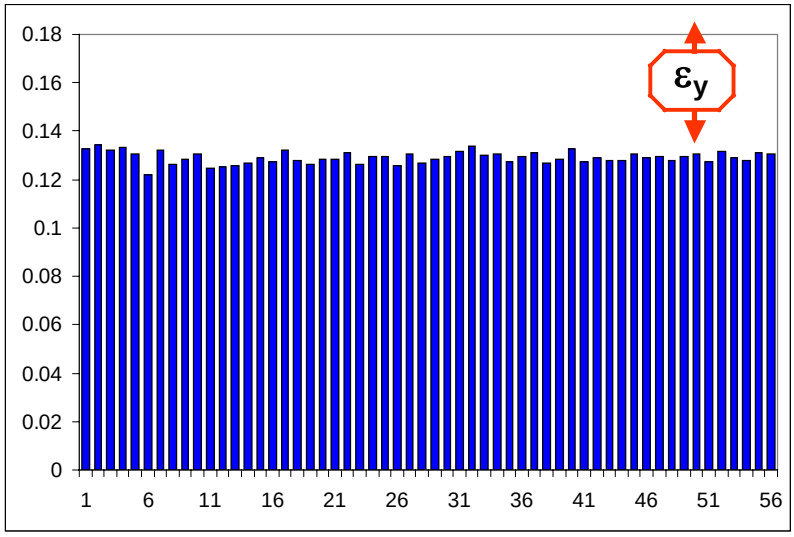

Figure 3-6: Normal strain in y-direction for each of 56 sections for branch H7C. (mean = 0.1291, standard deviation = 0.0024).

Figure 3-7 shows the in-plane shear strains associated with sectioning the block that contains branch H7C. The mean shear strain is –0.0013 with a standard deviation of 0.0016. The shear strains were very small and the net negative strain is caused by the fact that the fixture was rotated slightly relative to the mold when the tissue was embedded.

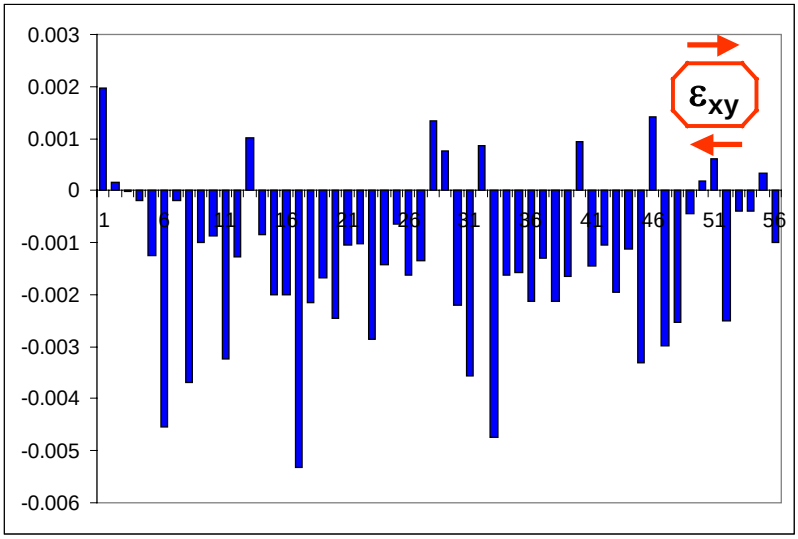

Figure 3-7: Shear strain in xy plane for each of 56 sections for branch H7C. Mean = -0.0013, standard deviation = 0.0016.

Figure 3-8 shows the mean strain components for all 56 sections used to reconstruct branch H7C. This figure emphasizes the low variability in the strain components by including the standard deviations. Also, the shear strain is relatively small, with both positive and negative values.

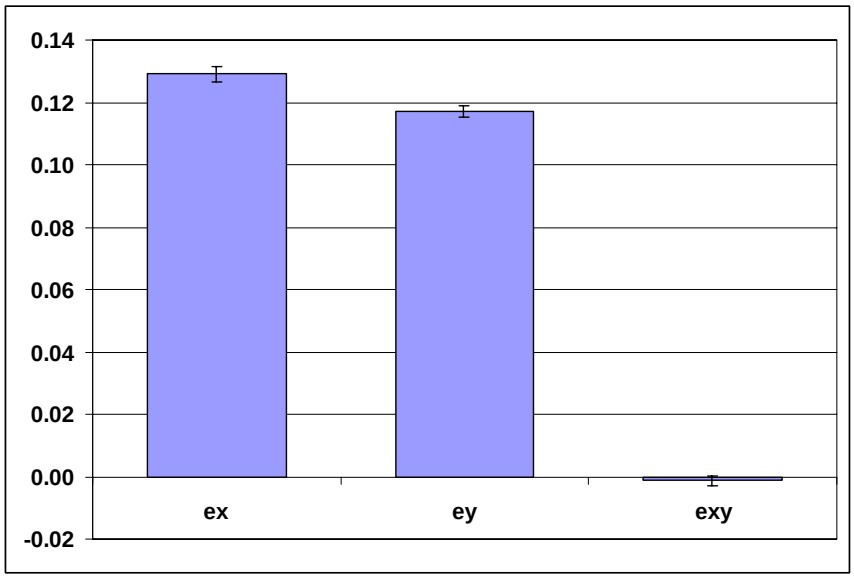

Figure 3-8: Mean strain components from the affine transformation for all 56 sections of branch H7C.

To improve the section quality and repeatability, the following variables were considered: block size, block orientation, blade angle, cutting speed, section thickness, bath surface tension, bath temperature, and bath time. While various block orientations were considered, the best results were obtained when the rectangular blocks were sectioned perpendicular to the long axis of the block. Within limits, varying the bath temperature and time had a minimal effect on the consistency and distortion of the resin sections. Surface tension clearly affected the results, and the most consistent results were obtained using distilled water in a room temperature bath that had been washed to remove detergents. As mentioned earlier, a small amount of a detergent could have been added

to reduce surface tension and limit the expansion of the sections. But no detergent was used because the section expansion had the benefit of reducing the magnitude of nonuniform deformations caused by sectioning. Also, the use of a detergent would have reduced section adherence to slides.

To reiterate, the coefficients of the transformation matrix were determined using redundant registration data to reduce error associated with measurements. The portion of the affine transformation associated with distortion was separated from the rigid body transformation. Because the distortion pattern had a small standard deviation, the mean normal strains in the x and y direction were used to correct the entire image stack. The mean shear strain was approximately zero and so no shear correction was made. The section alignment method will now be presented.

Aligning Sections with Image Features

Ultimately, image features were used to align sections, but this was only done after determining that the error in position using pin registration was large relative to the size of the arteries (about 10 μm to 20 μm). Appendix F presents a more complete discussion of how the pins might have been used to align sections and the validation work that revealed large errors in position.

As mentioned in Chapter 1, an image similarity measure (ISM) may be used to align serial sections when there is no common frame of reference. To use this alignment approach the sections must be close to one another and share a common set of structures. The general strategy is to displace and rotate one image over the other until the overall image similarity is maximized. A relatively simple image similarity measure is the mean square difference (MSD) between images (Studholme, Hill et al. 1997).

$$MSD = \frac{1}{N}\sum_{x \in X}\left[I_2(x) - I_1(x)\right]^2 \qquad \text{Equation 3.15}$$

In this equation N represents the number of pixels over coordinate space x, while I_1 and I_2 represent serial images. The result of an ISM is a scalar measure of the degree of similarity that exists between two images. In the case of the mean square difference, the image similarity measure is minimized during alignment.

The mean square difference in image intensities was used to align serial sections. The most rapid alignment of two images was achieved by first coarsely aligning the images visually and then using a gradient descent method to converge to the position where the mean square difference was a minimum (Press, Flannery et al. 1992). The MSD was minimized with respect to x, y and θ.

The MSD approach was programmed in Matlab, and a few worthwhile notes should be made about implementing such a program. Two matrices were created, one representing the x coordinates and another representing the y coordinates in the displaced and rotated image. When an image is rotated or displaced the new pixel locations do not precisely overlay the pixel locations of the other image, so bilinear interpolation is needed to generate pixels at the same locations. In addition, a mask must be used to zero the intensity values in the moved image that do not overlay the other image. This avoids an artificial penalty that would be imposed if the best alignment involves only limited overlap.

An automated MSD tool is available within Amira 3.1 (TGS, Inc.); however, testing revealed that this tool yielded different results than a Matlab implementation of the method described above. But the Amira function yielded inaccurate results when a mask was employed. This problem will be corrected in the next update of Amira.

Despite the problems in the automated alignment tool, Amira still correctly reported the actual MSD value. Given this value, incremental changes in translations and rotations can be made until the MSD is maximized and one section is aligned over the previous section. Since the alignment of two sections was verified with independent programming in Matlab, this manual alignment approach was used.

For image similarity measures to more accurately drive histological alignment, the serial images must be sufficiently close to one another such that they share common features. When reconstructing small arteries it is desirable to use structures besides wall edges, such as cellular details, extracellular matrix components, and even other small vessels. In the mesentery tissue the adipose cells are prevalent, and the walls of these cells are an example of the kind of feature that is shared between serial sections. If a greater interval is used between sections (e.g. 50 μm), it was found that the vessel structural information drove the alignment. Hence an artery that actually moved diagonally in the image plane as you moved through the stack tended to be represented by a vertically aligned column. With some experimentation a 10-micrometer interval (every other section) was found to provide adequate local detail to assure a relatively high similarity measure and good alignment.

To summarize, an affine transformation based on the registration holes was still used to correct for deformations but did not provide the most accurate alignment. Improved alignment was achieved by maximizing the mean square difference in image intensities between two images. The key to achieving good alignment for microvessel reconstruction is limiting the distance between sections so smaller features are shared between serial sections.

Reconstructing Vessel Surfaces

The previous sections described how deformations were determined and eliminated from each cross section and how the images were aligned into a three-dimensional stack. This section will discuss how this aligned stack of images was reconstituted into a surface representation that is suitable for finite element analysis.

The development of a 3D reconstruction technique was strongly influenced by three issues. First, the vessels are so small that the geometry must be reconstructed based on a limited number of sections. Second, the geometry is imported into a finite element model causing any inaccuracies in the geometry to be amplified in the stress distribution. Third, given the challenges associated with sectioning, the reconstruction technique must accommodate lost or damaged sections. With these issues in mind, a point-cloud reconstruction method was used. This method will be described after some background information that provides a context.

A histology-based approach not only allows for the identification of biological markers of inflammation but also assures sufficient in-plane resolution to capture the features of small mesenteric branches. But the spatial resolution in the depth dimension is considerably lower and can be a source of inaccuracy when using traditional surface reconstruction techniques like the marching cubes method. The marching cubes method is a contouring algorithm to create surfaces of constant scalar value in three dimensions (Lorensen and Cline 1987). This method reconstructs a surface by moving through a volume, voxel-by-voxel in an orderly manner. Most commonly, marching cubes algorithms use interpolation schemes to determine the transitional geometry between known cross sections. Interpolation can present a problem for histological data since

only a limited number of sections are available to reconstruct the geometry. Also small discontinuities or errors in the surface reconstruction can translate into large artifacts in the subsequent finite element analysis. Therefore, carefully considering how to best integrate the information from individual sections is important.

Using the segmentation techniques described earlier, the inner and outer edges of the wall were identified in each cross section. The edges were reduced to point data for both boundaries and this data was compiled into two sets of unstructured data points (a point cloud), assigning the appropriate depth to each section. Point clouds were used to separately create the inner and outer surfaces of the vessel wall. After preprocessing Geomagic Studio (Raindrop Geomagic, Inc.) was used to generate the surfaces, to edit point connectivity if necessary and to export inner and outer surfaces that are suitable for post-processing or for import into Ansys for finite element analysis. Geomagic Studio is a commercially available program designed for reverse engineering objects based on digitized surface data. This program uses weighted alpha shapes (Edelsbrunner and Mucke 1994; Edelsbrunner and Fu 1998; Edelsbrunner and Fu 2002), where the parameter α varies along the surface and controls the surface detail. A surface is created by filling the bounded volume with balls of different sizes, where the ball size is proportional to the weighting. The variable weighting encourages connections with neighboring points when the data is not spaced uniformly. Voronoi cells are generated to eliminate overlapping, then a Delaunay Complex of polygons is created on the surface (Barber, Dobkin et al. 1996). Geomagic Studio then uses a proprietary algorithm to identify the "persistent topology" (Edelsbrunner, Letscher et al. 2000). While enforcing sharp edges is possible with Geomagic Studio, the underlying approach lends itself well

to producing gradual transitions in curvature that are inherent in biological structures like arterial branches. Part of the appeal of this approach is that the program generates a surface, by treating a set of points as an integrated whole rather than using piecewise interpolation. Once a polygonal surface is complete, Geomagic Studio can be used to create a nonuniform rational b-spline (NURB) surface with continuity in curvature between patches.

The advantage of this approach over traditional voxel-based approaches is that all of the data describing a surface can be used to influence the local shape of the reconstruction. Most voxel-based approaches use interpolation to generate intermediate images based on from the images nearby. This interpolation tends to be computationally more intensive because all of the intensity information must be carried through the interpolation. In fact, substantial down sampling would be required to use a voxel-based approach with the images in this research. This down sampling would result in a significant loss in spatial resolution and an unnecessary compromise in the quality of the final reconstruction. For this research the loss of gray-level data does not hinder the development of a finite element model, since the inner and outer surfaces are all that are needed for the reconstruction. In fact, there is a distinct computational benefit to separating segmentation from reconstruction. This approach preserves the high spatial resolution of the boundaries in the original histological images without carrying along the rest of the cross sectional information through the interpolation/surface creation process. The disadvantage of a point cloud reconstruction is that it is more difficult and time-consuming to adjust segmentation because the intensity data was discarded earlier in the reconstruction process. If the surface features of interest are well defined, as they are in

microscopy, the inability to carry intensity data further through the process is a worthwhile trade-off.

Mesh smoothing was considered to reduce the noise in the surface data, but such techniques were used sparingly and primarily only when a discontinuity in the surface reconstruction was present. The purpose of mesh smoothing is to improve the appearance of the mesh and reduce the magnitude of surface noise and other localized surface irregularities before the data is imported into a finite element model. But care should be used in applying smoothing algorithms. For instance, the repeated application of Laplacian smoothing reduces surface curvature and tends to flatten the surface (Schroeder, Martin et al. 1998). In the case of a sphere or cylinder, Laplacian smoothing can cause a net loss in volume. In general the effect of smoothing is most pronounced where the surface curvature is large and the mesh density is low. Where smoothing was employed, the final geometry was qualitatively compared to the original geometry to make sure that changes in coordinate position were small.

Once the serial sections are aligned and deformations are corrected for, overlaying biological data from histology on the reconstruction is a simple matter. This is one of the great benefits of using histology to reconstruct geometry. Any biological data that can be stained for on GMA resin sections can be compared and potentially correlated with the mechanical environment. In future research, staining alternating sections for different biological characteristics may be possible so a greater variety of biological data can be compared and potentially correlated.

An important challenge in using Geomagic Studio is balancing the high in-plane resolution from histology with the relatively low out-of plane resolution. If the in-plane

resolution is much greater, the model produces webbing that enforces the in-plane connectivity over the out-of-plane connectivity. If the in-plane spacing is reduced to the size of the out-of-plane spacing too much detail can be lost. Based on the reconstructions done in the course of this research, the in-plane resolution should be about 2-5 times the out-of-plane resolution, although it is expected that these numbers may need to be adjusted on a case-by-case basis.

The reconstruction method that has been employed is well suited for reconstructing branch geometry based on a limited number of serial sections. Figure 3-9 shows a reconstruction created by fitting a surface to an unstructured set of data points (a point cloud) that represent the inner surface of the artery.

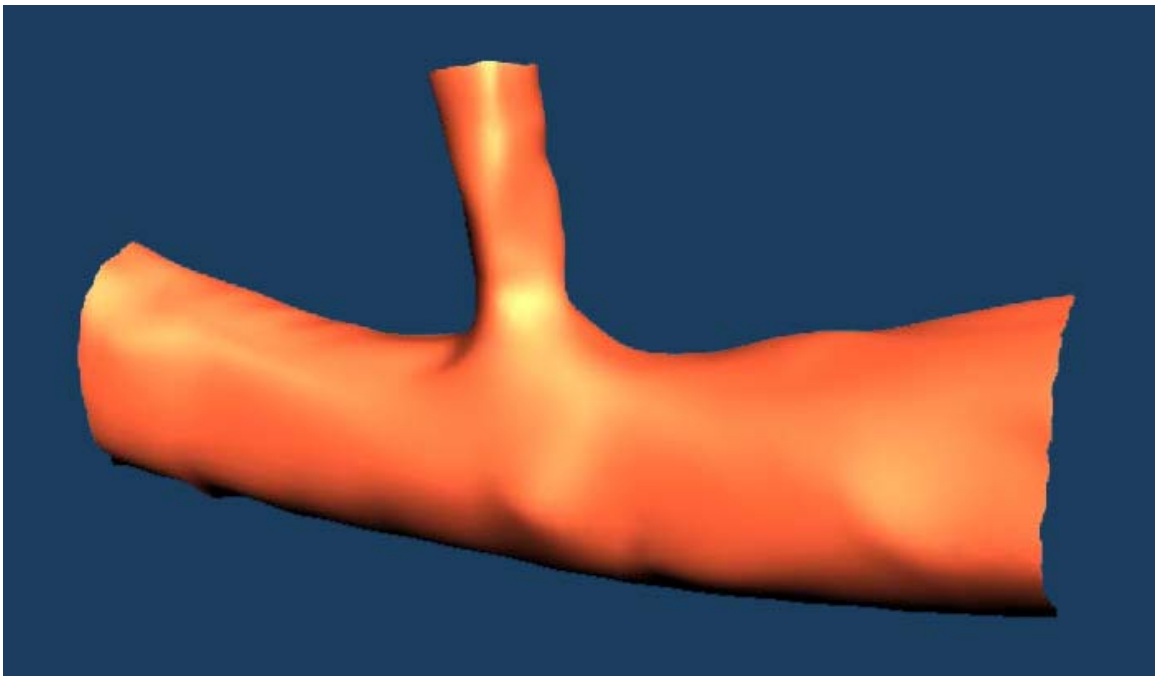

Figure 3-9: 3D Reconstruction of the inner surface of an arterial branch based on nine serial sections.

Determining Midplane Geometry and Wall Thickness

The inner and outer surfaces can be combined into a single model using Boolean operations to generate a solid. However, for reasons to be discussed in the next section,

generating midplane geometry from the two surfaces is desirable. The midplane geometry can be used to generate a variable thickness shell element model. This programming was done in Matlab and consisted of the following steps:

1. Generate separate inner and outer surfaces in Geomagic Studio
2. Export them as polygon meshes that consist of vertices and a topological connectivity map.
3. Determine a normal vector for each polygon on the inner surface. This normal is based on the cross product of vectors parallel to two of the polygon edges.
4. Use a modified ray tracing algorithm (Badouel 1990; Moller and Trumbore 1997) to determine the intersections between the normals of inner polygons and the outer polygonal surface. The efficiency of this process is enhanced by describing possible intersections with barycentric coordinates.
5. Store the length of each line segment as local thickness measurements.
6. Project halfway along each segment to generate a point at the midplane and store this coordinate.
7. Use spatially weighted interpolation to fill in thickness and midplane vertices where intersections do not occur. Some of the normals do not intersect polygons near the proximal and distal boundaries of the model.

The resulting point cloud was reconstructed in Geomagic Studio. It was demonstrated that the midplane surface definition was only minimally changed if the outer normals were projected to intersect the inner surface instead of vice-versa.

Reconstruction Validation

Validating the reconstruction of small arterial branches presents a challenge since the geometry is not known *a priori*. In addition the histology-based methods described in this research are destructive and do not afford a second independent way to determine geometry. The reconstruction validation consisted of two parts: 1) simulated histology to reproduce a known geometry and 2) comparisons to a proven reconstruction technique. In this section, these two approaches will be further described and validation results will be presented.

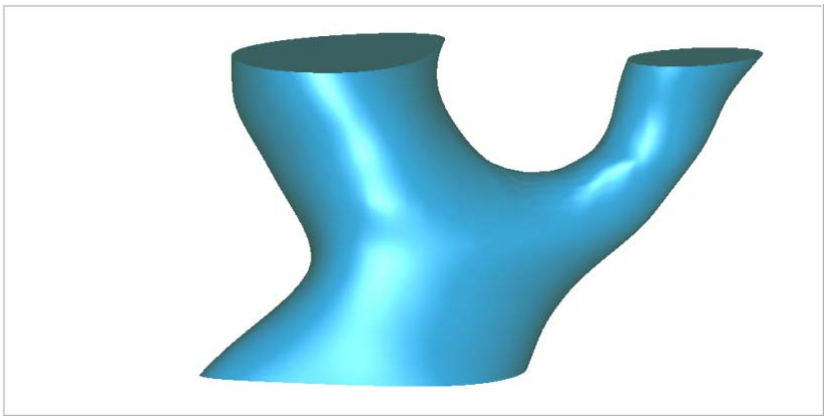

Figure 3-10: Standard model for validating the reconstruction methodology.

To simulate histology, an idealized model of a branch was created and this is shown in Figure 3-10. This model did not accurately represent a physical geometry, but was a detailed, well-defined model that contained all the basic features of a small arterial branch. This standard model was treated as a benchmark for evaluating the accuracy of reconstructions.

Determining the intersection of the standard model with a series of parallel planes simulated microtomy. This approach limits the judgments needed for segmentation and eliminates the variability associated with distortion correction and alignment. The

resulting model was then spatially compared to the original model to evaluate the accuracy of the reconstruction. The simulated microtomy produced a serial stack of binary images that delineate the boundary of the standard model. The pixels that describe the boundary of each surface were used to generate a set of evenly spaced points. Figure 3-11 illustrates how these points were used to generate a polygon model, which was ultimately wrapped with a NURB surface for improved continuity.

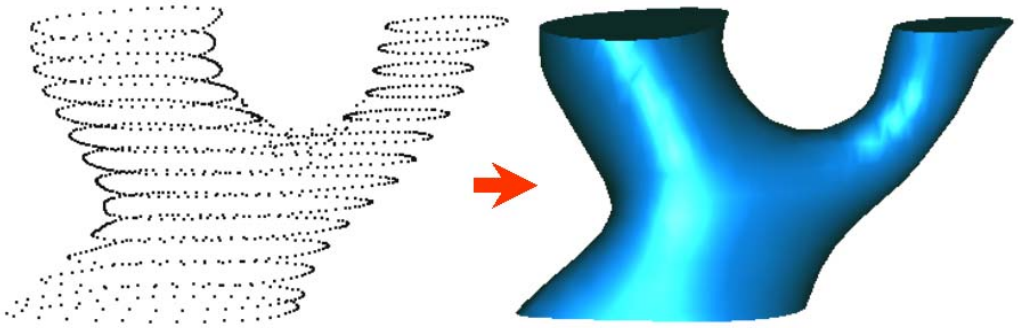

Figure 3-11: Simulated histology produces (left) a point cloud from the standard model and leads to a reconstruction (right) that can be spatially compared to standard model.

This was repeated for a decreasing number of divisions until the reconstruction process required manual intervention. The goal here was not only to see if a reconstruction could be produced, but also to establish minimum requirements for sampling in the depth plane. The model was also sectioned in different planes to determine how this affected the reconstruction accuracy and what sectioning plane might lead to superior reconstructions.

After the reconstruction, the resulting polygon model was compared to the original standard model and tolerances were determined as shown in Figure 3-12. Differences are shown as a color-coded map overlaid on the standard reconstruction. The magnitudes shown indicate the minimum distance from the original geometry and the

sign indicates whether the reconstructed geometry is outside or inside the original geometry (positive or negative respectively). While the distance scale for Figure 3-12 ranges from +7.3 μm to –7.3 μm, the actual range was less than ± 2 μm, with over 90 percent of the surface area within a narrower tolerance of ± 0.5 μm. Given the scale of this model (diameter of the vessels range between 100 and 300 μm), this tolerance translates to an error of about 0.5 percent in position and represents less than a two percent of the smallest diameter. Most of this error was caused by pixelation when cross-sectional images are created in the simulated histology.

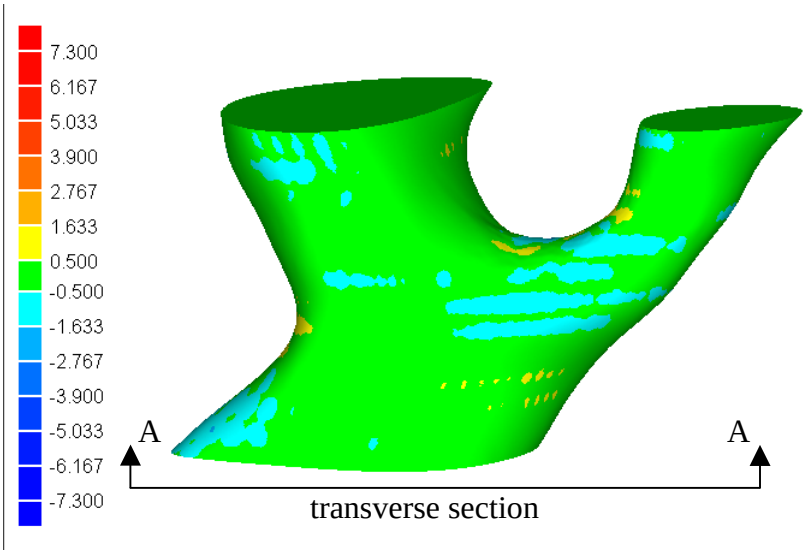

Figure 3-12: Comparison of baseline model to a reconstruction of baseline model based on 13 transverse sections. Note that the reconstructions overlay to within +2 μm and –2 μm, with the vast majority of the surface being within a ± 0.5 μm tolerance.

There was a small loss in volume (less than 0.5 percent) that was associated with movement of the boundary when it is pixelized to generate a point cloud. This error is substantially lower for the relatively high-resolution images produced during microscopy.

Note that the error tends to be larger where the vessel was not transversely sectioned, near the lower boundary in Figure 3-12 and in the saddle region.

In general, greater accuracy in the reconstruction was achieved when the model was sectioned transversely, as indicated in Figure 3-12. A variety of section depths were also considered to appreciate at what point the accuracy became severely compromised or the reconstruction process broke down altogether.

The second part of the reconstruction validation compared the point cloud reconstruction technique used in this research to another, more traditional, voxel-based reconstruction technique. These reconstructions were performed using sections from the standard model previously described to include a benchmark measure of the absolute accuracy. The more traditional approach consisted of nonlinear interpolation to generate intermediate images followed by surface creation using the marching cubes algorithm. The use of interpolation improved the out-of-plane resolution of the voxel stack and enhanced the overall accuracy of the reconstruction.

More specifically, the interpolation method used was adaptive control grid interpolation (ACGI), a method that has been benchmarked and used successfully with MRI data (Frakes, Conrad et al. 2003). ACGI treats serial sections as frames that do not vary with depth, but rather are distorted in the same plane with time. By laying out a series of control points, a velocity field can be generated that causes each image to morph into the next image in the depth plane. Once this mapping is determined between successive images, any number of intermediate images can be generated. ACGI strikes a balance between an ideal approach where every pixel is mapped (Optical Flow) and a more efficient approach where pixels are moved as undeformed blocks (block matching).

Once the control point mapping is determined for each new section, bilinear interpolation is used to fill in the pixel data between control points. The validation results are presented later in this chapter. It should be noted that all the validation work was done using a single surface. The greatest errors tend to occur on the inner surface where the curvature is generally greater. Errors for the outer surface are expected to be comparable, if not somewhat smaller. Also, the production of a midplane surface from inner and outer surfaces will tend to reduce random errors associated with position.

Figure 3-13 shows an ACGI based reconstruction of 13 transverse sections. Note that constraining points to discrete voxel locations produces the ridges in the model. Such artifacts are undesirable, but they can be minimized by increasing the in-plane resolution of the voxel stack by using volume or surface smoothing or by wrapping a NURB surface to the reconstruction. Since wrapping or fitting a surface can be done after either reconstruction, the results were compared prior to any such modifications. Note in Figure 3-13 that there is a local flat area in the saddle region. This is produced by the pixelation in the depth dimension and may also indicate some analytical difficulty in accurately interpolating data in this geometric transition. Since it is generally expected that the stresses will be high in the saddle region, such flattening may significantly increase the local stresses. This highlights one of the appealing aspects of a point cloud based reconstruction. With a well-implemented approach like the one that exists in Geomagic Studio it is relatively easy to accurately capture such transitions, even if they occur *in between* image planes.

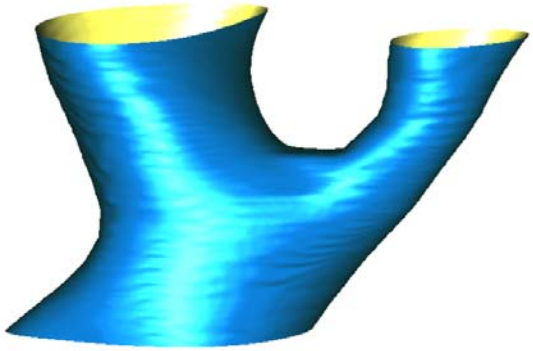

Figure 3-13: Polygonal surface produced by adaptive control grid interpolation (ACGI) followed by marching cubes surface creation.

Figure 3-14 shows the voxel-based reconstruction accuracy side-by-side with the point cloud reconstruction accuracy. The color-coded scale is the same for both reconstructions. This comparison shows that the error range is substantially smaller for the point cloud reconstruction and suggests that this method more accurately captures the standard geometry.

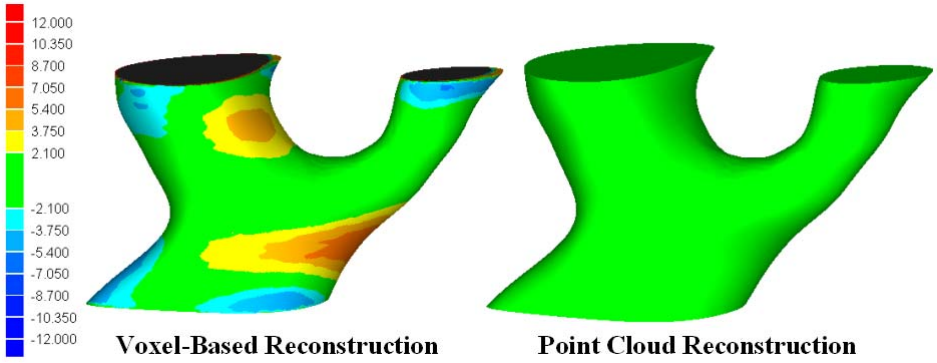

Figure 3-14: Comparison of a voxel-based reconstruction technique to a point cloud reconstruction.

The point cloud based reconstruction method employed in this research can accurately reconstruct a known geometry through simulated histology. Further, this point

cloud method produces more accurate reconstructions than traditional voxel-based methods when working with histological data. This improved performance is largely the result of preserving the high spatial resolution available in microscopy. The use of a point cloud also tends to produce more accurate reconstructions in transition regions. It should be noted that ACGI followed by marching cubes reconstruction has the benefit of carrying along intensity information so the model can be more readily resegmented should the need arise. Also, below a certain level, a point-cloud reconstruction can fail to capture the basic vessel topology and this limit is generally reached before a similar limit with ACGI. Initial work suggests that a combination of ACGI with point cloud reconstruction can improve the quality of the final reconstruction when the image modality does not have the high resolution afforded by bright field microscopy. Taken together, the reconstructions produced by simulating histology and the comparisons to a voxel-based reconstruction validate the use of point cloud reconstruction in this research.

Finite Element Analysis

Before describing the histology based finite element method, a brief description of a parametric model is presented since this influenced the methodology development. The histology-based finite element models will then be described. First, a section will describe how the geometric model was used to create finite element geometry. Next, the element selection and material properties will be discussed. A brief overview of the governing equations will be presented and then specific stress correlates will be discussed.

Although linear material properties were used to represent the incremental change in stress between the pressure-fixed state and systolic pressure, hyperelastic models were

also considered. These results are not presented in full, but the hyperelastic stress distributions were similar, particularly when comparing midplane stresses.

In addition to the histology-based approach that includes thickness variations, constant thickness models were also considered. These models were based on the same midplane geometry, but assumed constant thickness. This is not a realistic assumption, but represents an extreme case that helps illustrate the role that variable thickness plays in reducing intramural stresses at branch points. While constant thickness models were done for all branches, these results are not all presented in Chapter 4.

Idealized Parametric Finite Element Model

Early in this research, a parametric finite element model was developed to represent the geometry of an idealized branch. The benefit of such a model is that it permits the researcher to study how general trends in geometry affect the distribution and range of stresses. Such studies would be extremely challenging with a histology-based finite element model where the surface form is not governed by simple geometric parameters.

The parametric models provided insights into how arterial branches respond and deform with pressure and influenced the final form of the finite element models. The parametric models produced stress distributions that could only be roughly compared to the stress distributions from histology based finite element analysis. This emphasizes the need and value of a histology based finite element model.

The parametric models also provided a better forum for benchmarking the finite element method since the stresses are more readily compared to first order stress estimates (e.g. membrane model or thick-walled model). The parameter studies

highlighted how stresses at branch points are high and suggest that the fundamental geometry inherent in a branch limits how stresses may be reduced through adaptation.

Comparing results from various models helped drive the choice of shell elements over solid elements and also provided guidance about the mesh density needed to capture the distribution of stress. The parametric finite element model is discussed in much greater detail in Appendix J.

Histology-Based Finite Element Model

Sample Ansys code is presented in Appendix J and illustrates how the Ansys scripts were subdivided into logical segments of APDL code (Ansys Parametric Design Language). This modular format allows the user to make changes to the code without creating a new program for each permutation studied. The approach made it easier to change one aspect of a model without modifying the whole program. This was particularly important as the finite element approach evolved and decisions were made about boundary conditions, mesh density, material behavior, and solution procedures. A wide array of modeling assumptions were considered, and the batch approach made it possible to save and archive scripts for each case without excessive storage demands. Note that some of the results files were several hundred megabytes while the scripts were only a few kilobytes.

The general structure of the batch file was to have a master file that initialized a few items such as simulation name, and then called a series of scripts followed by selected post-processing steps.

1. “init.txt” - variables initialized, options selected for later conditional checks
2. “import_geom.txt” – geometry imported

3. “mat_props.txt” – material model defined
4. “mest.txt” – geometry meshed
5. “constraints.txt” – boundary conditions defined
6. “solve.txt” – finite element model solved

Some key features of this approach will be described here, but refer to Appendix J for further details.

Once the geometry is imported, the model boundaries are identified and extruded a short distance (about ¼ to ½ the vessel inner diameter). The extruded ends are constrained so displacements and rotations are zero. A series of boundary condition studies suggested that this method provided good numerical stability, permitted the use of the complete reconstruction, and tended to reduce the high local stresses that are associated with constraining the model. The extruded part of the model is deselected before post-processing and neither displayed nor considered further during the subsequent analysis. Longer extrusions did not necessarily further isolate boundary effects. None of the histological reconstructions exhibited a perfectly circular cross section at the ends of the model. When a noncircular cross section is extruded a long distance (say 2 diameters or more), it tends to impart an artificial load at the interface between the core model and the extruded portion. Stress and inflammation data in the upper and lower ten percent of the model is not included in the spatial comparisons to further reduce the influence of displacement boundary conditions.

Even with the use of linear elastic material properties, the finite element model was nonlinear. The formulation allowed the geometry and the direction of the pressure

load to be updated as the model deformed. The pressure load was applied incrementally to improve stability during the solution phase.

Finite Element Geometry from Histology

Using histological data to describe the geometry of an arterial branch is one of the unique aspects of this research. As described earlier, a curved surface with second order continuity was fitted over the original polygon surface. This surface was exported from Geomagic Studio as an IGES surface that can be readily imported into Ansys. The geometry is automatically loaded as a series of key points, lines, and areas that can be meshed. For a variable thickness model, Ansys requires that the surface geometry represent the midplane. The model is initially meshed and then the coordinates of the nodes are exported to Matlab. Data export is necessary because the node locations do not precisely correspond to the locations where thickness was measured. Therefore, a spatially weighted interpolation routine determines wall thickness at each node location and then these values are read back into Ansys as a real constant set. Appendix J shows how the real constant set is imported and also shows some sample data extraction programs. Data extraction programs were created for retrieving nodal data, element connectivity, stress component data, and principal stress data.

Element Selection

Ansys Shell Element Number 181 was used in the histology based finite element models. Shell elements were chosen instead of solid elements because they can more accurately capture through-the-thickness stress gradients. This is especially important for modeling arterial branches where blood pressure can produce large stress gradients.

Shell 181 is suitable for analyzing moderately thick shell structures. It is a 4-node element with six degrees of freedom at each node. Change in shell thickness is accounted for in nonlinear analyses. Shell 181 accounts for follower (load stiffness) effects of distributed pressures. This element has the ability to model multiple layers with a high number of integration points through the thickness (up to 9), a feature that makes the element well suited for capturing the complex state of stress near branch points. Nonlinear and orthotropic material properties are supported. In addition, Shell 181 can tolerate irregular shapes without much loss in accuracy.

In the preliminary studies solid elements were used. Solid elements are commonly used for three-dimensional problems because they are highly robust and are suitable for a wide range of problems. But solid elements must be stacked in the thickness direction to capture the complex bending behavior that occurs at arterial branches. The resulting mesh density can be very high, especially if a low aspect ratio element is to be preserved.

Because of these limitations, much work has been done to develop a specialized class of elements called shell elements. A shell structure is created by generating a doubly curved surface, often at the midplane of the wall. Hence, the shell element model is only one element thick, resulting in a substantial reduction in mesh density when compared to a solid element model. Shell elements do not have a precise generalized formulation and require some simplifying assumptions.

Consider the deformed shape in a plane cross section of a shell element, as shown in Figure 3-15. The simplest theory for the deformation of shells uses the Kirchhoff hypothesis and is shown in the top portion of Figure 3-15. This assumes that normals to

the surface remain normal after deformation. The alternative approach, shown below in Figure 3-15, uses the Mindlin hypothesis. The Mindlin hypothesis assumes that normal lines remain straight after deformations, but are not constrained to remain normal. The latter assumption adds complexity to the element formulation, but permits shear strain to be more accurately represented. In either formulation, the deformations anywhere through the wall may be determined based on the displacements and rotations of the midplane nodes.

As a practical matter, Kirchhoff shell elements are often used for thin shells, while Mindlin shell elements are more suitable for thick shells since they include the effects of transverse shear. Ansys Shell 181 was used in the histology based finite element models and is based on the Mindlin hypothesis. For more detail on the shell element used in this study, please refer to the Ansys 7.0 Theory Reference Manual and the Ansys 7.0 Elements Reference Manual.

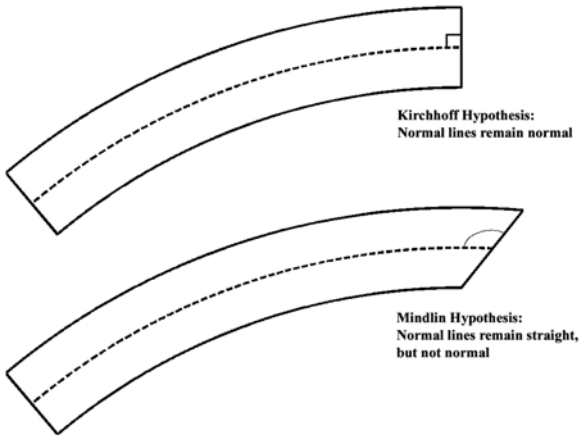

Figure 3-15: A schematic view of the Kirchhoff and Mindlin hypotheses for shell element formulation. Ansys shell 181 uses the Mindlin hypothesis, which includes transverse shear.

Mechanical Properties

Mechanical experiments were considered to determine the pressure-diameter relationship of intact mesenteric arteries. This data could be employed in a finite element model of a branch to more precisely determine the absolute magnitude of the stresses and strains. But collecting and interpreting such data poses difficulties, and the use of such data to model a branch introduces additional uncertainty. A preliminary cannulation experiment underscored the difficulties in trying to measure mechanical properties of mesentery arteries. This experiment revealed a significant delay between changes in input pressure at the heart and changes in the diameter in mesenteric arteries. Out-of-plane movement of the arteries was another critical problem since the mesenteric bed swells with increased pressure and the diameter must be visually captured using a microscope with a limited depth of field. Questions about what would be gained by overcoming experimental difficulties also motivated the use of finite element analysis. The mechanical behavior at branch points probably differs considerably from that of tubular sections. Since the mechanical stresses are largely a function of the pressure-fixed geometry, it is unclear what additional insights would be gained by a more accurate pressure-diameter relationship.

Because of the experimental difficulties and questions about what would be gained, published data were used as the basis for the constitutive relationship. Experimental pressure-diameter curves have been found for rat mesentery arteries (Halpern, Osol et al. 1984; Ceiler and Mey 2000; Bund 2001). An example of such a pressure-diameter curve is shown in Figure 3-16a. The passive strength of the vessel wall depends on the quantity and organization of collagen and elastin. At lower pressures

the strains are smaller and elastin bears more of the load and the vessel is relatively compliant. At higher pressures, collagen bears more of the load and the vessel becomes much more rigid. At high pressures, the adventitia may contribute to the bulk stiffness as well (Ogden and Schulze-Bauer 2000). A pressure diameter relationship for the mesentery artery as found by Ceiler and colleagues (Ceiler and Mey 2000) and a typical arterial stress-strain relationship as derived from canine thoracic aorta by Zhou and Fung (Zhou and Fung 1997) are shown in Figure 3-16b. Based on such data the stress-strain relationship may be defined.

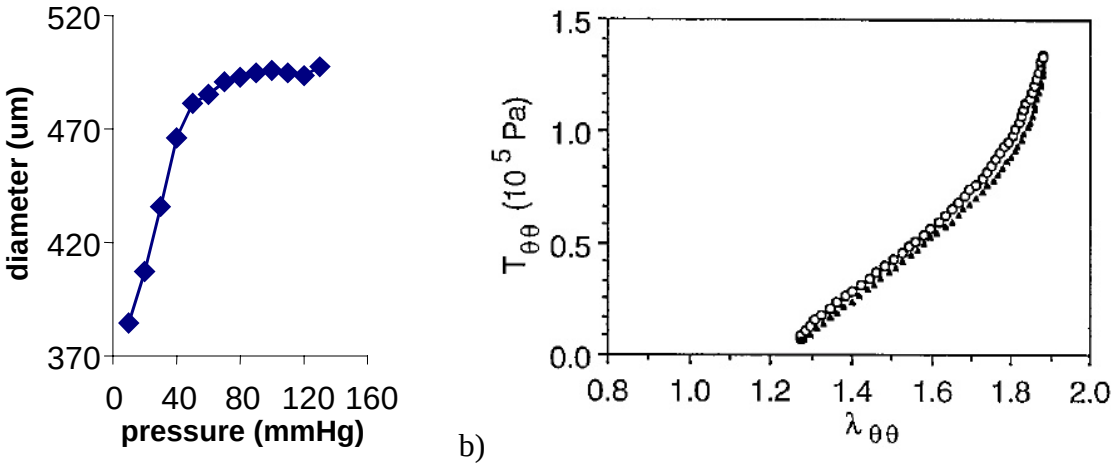

Figure 3-16 a) Sample pressure-diameter data for rat mesenteric arteries, adapted from [Ceiler et al. 2000]. b) The relationship between circumferential stretch ratio and Lagrangian stress in a canine thoracic aorta. Reproduced from [Zhou, 1997].

For structural analysis, the vessel wall was considered to extend from the lumen to the external elastic membrane separating the media from the adventitia. Hence the mechanical rigidity of the adventitia were indirectly incorporated into the finite element model by specifying mechanical properties that would produce a physiologic pressure-diameter relationship. The adventitia may play a secondary role in resisting pressure, but

because its structure is irregular and its mechanical function is not well understood, it was not included in the model.

The mesentery was pressure-fixed at 80 mmHg to better reflect the *in vivo* geometry. For purposes of this work, the focus is on the incremental increase in stress associated with pressure increases above the fixed state. For all hypertensive models the incremental pressure increase was 100 mmHg, reflecting a total pressure of 180 mmHg. The normotensive models used an incremental pressure increase of 40 mmHg, reflecting a total pressure of 120 mmHg. Because of pressure loads are incremental increases, the stress-strain relationship reflects the much stiffer incremental modulus of 2.0 MPa, and the stresses reported are actually changes in stress from the pressure-fixed state. For this linear elastic model, Poisson's ratio was specified at 0.49. The use of pressure-fixed geometry and incremental changes in pressure affects the magnitude of stresses, but the pattern of high and low stresses is believed to remain the same since the geometric deformations are much more limited.

A more accurate approach would have been to guess the zero pressure geometry and then deform the model by an 80 mmHg pressure load to represent the pressure-fixed state. This process would need to be repeated iteratively until the deformed geometry matched the pressure fixed geometry obtained from histology. Such a solution would be computationally intensive, and it is unclear whether the model would converge, especially given the full magnitude and complex nature of the strains that would be produced on the shell elements. This approach would have also increased the magnitude of artifacts produced at model boundaries.

As a supplement to the linear elastic material model, the Ansys material curve-fitting feature was used to evaluate experimental data and generate a hyperelastic material model. A five parameter Mooney-Rivlin hyperelastic model was considered for comparison to a linear material model. Results indicated that the hyperelastic models substantially increased computation time, decreased stability and did not significantly change the stress distributions.

Stress Correlates

A wide variety of stress measures were considered for comparison with inflammatory measures. Distinguishing longitudinal and circumferential stress components in the saddle region of a branch is difficult, thus more generalized stress quantities were employed. The stress components were recorded in global Cartesian coordinates, and then the following stress invariants were determined by forming an eigenvalue-eigenvector problem:

$$I_1 = \sigma_x + \sigma_y + \sigma_z \qquad \text{Equation 3.16}$$

$$I_2 = \sigma_x\sigma_y + \sigma_y\sigma_z + \sigma_z\sigma_x - \tau_{xy}^2 - \tau_{yz}^2 - \tau_{zx}^2 \qquad \text{Equation 3.17}$$

$$I_3 = \sigma_x\sigma_y\sigma_z + 2\tau_{xy}\tau_{yz}\tau_{zx} - \sigma_x\tau_{yz}^2 - \sigma_y\tau_{zx}^2 - \sigma_z\tau_{xy}^2 \qquad \text{Equation 3.18}$$

The two components with the largest absolute value corresponded closely to the in-plane stresses. While stress gradients through the wall were considered, the magnitude of stresses produced by the pressure load could be captured by focusing on the midplane. Midplane stresses are indicative of the average stress level through the wall, with the difference becoming more pronounced with increased nonlinearity.

Note that the first stress invariant, I_1, is indicative of the hydrostatic portion of the total stress. In fact, the hydrostatic portion of stress (σ_m) can be expressed as follows:

$$\sigma_m = \frac{\sigma_x + \sigma_y + \sigma_z}{3} = \frac{1}{3} I_1$$ Equation 3.19

This leads to the second deviatoric stress invariant:

$$J_2 = I_2 - \sigma_m = \frac{1}{6}(\sigma_x - \sigma_y)^2 + (\sigma_y - \sigma_z)^2 + (\sigma_z - \sigma_x)^2 - 6(\tau_{xy}^2 + \tau_{yz}^2 + \tau_{zx}^2)$$

Equation 3.20

The second deviatoric stress invariant is related to von Mises Equivalent Stress reflecting the fact that von Mises Stress is used as yield criteria:

$$\sigma_{vm} = \frac{1}{\sqrt{2}}\left[(\sigma_x - \sigma_y)^2 + (\sigma_y - \sigma_z)^2 + (\sigma_z - \sigma_x)^2 - 6(\tau_{xy}^2 + \tau_{yz}^2 + \tau_{zx}^2)\right]^{\frac{1}{2}}$$

Equation 3.21

Note the relationship between von Mises stress and the second deviatoric stress invariant:

$$\sigma_{vm} = \sqrt{3 \cdot J_2}$$ Equation 3.22

In addition, the maximum shear stress, τ_{sint}, was also considered.

$$\tau_{\text{sint}} = \max\left[\frac{|\sigma_1 - \sigma_2|}{2}, \frac{|\sigma_2 - \sigma_3|}{2}, \frac{|\sigma_3 - \sigma_1|}{2}\right]$$ Equation 3.23

Ansys uses the term “stress intensity” to describe the maximum difference between principal stresses. This term is used in the appendices but for purposes of visual and statistical comparisons stress intensity is the same as maximum shear stress.

Because the maximum principal stress corresponded very closely to the maximum in-plane stress within the wall, the maximal wall tension was approximated as follows:

$$T_{max\,wall\ tension} \cong \sigma_1 h \qquad \text{Equation 3.24}$$

In Equation 3.24, *h* represents the local wall thickness. A more accurate approach would be to resolve the principal stresses into in-plane and out-of-plane components based on the surface normal.

Early investigations indicated that the local curvature properties of the branch surface were indicative of the stresses produced by blood pressure. This technique is valuable because it provides a first order measure of intramural stresses that can be determined quickly and is available even when wall thickness data is not (Liao, Duch et al. 2004). Since more detailed finite element studies were conducted, the use of Gaussian curvature is described in Appendix F.

The cell density calculations were performed at the lumen surface, so generating stress values at this surface is desirable for direct comparisons. Therefore the nodal stresses were mapped to the lumen surface by using distance-weighted interpolation. A copy of the interpolation program is provided in Appendix F.

To summarize the development of the methods for stress analysis, the preliminary parameter studies provided a greater understanding of the issues and challenges associated with studying branches (e.g. required mesh density, appropriate displacement boundary conditions). The use of idealized geometry provided insights into the general distribution of stress without the idiosyncrasies associated with histology-based reconstructions. Shell elements were used because they could capture the high stress gradients that are present near branch points. An incremental linear elastic material

model was used. Stresses at the midplane of the branch geometry were ultimately compared to a biological marker of inflammation. The next section will describe how inflammation was measured.

Numerically Characterizing Inflammation

Earlier in this chapter, the identification of monocytes and macrophages was described (see "Cell Identification"). A considerable effort was focused on the use of immunological techniques to identify markers of inflammation. Unfortunately, neither radioisotopic *in situ* hybridization nor immunostaining techniques proved successful in combination with glycol methacrylate embedding. The immunological results tended to be weak, often nonspecific, and highly variable from section to section. For these reasons, monocytes and macrophages were identified by staining sections with a haematoxylin and eosin stain and examining the morphological characteristics at high magnification. A graphic user interface facilitated this process by allowing an observer to browse high magnification montages and click on cells that were monocytes or macrophages. The user interface stored the locations of each cell in image coordinates. This data was then compiled into a three-dimensional point cloud of cells based on section alignment and expressed in terms of physical coordinates. The cell distributions and cell density calculations will now be described.

Cell Distribution

Figure 3-17 shows an image of the cell distribution overlaid on a branch reconstruction. Even with multiple views like Figure 3-17, it is difficult to determine the location of cells and get a sense for where cells might be concentrated. It would be preferable to characterize the cell distribution in such a way that local concentrations of

cells would be visually more obvious. It is also desirable to quantify the concentration of cells in a way that can be more readily compared to the stress distribution.

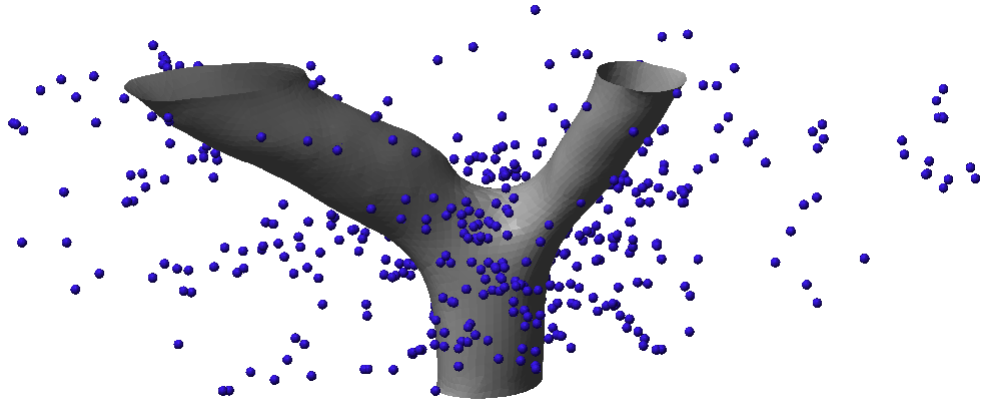

Figure 3-17: Monocyte/macrophage cells in proximity to a branch.

Cell Density - Calculated and Visualized at the Cell Centers

The key metric chosen for characterizing the distribution of cells is a true three-dimensional measure of cell density. The simplest measure of cell density is to divide the total cell count by the total volume, but this provides no insight into the spatial variation of cell density. For this reason, a spherical subvolume was defined and centered on each cell location. Figure 3-18 shows a 100 μm radius sphere centered on a cell to determine cell density. Choosing the radius of the sphere was not an exact science. It is desirable for the radius to be large enough that the sphere overlaps several cells otherwise the cell density measures would only be based on discrete cell counts of a few cells and would appear very noisy when viewed collectively. This small radius size would make it difficult to see trends within the branch. As an upper bound, the radius must be markedly smaller than the complete region of study. If the radius is very large it becomes difficult

to see data trends due to the blending of cell density calculations. For the branches studied a radius of 100 to 175 μm provided a good balance between noise effects at the low end and blending effects at the high end. The general trends in the models could be seen over a wide range, but a 150 μm radius was used because it was visually informative for all the models.

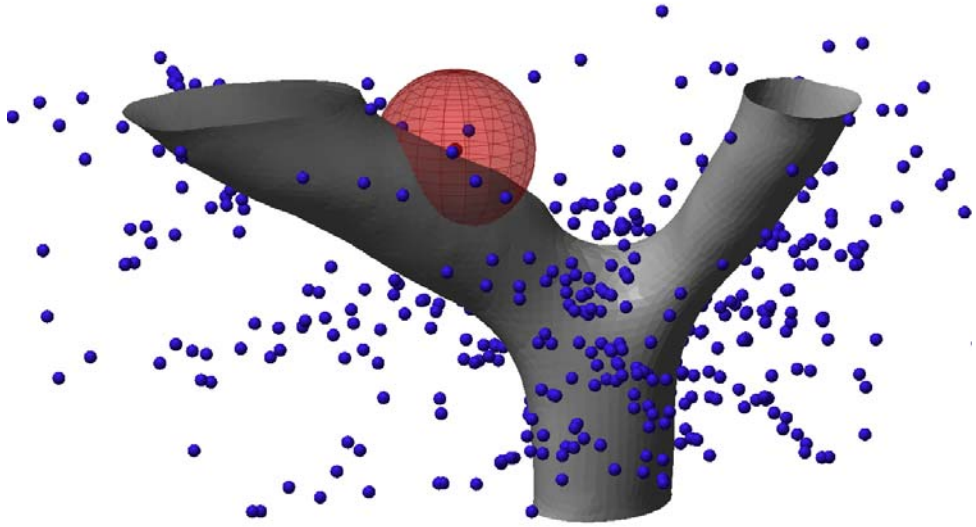

Figure 3-18: Branch showing a spherical subvolume that was used to calculate cell density. This sphere has a radius of 100 μm, although 150 μm was used for the final cell density calculations.

The most direct method for determining cell density is to divide the number of cells within a sphere by the volume available for cells.

$$cell\ density = \frac{\#cells_{sphere}}{V_{ext}} \qquad \text{Equation 3.25}$$

The volume available for cells is referred to as the external volume (V_{ext}). In general, V_{ext} is less than the total volume of the sphere because of the lumen and other regions where cells cannot be present. The simplest approach would be to count external

voxels that are within each spherical subvolume. But there are about ten-fold more external voxels than internal voxels. Some of the matrix operations become unwieldy with such a large array of voxels, therefore an alternative approach was used.

The more efficient approach involves determining all of the parts of the spherical volume that are not available for inflammatory cells and subtracting them from the spherical volume. While this approach involves more steps, it is approximately 100-fold faster. The remainder of this section describes the components of the cell density calculation as it was implemented in this research.

Given a radius R, the original unmodified volume of a sphere is:

$$V_{sphere} = \frac{4}{3}\pi R^3 \qquad \text{Equation 3.26}$$

But several adjustments must be made to the volume calculation to accurately determine cell density. As illustrated in Figure 3-18, the spherical volume can extend into the lumen. But cells are not present within the lumen so this portion of the volume must be excluded from consideration before cell density can be accurately calculated. To calculate lumen volume, a masked image stack was imported into Matlab and a voxel map was created. Then, for each spherical subvolume, the distance from the cell center to each lumen voxel was calculated:

$$distance_{center} = \sqrt{(x_{voxel} - x_{center})^2 + (y_{voxel} - y_{center})^2 + (z_{voxel} - z_{center})^2}$$

Equation 3.27

Any lumen voxel with a Euclidean distance less than the radius is within the sphere and is summed as an inner voxel:

$$\#voxels_{\text{int}} = \sum voxels_{lumen} \in distance_{\text{center}} \le R \qquad \text{Equation 3.28}$$

The portion of the volume that is within the lumen is simply the sum of the internal voxels times the volume of a single voxel.

$$V_{\text{int}} = \#voxels_{\text{int}} \cdot \Delta x \Delta y \Delta z \qquad \text{Equation 3.29}$$

The last component of the volume calculation involves determining if part of the subvolume extends outside the model space. Since there are no cell data outside the model space, the effective volume must be reduced. Figure 3-19 illustrates how the effective volume must be reduced near the upper boundary of the model space.

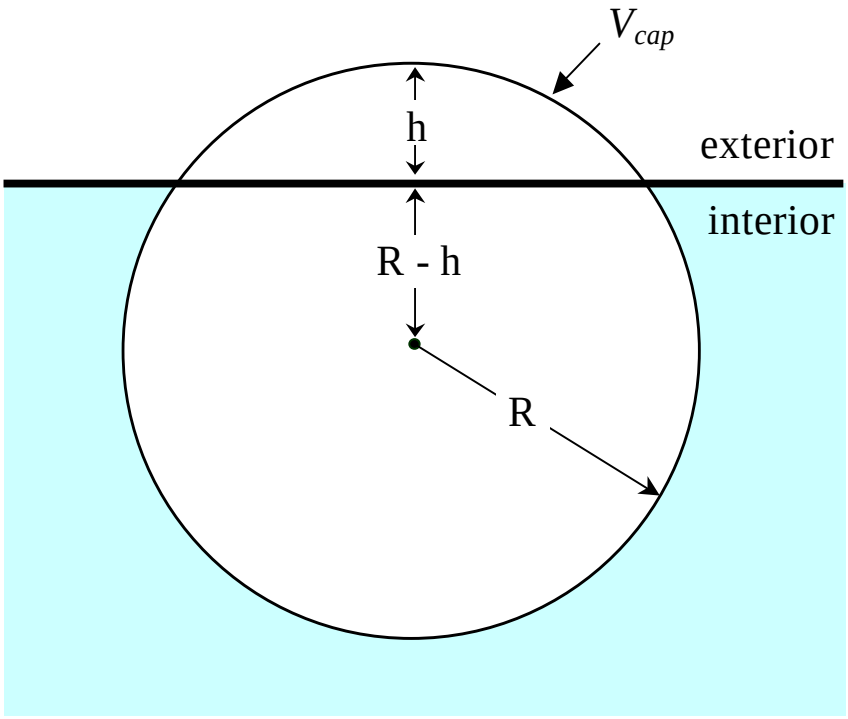

Figure 3-19: This figure shows the volume correction, V_{cap} that is necessary when a spherical subvolume overlaps a model boundary.

The volume outside the boundary is called V_{cap} and is described by the following equation:

$$V_{cap} = \frac{1}{3}\pi h^2 (3R - h) \qquad \text{Equation 3.30}$$

This boundary-related adjustment is easily and efficiently implemented since a distance test and possible adjustment only needs to be performed once per layer.

The final adjustment to obtain an accurate density measure needs to be made because the first and last sections contain cells, but only half of these voxels are within the model space. The most efficient adjustment is to count boundary cells as half-cells.

$$\#cells_{sphere} = \#cells_{interior} + \frac{1}{2} \cdot \#cells_{boundary} \qquad \text{Equation 3.31}$$

The volume available for inflammatory cells, V_{ext}, is:

$$V_{ext} = V_{sphere} - V_{cap} - V_{\text{int}} \qquad \text{Equation 3.32}$$

The right side of equation 3.32 represents the less direct, but much more computationally efficient method to determine the volume available for inflammatory cells.

$$cell\ density = \frac{\#cells_{sphere}}{V_{ext}} = \frac{\#cells_{sphere}}{V_{sphere} - V_{cap} - V_{int}} \qquad \text{Equation 3.33}$$

This equation reflects the equivalency of the direct and an indirect method for calculating cell density and provides a means to validate the cell density calculations. In the development of the Matlab programming, the ability to compare these results helped debug the code and helped avoid conceptual errors. For a sample case, cell density was determined by both methods, and cell density measurements were found to be accurate to within 0.5 percent. The small difference in calculated cell density can be attributed to the error in volume measurement associated with counting discrete voxels.

$$V_{ext} = \frac{4}{3}\pi R^2 - \frac{1}{3}\pi h^2 (3R - h) - \sum voxels_{\text{int}} \cdot \Delta x \, \Delta y \, \Delta z \qquad \text{Equation 3.34}$$

Figure 3-20 shows a sample cell density distribution where the cells are color-coded with a local measure of cell density. Front and rear views of all cell density distributions are presented in the Chapter 4. Please see Appendix I for the programs used to calculate and visualize cell density.

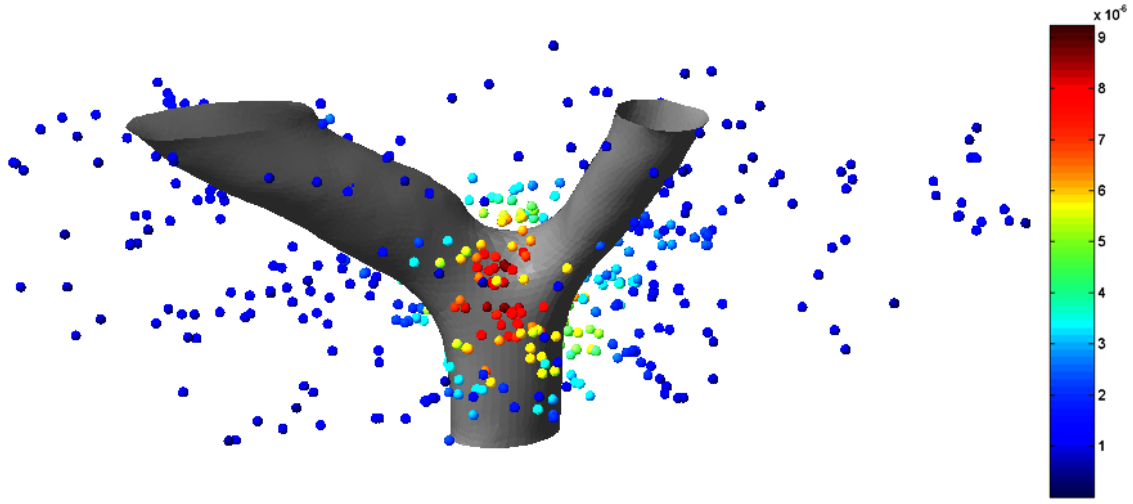

Figure 3-20: Cell density distribution shown as a color-coding on cells (scale:1 inch ≈ 290 μm).

Cell Density - Calculated and Visualized on the Vessel Surface

In the previous section the method for quantifying cell density was described. Ultimately the cell density was quantified in proximity to each cell and this value was used to color code the cells. Therefore even where the three-dimensional position of cells is not immediately obvious from a particular view, the color-coding specifies cell density and conveys essential informal about the distribution of inflammation. Such color-coded maps are informative, but it is desirable to express cell density in a way that is directly comparable to stress results.

For this reason, the approach described in the previous section was modified so that cell density was calculated at the luminal surface. The luminal surface consists of a

series of triangular patches that consist of three vertices and topological map that indicates the connectivity. Instead of centering the spherical subvolume on the cells the spherical subvolume is centered on each vertex of the surface to obtain a local measure of cell density.

$$distance_{surf-cell} = \sqrt{(x_{surf} - x_{cell})^2 + (y_{surf} - y_{cell})^2 + (z_{surf} - z_{cell})^2}$$

Equation 3.35

$$distance_{surf-voxel} = \sqrt{(x_{surf} - x_{voxel})^2 + (y_{surf} - y_{voxel})^2 + (z_{surf} - z_{voxel})^2}$$

Equation 3.36

Given this adjustment in the test criteria for counting cells and voxels, the rest of the work from the previous section also applies to generating cell density values at each vertex of the surface. Figure 3-21 shows a sample color-coded map. Note that here the essential information about cell distribution, cell density, is represented by the color-coding of the vessel surface. Therefore the cells themselves do not necessarily have to be visualized.

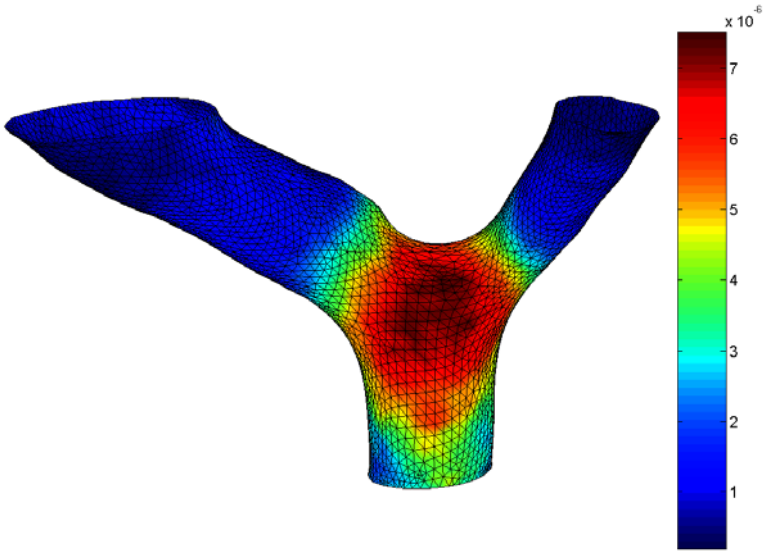

Figure 3-21: Cell density distribution mapped to lumen surface.

The computational efficiency of the previously described method is even more significant when the cell density calculations are centered on the vessel surface since there are many more vertices than there are cells.

Wall Thickness as a Measure of Inflammation

The method used to determine wall thickness was described previously, and the results of these calculations are presented in the Chapter 4. Since medial thickening is associated with inflammation, wall thickness may be considered a secondary measure of inflammation. The difficulty is that variations in wall thickness occur independent of inflammation, and no reference state is available to help distinguish naturally occurring variations in wall thickness from inflammatory changes. Because of this difficulty, wall thickness is not the primary focus when discussing inflammation.

Creation of a Branch Proximity Measure

In addition to comparing variables measured at the same three-dimensional location, it is possible to generate a one-dimensional measure of the spatial proximity of a surface point to the origin of a branch. To generate this measure, the center of each branch must first be identified. This is relatively simple where there is a large difference in the size of the vessels. At these locations, a point is identified on the centerline of the daughter vessel where it originates from the mother vessel. This can be graphically determined by visually sectioning a model with a plane. For the branches that forked into similarly sized daughter vessels, the point is identified on the wall where flow division occurs. Geometrically, this is the center of the hyperparabolic surface in the plane where branching takes place.

Once the branch centers are identified, the Euclidean distance from each surface point is calculated and the minimum of these distances reflects the relative proximity of each surface point from the closest branch center. Hence the term "branch proximity" will be used to indicate the inverse of the distance from the branch. Sample Matlab code to generate this variable is provided in Appendix H.

Methods for Comparing Stress to Inflammation

This section describes the approaches used to compare data. Because of great variation in geometry from branch to branch, most of the comparisons were focused on spatially comparing different characteristics (e.g. stress versus cell density) within a given branch. A sample case is used when discussing the methods to help clarify how these methods were employed. The sample case is H7A, a branch from a rat harvested 7-days after hypertension was induced using Angiotensin II.

Visual Comparisons

Visual comparisons can take on a number of forms. The primary means of visually comparing branch data consisted of side-by-side comparisons of two variables as shown in Figure 3-22. Note that the wall tension data is low near the branch boundaries. As discussed previously, this is caused by the finite element boundary conditions. When visually comparing the data, it is important not to focus on the boundary data for the mechanical models. All numerical comparisons were done only after eliminating data points that are within a specified distance of the upper or lower boundary.

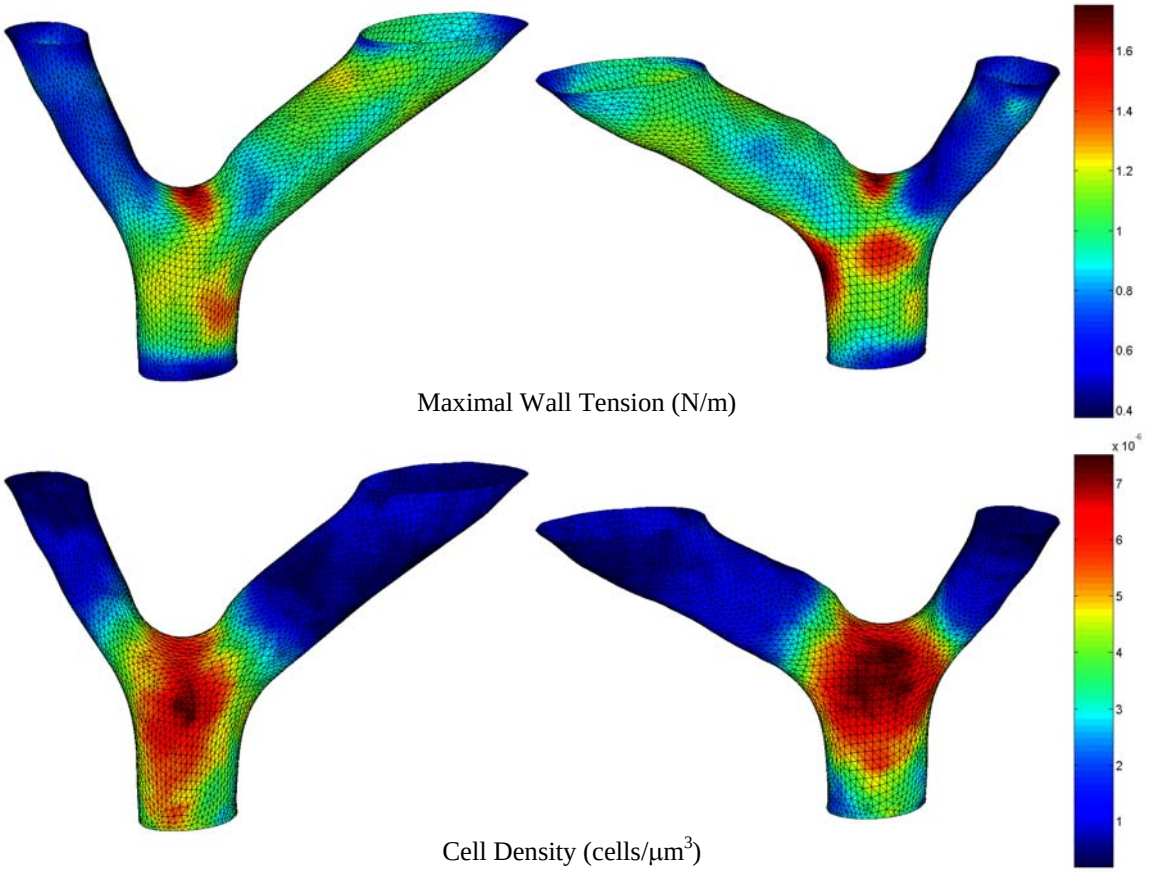

Figure 3-22: Visual comparison of the spatial distribution of two branch characteristics. Maximal wall tension and cell density are being compared, but the focus here is on the method and not on the results.

The results of the visual comparisons like the one illustrate in Figure 3-22 will be discussed in detail in Chapter 4. In this particular case, there is a strong spatial correspondence between the peaks in wall tension (indicated by red) and the peaks in cell density (also indicated by red). For illustrative purposes this will be discussed further in this section, but please see Chapter 4 for the formal presentation and discussion of results.

Another visual tool that was used to evaluate relationships between the data was a thresholding technique where the surface was color-coded with a single color when

values exceeded some specified threshold. The appeal of this approach is that it recognizes that the mapping of variables may not be strong over the entire range, but that the peak in one variable may still correspond with the peak in another variable. For example, peak stresses may stimulate inflammatory changes like high monocyte/macrophage density, while lower stresses have no meaningful connection to the relative magnitude of cell density.

In practice, the upper quartile of data for two branch characteristics was identified. These quartiles might be marked on separate visualizations that are presented side-by-side. But since less information is being presented, the results may be shown together on the same visualization. The region of overlap between the upper quartiles is identified logically with Boolean operations and represented visually by a unique color. This process is illustrated for the sample case in Figure 3-23.

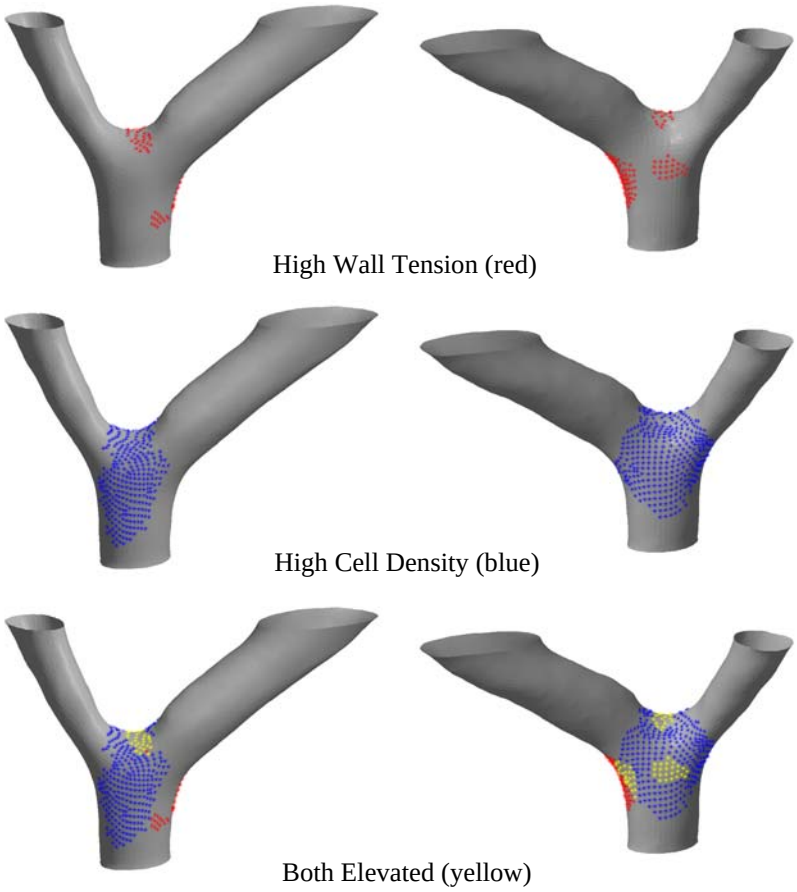

Figure 3-23: Illustrates the use of pseudocolor to identify regions where two surface characteristics are elevated. The top set shows the regions of high wall tension in red, the middle set shows the regions of high cell density in blue, and the bottom set shows the combined image with the locations where both values are elevated are shown in yellow. In general the bottom view is all that is needed to make comparisons.

The advantage of using thresholding is that it provides a quick assessment of the spatial correspondence between two branch characteristics. But this approach requires judgment about what level of signal/response should be represented and only represents the values in a binary manner. These disadvantages can pose a problem and possibly mask positive signal. Figure 3-22 suggested that there is a strong correspondence between the regions of high wall tension and high cell density for this branch. However,

as Figure 3-23 illustrates, the use of thresholding can mask the correspondence that exists, especially when the thresholding range is small. Thresholding was used as a preliminary tool to evaluate the spatial similarity in two branch characteristics, but these intermediate results will not be further discussed. Based on these results it is clear that the comparisons between models should extend beyond visualizations to statistical tests.

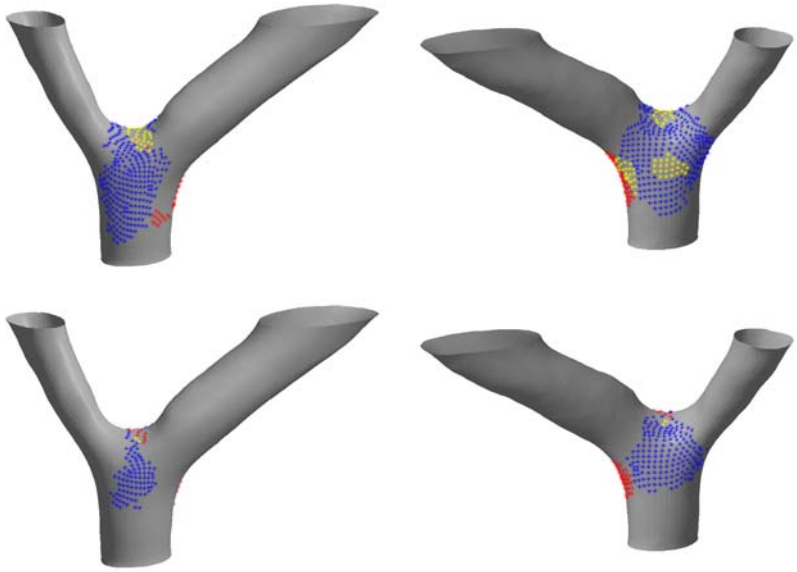

Figure 3-24: This figure illustrates how different thresholds can affect visual comparisons between two variables. In this case, maximal wall tension (red) is plotted with cell density (blue). The region of overlap is shown in yellow. The top 33 percent of values, by magnitude, are shown in top half of figure. The top 20 percent of values, by magnitude, are shown in bottom half of figure. A more sophisticated method than a binary test appears to be needed.

Statistical Comparisons – Spearman Rank Correlations

Much can be learned from making side-by-side comparisons of visualizations. But it is desirable to reduce these comparisons to a more rigorously testable hypothesis. The ultimate goal is to determine if a spatial relationship exists between variables. Statistical tests can provide an objective means to accomplish this goal. After a brief

examination of the statistical characteristics of the data, two approaches to making statistical comparisons will be described. First, the method of comparing two characteristics by Spearman rank correlations will be described. Second, a Wilcoxon rank sum test will be presented based on different groupings of data.

As Figure 3-25 illustrates, the variables studied in this research do not generally exhibit normal distributions. In fact, the histogram (Figure 3-25a) and the cumulative distribution (Figure 3-25b) show a highly non-normal distribution of cell density. The high number of surface points with a low cell density is marked evidence of non-normality. The Anderson-Darling Normality Test yields an A-squared value of 136.0, also reflecting the non-normality of this distribution. This A-squared value reflects the squared difference in distance between the actual distribution and a normal cumulative distribution (Romeu 2003). This distance measure is more heavily weighted at the ends, explaining the particularly high value of A-squared in this example. The p-value associated with this result is less than 0.0001, indicating a high degree of confidence in the result. These results are typical and underscore the need to use nonparametric statistical methods to analyze the data.

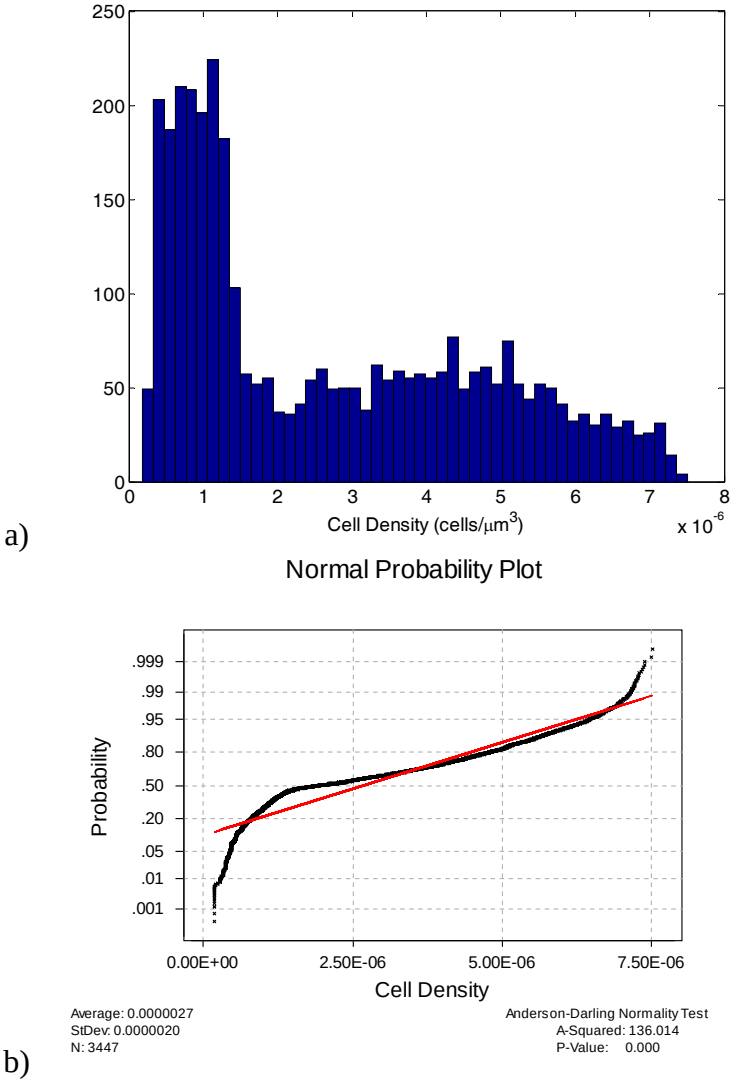

Figure 3-25: The histogram (a) and the cumulative distribution (b) of cell density in this example exhibit a highly non-normal distribution. These results are typical and underscore the need to use nonparametric statistical methods to analyze the data.

The most obvious statistical comparison is to examine whether two variables are correlated. Toward this end, a variety of variables represented at each surface point were compared. To discuss the statistical methods, the example of wall tension and cell density is used, as indicated in Figure 3-26. First, there is clearly not a strong linear

relationship between changes in wall tension and changes in cell density. A linear regression fit is shown on this plot and the trend of increasing cell density with increasing wall tension is evident. The trend is consistent with the general hypothesis of this research, but the strength of the correlation is low as reflected be the R-squared value of 0.074.

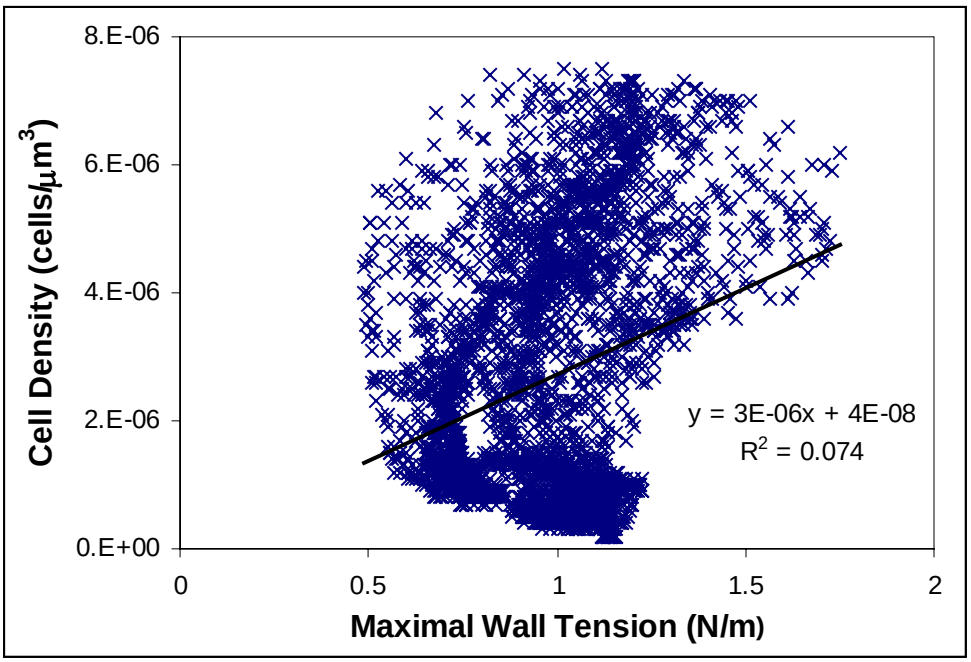

Figure 3-26: Wall Tension versus Cell Density for Branch H7A. The linear regression line is plotted. While the trend is consistent with what was hypothesized, the R-squared value is low at 0.074.

Since the data is not normally distributed, a Spearman rank correlation was considered as an alternative to regression. Like regression, the Spearman rank correlation can be used to compare two independent random variables. Unlike regression, this approach uses the ranking of the values instead of the values themselves. The rank is the position of a value in the list of values ordered from smallest (rank 1) to largest.

This nonparametric approach involves ranking both variables and then using these rankings as a distribution-free substitute for the original values. The strength of the association between the rankings can be characterized using the Spearman rank correlation coefficient ($r_{spearman}$) as follows:

$$r_{spearman*} = 1 - \frac{6\sum_{i=1}^{n}(R_i - S_i)^2}{n(n^2 - 1)} \qquad \text{Equation 3.37}$$

R_i is the rank of x_i among all values of x, S_i is the rank of y_i among all values of y and n is the number of observations. In essence, this equation is a sum of the difference between the rankings of paired observations on the surface of the branch.

A more accurate measure of correlation may be obtained by accounting for ties by assigning them the average of their ranks. For instance, if the highest two ranked observations have the same value then their rank becomes 1.5, the average of the ranks of the two observations. The equation with an adjustment for ties is shown below:

$$r_{spearman} = \frac{1 - \frac{6}{n^3 - n}\left[\sum_{i=1}^{n}(R_i - S_i)^2 + \frac{1}{12}\sum_{k=1}^{nx_{ties}}(f_k^3 - f_k) + \frac{1}{12}\sum_{m=1}^{ny_{ties}}(g_m^3 - g_m)\right]}{\sqrt{1 - \frac{\sum_{k=1}^{nx_{ties}}(f_k^3 - f_k)}{n^3 - n}}\sqrt{1 - \frac{\sum_{m=1}^{ny_{ties}}(g_m^3 - g_m)}{n^3 - n}}}$$

Equation 3.38

In this equation, f_k is the number of ties in the kth group of ties among all x values and g_m is the number of ties in the mth group among all y values. Sample Matlab code for determining the Spearman rank correlation for all models is shown in Appendix K.

A perfect positive correlation would mean that the ranking of two variables would be identical at a given location. The corresponding $r_{spearman}$ value would be 1.0.

Conversely, a perfect negative correlation means the rankings of the first variable are the inverse of the rankings of the second variable ($r_{spearman}$ = -1.0). The significance of the Spearman rank coefficient is dependent on the number of observations, and for a large number of observations (more than 30) the coefficient can be normalized as follows:

$$Z_{spearman} = r_{spearman}\sqrt{n-1} \qquad \text{Equation 3.39}$$

Ideally this statistic can be used to determine the area under the normal curve and a measure of confidence as to whether a correlation exists. In the case of wall tension versus cell density, $r_{spearman}$ is 0.124 and the $Z_{spearman}$ is 7.3. This suggests that cell density increases with increasing wall tension and that is highly unlikely that this trend is masked by random variation in the data ($\alpha < 0.005$).

The Spearman rank sum test was validated by comparing the program results to a variety of sample cases where the results were known. This included comparison to published data, comparison to randomly generated data, and comparisons to perfect positive and negative correlations. Note that the order of the variables does not affect the Spearman rank correlation because the values are replaced with rankings, and the strength of the correlation is based on the sum of the square of the differences.

Maximal wall tension, a variety of stress invariants, cell density, wall thickness and distance from branch center were all considered and the results from the Spearman rank correlations will be presented and discussed in the Chapter 4.

A variety of nonlinear curve fits were examined and none significantly improved the strength of the correlation. A great deal of variability exists in the data due to the complexity of the three-dimensional architecture and the simplifying assumptions used to evaluate the pressure response.

Statistical Comparisons – Wilcoxon Rank Sum Tests

An alternative to correlation over the full range of data was also considered. Recall that high mechanical loads are hypothesized to stimulate inflammatory changes. It seems reasonable that stress or wall tension might not be correlated over the full range of data, but that above some threshold value the mechanical loading becomes a stimulus for localized inflammatory response. To evaluate the possibility of such a relationship between variables, a Wilcoxon rank sum test was performed.

A Wilcoxon rank sum test is a nonparametric test that requires two samples and seeks to find if there is a significant difference in the medians of the two samples. For this research the surface points are divided into two groups based on the magnitude of the first variable. For example, the upper quartile of wall tension values might represent one group, while the remaining values represent the second group. If no relationship exists between wall tension and cell density then the distribution of cell density values would not differ between the two groups. This in fact is the null hypothesis in a Wilcoxon rank sum test. Because the cell density is not normally distributed, the density values are replaced with the ranking of density values for the combined set. The mean values of cell density for the two groups are compared to see if there is a significant difference. The Wilcoxon rank sum test examines the likelihood that a second group was from the same population as the first group. This statistical test is a natural extension of the thresholding shown in the visual comparisons in Figure 3-23 and Figure 3-24. The additional benefit of the statistical test is that it considers the relative magnitude of the values above the threshold level and provides an objective measure of the difference between the groups.

The Wilcoxon rank-sum test is an alternative to the two-sample t-test and it is the appropriate choice when the data is not normally distributed (Walpole and Myers 1993). The sum of the ranks can be described by the following equation:

$$w_1 + w_2 = \frac{(n_1 + n_2)(n_1 + n_2 + 1)}{2} \qquad \text{Equation 3.40}$$

where

w_1 = sum of the ranks of the smaller sample

w_2 = sum of the ranks of the larger sample

n_1 = number of observations in the smaller sample

n_2 = number of observations in the larger sample

This test is intuitively more meaningful if the expected mean value is subtracted from w_1 and w_2, leading to:

$$u_1 = w_1 - \frac{n_1(n_1 + n_2 + 1)}{2} \qquad \text{Equation 3.41}$$

$$u_2 = w_2 - \frac{n_2(n_1 + n_2 + 1)}{2} \qquad \text{Equation 3.42}$$

In this form the mean values u_1 and u_2 are approximately zero when there is no difference in the means of the two groups (i.e. when the null hypothesis is true). Expressing the means in this form permits the use of standard tables to evaluate the similarity between two groups.

For large samples the sampling distribution of rank values approaches a normal distribution. When n_2 is greater than 20 and n_1 is greater than 8, one can generate a statistic for a standard normal distribution:

$$Z_{wilcoxon} = \frac{U_1 - \mu_{U_1}}{\sigma_{U_1}}$$ Equation 3.43

where

$$\mu_{U_1} = \frac{n_1 n_2}{2}$$ Equation 3.44

$$\sigma_{U_1} = \sqrt{\frac{n_1 n_2 (n_1 + n_2 + 1)}{12}}$$ Equation 3.45

In this case the mean normalized rank is zero and the variance is 1 and a normal distribution table may be used. An appealing feature of the Wilcoxon rank sum test is that it is not restricted to non-normal populations. It can be used in place of a two-sample t-test when the populations are normal, although the power is smaller. For strongly non-normal populations a Wilcoxon rank-sum test is superior.

One additional modification that was made in the use of this test was to adjust for ties in ranking before doing the rank summation. A Matlab program was written to automate this process and the program was designed so it could be integrated into a Spearman rank correlation or a Wilcoxon rank sum test. The Wilcoxon rank sum test results were validated by comparing them to the results from Minitab 12.0. Note that Minitab refers to the Wilcoxon rank sum test as a Mann-Whitney Test. Minitab uses this name to avoid confusion with the Wilcoxon *signed* rank test, which examines differences in paired observations (Ryan and Joiner 2001). Additional validation work included testing for perfect positive and negative correlations as well as confirming no correlation for randomly generated samples.

So in the example of maximal wall tension and cell density, first the data is divided into two groups. The high wall tension group is the upper quartile of wall tension

values based on magnitude. The second group consists of the lower three quartiles of wall tension. Based on this grouping the monocyte/macrophage cell density was compared for the two groups. For branch H7A this test revealed U = 57076 which is significantly different than zero, given the sample size ($p < 0.05$). Based on the mean and standard deviation of the rankings, the equivalent normalized statistic, $Z_{wilcoxon}$, is 6.4, indicating high confidence in the test. The raw data for the Wilcoxon rank sum tests is presented in Appendix K, with limited data and general observations discussed in Chapter 4.

CHAPTER 4:

RESULTS AND DISCUSSION

Three-Dimensional Reconstruction

Surface Reconstruction

Over the next several pages the inner wall reconstructions from seven branches will be presented. As described earlier, each sample was harvested *en masse* with the mesentery of rat to minimize the deformations during embedding. It was only during microscopy that specific branches were identified and studied. The surface geometry varied considerably from sample to sample (see Appendix C for more information). The descriptions will focus on specific geometric characteristics of each surface with the goal being to enhance the reader's understanding of the specific characteristics of each surface model. All of the branches are oriented with proximal end of the mother vessel at the bottom of the figure. Most of the branches exhibited, to some degree, elliptical transverse cross sections away from the branch center. Possible reasons for this and the mechanical implications will be discussed later.

A pattern will be repeated throughout the presentation of individual results, whether the data is surface description, wall thickness, stresses, or cell density. First, the four 7 day hypertensive branches will be presented, then the one 21-day hypertensive branch, and finally the two normotensive branches. For each branch two opposing views

will be shown side-by-side. For convenience, the left view is called the front view, while the right view is called the back view. For greater clarity the range of color-coded information will be scaled individually for each branch, Appendix A shows a set of color coded maps grouped by branch for easier comparison between characteristics for a given branch. These results are scattered through this chapter, and are repeated in Appendix A for greater convenience. Alternatively Appendix B shows a set of color-coded maps that share the same scale. These maps are grouped by characteristic to facilitate comparisons between branches. Please refer to these if there are questions about the relative magnitude of the plotted quantities.

For convenience, the description of the samples and sample labeling from Chapter 3 is repeated here in Table 4-1. The naming convention will be used henceforth with some reminders.

Table 4-1: Summary of Sprague-Dawley rat experiments, reiterating the naming convention for the samples to be discussed.

Sample Name	Pressure State	Drug Treatment	Rat Identifier
H7A	Hypertensive	7-day exposure to Angiotensin II	R5
H7B	Hypertensive	7-day exposure to Angiotensin II	R8
H7C	Hypertensive	7-day exposure to Angiotensin II	R1D
H7D	Hypertensive	7-day exposure to Angiotensin II	R4
H21A	Hypertensive	21-day exposure to Angiotensin II	R10B
NA	Normotensive	none	R2
NB	Normotensive	none	R3

Figure 4-1 shows the front and back view of the inner surface reconstruction for branch H7A. This branch was harvested after a seven-day exposure to Angiotensin II.

When considering the branch centerlines, the branching does not occur in a plane. The two distal ends arch backwards when viewed from the front (left hand image in Figure 4-1).

Figure 4-2 shows branch H7B, also harvested after a 7-day exposure to Angiotensin II. This branch was similar in character to H7A. The main branch was a nearly balanced bifurcation that arched backward out-of-plane. However there was a small tertiary branch splitting off in close proximity to the main branch. This tertiary branch was difficult to reconstruct since it only spanned a few sections and was oriented approximately longitudinally with the sectioning plane. A submodel was created of this feature using every section and this submodel was incorporated into the larger model. The branch was ultimately truncated in close proximity to the surface of its parent vessel. This eliminated the need for special boundary conditions in the finite element model.

Figure 4-3 is branch H7C, the third of four branch geometries from a 7-day hypertensive rat. This was the first rat tissue harvested and the harvest method differed from later harvests. In this case the mesentery was rolled in filter paper before processing to concentrate the tissue in one region of the block. The benefit of rolling is that it concentrates the mesentery in a smaller area and facilitates the location of branches. A drawback of rolling is that a non-physiological loading may be placed on the sample as it is rolled. It is possible that rolling this sample produced the elliptical cross section of the mother vessel, but it is also possible that physiologic boundary conditions produce this effect. This second possibility is discussed in greater detail in the context of stress analysis later in this chapter. Note the mother vessel follows an essentially straight path while three secondary, much smaller daughter vessels originate from the main vessel.

The fourth and final 7-day hypertensive branch is H7D, shown in Figure 4-4. The centerline of the geometry of this branch is nearly planar, and this branch exhibited the greatest disparity in size between the mother vessel and the primary daughter vessel. The reconstruction of this branch posed the most significant challenges. The change in direction of the main vessel is an unusual characteristic of this geometry. This bend might be a natural characteristic of the *in vivo* geometry, but it is also possible this bend is an artifact of deformations during embedding or an error in alignment. It is important to note that this branch was positioned at the periphery of the embedded sample, which means the branch is more susceptible to gross deformations before it was embedded. This peripheral location also makes this case more prone to errors in alignment, since there are fewer tissue features nearby.

Figure 4-5 shows branch H21A, from a rat subjected to a 21-day exposure to Angiotensin II before the mesentery was harvested. While this was the thickest model in proportion to its size, the surface model was similar to that in Figure 4-1 and Figure 4-2. There was less of an arch in the geometry and the transition region of the branch was somewhat larger and more bulbous.

Branch NA is shown in Figure 4-6 and this represents the first of two normotensive samples. This was not the largest diameter vessel studied, but the geometry spanned a very large distance at its distal end. This can largely be attributed to the fact that the vessel was not transversely aligned with the sectioning plane. Also the branches diverge at approximately a 90-degree angle without changing course.

Figure 4-7 shows NB, the second normotensive sample. This is one of the smallest branches and the daughter vessels diverge at a relatively narrow angle when compared to the rest of the branches.

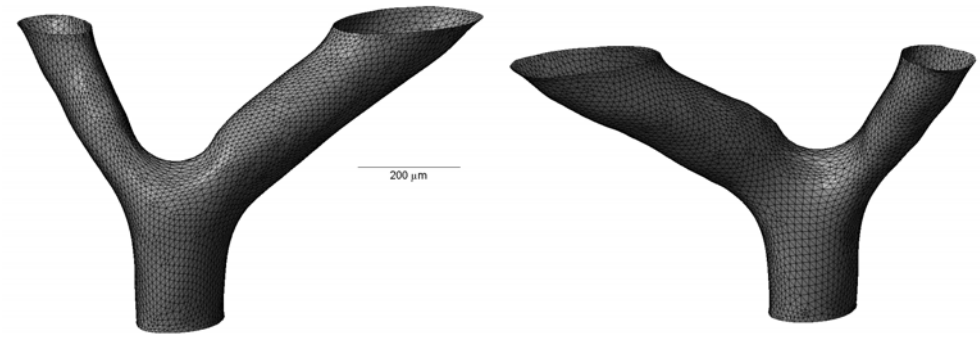

Figure 4-1: Front and back views of the inner surface reconstruction for branch H7A, harvested after 7 days of hypertension.

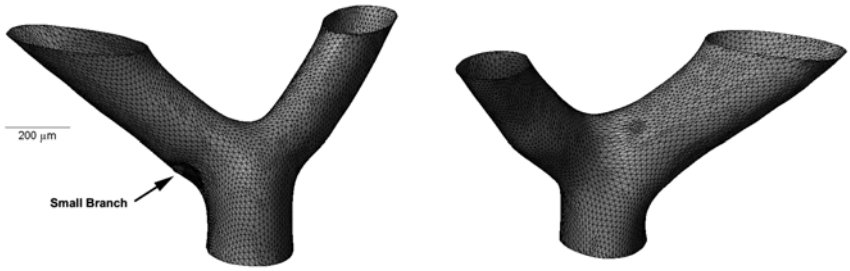

Figure 4-2: Front and back views of the inner surface reconstruction for branch H7B, harvested after 7 days of hypertension.

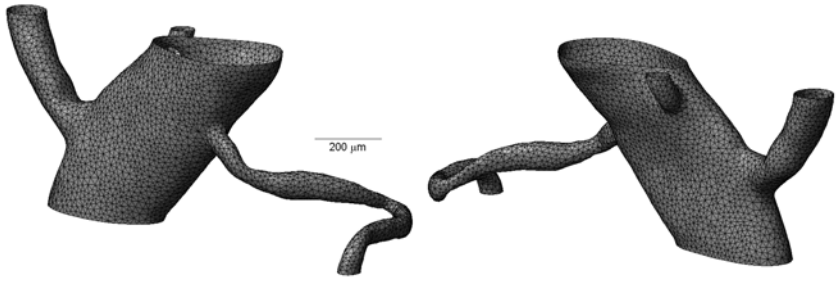

Figure 4-3: Front and back views of the inner surface reconstruction for branch H7C, harvested after 7 days of hypertension.

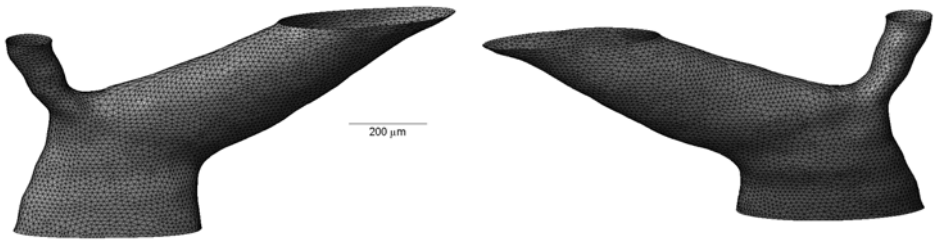

Figure 4-4: Front and back views of the inner surface reconstruction for branch H7D, harvested after 7 days of hypertension.

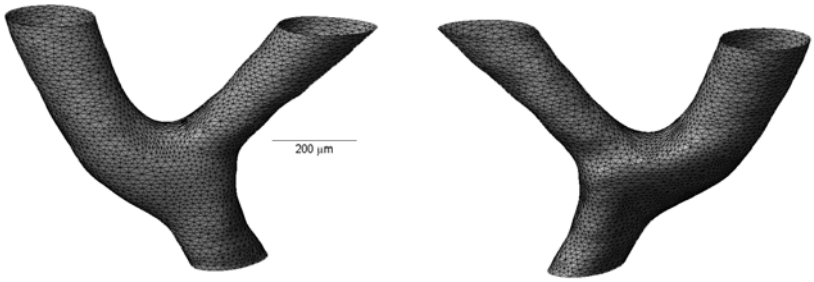

Figure 4-5: Front and back views of the inner surface reconstruction for branch H21A, harvested after 21 days of hypertension.

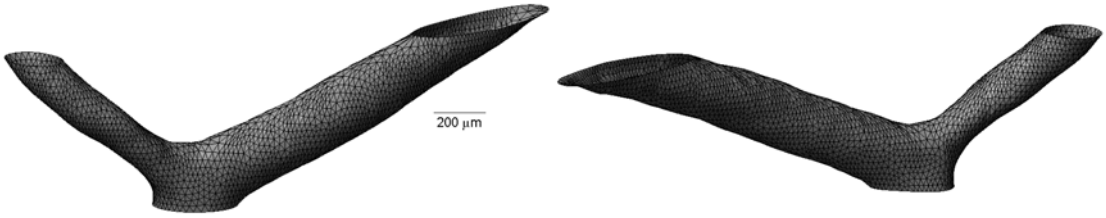

Figure 4-6: Front and back views of the inner surface reconstruction for branch NA, harvested from normotensive rat.

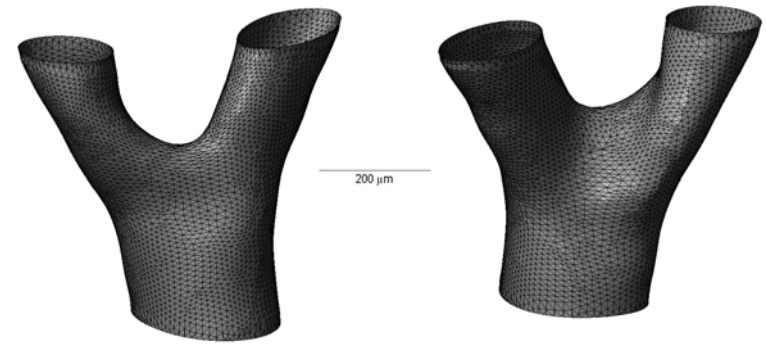

Figure 4-7: Front and back views of the inner surface reconstruction for branch NB, harvested from normotensive rat.

Wall Thickness Distribution

So far the inner surface geometry has been presented. As discussed in Chapter 3, an outer surface model was also created and then rays emanating from each interior polygon were used to determine intersections with the outer surface. Using this method, the thickness distribution was defined for the complete model. The next series of figures present the results of these thickness measurements as color-coded maps overlaid on the inner surface.

In general there was considerable variation in wall thickness, especially through the transition regions of each branch. The pattern was not always regular or predictable, as the individual results will show. Table 4-2 summarizes the thickness data, indicating minimum thickness, maximum thickness, mean thickness and standard deviation. Such data is of limited utility, but indicates the general variability present in wall thickness.

Table 4-2: Summary table of wall thickness (in μm) variation within each branch.

Wall Thickness (μm)	H7A	H7B	H7C	H7D	H21A	NA	NB
Minimum Wall Thickness	11.4	21.8	9.3	14.8	24.7	20.1	14.8
Maxmimum Wall Thickness	39.9	54.8	43.1	47.0	57.6	32.4	42.1
Mean Wall Thickness	20.6	38.3	26.5	24.4	37.2	26.7	23.8
Standard Deviation	5.5	6.9	7.5	5.5	5.8	1.7	6.3

Figure 4-8 shows the distribution of wall thickness through branch H7A. As expected there is a general trend of decreasing thickness through the branch. But there are two focal regions of high wall thickness in the branch transition region. Both of the localized peaks are near the branch center, in regions where the principal radii of

curvature are likely to be on opposite sides of the wall (i.e., where Gaussian Curvature is negative).

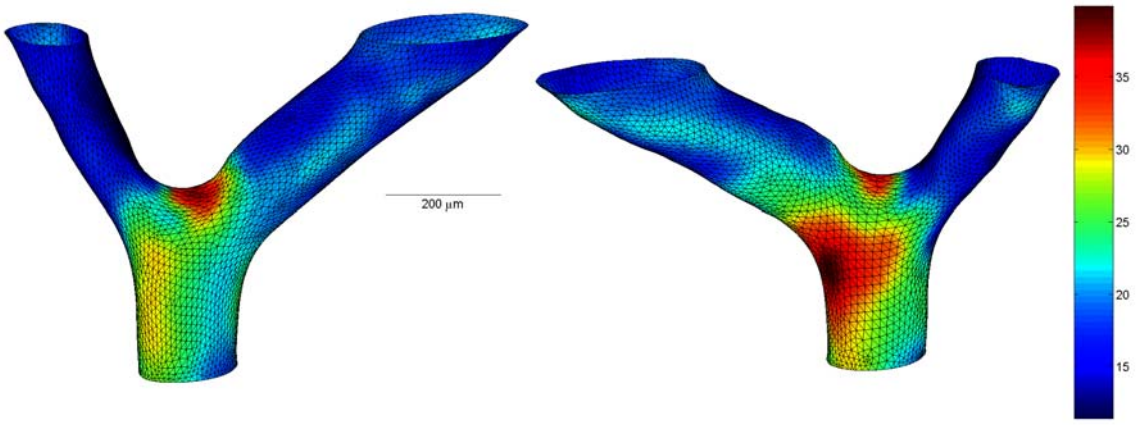

Figure 4-8: Wall thickness (μm) for branch H7A after 7 days of hypertension.

Figure 4-9 shows the wall thickness distribution for branch H7B. This geometry also exhibits high wall thickness in proximity to the branch, but a more diffuse high thickness in the mother vessel proximal to the branch point. Note the tertiary branch is highlighted with the inset view because the patch density is higher here and the patch edges mask the color-coding.

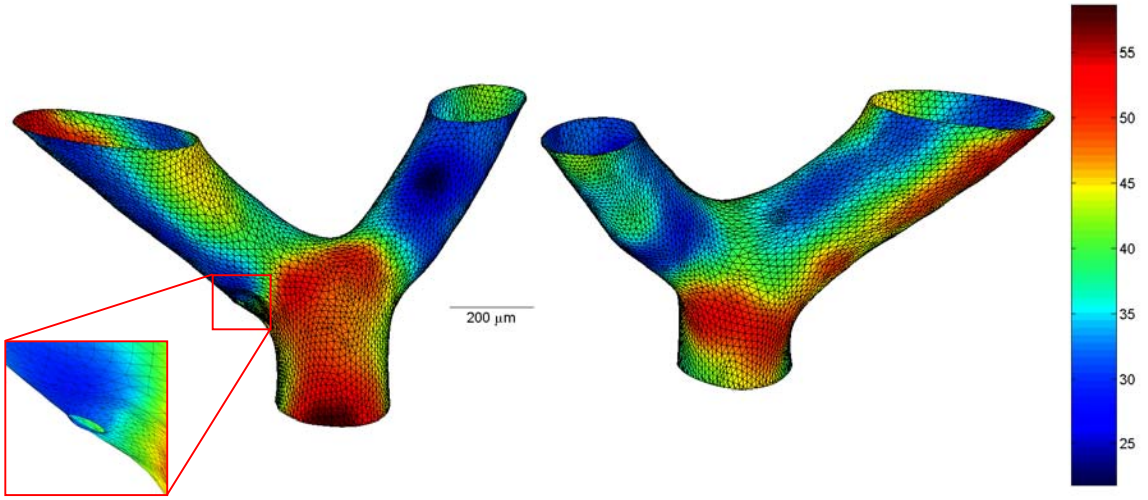

Figure 4-9: Wall thickness (μm) for branch H7B after 7 days of hypertension.

The distribution of wall thickness for branch H7C is shown in Figure 4-10. There is a significant variation in wall thickness through this model. As Table 4-2 indicates the mean thickness is 26.7 μm with a standard deviation of 7.8 μm. If the standard deviation is normalized by the mean thickness, this branch geometry is shown to exhibit the greatest variation among all models. This large variation can be explained by the large difference in the size of mother and daughter vessels. It is still noteworthy the wall thickness was locally higher in proximity to the branches, particularly in regions where mechanically unfavorable surface characteristics are present (i.e. highly negative Gaussian curvature).

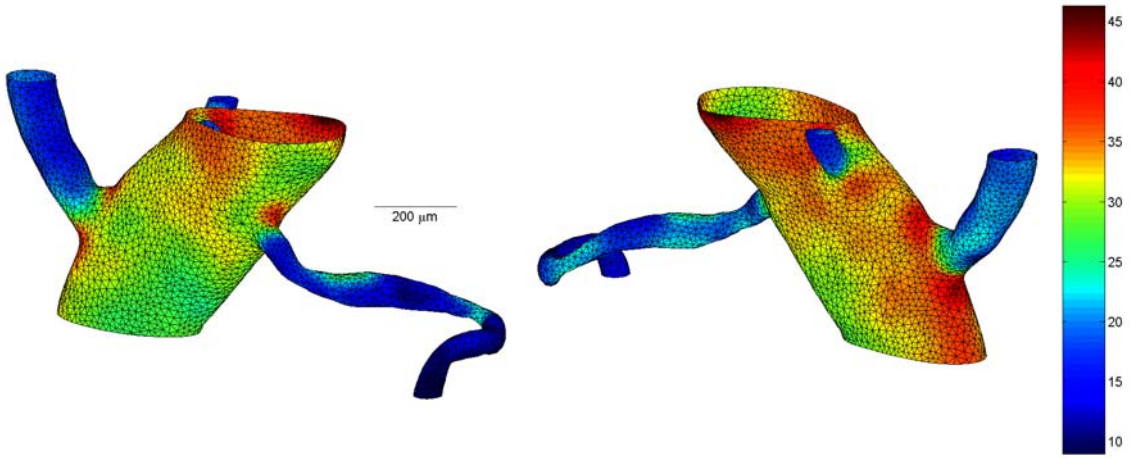

Figure 4-10: Wall thickness (μm) for branch H7C after 7 days of hypertension.

Figure 4-11 shows wall thickness for branch H7D, the fourth and final branch from a 7-day hypertensive animal. Like H7C this branch shows a large difference in parent-daughter vessel size. But in this model, wall thickness varies more distinctly with circumferential location. This geometry exhibits the greatest departure from a circular transverse cross-section. There is some concern that the elliptical cross-section is an artifact produced during processing, however the substantial variation in wall thickness

suggests there has been a developmental or adaptive response to the elliptical geometry. The observations and discussions of this are mixed with the underlying mechanics and so this will be discussed in greater detail in the context of the finite element analysis.

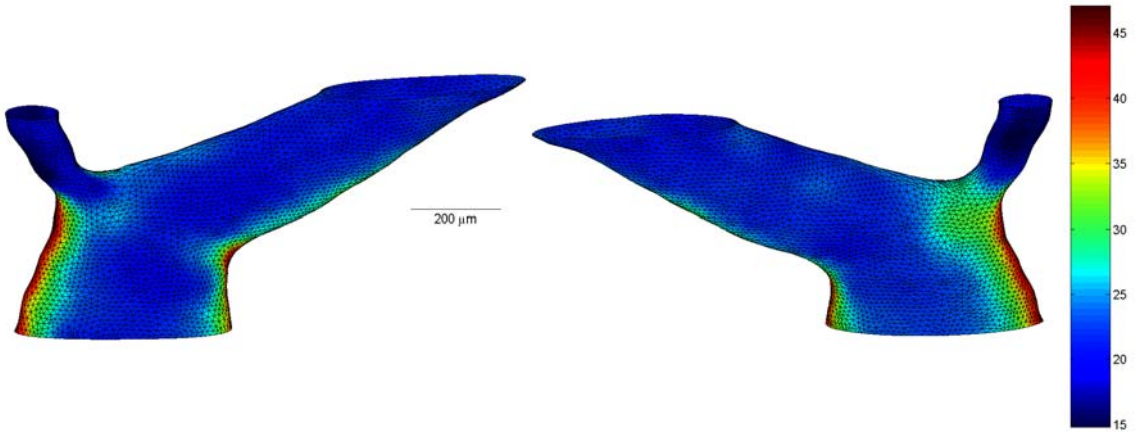

Figure 4-11: Wall thickness (μm) for branch H7D after 7 days of hypertension.

Figure 4-12 shows the wall thickness distribution for H21A, which is from a 21-day hypertensive rat. Note that wall thickness peaks in all three regions where the surface curvature conditions are unfavorable and might produce high midplane stresses. The average wall thickness in this model was 36.7 μm, which is large relative to the size of the branch. This is consistent with the increased medial thickening occurring after a longer exposure to hypertension. Interestingly, the normalized standard deviation in wall thickness was comparatively low, suggesting that the medial thickening was not highly localized after 21 days of hypertension and that some normalization in wall thickness had occurred at this time point.

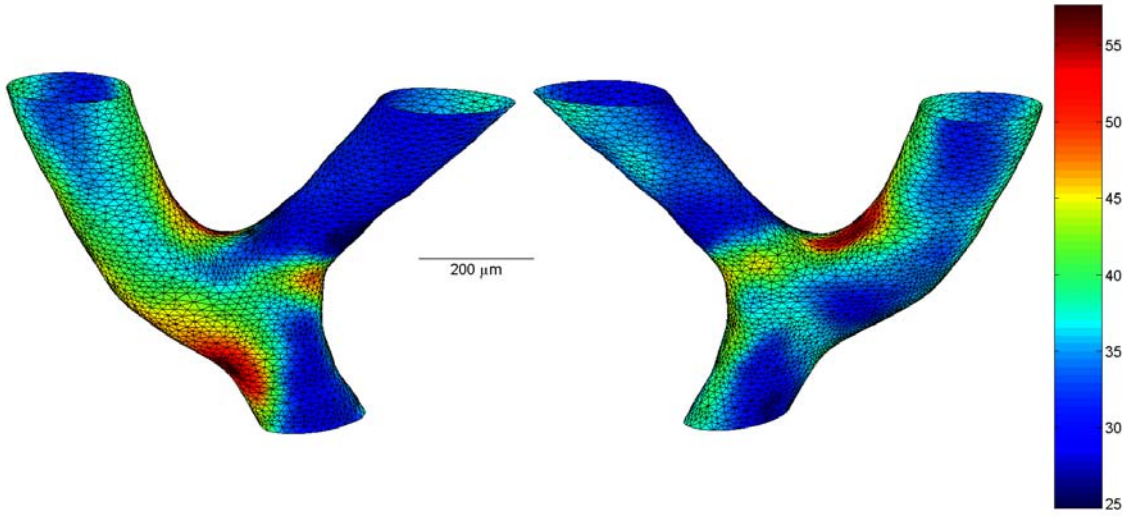

Figure 4-12: Wall thickness (μm) for branch H21A after 7 days of hypertension.

Figure 4-13 shows the wall thickness variation for branch NA, the first of two normotensive samples. This sample exhibited relatively small variation in thickness that was irregularly distributed. Wall thickness was not locally greater near the branch. Not surprisingly for a normotensive case, the wall thickness was relatively low when normalized by branch size. The normalized standard deviation in wall thickness for this branch was the lowest among all branches, suggesting there was comparatively little variation in wall thickness for this normotensive branch.

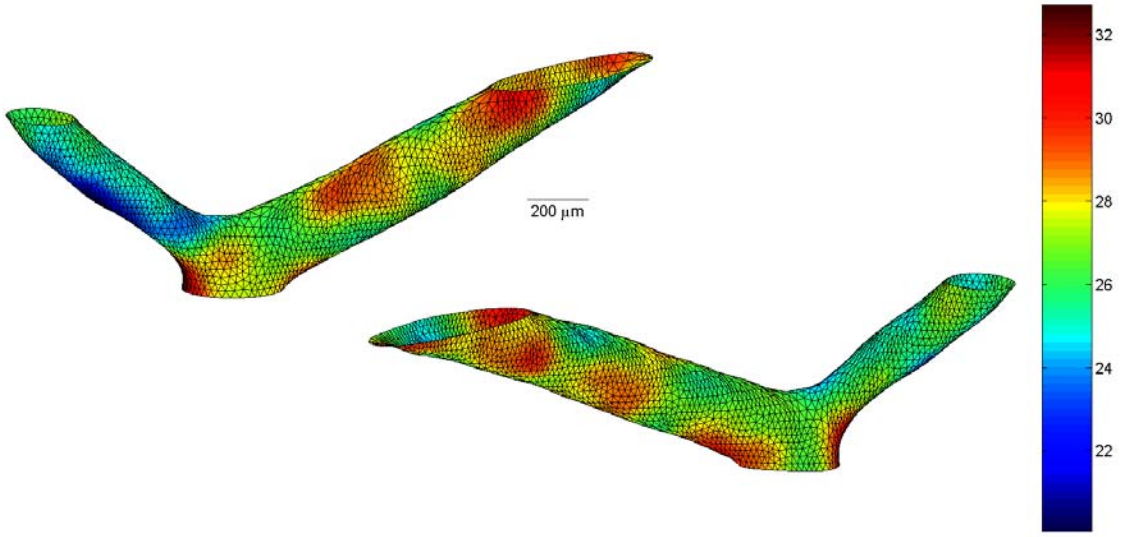

Figure 4-13: Wall thickness (μm) for branch NA, from a normotensive rat.

Figure 4-14 shows the wall thickness variation in NB, the other normotensive branch. For this model the variation in wall thickness was greater than for NA, and the wall thickening was localized in the mother vessel, upstream of the bifurcation. While there is not an obvious explanation for this pattern, it is clear that thickness is not high at the point of flow division (i.e. in the saddle region).

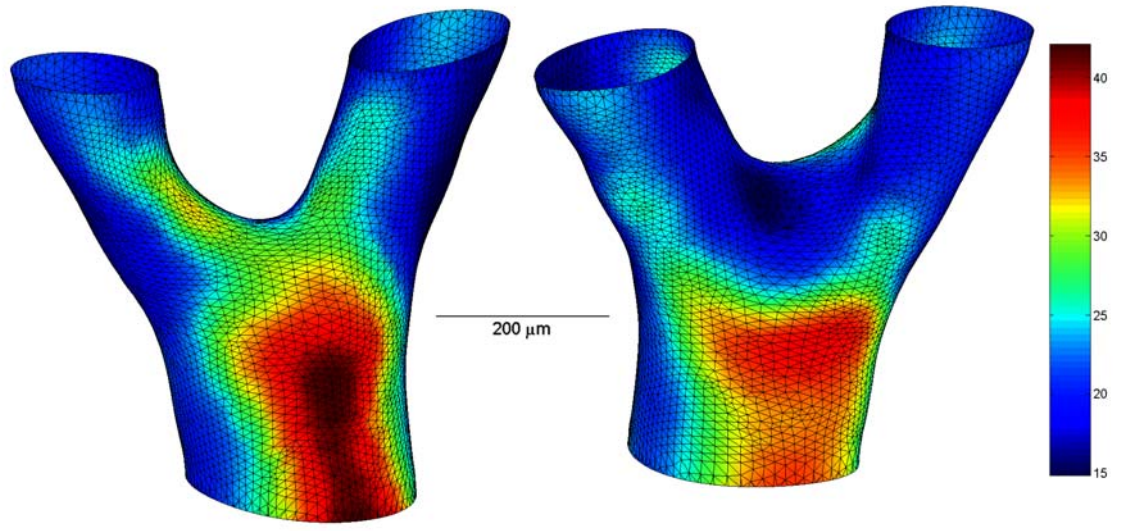

Figure 4-14: Wall thickness (μm) for branch NB, from a normotensive rat.

Stress and Wall Tension

The consideration of mechanical stimuli included a variety of possible stress correlates, but also included the maximal wall tension. Since strains are related to stresses, they tend to be redundant when making first order comparisons of phenomena. From a mechanistic perspective, the distinction between stress and strains is more important and should be revisited. Also, the difference between stresses and strains becomes more significant for hyperelastic models than for the linear elastic incremental stresses presented through much of this research. Wall tension combines in-plane stresses with intramural thickness, in a way that collapses the three-dimensional state of stress to a two-dimensional description at the midplane of the vessel wall.

Recall from the methods discussion that the mesentery was pressure fixed at 80 mmHg and so the finite element models reflect incremental changes in stress and strain above this pressure fixed state. For hypertensive branches the incremental pressure increase was 100 mmHg, while for normotensive branches the incremental pressure increase was 40 mmHg.

As discussed earlier, the difficulty in measuring stresses at branches in these small mesenteric arteries led to the estimation of the stress distribution using the finite element method. This is justified, in part, by recognizing that the goal is to evaluate the general distribution of stresses or other mechanical stimuli. In this light, the results of stress analysis are presented below.

Both a linear elastic and hyperelastic constitutive relationship were considered. Because the focus is on incremental stresses from the pressure fixed state, it turns out there were not substantial differences between the two material models, especially for

stresses at the midplane. Figure 4-15 is an Ansys display of maximum principal stress results for linear elastic and hyperelastic models. The pattern of stresses in the two models is very similar. Note that differences in the stress ranges account for much of the difference in the color ranges. A linear elastic model was used because of similarities such as these.

a) b)

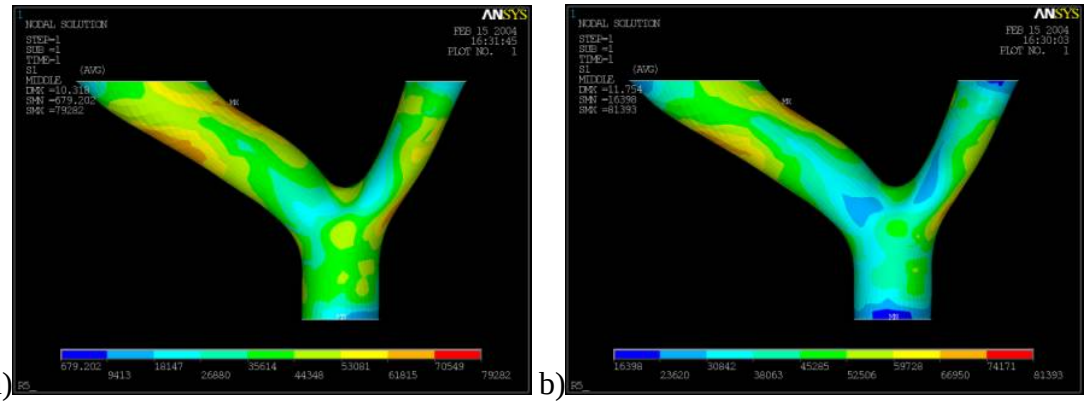

Figure 4-15: Compare maximum principal stress distributions in branch H7A for a) linear and b) hyperelastic constitutive models.

Figure 4-16 shows the distribution of von Mises equivalent stress at the midplane of branch H7A. This branch is one of four samples harvested after 7 days of Angiotensin II induced hypertension. As discussed in Chapter 3, these stresses are associated with the incremental change in pressure between the pressure at fixation and the systolic pressure. Surprisingly, the von Mises stresses did not peak in the saddle region. The greatest stresses were in the larger vessel distal to the bifurcation. The regions of high stress correspond to regions where the wall is relatively thin. Conversely, the saddle region with its unfavorable curvature characteristics did not produce high midplane stresses largely because of higher localized thickness in this region. This suggests the adaptive response of the vessel wall may be locally highly controlled by the mechanical environment. But wall thickness is coupled both to the state of stress and to the state of

inflammation, making it difficult to separate stress as a stimulus from inflammation as a response.

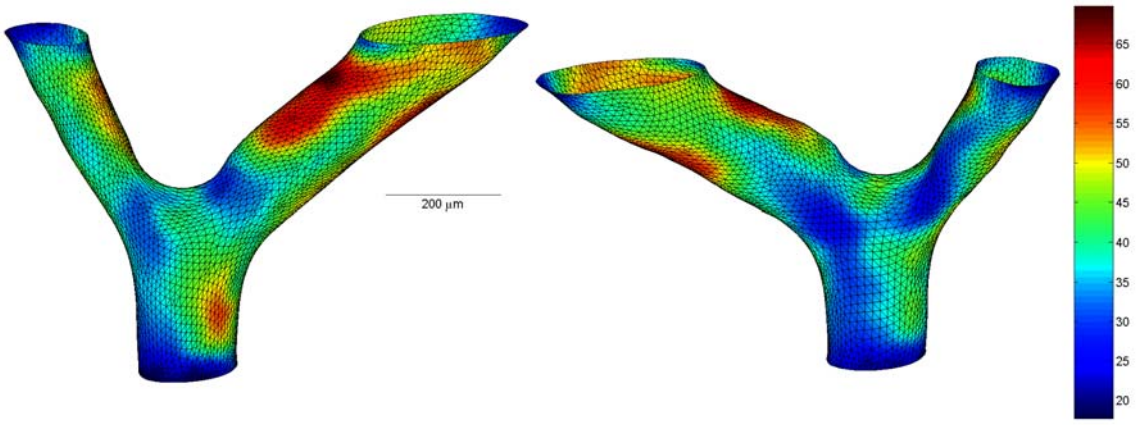

Figure 4-16: Von Mises stress distribution in kPa for branch H7A, after 7 days of hypertension.

In concert with von Mises stress, a second mechanical correlate was considered that seeks to limit the impact of wall thickness variations. Maximal wall tension was also considered for each branch. The maximal wall tension is calculated by multiplying the maximum in-plane stress by the local wall thickness. This gives a better measure of the two-dimensional in plane response of the wall due to pressure. Figure 4-17 shows the maximal wall tension for the same branch as Figure 4-16. Note that, in this case, the wall tension is highly elevated in the primary saddle region at the point of flow division and also in a secondary saddle region evident in the righthand/rear view.

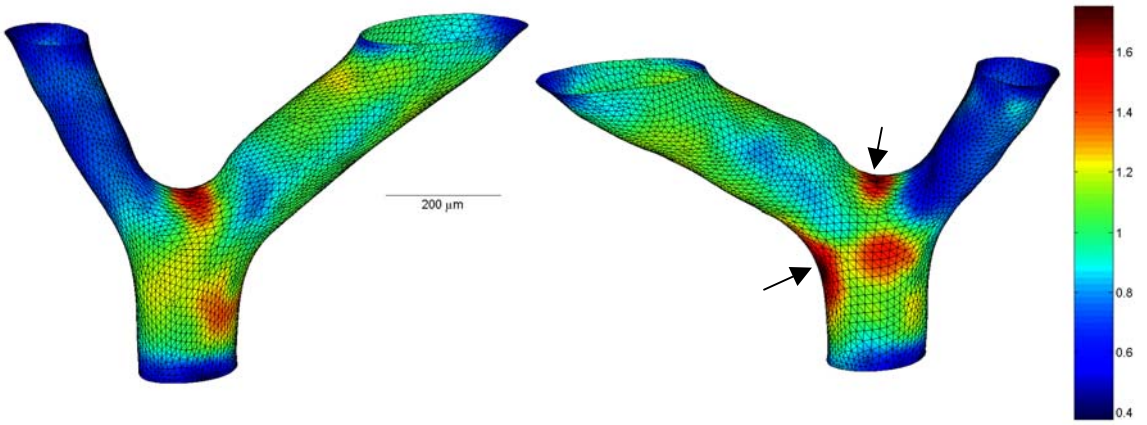

Figure 4-17: Maximal wall tension in N/m for branch H7A, after 7 days of hypertension.

Figure 4-18 shows the von Mises stress distribution for H7B, a 7-day hypertensive branch. The range of stresses is considerably higher with a localized peak in proximity to the tertiary branch. This region of the model is magnified because the patch edges make it difficult to see the stress distribution near this tertiary branch. Similar to H7A, a local maximum of about 70 kPa occurs in the saddle region with somewhat lower peaks of about 60 kPa in both arteries distal to the branch point. The pattern of stresses around the tertiary branch is similar to what is produced by introducing a hole into a plate that is in tension. Extending the small vessel further away from the main vessel shifted the location of the peak distally but did not eliminate the stress concentration.

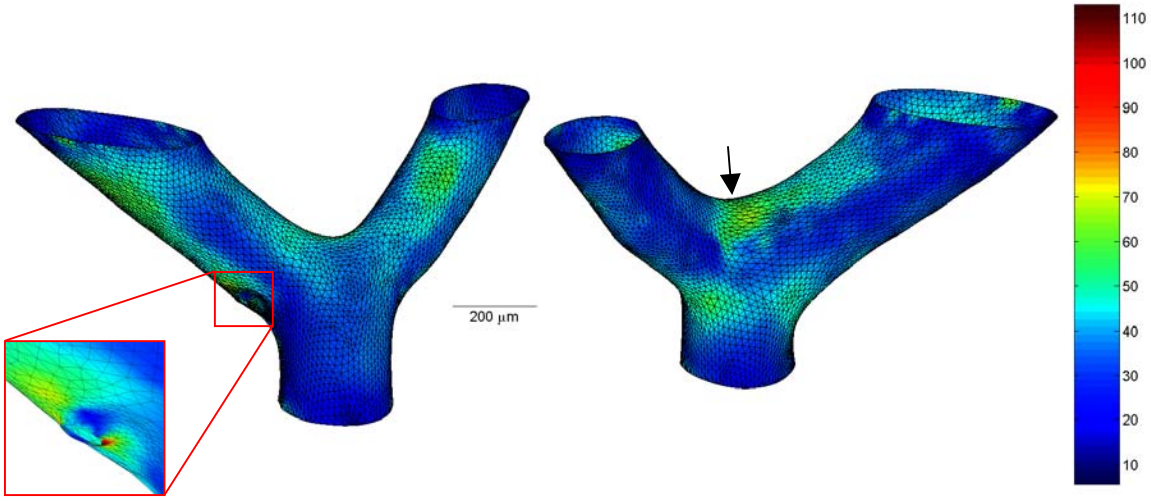

Figure 4-18: Von Mises stress distribution in kPa for branch H7B, after 7 days of hypertension.

Figure 4-19 shows the maximal wall tension within the wall for branch H7B. A diffuse peak in wall tension of 3.6 N/m is evident in the rear view as indicated by the arrow. Secondary peaks of about 2.5 N/m can be seen in the flow divider region in both the front and back views. A high wall tension is present in the transition region for the tertiary branch shown in the inset.

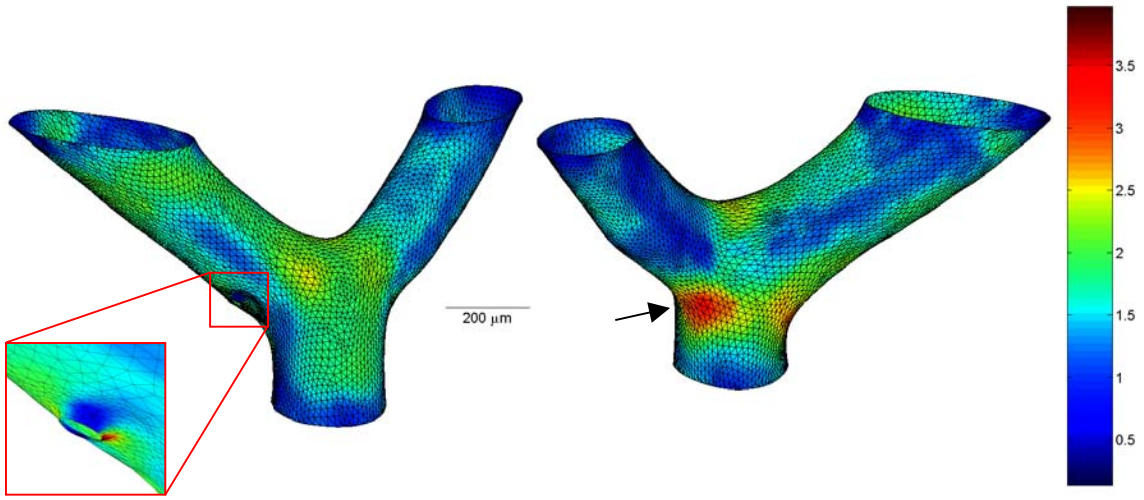

Figure 4-19: Maximal wall tension in N/m for branch H7B, after 7 days of hypertension.

Figure 4-20 shows the von Mises stress distribution within H7C, from a 7-day hypertensive rat. This geometry includes three smaller arteries that branch off from the main vessel. It is clear that stress peaks of about 100 kPa occur in proximity to each branch. A plane of branching can be defined by the centerlines of two vessels in proximity to the branch point. Stress peaks tend to occur in this plane, above and below the origination point of each daughter vessel. Also, for each case, the greater intramural stress occurs on the acute side of the transition region as exemplified with the arrows in the rear view. This trend is consistent with the unfavorable pressure-curvature characteristics that might be identified using the Law of Laplace.

A high von Mises stress occurs near the proximal end of the mother vessel in H7C. Since geometric data was not available below this point, it is unclear whether this stress is caused by a branch or curve upstream. It is possible this elevated stress is in part a boundary effect associated with how the branch is constrained for finite element analysis. Although the presence of a high cell density in this same location suggests this is not merely a FEM artifact.

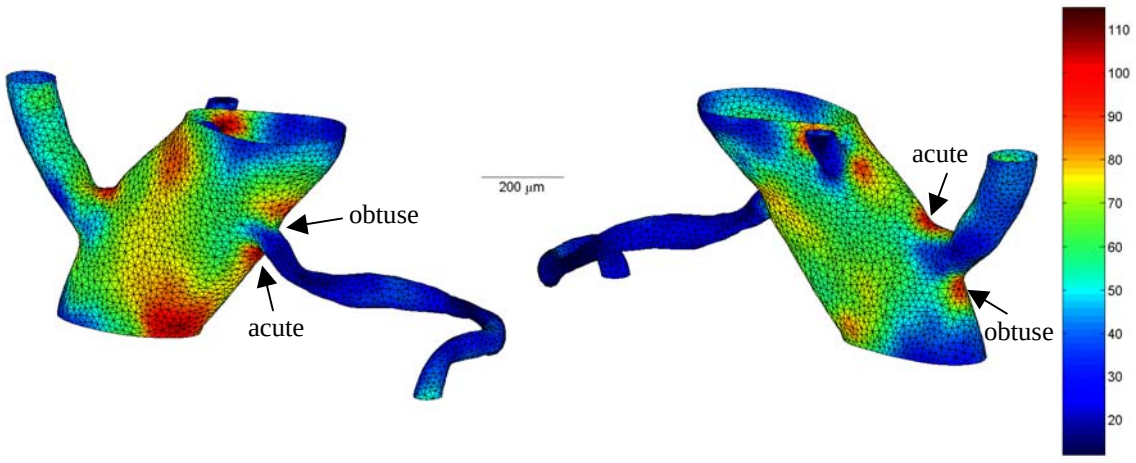

Figure 4-20: Von Mises stress distribution in kPa for branch H7C, after 7 days of hypertension.

The maximal wall tension for H7C is shown in Figure 4-21. The distribution of wall tension is similar to the pattern of von Mises stress in Figure 4-20. The percent variation is somewhat larger and this can be attributed to the fact that the maximal wall tension is based on the magnitude of a single tensor value where the orientation of the tensor varies through the model. By contrast, von Mises stress is an equivalent stress that can be large even when the first principal stress is small. Away from the branch transition regions, both the stresses and the wall tension tend to be lower in smaller vessels. This size effect reflects the lower radius-to-thickness ratio present in the smaller vessels.

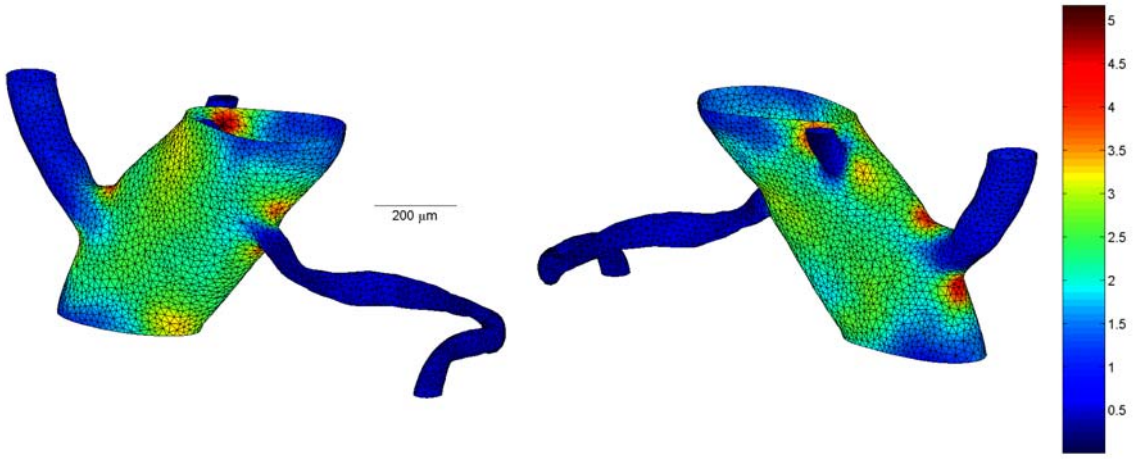

Figure 4-21: Maximal wall tension in N/m for branch H7C, after 7 days of hypertension.

Figure 4-22 shows the von Mises stress distribution for branch H7D. As mentioned previously, the reconstruction of this branch was problematic due to the location of the branch near the periphery of the block and the lack of surrounding tissue to provide support or assist in alignment. The bend represented at the bifurcation could be exaggerated since only limited external tissue features were available to aid in

alignment. This is reiterated, because the pattern of stress exhibited in Figure 4-22 had some unusual characteristics.

While there is a localized peak of about 100 kPa in the saddle region and a similar peak in the bend on the opposite side of the branch, the highest stresses were produced in the mother vessel just upstream of the branch. Two large regions of high stress are shown with white ellipses in Figure 4-22. The localized flattening (i.e. low curvature) and low wall thickness mean intramural stresses must be large to resist the pressure load. An alternative explanation of this stress pattern was proposed earlier, in the context of wall thickness variations. It is possible the mesenteric bed might be exposed to nonuniform external loads. Since these loads were not modeled, the finite element results may not be fully representative of the actual stresses. It was clear during the reconstruction process that this vessel had a unique, highly oblique cross section. It remains unclear whether this phenomenon is characteristic of the *in vivo* geometry or an artifact produced during reconstruction, but some observations can still be made. First, the mother vessel exhibits a highly oblique transverse cross section. This oblique cross section is present both proximally and distally to the branch point. Geometrically, this elliptical cross section explains the localized flattening seen in three dimensions. One can conclude that the unusual distribution of stress is produced by compression in the direction normal to the plane of the branch. The two possibilities are that this is a histological artifact or a true *in vivo* boundary effect that is not accounted for in the finite element analysis.

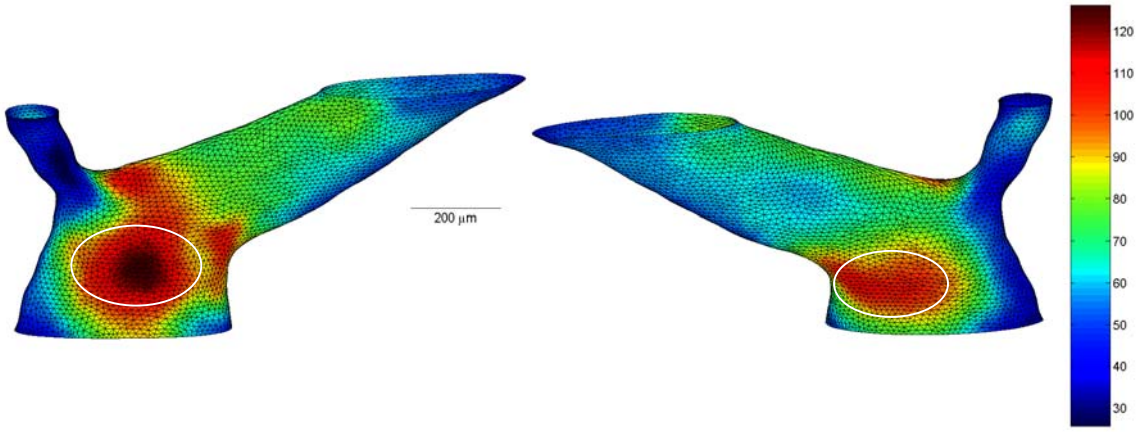

Figure 4-22: Von Mises stress distribution in kPa for branch H7D, after 7 days of hypertension.

Given the location of the branch at the periphery of the embedded tissue, this branch would be more likely to be subjected to nonuniform compression during processing and embedding. This might lead one to conclude that the unusual geometry is produced by histological artifact.

However, wall thickness was observed to be greatest along the long axis of the ellipses (see Figure 4-11). This suggests that nonuniform *in vivo* boundary forces may cause the unusual shape. For example, it is clear that the mesentery is contained within two sheets and the vessels tend to be oriented in the plane of the sheet. The mesentery, as a whole, serves the dual purpose of vascularizing the small intestines and physically retaining them within a compartment of the abdominal cavity (Gray 1973). This retention of the small intestines could produce a compressive load normal to the plane of the mesentery and generally normal to the plane of mesenteric artery bifurcation.

So the elliptical cross sections seen in the model may reflect the nonuniform *in vivo* loading conditions. If this is indeed the case, the boundary conditions of the finite

element model should be modified to include an external traction. The effect of this external traction would be to reduce the stresses in the plane where flattening occurs.

Figure 4-23 illustrates how the structure and function of the mesentery bed may affect the mechanical environment. The key concept is that the mesentery bed as a whole may be under an external load compressing the tissue preferentially along one axis. Such a load would help explain the elliptical transverse sections evident in several of the histology-based reconstructions. A traction load like the one proposed in Figure 4-23 might be implemented in the finite element analysis to get a more accurate estimate of the circumferential stress distribution. The external traction would tend to reduce the stresses where the wall is locally flattened (see Figure 4-22) by offering an external force balance to the internal pressure. The presence of such a traction load has not been confirmed although the pattern of stress through the wall, the variation in wall thickness, and the elliptical cross sections all suggest that such a load may be present. Even if the evidence clearly indicated the presence of such external loads, the magnitude and character of these loads are not understood well enough to implement them in the current finite element models.

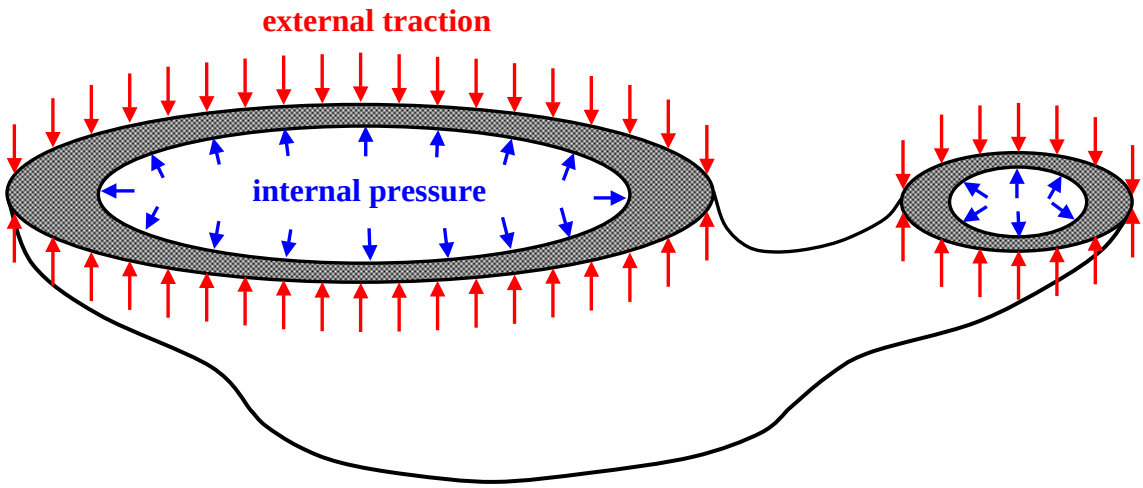

Figure 4-23: This figure illustrates a traction boundary condition that might be appropriate for the mesentery. Such a traction would help explain the elliptical transverse sections and the unusual circumferential pattern of wall thickness seen in some of the branches.

To a lesser extent, the branch H7C is affected like H7D (refer back to Figure 4-20). The main vessel has an elliptical cross section and has elevated circumferential stress where the curvature is low. But other branches also have elliptical cross sections away from the transition geometry. Although the magnitude of eccentricity tended to be lower than that seen in H7C and H7D, it still was pronounced for other models, particularly when the focus was on stress gradients through the wall.

Figure 4-24 illustrates how an elliptical cross section can affect the stress distribution through the wall. Figure 4-24a is a plot of the stress difference between von Mises stress at the inner and outer wall. Positive values indicate a bending load that increases curvature, while negative values indicate a bending load that decreases curvature. The circumferential pattern of positive and negative values around the mother vessel indicates the elliptical shape of the section governs this stress distribution. Figure

4-24b shows the absolute value of the difference in von Mises stress through the wall and this reduces the range, but emphasizes the inflection points in the circumferential pattern. This circumferential variation made it difficult to focus on through-the-wall gradients and identify other trends. For this reason, the midplane stress results were emphasized.

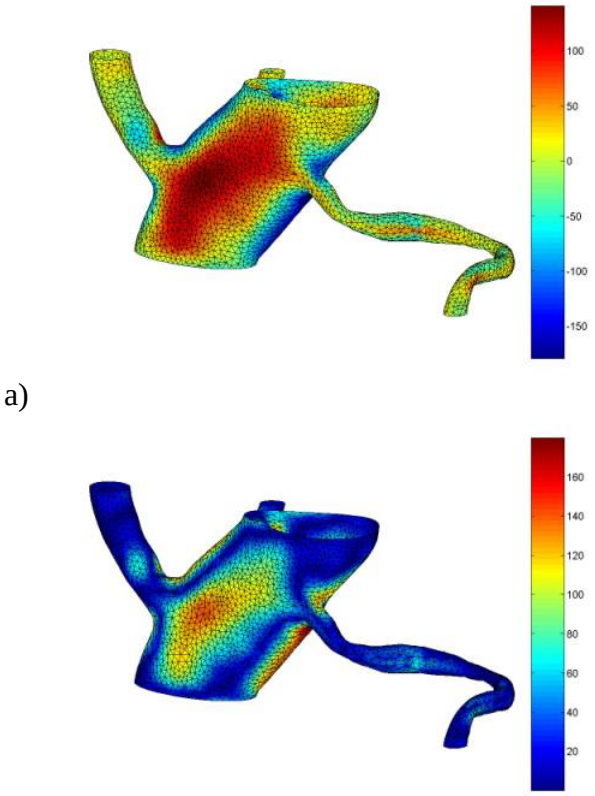

a)

b)

Figure 4-24: Sample stress differences illustrating the effect of elliptical cross sections. Von Mises stress difference through the thickness (a) and absolute value of stress difference (b).

The maximal wall tension for branch H7D is shown in Figure 4-25. This 7-day hypertensive branch exhibited the greatest magnitude in wall tension at about 4.7 N/m. The peak wall tension is locally highest in the saddle region where the mother vessel changes direction as indicated by the arrow. Secondary peaks are seen on either side of

the small branch in the plane of branching. These secondary peaks are about 3.0 N/m, which is greater than the primary wall tension peaks in most of the rest of the branches.

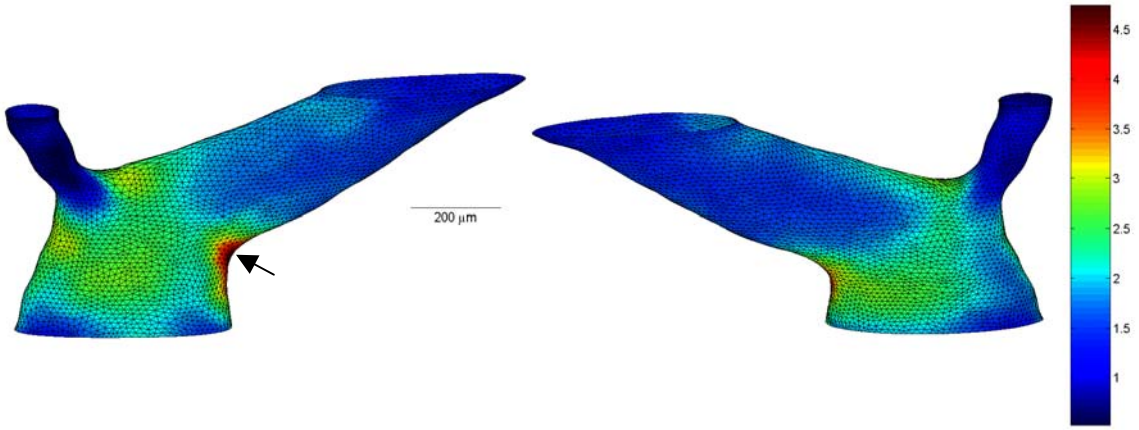

Figure 4-25: Maximal wall tension in N/m for branch H7D, after 7 days of hypertension.

Figure 4-26 shows the von Mises stress distribution in kilopascals for a branch after 21 days of hypertension. The greatest stress is in the transition region at the point of flow division. A secondary peak can be seen in the right hand view. This peak starts in a secondary saddle region before the point of flow division. The peak stresses correspond closely to the regions of high wall thickness. This is of interest since a significant amount of remodeling has occurred at this point.

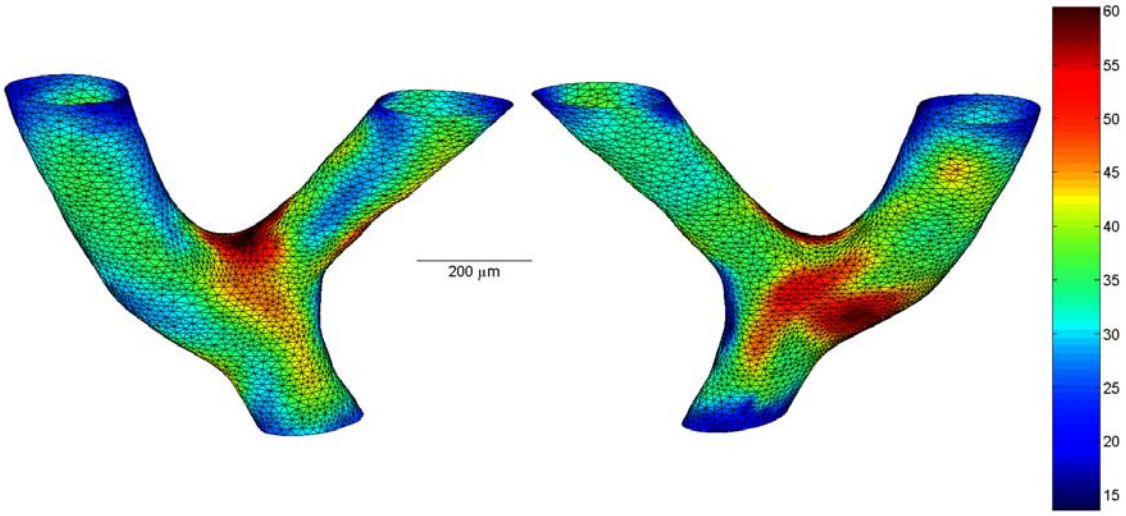

Figure 4-26: Von Mises stress distribution in kPa for branch H21A, after 21 days of hypertension.

Figure 4-27 shows the maximal wall tension for H21A, the 21-day hypertensive branch. Because of the general correspondence between regions of high stress and high thickness, it is not surprising that this wall tension distribution is very similar to the von Mises stress distribution. A large peak of 2.6 N/m occurs in the saddle region, as before. However another local peak of similar magnitude can be seen in the left hand view of Figure 4-27, proximal to the point of division. This corresponds to another region where the curvature characteristics are mechanically unfavorable and the wall thickness is high (see Figure 4-12).

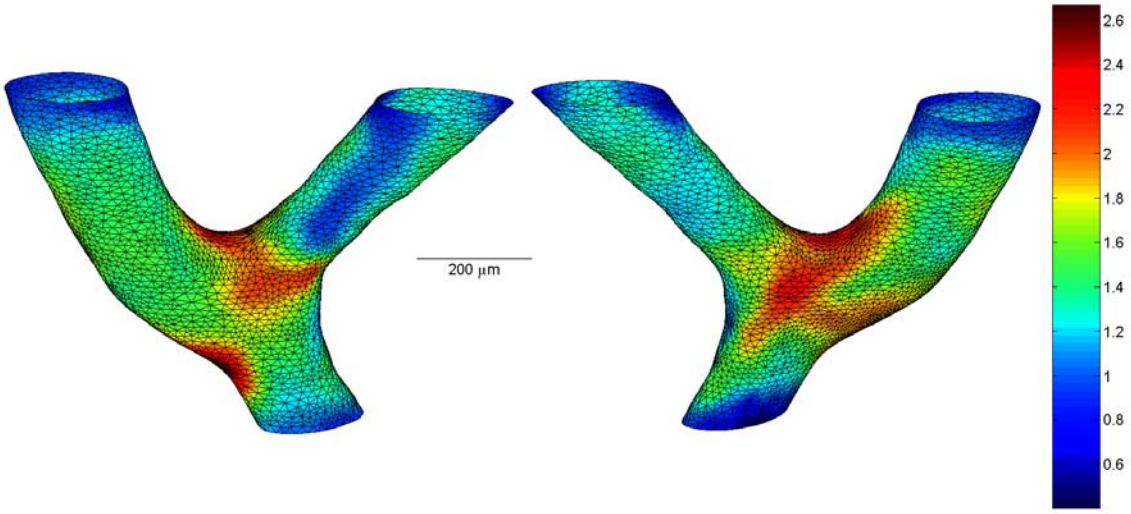

Figure 4-27: Maximal wall tension in N/m for branch H21A, after 21 days of hypertension.

Figure 4-28 shows the von Mises stress distribution for the first of two normotensive cases, branch NA. This branch is unusual because it has nearly a 90 degree branch angle. Because of the normotensive condition, the incremental stresses are comparatively low, with a maximum of about 31 kPa. Despite the lower magnitude, the general pattern of stresses is not strikingly different for this normotensive case than the previously discussed hypertensive cases. Stress is locally highest at the point of flow division, with a smaller secondary peak in the transition region as indicated.

In general the stress distribution is locally affected by the boundary conditions at the top and bottom of each model. For stability, the branches must be artificially constrained to zero displacement *near* the boundaries of known geometry (see Chapter 3 for details of how the model is extruded, but the extruded portion is not considered during the analysis of stresses). Commonly the stress is low because the displacements are limited, but in some cases a net load is concentrated at the boundary to produce high stresses independent of large displacements.

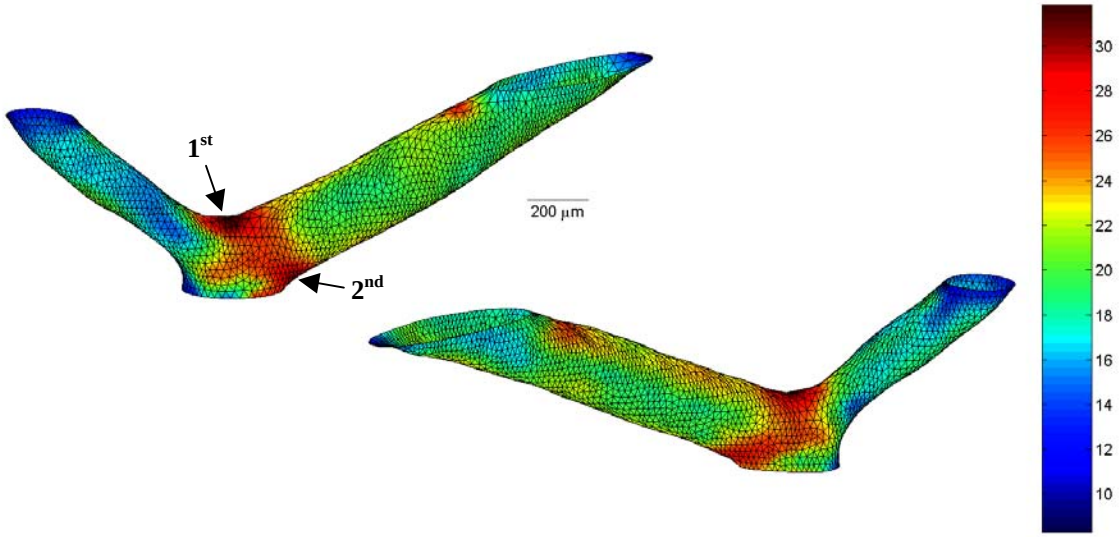

Figure 4-28: Von Mises stress distribution in kPa for NA, a normotensive branch.

The maximal wall tension for branch NA is shown in Figure 4-29. Again the distribution of wall tension is similar to that for von Mises stress seen in the previous figure. Note the smaller daughter vessel exhibits a lower level of wall tension than the larger daughter vessel. This size effect reflects the fact that wall tension generally decreases with decreasing vessel size.

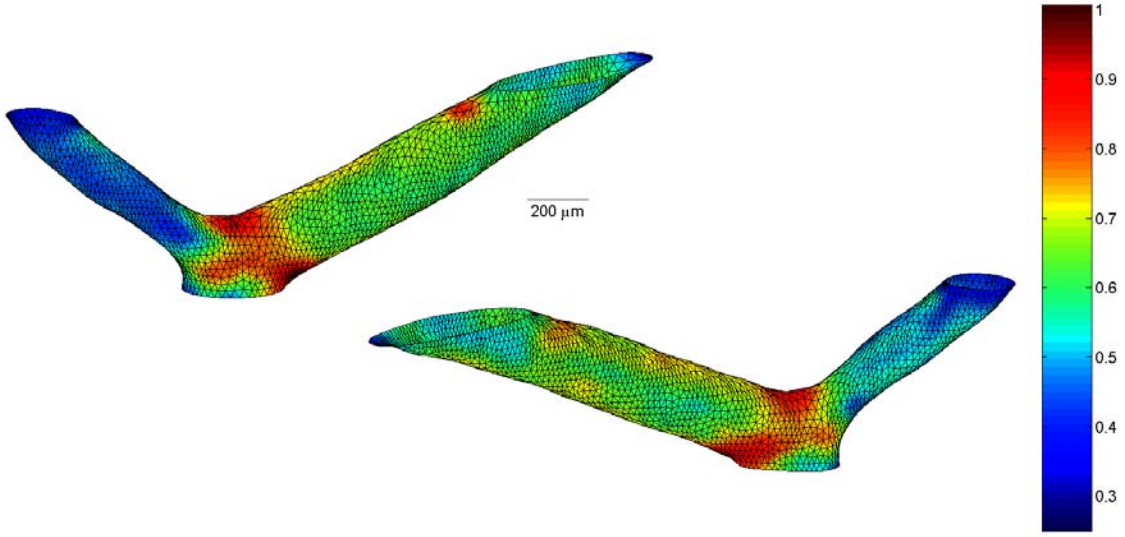

Figure 4-29: Maximal wall tension in N/m for NA, a normotensive branch.

Figure 4-30 shows the von Mises stresses for branch NB, the second normotensive case. This branch exhibits the most acute branch angle among all cases studied. The highest incremental stress change occurred at the point of flow division and was about 40 kPa. Because this was a normotensive model the incremental pressure increase from the pressure fixed state was 40 mmHg rather than 100 mmHg. This lower incremental pressure change helps explain the comparatively low magnitude of stresses. While this branch has some of the features of stress concentrations seen elsewhere, the pattern of stresses is not so localized on the saddle region, with multiple secondary peaks elsewhere through the geometry. It is also striking how dissimilar the pattern of von Mises stress is from the pattern of wall thickness in Figure 4-14. The stress peaks tend to occur in the plane of branching (approximately the plane of the paper in these figures). By contrast the maximum wall thickness occurs out of this plane, most prominently on the surface *normal* to the plane of branching.

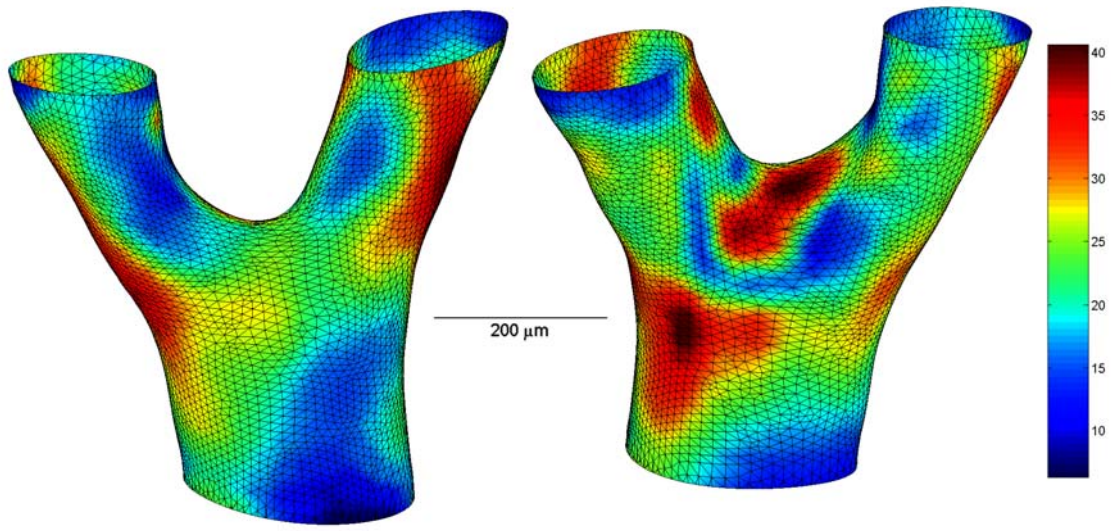

Figure 4-30: Von Mises stress distribution in kPa for NB, a normotensive branch.

Figure 4-31 shows the maximal wall tension in N/m for normotensive branch NB. The pattern of wall tension is distinctly different from the von Mises stress distribution shown above, but shares strong similarities with the pattern of wall thickness (see Figure 4-14). This suggests wall tension is more significantly influenced by the variation in wall thickness than the variation in stress. It should also be noted that the von Mises stress could be high even when the maximum in plane stress is not highly positive. This condition is possible in the saddle region and might help explain the low wall tension in this location. Like the distribution of wall thickness, the maximal wall tension is greatest on the surface normal to the plane of branching.

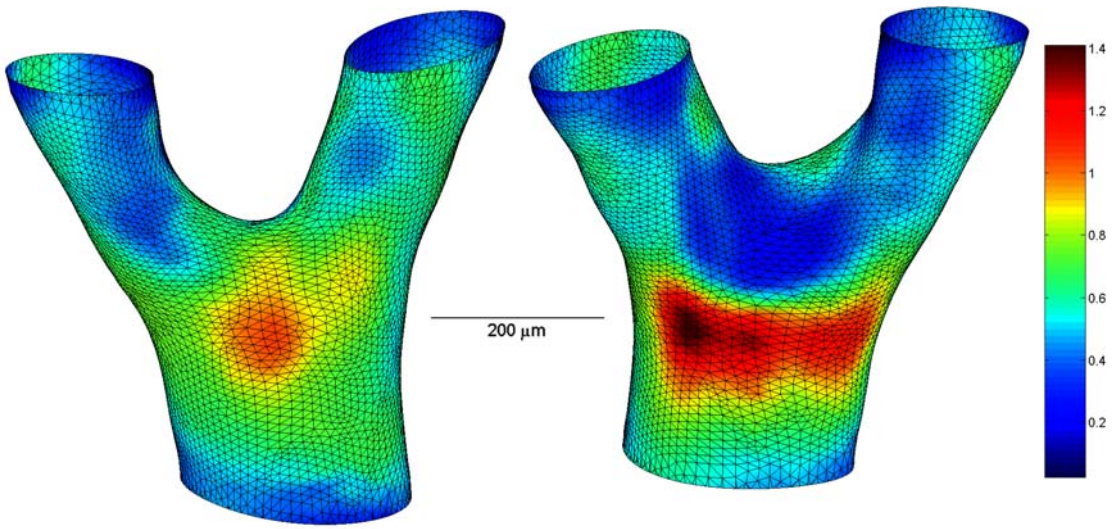

Figure 4-31: Maximal wall tension in N/m for NB, a normotensive branch.

Inflammatory Cell Density

As previously discussed, cell density is a local measure of the number of monocytes and macrophages within a subvolume. Among the results, the subvolume size was a 150 μm sphere for all cases. The results and discussion of monocyte/macrophage density are divided into two parts. First average cell densities will be presented collectively for all branches. This makes it easier to assess the relative level of inflammation between models and test conditions. Then the individual cell density distribution will be presented separately for each branch. This approach is more informative about the spatial variation of cell density within a given branch.

Average Cell Densities for All Branches

Figure 4-32 shows two bar charts of the average cell density centered on the lumen surface. Each value in Figure 4-32a represents an average of all cell density measurements made on the surface of the specified branch. The results are grouped by

test condition. Figure 4-32b shows the average for each test condition and is calculated directly from Figure 4-32a.

While the sample sizes are small, there are still marked differences in cell density between the normotensive and hypertensive groups. Normotensive branch NA exhibited the lowest cell density at 4.4E-6 cells/μm^3, while 7-day hypertensive branch H7D exhibited the highest cell density at 5.6E-6 cells/μm^3. The single 21-day hypertensive sample suggests that the monocyte/macrophage cell density remains high after 21 days.

a)

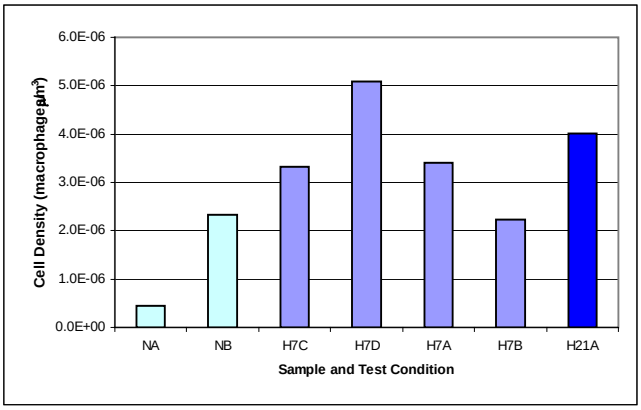

b)

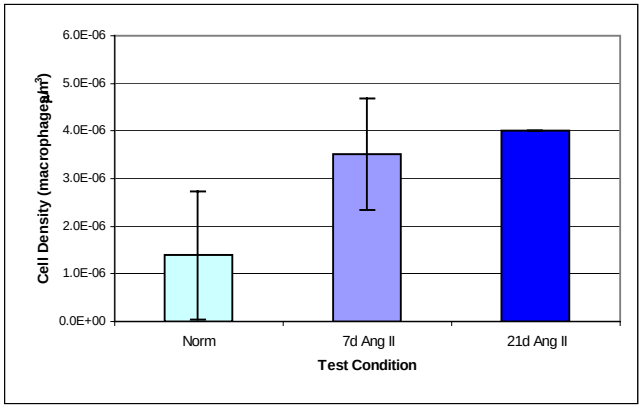

Figure 4-32: Average cell density on lumen surface a) for each sample and b) for each test condition.

Figure 4-33 shows a similar pair of bar charts, but in this case the cell density calculations are centered on the cells. The average cell densities measured in this way are

similar to the average on the lumen surface (compare with Figure 4-32) and the general trends are also similar. As a reminder of the distinction between the two cell density measurements please refer to Figure 3-20 and Figure 3-21. In general, the average cell densities are lower when the subvolumes are centered on the surface rather than the cells. This can be explained by the fact that portions of most branch surfaces have no inflammatory cells nearby, while the cell-centered calculations are guaranteed at least one cell per subvolume.

a)

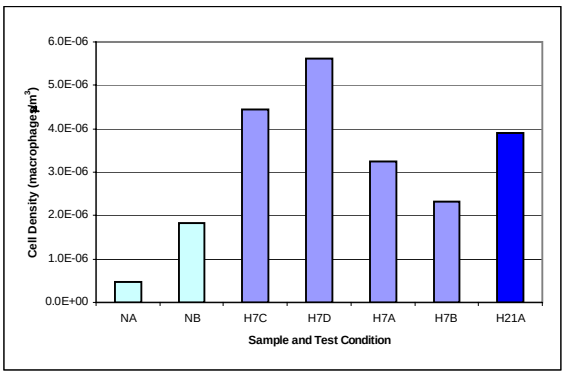

b)

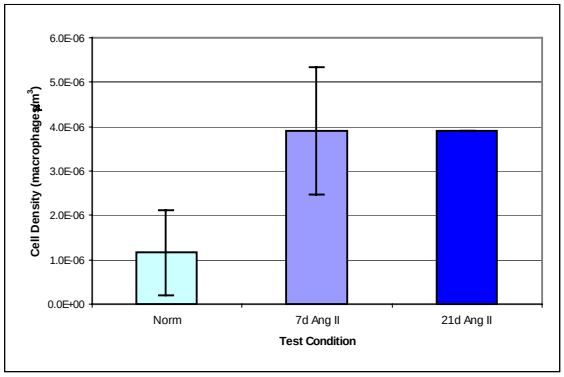

Figure 4-33: Average cell density centered on cells
a) for each sample and b) for each test condition

Figure 4-33 indicates the two normotensive branches exhibit the least inflammation; although branch NB has a comparable level of inflammation to the lowest of the hypertensive cases, branch H7B.

Cell Density Distribution for Each Branch

This section will focus on the spatial variation of monocyte/macrophage density within each branch. First the results for each branch will be presented and discussed individually. Each of the four 7 day hypertensive branches will be presented, followed by the 21-day hypertensive branch and then finally the two normotensive branches. After each case is presented individually some generalizations and observations will be offered.

Figure 4-34 and Figure 4-35 is the first pair of figures describing cell density. For each branch, the first figure shows the projection of monocyte/macrophage density on to the surface. The second figure shows the centroids of the cells. As described earlier, a small sphere represents each cell and is color-coded with a local measurement of cell density. The color-coding for cell density enhances the two-dimensional representation of this three-dimensional phenomenon. The general distributions produced by these two representations are similar, but each approach has its advantages. The surface representation facilitates comparison with vessel geometry and mechanical stresses. But the color-coded cells provide some additional information. First, the cells themselves are more intuitively connected to the cell data and second, this visualization approach can show increased cell density even when the cells are not in close proximity to the vessel surface.

Figure 4-34 shows the front and back view of cell density for branch H7A after 7 days of hypertension. To facilitate comparison with stresses, the cell density is mapped to the surface of the branch as described previously. A high cell concentration is located in close proximity to the branch point. Further, the cell density is high through the transition region where unfavorable curvature characteristics are present. Conversely, the

cell density away from the branch center is considerably lower, particularly near the distal ends of the branch geometry.

Figure 4-35 shows the same views of the branches, but in this case the cell density calculations are centered on the cells. The only regions of high cell density are in close proximity to the cell surface, so this method of visualizing inflammation provides similar information to the surface map in Figure 4-34. The apparent proximity of cells with a high cell density near cells with low cell density is an illusion caused by compressing the three-dimensional map into two dimensions. This underscores the added value of color-coding the cells with a measure of cell density.

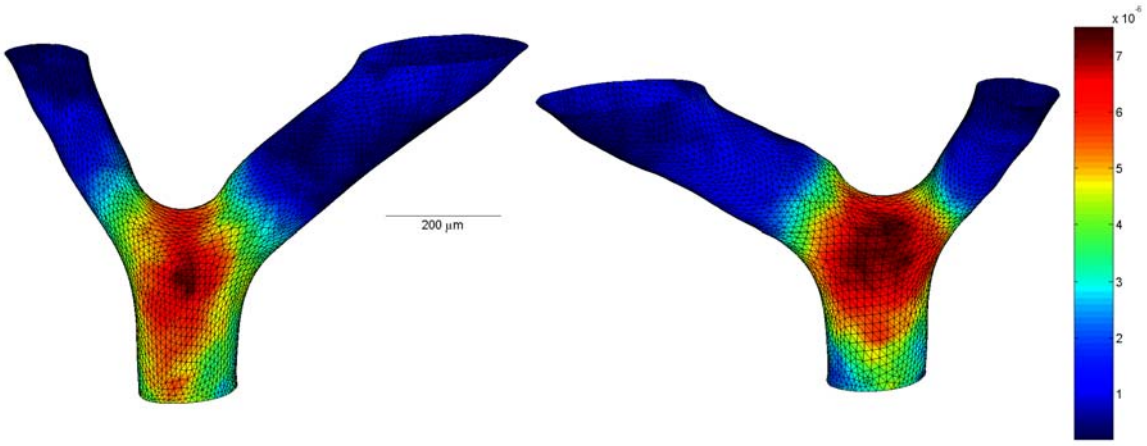

Figure 4-34: Monocyte/macrophage cell density (cells/µm^3) for branch H7A after 7 days of hypertension. Density is calculated for a 150 µm spherical subvolume centered on the surface.

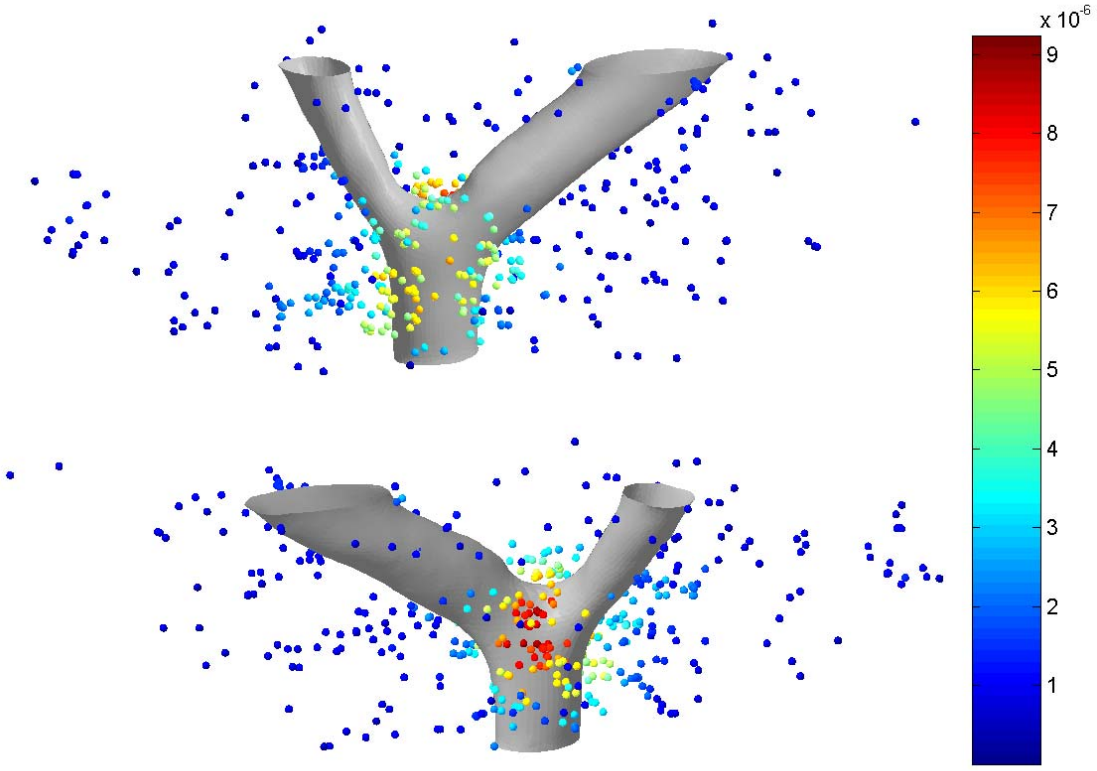

Figure 4-35: Cell density for branch H7A after 7 days of hypertension. Density is calculated for 150 µm spherical subvolumes centered on each cell.

Because most of the monocytes and macrophages were present in the adventitial and periadvential tissue, there was some concern that high medial thickness substantially changed the pattern of inflammation. To examine this, a case study was done where the inflammation was mapped to the outer medial surface and all cells inside this surface were excluded from consideration. Figure 4-36 shows two cell density maps and illustrates that the exclusion of the media did not substantially affect the magnitude or distribution of inflammation. The exclusion of medial volume and cells represents an extreme case for how to accommodate the cell density calculations. The similarity in the results demonstrates that an accurate representation of cell density can be obtained independent of any special handling of inflammatory cells within the media. This can largely be attributed to the requirement that the subvolume radius for density calculations be substantially larger than the wall thickness.

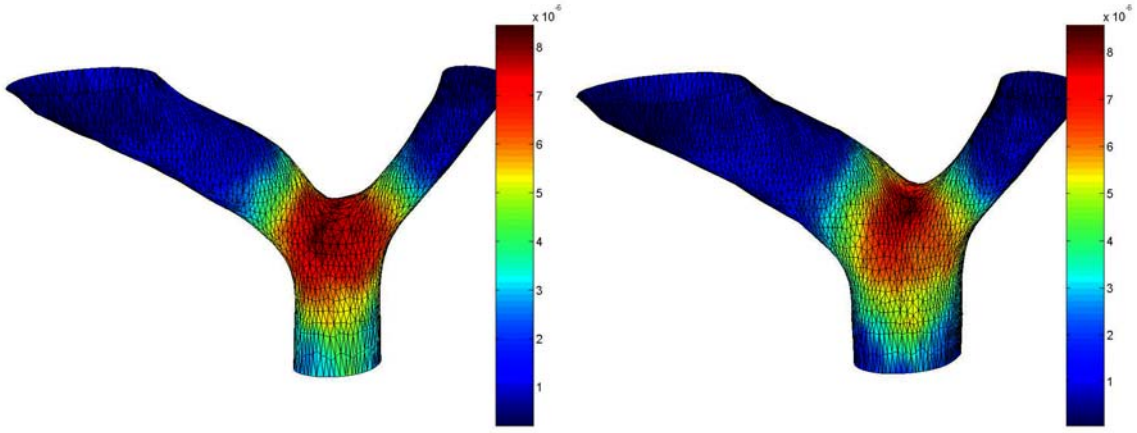

Figure 4-36: Cell density distribution (cells/μm^3) based on lumen surface (left) compared to the distribution for the external medial surface (right). The medial volume and any cells contained therein were excluded for the medial surface on the right.

Figure 4-37 shows the two views of cell density calculated at the vessel surface of branch H7B after 7 days of hypertension. The surface of the branch is color-coded with a

local measure of cell density. A local maximum is present in the saddle region of the main branch, but the magnitude of this inflammation is small in comparison to the focal inflammation that surrounds the tertiary branch. The tertiary branch region is magnified and shown in an inset because the small patches in this region interfered with the surface color-coding.

Figure 4-38 shows the individual inflammatory cells for branch H7B, color-coded for cell density. The maximum cell density measured in this model was similar to the other hypertensive branches, but the mean density was the lowest among hypertensive branches. As indicated previously, the region of high cell density is near the tertiary branch. The high cell density extends away from the point of origination of the tertiary branch. While it was not possible to accurately reconstruct the branch as it extended away from the larger vessel, the path of high inflammation roughly corresponds to the path of this vessel. Note that if this vessel had been reconstructed, the resulting mask would further reduce the volume available for monocytes and macrophages and increase the magnitude of cell density. So not modeling this small vessel along its length underestimates the local peak in cell density.

Figure 4-39 shows the cell density measured at the vessel surface of branch H7C after 7 days of hypertension. Cell density is elevated in proximity to each branch point. In addition, cell density is high at the proximal end of the mother vessel. Note that cell density is very low at the distal end of the long daughter vessel.

Figure 4-40 shows the cell density measured at each cell location. The general pattern is similar, but the small distal branch indicates a lower cell density than the surface map. The precise reason for this difference is not clear, but it is generally clear

that the density calculations near the boundary are more sensitive to changes in position, since the volume available for cells is smaller. Note that the cell spacing appears more segregated to discrete layers because every fifth section was inspected for inflammatory cells. In most studies cells were identified in every fourth section. Naturally there was a commensurate change in the sample volumes so that density measures at these two intervals would be comparable.

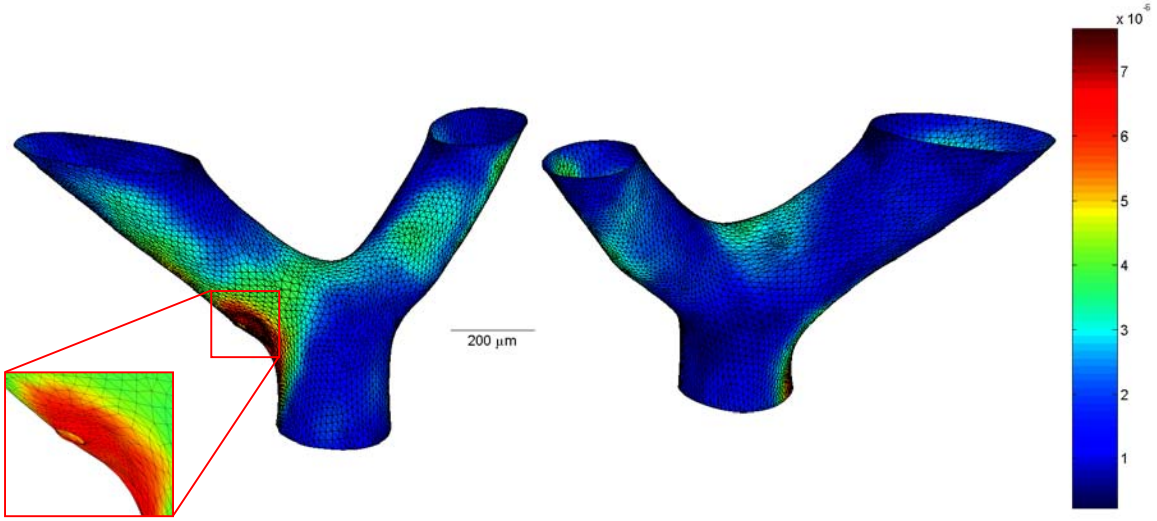

Figure 4-37: Monocyte/macrophage density (cells/µm^3) for branch H7B after 7 days of hypertension. Density is measured on the surface.

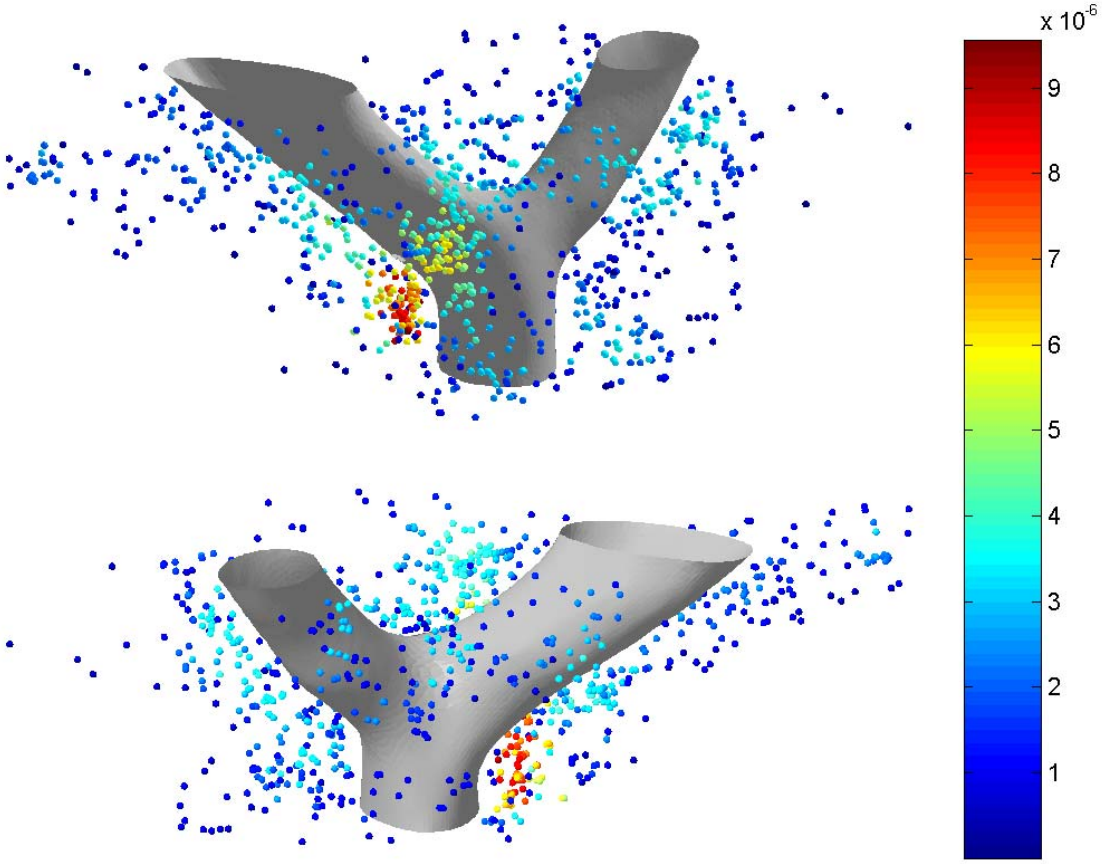

Figure 4-38: Cell density for branch H7B after 7 days of hypertension. Density is measured for subvolumes centered on each cell.

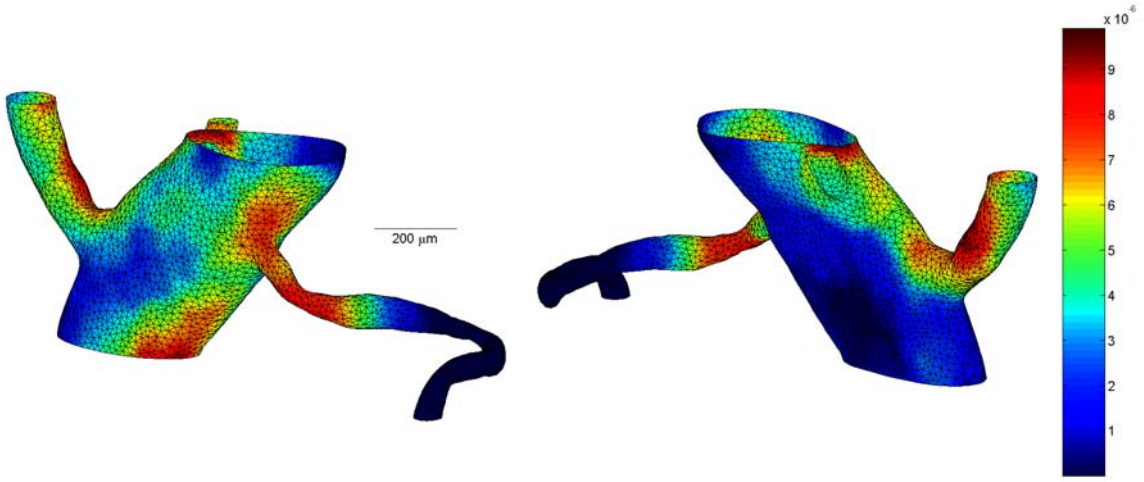

Figure 4-39: Monocyte/macrophage density (cells/µm^3) for branch H7C after 7 days of hypertension. Density is measured at the vessel surface.

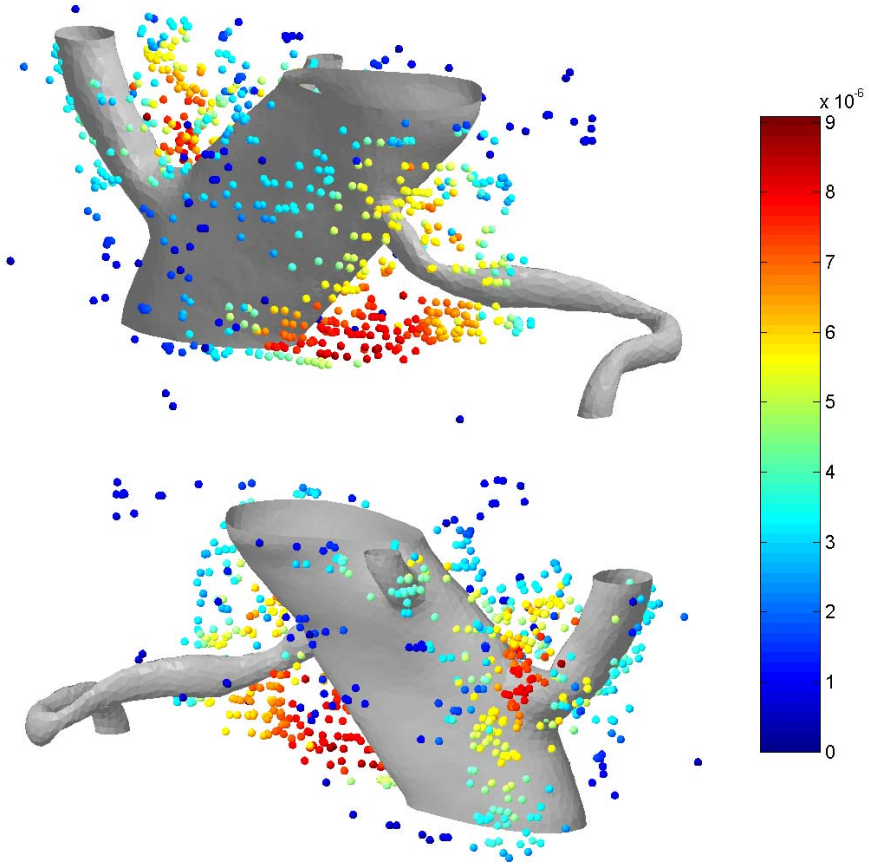

Figure 4-40: Cell density for branch H7C after 7 days of hypertension. Density is measured for subvolumes centered on each cell.

Figure 4-41 shows the cell density at the vessel surface for H7D, the fourth and last 7-day hypertensive branch. This branch exhibited the greatest cell density of 20E-6 cells/μm^3, with the high concentration occurring in proximity to the branch. The radius of 150 μm used for density calculations in this branch was somewhat large given the small size of the daughter vessel. The daughter vessel is about 110 μm in diameter, and so a 150 μm radius includes cells from both sides of the vessel. This makes it difficult to see the circumferential variation in cell density on the surface in this region.

Figure 4-42 more clearly demonstrates that the cell density is highest where the branch angle is acute. The concentration of cells extends from the saddle region distally along the path of the small vessel. Cells are distributed throughout the model in the plane of branching, but there is a distinct and highly localized concentration of cells in this region of the model.

Figure 4-43 shows the monocyte/macrophage cell density color-coded to the surface of H21A, a 21-day hypertensive branch. The peak cell density is 9.4E-6 cells/μm^3 at the point of flow division. Two local peaks of about 8.0E-6 cells/μm^3 each can be seen in the right/rear view. One of these peaks, designated as Region B, is in the transition region of the branch and corresponds to the location of unfavorable curvature characteristics. The other local peak, designated as Region A, occurs in the larger daughter vessel downstream of the point of flow division.

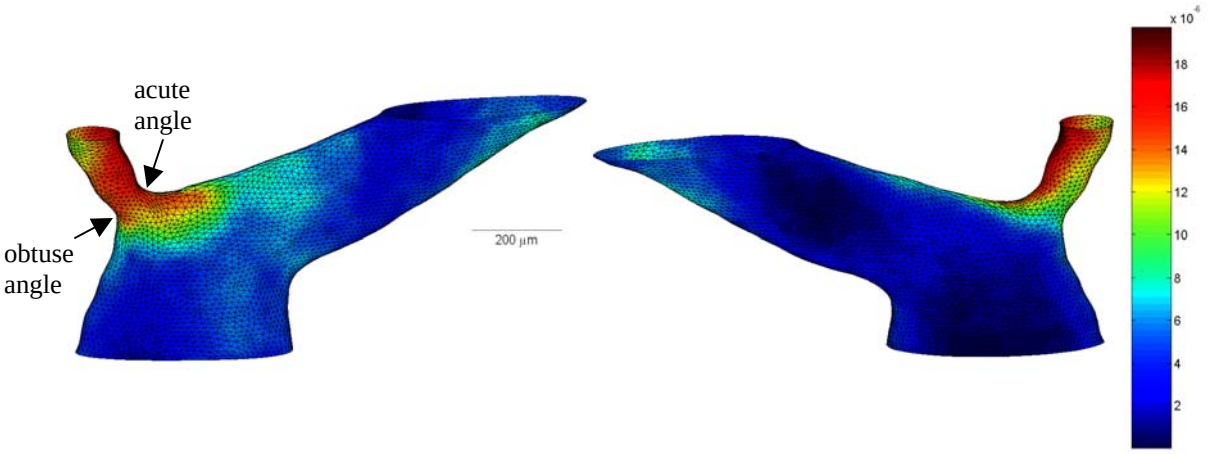

Figure 4-41: Monocyte/macrophage density (cells/µm^3) for branch H7D after 7 days of hypertension. Density is measured at vessel surface.

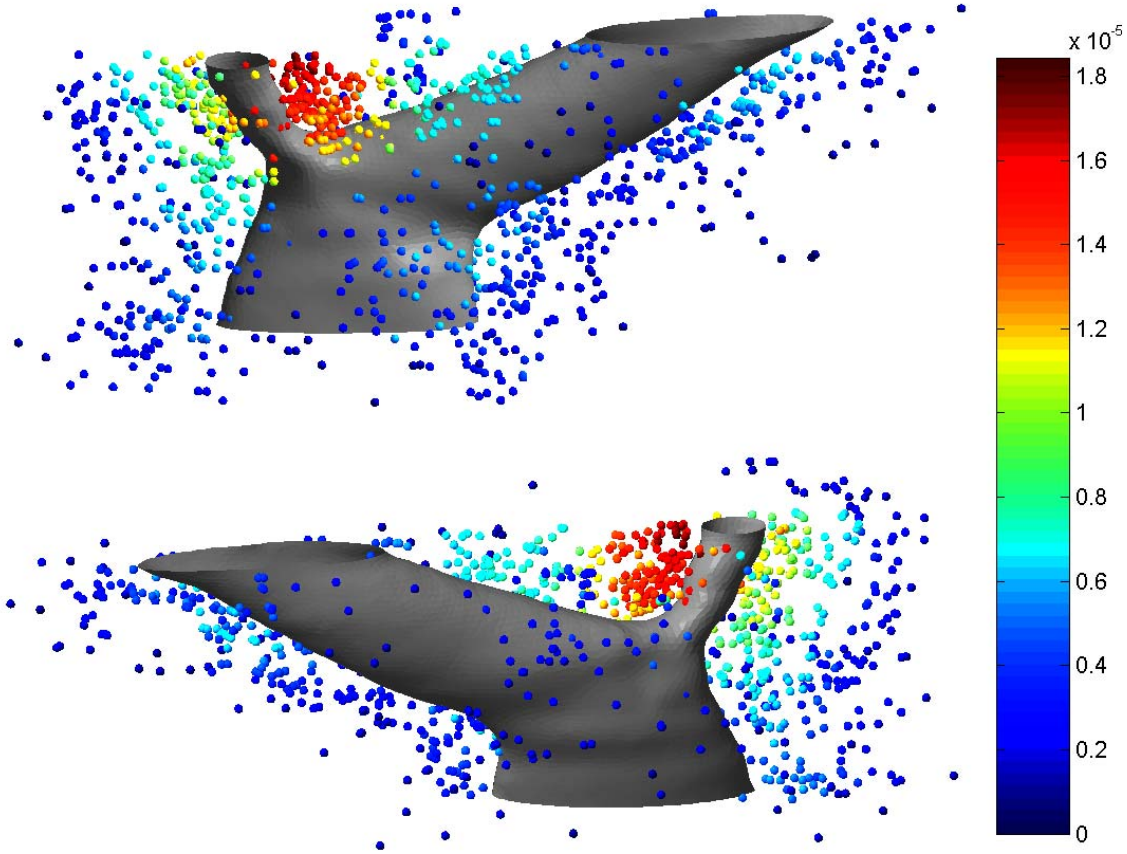

Figure 4-42: Cell density for branch H7D after 7 days of hypertension. Density is measured for subvolumes centered on each cell.

The cell density coded to the individual cells around branch H21A is shown Figure 4-44. The highest cell density is in the periadventitial region above the point of flow division and this corresponds well with the surface map shown in Figure 4-43. Interestingly, the two secondary regions of high cell density extend away from the branch surface. These regions are identified by ellipses and are labeled Region A and Region B, respectively. Region A is near the upper boundary of histological data, so it is possible that an unidentified distal branch is responsible for this concentration. Region B extends away from the distal branch but appears to be associated with a focal surface peak as indicated in Figure 4-43.

Figure 4-45 shows normotensive branch NA, with the surface color-coded with cell density. As discussed earlier this branch exhibited the lowest cell density among all branches studied, with a peak density of only 1.6E-6 cells/μm. This relatively sparse distribution of monocytes and macrophages included large regions where no cells were present. The regions of relatively high density were scattered, with local peaks in the saddle region, along the daughter vessel and near the distal ends. Unlike most of the hypertensive cases, the pattern of inflammation in this normotensive branch does not appear to be strongly associated with specific features.

Figure 4-46 shows the individual cells and the cell density for normotensive branch NA. The highest cell density measured in this manner was about 1.3E-6 cells/μm^3. This peak occurred at the distal end of the smaller daughter vessel.

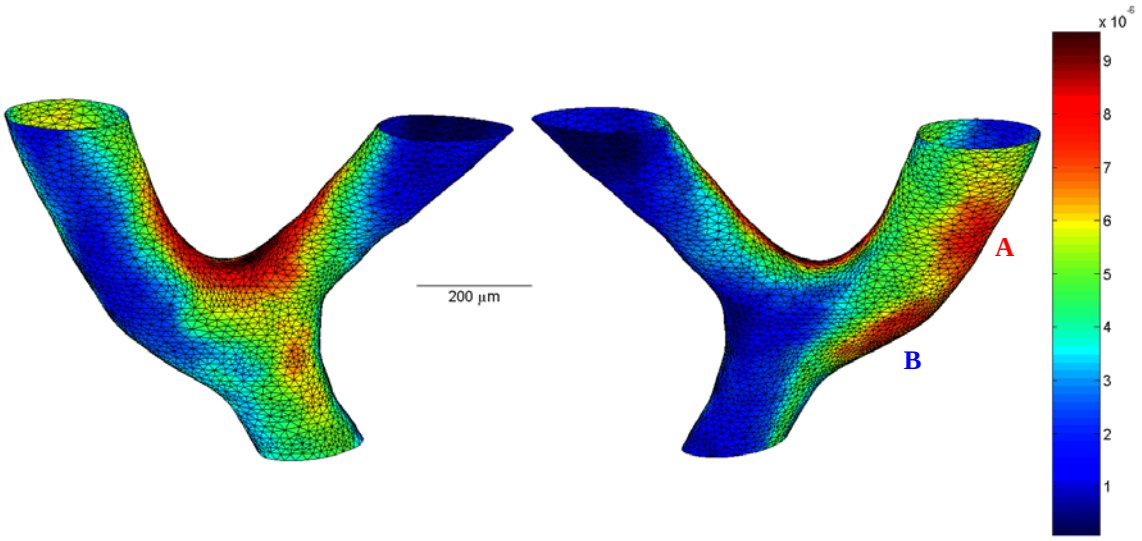

Figure 4-43: Monocyte/macrophage density (cells/µm^3) for branch H21A after 21 days of hypertension. Regions A and B are local peaks that appear to extend out from surface.

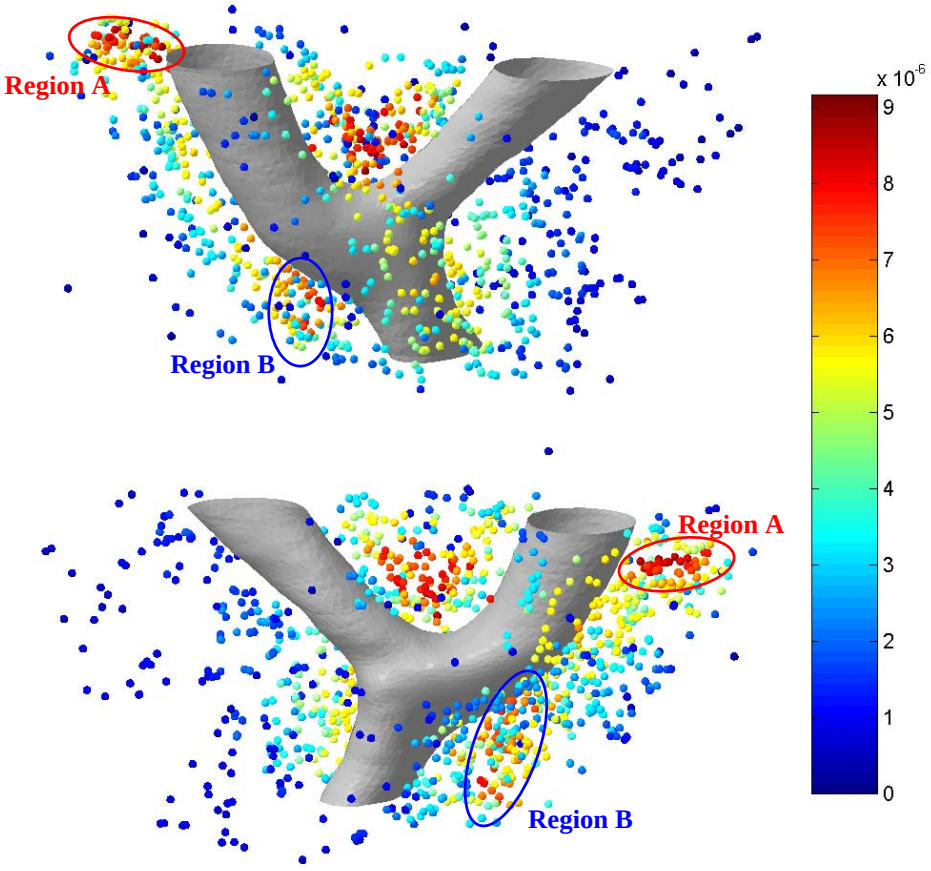

Figure 4-44: Cell density for branch H21A after 21 days of hypertension. Density is measured for subvolumes centered on each cell.

Figure 4-47 shows the surface-based representation of cell density for NB, a normotensive branch. Not surprisingly, the peak cell density of 5.7E-6 cells/μm^3 was markedly lower than the lowest peak among the hypertensive branches. However, like the typical pattern seen in hypertensive branches, the greatest cell density is at the point of bifurcation. A secondary peak of about 5.0E-6 cells/μm^3 as indicated by the arrow in Figure 4-47.

Figure 4-48 is the companion figure for branch NB, showing the individual cells color-coded for cell density. Both concentrations of cells are evident in this view and it is also more evident that the general level of cell density is considerably higher in this normotensive branch than in NA (refer back to Figure 4-46 and Figure 4-47).

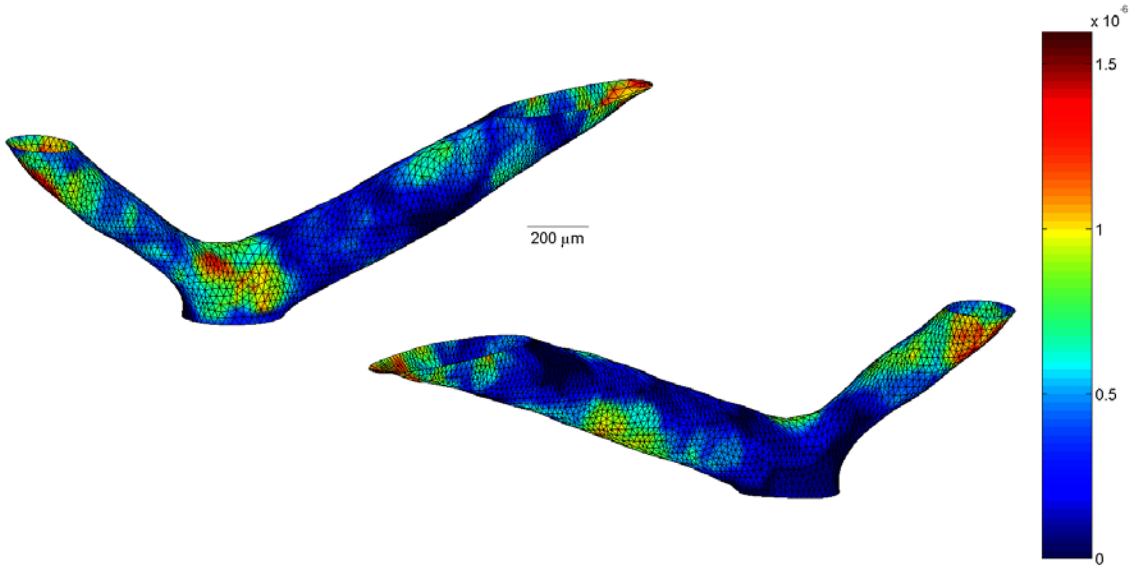

Figure 4-45: Monocyte/macrophage density (cells/µm^3) for branch NA, from a normotensive rat. Density is measured at vessel surface.

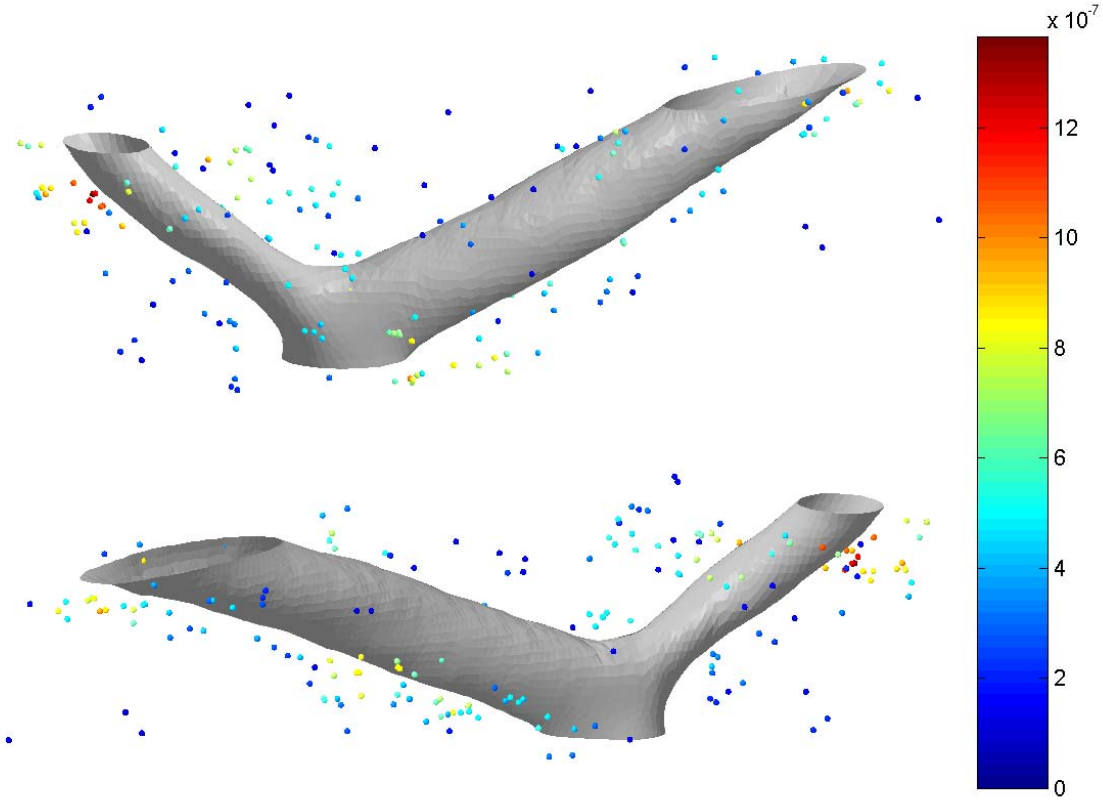

Figure 4-46: Cell density in NA, a normotensive branch. Density is measured for subvolumes centered on each cell.

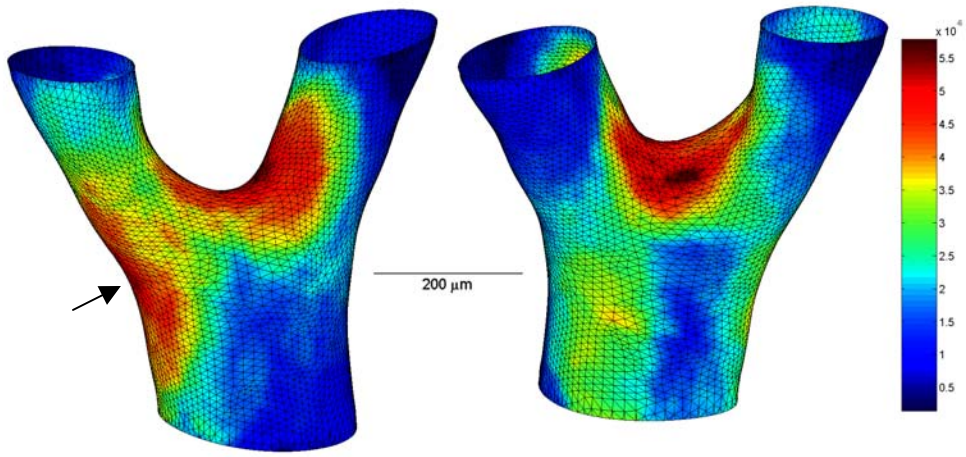

Figure 4-47: Monocyte/macrophage density (cells/µm^3) for branch NB, from a normotensive rat. Density is measured at vessel surface.

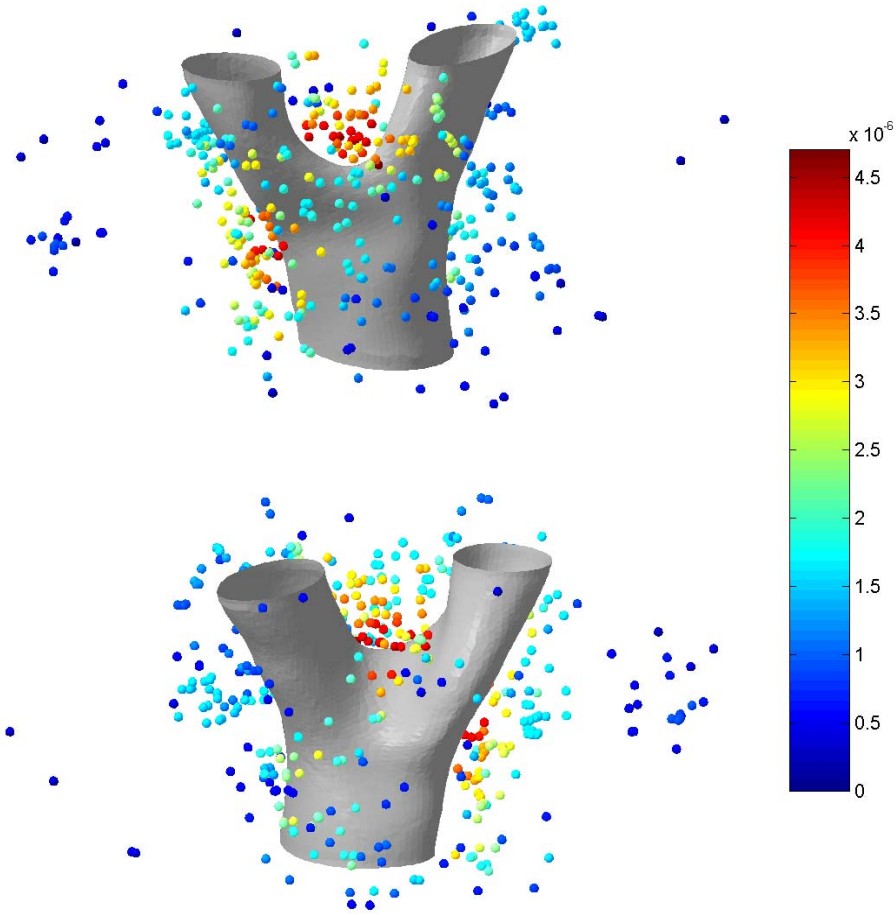

Figure 4-48: Cell density in NB, a normotensive branch. Density is measured for subvolumes centered on each cell.

Mean Values of Branch Characteristics

Table 4-3 shows summary data of mean and maximum values of various branch characteristics. These values are based on a sub-sample of the data, eliminating the upper and lower 10 percent of vertices because of the influence of boundary conditions on the magnitude of stresses near the finite element model boundaries. Caution should be used when directly comparing the results. For example, wall thickness may be highly influenced by the relative size of the vessels being considered. But the general trends suggest that increased stress and wall tension produce higher levels of inflammation.

Table 4-3: Summary data showing mean and maximum values for various branch characteristics. Note that this data is a sub-sample of the complete range, corresponding to the more limited range of stresses not near the model boundaries.

Branch ID	Mean Thickness μm	Maximum Thickness μm	Mean Von Mises Stress KPa	Maximum Von Mises Stress KPa	Mean Wall Tension N/m	Maximum Wall Tension N/m	Mean Cell Density cells/mm^3	Maximum Cell Density cells/mm^3
H7A	20.6	39.9	43.0	69.7	0.98	1.75	2680	7509
H7B	38.3	54.8	39.6	112.9	1.67	3.97	2593	7655
H7C	26.5	43.1	52.6	114.8	1.69	4.99	3476	9576
H7D	24.4	47.0	71.9	126.1	1.94	4.74	5152	18321
H21A	37.2	57.6	37.5	60.3	1.55	2.66	4223	9526
NA	26.7	32.4	20.4	31.8	0.62	0.96	427	1595
NB	23.8	42.1	24.8	40.5	0.63	1.41	2655	5784

Visual Comparisons of Branch Characteristics

In the previous section a variety of variables were presented as color-coded ranges on the lumen surface. The distributions of von Mises stress, maximal wall tension, wall thickness, and cell density have all been presented. This section will focus on making spatial comparisons between variables for a given branch. Although two different

approaches were used to characterize cell density, only the surface mapping approach will be discussed here since it is more readily compared to the mechanical results.

Visualization is a powerful tool for presenting information and making connections between data. In the context of this work, the visualizations are the color-coded maps of characteristics overlaid on the branch geometry. The individual visualizations will not be repeated here, but tables will be presented to summarize some of the side-by-side visual comparisons. Appendix A and Appendix B contain the core set of visualizations that will be discussed.

Table 4-4 summarizes the visual assessments about whether selected vessel characteristics are elevated in proximity to the branch. The author made these assessments before the statistical work was completed. A second individual made independent assessments that were comparable but not identical. A positive relationship indicates the branch characteristic appears to be elevated in proximity to the branch. A negative relationship indicates the characteristic appears to be elevated away from the branch. A tilde indicates the visual assessment about branch proximity was unclear. While additional assessments were completed, not all combinations of all variables are presented here. For instance, the magnitude and distribution of maximum intramural shear stress is similar to von Mises stress. Therefore including the color-coded representations of this intramural shear stress would not add significantly to the presentation and discussion of the results.

As indicated by the first row in Table 4-4, a visual assessment suggests cell density is elevated near the branch center for almost all branches. The exception is branch NA, one of the two normotensive branches. Branch NA had the lowest average

cell density. Small regions of elevated cell density were scattered through out the branch geometry with no clear pattern.

The second row in Table 4-4 summarizes the pattern of wall thickness. The tilde indicates the pattern is not clearly positive or negative for branch H7D and branch NB. Wall thickness is generally elevated for the hypertensive models, with no clear pattern between the two normotensive cases. A natural decrease in wall thickness from the proximal to distal ends of each branch is expected and can mask local variations in thickness in the transition region. The decrease is most prominent when there is a large difference in the mother and daughter vessel diameter. This is true for branch H7C where the transition pattern can still be seen and for branch H7D where the pattern is unclear.

Table 4-4: Summary of qualitative visual assessments about whether the specified characteristics are elevated in proximity to the branch.

Visual Assessment of Proximity	H7A	H7B	H7C	H7D	H21A	NA	NB
Cell density elevated near branch?	POS	POS	POS	POS	POS	~	POS
Wall thickness elevated near branch?	POS	POS	POS	~	POS	NEG	~
Von Mises stress elevated near branch?	NEG	POS	POS	POS	POS	POS	~
Wall tension elevated near branch?	POS	POS	POS	~	POS	POS	~

The third row of Table 4-4 contains the visual assessments of proximity for von Mises stress. The results indicate that von Mises stress is generally elevated in proximity to the branch. Four of the five hypertensive branches indicate a pattern of elevated stresses near the branch point. The stress peak in model H7B corresponds with the origin of a tertiary branch.

The final row indicates that maximal wall tension is locally greater in proximity to the branch. This is true for all models, except for branch H7D where the greatest wall tension occurs on the opposite side of the mother vessel from the branch. Because two secondary peaks are present near the branch, the pattern is not entirely opposite and a tilde is used to indicate no clear trend.

More can be learned by visually comparing branch characteristics to one another in the absence of the distance/proximity measure. Toward this end, Table 4-5 summarizes comparisons of selected branch characteristics. By evaluating the similarities and differences in the locations of peak values, the correspondence in distributions is qualitatively described as positive (POS), negative (NEG), or neutral (~).

The first row provides a visual assessment of the correspondence between the pattern of wall thickness and cell density. In general, cell density appears to be negatively correlated with wall thickness. This is interesting, since wall *thickening* is a manifestation of inflammation and the hypertensive models generally exhibit greater wall thickness. It does appear that the natural variations in wall thickness tend to mask patterns that might be seen with wall *thickening*. But a negative trend is present and tends to indicate that the local regions where the media is thin reflect increased intramural stresses and the need for an adaptive response. This is consistent with elevated monocyte/macrophage migration to the adventitia. To more rigorously examine the possible trends with this data would require a decoupling of thickness from thickness changes.

The distribution of von Mises stress and cell density is compared in the second row. Despite the hypothesized connection between stress and cell density, the visual

comparisons do not suggest a strong trend. From Table 4-4 it was clear that both von Mises stress and cell density were locally high in proximity to the branch center. But despite this similarity, the distributions do not generally correspond to one another. For some cases the lack of correspondence was remarkable, with nearly no overlap between stress peaks and cell density peaks.

Table 4-5: Summary of visual comparisons between selected branch characteristics. Positive, negative or no correlations are indicated.

Visual Assessment of Correlation	H7A	H7B	H7C	H7D	H21A	NA	NB
Correspondence between wall thickness and cell density?	POS	~	NEG	NEG	~	NEG	NEG
Correspondence between Von Mises stress and cell density?	NEG	~	POS	NEG	POS	~	~
Correspondence between wall tension and cell density?	POS	POS	POS	~	POS	~	NEG
Correspondence between Von Mises stress and wall thickness?	NEG	NEG	~	NEG	NEG	~	NEG
Correspondence between wall tension and thickness?	POS	POS	POS	POS	POS	NEG	POS

As the third row in Table 4-5 indicates, the peaks in wall tension and cell density exhibit positive correspondence for most cases. Branch H7D does not exhibit a strong relationship, but this appears to be due to the atypical distribution of wall tension in this model. A large peak opposite the branch point suggests a negative correlation, but a smaller local maximum in the saddle region suggests some positive correspondence with the net effect being neutral. Branch NB does show localized peaks in wall tension and cell density near the branch point, however the locations of these peaks do not correspond to one another. This leads to a negative correspondence for NB, as reflected in the third row of Table 4-5

The distribution of von Mises stress exhibits a negative correspondence to wall thickness for almost all cases (see row 4 of Table 4-5). The exceptions to the trend are branch H7C and branch NA where the visual pattern is not clear. In branch H7C, the decrease in midplane stresses is considerable between the mother vessel and the various daughter vessels. This decrease makes it difficult to discern the effect of the transition geometry on stress and may mask a positive correspondence. Branch NA contains some overlap but more stress peaks are not spatially collocated with high wall thickness.

The fifth row shows that the peaks in wall tension correspond with the peaks in wall thickness. This positive trend is not surprising since wall tension is the product of the maximum in-plane stress and the wall thickness. Although, considering membrane theory, it is more intuitive to think of membrane stress as being approximately equal to wall tension *divided* by the wall thickness.

These tables are not intended to take the place of side-by-side comparisons, but simply to provide a brief summary of some of the trends. Visualizations can be an efficient way to convey information quickly, but there is inherent subjectivity in drawing conclusions based purely on visual comparisons. For this reason a series of statistical tests were performed and will be discussed in the next section.

Statistical Comparisons of Branch Characteristics

Two types of statistical tests were performed. First Spearman rank correlation tests were performed on paired observations in an attempt to identify significant correlations. But Wilcoxon rank sum tests were also considered. The Wilcoxon rank sum tests determine if a significant difference exists between the means of two samples.

This test is one way to evaluate if a threshold must be exceeded before a relationship is evident (e.g. a stimulus-response relationship between stress and inflammation).

Spearman Rank Correlations

To help evaluate the relationship between variables, Spearman rank correlation tests were performed between various branch characteristics. Of particular interest was whether mechanical loads, cell density, or wall thickness were elevated in proximity to branch points. In Chapter 3 it was discussed how the minimum distance from the branch can be used as a proximity measure.

Figure 4-49 shows the minimum distance from a branch center of each surface point versus the corresponding monocyte/macrophage cell density. This particular data is for branch H7A, harvested after 7 days of hypertension. The figure indicates a trend of decreasing cell density moving away from the branch center. For this comparison the Spearman rank correlation coefficient, $r_{spearman}$, is –0.79. This correlation coefficient is very high, even for small sample sizes. Taking into account the large sample size (n = 3447) yields the standard normal score of –46.2, indicating a very high level of confidence in the negative correlation.

Care should be taken when considering the high standard normal scores. These scores are very high in part because of the high number of points representing the surface. But some of the variables may be oversampled and not represent fully independent observations. For example, cell densities calculated at adjacent surface points are based on very similar subvolumes. But even if the data were downsampled by ten-fold the Z scores would be reduced by the square root of 10, and still be highly significant for most cases. For the particular case shown in Figure 4-49, a 10-fold decrease in the sample size

would reduce the Z-score to –15.4. This results in the rejection of the hypothesis that there is no correlation (null hypothesis) with a p-value << 0.01.

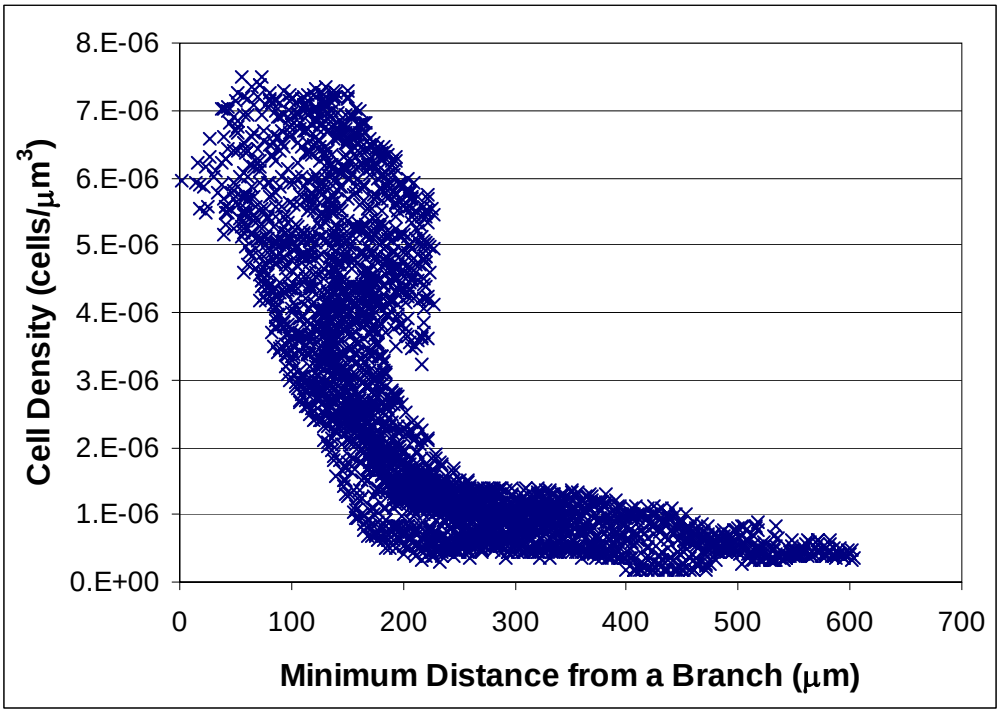

Figure 4-49: The minimum distance from a branch can be used as a measure of proximity. For each surface point, the distance to the nearest branch can be plotted with cell density. This particular plot is for hypertensive branch H7A. The highest stresses clearly occur near the branch and tend to decrease as the distance from the branch increases.

It would be inefficient to present the results from each branch in the manner shown above. So tables will be presented to summarize all the branch results for a given characteristic. These summary tables show whether there is a relationship between the values at surface points and their proximity to the branch center. Each column represents the data for one branch. This data includes filtered sample size, the mean and standard deviation of the two variables being correlated, the Spearman rank correlation coefficient (r_s) and the standard normal score (Z). The sign of the normal score indicates whether there is a positive or negative correlation. But the significance of the correlation must

also be checked using a two-tailed test. The null hypothesis is that there is no correlation between the two variables. The standard normal score (Z) indicates a confidence interval and probability (p-value) that the null hypothesis will be rejected when it is true. If the p-value is less than the target significance, then the null hypothesis can be rejected.

The correlations between wall thickness and branch proximity are shown in Table 4-6. All of the hypertensive models exhibit a decrease in wall thickness moving away from the branch center. This is not surprising since there are fundamental mechanical reasons why wall thickness should be elevated in the branch transition region. Surprisingly, the same trend is not present for the two normotensive cases. Both normotensive branches indicate wall thickness is greater away from the branch than near it. It is reasonable to assume that under normal pressures the branch structure is already optimized, but remodeling may be necessary after the onset of hypertension. Researchers have observed signs of non-homogeneity at branch points (Beattie 1998; Finlay, Whittaker et al. 1998; Liu 1998), and it is possible the extracellular matrix organization is substantially different near branches. Greater collagen content may be present where the loading pattern is more complex and less predictable. Such an organization might be better suited to the loading, but might also be less able to respond and adapt to the onset of hypertension. By this thinking, the increased wall thickness seen in the hypertensive models may be part of an adaptive response to the increased pressure.

Table 4-6: Spearman rank correlations for wall thickness versus distance from nearest branch.

Spearman Rank Correlation:	H7A	H7B	H7C	H7D	H21A	NA	NB
Sample Size	3447	4661	3085	3808	3230	2055	4404
Mean Wall Thickness (μm)	20.6	38.3	26.5	24.4	37.2	26.7	23.8
Standard Deviation	5.5	6.9	7.5	5.5	5.8	1.7	6.3
Mean Distance (μm)	232.6	251.5	225.5	327.3	214.4	512.4	200.3
Standard Deviation	114.6	125.5	147.2	192.2	79.6	290.0	62.0
Correlation Coefficient (r_s)	-0.2729	-0.0850	-0.4884	-0.0813	-0.2256	0.1664	0.0341
Standard Normal Score (Z)	-16.02	-5.80	-27.12	-5.02	-12.82	7.54	2.26
Two-Tailed Test:							
Level of Significance (α)	0.05	0.05	0.05	0.05	0.05	0.05	0.05
Lower Critical Value	-1.960	-1.960	-1.960	-1.960	-1.960	-1.960	-1.960
Upper Critical Value	1.960	1.960	1.960	1.960	1.960	1.960	1.960
p-value	0.000000	0.000000	0.000000	0.000001	0.000000	0.000000	0.023636
Reject the null hypothesis?	YES	YES	YES	YES	YES	YES	YES

Table 4-7 shows the Spearman rank correlations between cell density and distance from the nearest branch. As indicated by the standard normal scores, a strong correlation exists between cell density and this measure of branch proximity. This indicates cell density is greater near the branch point. The exception to this trend is the normotensive branch NA, which exhibits a modestly positive correlation.

Table 4-7: Spearman rank correlations for cell density versus distance from nearest branch.

Spearman Rank Correlation:	H7A	H7B	H7C	H7D	H21A	NA	NB
Sample Size	3447	4661	3085	3808	3230	2055	4404
Mean Cell Density (cells/μm^3)	2.68E-06	2.59E-06	3.48E-06	5.15E-06	4.22E-06	4.27E-07	2.65E-06
Standard Deviation	2.03E-06	1.45E-06	2.43E-06	3.78E-06	1.98E-06	3.03E-07	1.18E-06
Mean Distance (μm)	232.6	251.5	225.5	327.3	214.4	512.4	200.3
Standard Deviation	114.6	125.5	147.2	192.2	79.6	290.0	62.0
Correlation Coefficient (r_s)	-0.7870	-0.4134	-0.5120	-0.3527	-0.3718	0.0645	-0.7096
Standard Normal Score (Z)	-46.20	-28.22	-28.43	-21.76	-21.13	2.93	-47.09
Two-Tailed Test:							
Level of Significance (α)	0.05	0.05	0.05	0.05	0.05	0.05	0.05
Lower Critical Value	-1.960	-1.960	-1.960	-1.960	-1.960	-1.960	-1.960
Upper Critical Value	1.960	1.960	1.960	1.960	1.960	1.960	1.960
p-value	0.000000	0.000000	0.000000	0.000000	0.000000	0.003445	0.000000
Reject the null hypothesis?	YES	YES	YES	YES	YES	YES	YES

Table 4-8 shows the Spearman rank correlations between wall tension and the minimum distance from a branch center. The results are significant for all 7 models and the general trend is that wall tension tends to decrease with increased distance from the branch center. H7A, a 7-day hypertensive branch and H7B, a normotensive branch

exhibit a trend of increased wall tension moving away from the branch center. Branch H7A appears to be strongly influenced by a region of low wall tension near but downstream from the branch point. This helps explain the disparity between the positive visual correspondence and this negative correlation.

Table 4-8: Spearman rank correlations between maximal wall tension and a proximity measure, the distance from the nearest branch.

Spearman Rank Correlation:	H7A	H7B	H7C	H7D	H21A	NA	NB
Sample Size	3447	4661	3085	3808	3230	2055	4404
Mean Wall Tension (N/m)	0.981	1.669	1.686	1.944	1.552	0.623	0.627
Standard Deviation	0.205	0.381	0.908	0.575	0.289	0.102	0.182
Mean Distance (μm)	232.6	251.5	225.5	327.3	214.4	512.4	200.3
Standard Deviation	114.6	125.5	147.2	192.2	79.6	290.0	62.0
Correlation Coefficient (r_s)	0.1812	-0.2461	-0.4021	-0.2788	-0.5707	-0.1818	0.0894
Standard Normal Score (Z)	10.63	-16.80	-22.33	-17.20	-32.43	-8.24	5.94
Two-Tailed Test:							
Level of Significance (α)	0.05	0.05	0.05	0.05	0.05	0.05	0.05
Lower Critical Value	-1.960	-1.960	-1.960	-1.960	-1.960	-1.960	-1.960
Upper Critical Value	1.960	1.960	1.960	1.960	1.960	1.960	1.960
p-value	0.000000	0.000000	0.000000	0.000000	0.000000	0.000000	0.000000
Reject the null hypothesis?	YES	YES	YES	YES	YES	YES	YES

Table 4-9 shows the Spearman rank correlations between von Mises stress and the minimum distance from a branch center. With the exception of branch H7A, all of the hypertensive branches exhibited a trend of greater stress in proximity to the branch. Between the two normotensive branches, branch NA exhibited the same trend of greater stress near the branch while the results were not statistically significant for branch NB.

Table 4-9: Spearman rank correlations for von Mises stress versus distance from nearest branch.

Spearman Rank Correlation:	H7A	H7B	H7C	H7D	H21A	NA	NB
Sample Size	3447	4661	3085	3808	3230	2055	4404
Mean Von Mises Stress (kPa)	43.0	39.6	52.6	71.9	37.5	20.4	24.8
Standard Deviation	8.3	9.0	19.8	20.1	6.9	2.8	6.2
Mean Distance (μm)	232.6	251.5	225.5	327.3	214.4	512.4	200.3
Standard Deviation	114.6	125.5	147.2	192.2	79.6	290.0	62.0
Correlation Coefficient (r_s)	0.5057	-0.2496	-0.3123	-0.0749	-0.4159	-0.1780	-0.0026
Standard Normal Score (Z)	29.69	-17.04	-17.34	-4.62	-23.63	-8.07	-0.17
Two-Tailed Test:							
Level of Significance (α)	0.05	0.05	0.05	0.05	0.05	0.05	0.05
Lower Critical Value	-1.960	-1.960	-1.960	-1.960	-1.960	-1.960	-1.960
Upper Critical Value	1.960	1.960	1.960	1.960	1.960	1.960	1.960
p-value	0.000000	0.000000	0.000000	0.000004	0.000000	0.000000	0.864861
Reject the null hypothesis?	YES	YES	YES	YES	YES	YES	NO

Table 4-10 summarizes the comparison of maximum intramural shear stress with distance from the nearest branch for each surface point. Note the very strong similarities to the von Mises stress comparisons in Table 4-9. Not only are these shear stress trends identical to the von Mises stress trends for each branch, but also the standard normal scores are numerically very similar. This is not surprising since both stresses are associated with yield criteria and the maximum intramural shear stress represents the most dominant component used to determine von Mises stress. The maximum intramural shear stress results will be omitted from further comparisons because of this strong similarity to the von Mises stress patterns. Based on similar reasoning, the second invariant of the stress deviator (J_2) will not be presented.

Table 4-10: Spearman rank correlations for maximum intramural shear stress versus distance from nearest branch.

Spearman Rank Correlation:	H7A	H7B	H7C	H7D	H21A	NA	NB
Sample Size	3447	4661	3085	3808	3230	2055	4404
Mean Stress Intensity (kPa)	48.8	44.5	59.2	80.5	42.2	23.2	27.7
Standard Deviation	9.9	9.8	22.4	21.9	7.6	3.4	7.0
Mean Distance (μm)	232.6	251.5	225.5	327.3	214.4	512.4	200.3
Standard Deviation	114.6	125.5	147.2	192.2	79.6	290.0	62.0
Correlation Coefficient (r_s)	0.4900	-0.2049	-0.3114	-0.0564	-0.3897	-0.2061	-0.0168
Standard Normal Score (Z)	28.77	-13.99	-17.29	-3.48	-22.15	-9.34	-1.11
Two-Tailed Test:							
Level of Significance (α)	0.05	0.05	0.05	0.05	0.05	0.05	0.05
Lower Critical Value	-1.960	-1.960	-1.960	-1.960	-1.960	-1.960	-1.960
Upper Critical Value	1.960	1.960	1.960	1.960	1.960	1.960	1.960
p-value	0.000000	0.000000	0.000000	0.000497	0.000000	0.000000	0.265108
Reject the null hypothesis?	YES	YES	YES	YES	YES	YES	NO

Table 4-11 summarizes the Spearman rank correlations between the first stress invariant and the minimum distance from a branch center. The first stress invariant (I_1) is the sum of the normal components and is equal to three times the hydrostatic portion of the stress tensor. Because of this linear relationship, the rankings of the first stress invariant are equal to the rankings of the hydrostatic portion of stress. There is a general trend of decreasing I_1 with increasing distance from the branch, but H7C and NB exhibit an opposing trend and the trend is not statistically significant for H7B.

Table 4-11: Spearman rank correlations for first stress invariant versus distance from nearest branch.

Spearman Rank Correlation:	H7A	H7B	H7C	H7D	H21A	NA	NB
Sample Size	3447	4661	3085	3808	3230	2055	4404
Mean First Stress Invariant (kPa)	78.8	63.1	91.2	131.2	63.6	37.1	38.9
Standard Deviation	14.2	15.5	34.0	39.3	10.9	4.8	15.4
Mean Distance (μm)	232.6	251.5	225.5	327.3	214.4	512.4	200.3
Standard Deviation	114.6	125.5	147.2	192.2	79.6	290.0	62.0
Correlation Coefficient (r_s)	0.5667	-0.0104	-0.2300	-0.0428	-0.1108	-0.1154	0.2265
Standard Normal Score (Z)	33.26	-0.71	-12.77	-2.64	-6.29	-5.23	15.03
Two-Tailed Test:							
Level of Significance (α)	0.05	0.05	0.05	0.05	0.05	0.05	0.05
Lower Critical Value	-1.960	-1.960	-1.960	-1.960	-1.960	-1.960	-1.960
Upper Critical Value	1.960	1.960	1.960	1.960	1.960	1.960	1.960
p-value	0.000000	0.477227	0.000000	0.008230	0.000000	0.000000	0.000000
Reject the null hypothesis?	YES	NO	YES	YES	YES	YES	YES

The proximity measures in the previous tables indicate that wall thickness, von Mises stress, maximal wall tension and cell density are generally elevated in proximity to

the branch. But it is unclear whether the spatial correlations extend to direct point-by-point comparisons of characteristics. To determine if, for example, von Mises stress and cell density are correlated these characteristics are treated as paired observations at each point on the surface. This is similar to what was done for the proximity comparisons above, but here the proximity information is discarded in favor of direct comparisons between other characteristics. So, for instance, if peaks in two branch characteristics are near one another but not coincident there may be no positive correlation. In reality the data values gradually change, so there does not need to be a precise one-to-one correspondence of peaks for a positive correlation to exist.

Over the remainder of this section the following characteristics will be compared using Spearman rank correlations:

1. wall thickness versus cell density
2. wall tension versus cell density
3. von Mises stress versus cell density
4. First Stress Invariant versus cell density
5. wall tension versus wall thickness
6. von Mises stress versus wall thickness
7. First Stress Invariant versus wall thickness

Other characteristics and combinations of characteristics were considered, but did not add substantially to the list provided above.

Table 4-12 shows the correlations between wall thickness and cell density. The trend is negative for all cases except H7A, where the trend is strongly positive. Branch H7C exhibits a negative trend but the correlation has a p-value of 0.112 which is not

significant enough to reject the null hypothesis at $\alpha = 0.05$. So it appears that cell density is generally high where wall thickness is low. This is a surprising result since cell density and wall thickness are both elevated in proximity to the branch (see Table 4-7 and Table 4-6). One might expect a strong, *positive* correlation between cell density and wall thickness, rather than the negative correlation that exists. A visual comparison of the two color-coded distributions corroborates what these statistical tests indicate: the peaks in cell density and wall thickness do not generally correspond. This is evidence of the power of the statistical method to resolve subtle spatial differences in the distribution of branch characteristics. This also suggests that wall thickness cannot be used as an indicator of the distribution of inflammatory changes. Increased inflammation in the adventitia adjacent to locations where the media is comparatively thin is consistent with an adaptive response to elevated intramural stress.

Table 4-12: Spearman rank correlations between wall thickness and cell density.

Spearman Rank Correlation:	H7A	H7B	H7C	H7D	H21A	NA	NB
Sample Size	3447	4661	3085	3808	3230	2055	4404
Mean Wall Thickness (μm)	20.6	38.3	26.5	24.4	37.2	26.7	23.8
Standard Deviation	5.5	6.9	7.5	5.5	5.8	1.7	6.3
Mean Cell Density (Cells/μm^3)	2.68E-06	2.59E-06	3.48E-06	5.15E-06	4.22E-06	4.27E-07	2.65E-06
Standard Deviation	2.03E-06	1.45E-06	2.43E-06	3.78E-06	1.98E-06	3.03E-07	1.18E-06
Correlation Coefficient (r_s)	0.5985	-0.3537	-0.0286	-0.1083	-0.0756	-0.2017	-0.0436
Standard Normal Score (Z)	35.13	-24.14	-1.59	-6.68	-4.30	-9.14	-2.90
Two-Tailed Test:							
Level of Significance (α)	0.05	0.05	0.05	0.05	0.05	0.05	0.05
Lower Critical Value	-1.960	-1.960	-1.960	-1.960	-1.960	-1.960	-1.960
Upper Critical Value	1.960	1.960	1.960	1.960	1.960	1.960	1.960
p-value	0.000000	0.000000	0.112151	0.000000	0.000017	0.000000	0.003783
Reject the null hypothesis?	YES	YES	NO	YES	YES	YES	YES

Table 4-13 shows the Spearman rank correlation between maximal wall tension and cell density. Three of the five hypertensive branches exhibit a substantially positive correlation, while both of the normotensive branches are negatively correlated. For branch H7B the correlation is weak and it is not possible to reject the null hypothesis.

This is the case despite the maximal wall tension and cell density both occurring at the tertiary branch. It turns out that the tertiary branch produces both high and low stress, much like a hole in a plate under tension. The net effect is a week correlation over the full range of data. Branch H7D shows a negative correlation reflecting the fact that wall tension has a peak on the opposite side of the mother vessel in a region where cell density is low.

Table 4-13: Spearman rank correlations between maximal wall tension and cell density.

Spearman Rank Correlation:	H7A	H7B	H7C	H7D	H21A	NA	NB
Sample Size	3447	4661	3085	3808	3230	2055	4404
Mean Wall Tension (N/m)	0.981	1.669	1.686	1.944	1.552	0.623	0.627
Standard Deviation	0.205	0.381	0.908	0.575	0.289	0.102	0.182
Mean Cell Density (Cells/μm^3)	2.68E-06	2.59E-06	3.48E-06	5.15E-06	4.22E-06	4.27E-07	2.65E-06
Standard Deviation	2.03E-06	1.45E-06	2.43E-06	3.78E-06	1.98E-06	3.03E-07	1.18E-06
Correlation Coefficient (r_s)	0.1239	-0.0121	0.0952	-0.1463	0.2738	-0.2230	-0.0298
Standard Normal Score (Z)	7.28	-0.83	5.29	-9.03	15.56	-10.11	-1.98
Two-Tailed Test:							
Level of Significance (α)	0.05	0.05	0.05	0.05	0.05	0.05	0.05
Lower Critical Value	-1.960	-1.960	-1.960	-1.960	-1.960	-1.960	-1.960
Upper Critical Value	1.960	1.960	1.960	1.960	1.960	1.960	1.960
p-value	0.000000	0.407150	0.000000	0.000000	0.000000	0.000000	0.048223
Reject the null hypothesis?	YES	NO	YES	YES	YES	YES	YES

Table 4-14 shows the Spearman rank correlations between von Mises stress and cell density. It was expected that a stronger pattern would be evident with this particular comparison. Both H7A and NA showed a strikingly different pattern, primarily because the von Mises stress peaks did not occur in the transition region. In addition, normotensive branch NB presented a positive correlation, despite very low stress levels in the transition region. As discussed earlier, maximum intramural shear stress comparisons are not presented because they are very similar to the results for von Mises stress in Table 4-14.

Table 4-14: Spearman rank correlations between von Mises stress and cell density.

Spearman Rank Correlation:	H7A	H7B	H7C	H7D	H21A	NA	NB
Sample Size	3447	4661	3085	3808	3230	2055	4404
Mean Von Mises Stress (kPa)	43.0	39.6	52.6	71.9	37.5	20.4	24.8
Standard Deviation	8.3	9.0	19.8	20.1	6.9	2.8	6.2
Mean Cell Density (Cells/μm^3)	2.68E-06	2.59E-06	3.48E-06	5.15E-06	4.22E-06	4.27E-07	2.65E-06
Standard Deviation	2.03E-06	1.45E-06	2.43E-06	3.78E-06	1.98E-06	3.03E-07	1.18E-06
Correlation Coefficient (r_s)	-0.6118	0.3332	0.1147	-0.2427	0.3383	-0.1975	0.0711
Standard Normal Score (Z)	-35.91	22.74	6.37	-14.97	19.22	-8.95	4.72
Two-Tailed Test:							
Level of Significance (α)	0.05	0.05	0.05	0.05	0.05	0.05	0.05
Lower Critical Value	-1.960	-1.960	-1.960	-1.960	-1.960	-1.960	-1.960
Upper Critical Value	1.960	1.960	1.960	1.960	1.960	1.960	1.960
p-value	0.000000	0.000000	0.000000	0.000000	0.000000	0.000000	0.000002
Reject the null hypothesis?	YES	YES	YES	YES	YES	YES	YES

Table 4-15 summarizes the Spearman rank correlations between the first stress invariant and cell density. As previously mentioned, the first stress invariant is proportional to the hydrostatic stress. In the context of a Spearman rank correlation the two stresses yield identical results. A general trend is not apparent when the data is taken together.

Table 4-15: Spearman rank correlations between the first stress invariant and cell density.

Spearman Rank Correlation:	H7A	H7B	H7C	H7D	H21A	NA	NB
Sample Size	3447	4661	3085	3808	3230	2055	4404
Mean First Stress Invariant (kPa)	78.8	63.1	91.2	131.2	63.6	37.1	38.9
Standard Deviation	14.2	15.5	34.0	39.3	10.9	4.8	15.4
Mean Cell Density (Cells/μm^3)	2.68E-06	2.59E-06	3.48E-06	5.15E-06	4.22E-06	4.27E-07	2.65E-06
Standard Deviation	2.03E-06	1.45E-06	2.43E-06	3.78E-06	1.98E-06	3.03E-07	1.18E-06
Correlation Coefficient (r_s)	-0.6650	0.1641	0.1165	-0.3149	0.1206	-0.1598	-0.0514
Standard Normal Score (Z)	-39.03	11.20	6.47	-19.43	6.85	-7.24	-3.41
Two-Tailed Test:							
Level of Significance (α)	0.05	0.05	0.05	0.05	0.05	0.05	0.05
Lower Critical Value	-1.960	-1.960	-1.960	-1.960	-1.960	-1.960	-1.960
Upper Critical Value	1.960	1.960	1.960	1.960	1.960	1.960	1.960
p-value	0.000000	0.000000	0.000000	0.000000	0.000000	0.000000	0.000642
Reject the null hypothesis?	YES	YES	YES	YES	YES	YES	YES

Correlations were also considered between load characteristics and wall thickness. Table 4-16 shows that maximal wall tension is positively correlated with wall thickness for all cases. It is not surprising that wall tension would vary with wall thickness,

especially if one considers that arterial tissue tries to maintain the stresses and/or strains within some homeostatic range (Masuda, Bassiouny et al. 1989; Glagov, Bassiouny et al. 1997). The accuracy of this observation is limited to the extent that maximal wall tension can be represented as maximum midplane stress component multiplied by the thickness.

Table 4-16: Spearman rank correlations between maximal wall tension and wall thickness.

Spearman Rank Correlation:	H7A	H7B	H7C	H7D	H21A	NA	NB
Sample Size	3447	4661	3085	3808	3230	2055	4404
Mean Wall Tension (N/m)	0.981	1.669	1.686	1.944	1.552	0.623	0.627
Standard Deviation	0.205	0.381	0.908	0.575	0.289	0.102	0.182
Mean Wall Thickness (μm)	20.6	38.3	26.5	24.4	37.2	26.7	23.8
Standard Deviation	5.5	6.9	7.5	5.5	5.8	1.7	6.3
Correlation Coefficient (r_s)	0.5591	0.4242	0.7442	0.3857	0.4218	0.4284	0.4580
Standard Normal Score (Z)	32.82	28.96	41.33	23.80	23.97	19.42	30.39
Two-Tailed Test:							
Level of Significance (α)	0.05	0.05	0.05	0.05	0.05	0.05	0.05
Lower Critical Value	-1.960	-1.960	-1.960	-1.960	-1.960	-1.960	-1.960
Upper Critical Value	1.960	1.960	1.960	1.960	1.960	1.960	1.960
p-value	0.000000	0.000000	0.000000	0.000000	0.000000	0.000000	0.000000
Reject the null hypothesis?	YES	YES	YES	YES	YES	YES	YES

Table 4-17 shows the Spearman rank correlations between von Mises stress and wall thickness. For most cases, von Mises stress is negatively correlated with wall thickness. Four of five hypertensive cases exhibit strongly negative correlations. Considering the branch as an optimally designed pressure vessel, one might hypothesize that the thickness is locally adapted to maintain the state of stress between some limited range. But the variable thickness finite element models still indicate a highly nonuniform distribution of stress. Since heterogeneity is not considered, it is possible that the vascular tissue at branches remodels to become stiffer in regions of high stress.

Table 4-17: Spearman rank correlations between von Mises stress and wall thickness.

Spearman Rank Correlation:	H7A	H7B	H7C	H7D	H21A	NA	NB
Sample Size	3447	4661	3085	3808	3230	2055	4404
Mean Von Mises Stress (kPa)	43.0	39.6	52.6	71.9	37.5	20.4	24.8
Standard Deviation	8.3	9.0	19.8	20.1	6.9	2.8	6.2
Mean Wall Thickness (μm)	20.6	38.3	26.5	24.4	37.2	26.7	23.8
Standard Deviation	5.5	6.9	7.5	5.5	5.8	1.7	6.3
Correlation Coefficient (r_s)	-0.6092	-0.3934	0.5523	-0.1685	-0.3941	0.1382	-0.5341
Standard Normal Score (Z)	-35.76	-26.85	30.67	-10.40	-22.39	6.26	-35.44
Two-Tailed Test:							
Level of Significance (α)	0.05	0.05	0.05	0.05	0.05	0.05	0.05
Lower Critical Value	-1.960	-1.960	-1.960	-1.960	-1.960	-1.960	-1.960
Upper Critical Value	1.960	1.960	1.960	1.960	1.960	1.960	1.960
p-value	0.000000	0.000000	0.000000	0.000000	0.000000	0.000000	0.000000
Reject the null hypothesis?	YES	YES	YES	YES	YES	YES	YES

Table 4-18 shows the correlations between the first stress invariant and wall thickness for each branch. These results are similar to the von Mises stress results previously presented.

Table 4-18: Spearman rank correlations between the first stress invariant and wall thickness.

Spearman Rank Correlation:	H7A	H7B	H7C	H7D	H21A	NA	NB
Sample Size	3447	4661	3085	3808	3230	2055	4404
Mean First Stress Invariant (kPa)	78.8	63.1	91.2	131.2	63.6	37.1	38.9
Standard Deviation	14.2	15.5	34.0	39.3	10.9	4.8	15.4
Mean Wall Thickness (μm)	20.6	38.3	26.5	24.4	37.2	26.7	23.8
Standard Deviation	5.5	6.9	7.5	5.5	5.8	1.7	6.3
Correlation Coefficient (r_s)	-0.6333	-0.2955	0.4658	-0.2633	-0.3470	0.0850	-0.3352
Standard Normal Score (Z)	-37.18	-20.17	25.87	-16.24	-19.72	3.85	-22.24
Two-Tailed Test:							
Level of Significance (α)	0.05	0.05	0.05	0.05	0.05	0.05	0.05
Lower Critical Value	-1.960	-1.960	-1.960	-1.960	-1.960	-1.960	-1.960
Upper Critical Value	1.960	1.960	1.960	1.960	1.960	1.960	1.960
p-value	0.000000	0.000000	0.000000	0.000000	0.000000	0.000117	0.000000
Reject the null hypothesis?	YES	YES	YES	YES	YES	YES	YES

The Spearman rank correlations indicate that von Mises stress, maximal wall tension, wall thickness and cell density are each negatively correlated with distance from the branch. This means each of these branch characteristics exhibits a positive correlation with branch proximity.

Wilcoxon Rank Sum Test

An alternative to Spearman rank correlations over the full range of data is to consider that some threshold value must be exceeded before a stimulus-response pattern emerges. If this is the case, a potential cause-effect relationship might be masked by variations in data below the threshold level, which have little or no influence. For this reason a Wilcoxon rank sum statistical analysis was performed. As described in Chapter 3, the population of surface points is segregated into two groups depending on the threshold value of the first variable. A second variable is then examined for the two groups or samples. If there is no relationship between the variables, the two samples have been formed by a random selection process. The null hypothesis in a Wilcoxon rank sum test is that the samples are from the same population. Based on the rank sum, the number observations, and the confidence interval, the null hypothesis is accepted or rejected. Because this test does not require samples of the same size, the data can be divided into groups based on quartiles or some other measure emphasizing differences in the data. In the following cases the data was divided into quartiles based on the first variable and then the upper quartile was compared to the lower three quartiles. Appendix K contains a more extensive set of statistical test results and selected results are presented below.

Two approaches were used to create groups. The first approach involved dividing the points into *quartile ranges* based on one branch characteristic. The upper quartile range represents the first group while the lower three-quarters of the range constitute the second group. The second approach involved first assigning an overall rank to each value and then taking the upper ten percent of the ranks as one group and the lower 90

percent as a second group. By using the rank of the values instead of the values themselves, the distribution becomes uniform and the number of values is predictable. The upper ten percent of ranks represents *upper ten percent of the total number* of values.

Table 4-19 shows the Wilcoxon rank sum test results for two groups of cell densities. Group A represents surface points in the upper quartile range of wall tension. The rest of the surface points forms group B. For example, for branch H7A, the maximum wall tension value is roughly 1.7 N/m and the minimum is 0.3 N/m. Therefore values between 1.2 N/m and 1.7 N/m represent the upper quartile of values (Group A). Since the distribution is not normal, only 82 of the 3447 observations fall within the upper value quartile of values. This represents 2.4 percent of the total number of observations. The positive standard normal scores indicate a positive trend for all cases. Cell density *appears* to be greater in the high wall tension group than the low wall tension group. However, because the sample size is small, the results are only significant for 2 of the 7 cases. The significance of the results is directly affected by the very small size of the high wall tension group. For this reason, an alternative grouping method was considered. As previously mentioned, the surface points were segregated into two groups based on *number* rather than *value*.

Table 4-19: Wilcoxon rank sum test results. Cell density is grouped based on wall tension range. The upper quartile range of wall tension forms the first sample and the lower three quartiles form the second sample.

Wilcoxon Rank Sum Test
Cell Density grouped by Upper Quartile of *Values* for Wall Tension

	H7A	H7B	H7C	H7D	H21A	NA	NB
Level of Significance (α):	0.05	0.05	0.05	0.05	0.05	0.05	0.05
Sample Size for Group A:	82	19	17	35	63	61	105
Sum of Ranks for Group A:	2.38E+05	5.08E+04	3.13E+04	8.18E+04	1.11E+05	6.62E+04	2.49E+05
Mean Rank for Group A:	2906	2671.9	1842.8	2336.7	1758.3	1084.6	2369
Sample Size for Group B:	3365	4642	3068	3773	3167	1994	4299
Sum of Ranks for Group B:	5.70E+06	1.08E+07	4.73E+06	7.17E+06	5.11E+06	2.05E+06	9.45E+06
Mean Rank for Group B:	1695.2	2329.6	1541.3	1900.5	1612.7	1026.3	2198.4
Total Population Size:	3447.0	4661	3085	3808	3230	2055	4404
Total Sum of Ranks:	5.94E+06	1.09E+07	4.76E+06	7.25E+06	5.22E+06	2.11E+06	9.70E+06
Standard Deviation of Group A:	8904.1	5853.6	3662.3	6474.3	7329.5	4565.1	12872
Standard Normal Score of A:	10.89	1.11	1.39	2.34	1.23	0.76	1.36
Two-Tailed Test:							
Lower Critical Value:	-1.9600	-1.9600	-1.9600	-1.9600	-1.9600	-1.9600	-1.9600
Upper Critical Value:	1.9600	1.9600	1.9600	1.9600	1.9600	1.9600	1.9600
p-value:	0.0000	0.2685	0.1641	0.0195	0.2197	0.4494	0.1745
Reject the null hypothesis?	YES	NO	NO	YES	NO	NO	NO

Table 4-20 shows the alternative grouping. The first group still represents the surface points with high wall tension, but in this case the group consists of ten percent of all the surface points. Group A is considerably larger for this case compared to the first group shown in Table 4-19. This improved the significance of the results leading to 4 of 7 cases being considered significant. One case that exhibited significance (branch H7B) also indicated a negative trend. When this branch is considered in detail, the trend reversal is easier to understand. Branch H7B, a hypertensive branch, has a small tertiary branch that is a focal point for high stress/high wall tension. Visually the tertiary branch corresponds to a broad region of high cell density. It turns out that the stress is highly localized and only represented by a limited number of surface points (see Figure 4-19). In addition, high gradients are present in this region because the tertiary branch acts like a

hole in a plate during uniaxial loading. So as the wall tension sample size increases, other regions of the branch are sampled and the trend becomes less clear.

Table 4-20: Wilcoxon rank sum test results. Cell density is grouped by upper ten percent of values for wall tensions.

Wilcoxon Rank Sum Test
Cell Density grouped by Upper Ten Percent of *Ranks* for Wall Tension

	H7A	H7B	H7C	H7D	H21A	NA	NB
Level of Significance (α):	0.05	0.05	0.05	0.05	0.05	0.05	0.05
Sample Size for Group A:	345	466	309	381	323	206	441
Sum of Ranks for Group A:	9.52E+05	1.02E+06	5.55E+05	7.40E+05	5.72E+05	2.22E+05	9.71E+05
Mean Rank for Group A:	2758.1	2179.6	1796.7	1941.5	1770.8	1079.2	2200.7
Sample Size for Group B:	3102	4195	2776	3427	2907	1849	3963
Sum of Ranks for Group B:	4.99E+06	9.85E+06	4.21E+06	6.51E+06	4.65E+06	1.89E+06	8.73E+06
Mean Rank for Group B:	1609	2347.8	1514.8	1900.4	1598.2	1022.3	2202.7
Total Population Size:	3447.0	4661	3085	3808	3230	2055	4404
Total Sum of Ranks:	5.94E+06	1.09E+07	4.76E+06	7.25E+06	5.22E+06	2.11E+06	9.70E+06
Standard Deviation of Group A:	17536	27558	14852	20358	15900	8078.4	25329
Standard Normal Score of A:	20.34	-2.56	5.28	0.69	3.15	1.31	-0.03
Two-Tailed Test:							
Lower Critical Value:	-1.9600	-1.9600	-1.9600	-1.9600	-1.9600	-1.9600	-1.9600
Upper Critical Value:	1.9600	1.9600	1.9600	1.9600	1.9600	1.9600	1.9600
p-value:	0.0000	0.0105	0.0000	0.4884	0.0016	0.1914	0.9750
Reject the null hypothesis?	YES	YES	YES	NO	YES	NO	NO

Some additional Wilcoxon rank sum results are presented in Appendix K. This test appears to be sensitive to small changes in the thresholding level used to divide the population into two samples. In addition, several cases do not yield statistically significant results. For some cases, like H7B in Table 4-19 and Table 4-20, the trend can change from positive to negative based on how the data is segregated into two groups. As with H7B the differences can usually be physically explained, but this sensitivity to changes in group sizes and the need for additional explanations limits the utility of the Wilcoxon rank sum test. After all, the statistical tests are designed to objectively determine whether specific correlations are manifest in the data. It appears that the

Wilcoxon rank sum test, as implemented, does not add substantially to the visual and statistical comparisons previously presented.

Summary of Visual and Statistical Comparisons

There is a considerable amount of variability in the data, independent of any localized inflammatory changes. Branch sizes vary, branch angles vary, and the change in vessel size is significantly different from branch to branch. In addition it is apparent that there is significant spatial variability within a given branch. Wall thickness can change by two or three fold within the transition region. All these factors contribute to the difficulties in statistically comparing the spatial distribution of branch characteristics.

The visual comparisons were completed before the statistical comparisons. Since the visual and statistical comparisons were presented independently, they are summarized side-by-side in Table 4-21 and Table 4-22. Generally there were strong similarities between the results. Note that the positive (POS), negative (NEG) or neutral (~) designations for the Spearman rank correlations are based on the sign and significance of the standard normal score. One important source of differences is that the visual comparisons tended to emphasize correspondence of the peaks rather than correspondence over the full range of values. It might have been possible to review and modify the visual assessment, based on the full range of data, but any such changes might be prejudiced by the knowledge of the statistical results.

When summarizing the statistical evaluations, keep in mind that distance is an inverse measure of proximity. Therefore in Table 4-21 the positive correlations are associated with negative correlation coefficients from the earlier Spearman rank correlation tables.

The visual and statistical comparisons both demonstrate that cell density was elevated in proximity to the branch for all branches except NA. For branch NA the visual pattern was scattered and unclear, while the statistical correlations indicated a negative correlation. The negative correlation was comparatively weak, with the lowest p value among all cases.

While the pattern of high cell density may not be generally elevated for the two normotensive cases, all of the hypertensive branches exhibited elevated cell density in the branch transition region. The pattern of inflammation tended to be highly localized, suggesting that branches are focal points for monocyte and macrophage recruitment. This is strong evidence supporting the hypothesis that inflammation is more concentrated in proximity to arterial branches.

For wall thickness, the visual and statistical tests were similar to one another, but there was less certainty in the visual assessments. The general pattern indicated a positive relationship between wall thickness and branch proximity. This was true for all hypertensive branches but not true for one normotensive branch and unclear for the other.

Table 4-21: A summary of visual comparisons and Spearman rank correlations indicating if selected variables are elevated in proximity to branch center.

Visual & Statistical Summary	H7A	H7B	H7C	H7D	H21A	NA	NB
	Cell density elevated near branch?						
Visual Assessment	POS	POS	POS	POS	POS	~	POS
Spearman Rank Correlation	POS	POS	POS	POS	POS	NEG	POS
	Wall thickness elevated near branch?						
Visual Assessment	POS	POS	POS	~	POS	NEG	~
Spearman Rank Correlation	POS	POS	POS	POS	POS	NEG	NEG
	Von Mises stress elevated near branch?						
Visual Assessment	NEG	POS	POS	POS	POS	POS	~
Spearman Rank Correlation	NEG	POS	POS	POS	POS	POS	~
	Wall tension elevated near branch?						
Visual Assessment	POS	POS	POS	~	POS	POS	~
Spearman Rank Correlation	NEG	POS	POS	POS	POS	POS	NEG

Table 4-21 also shows identical trends for the visual and statistical comparisons of von Mises stress to branch proximity. Most branches indicate a positive correspondence, but branch H7A indicated a negative trend and branch NB indicated no clear relationship. These results were similar to other midplane stress results.

A similar strong relationship was evident between maximal wall tension and branch proximity. A notable exception to this was branch H7A. Surprisingly the visual trend was clearly positive, but the Spearman rank correlation coefficient indicated a negative trend. This occurred because the lowest wall tensions occur in the smaller daughter vessel near the branch point. Even though the geometric transition has occurred where the wall tension is low, this region is close enough to the branch to affect the results. This illustrates how information can be lost by reducing data to a simple

measurement of proximity or a statistical measure of positive or negative correlation. The inherent complexity of the branches makes it difficult to generalize and simplify in this manner. These kinds of subtleties in data analysis also underscore the need to present three-dimensional distributions side-by-side with statistical correlations.

The visual and statistical comparisons of stresses and wall tension to branch proximity provide the means to determine mechanical loads are elevated near branch points. The positive visual and statistical correlations between von Mises stress and branch proximity and between wall tension and branch proximity support the hypothesis that mechanical loads are elevated near branches.

Table 4-22 is a summary table of selected visual and statistical comparisons between variables. The first set of data indicates wall thickness is negatively correlated with cell density for most cases. This is somewhat surprising since both wall thickness and cell density are elevated near the branch point, but this does indicate a lack of one-to-one correspondence between the locations of high thickness and the locations of high cell density.

Table 4-22: A summary of visual comparisons and Spearman rank correlations between selected variables.

Visual & Statistical Summary	H7A	H7B	H7C	H7D	H21A	NA	NB
	Wall thickness versus cell density?						
Visual Correspondence	POS	~	NEG	NEG	~	NEG	NEG
Spearman Rank Correlation	POS	NEG	~	NEG	NEG	NEG	NEG
	Von Mises stress versus cell density?						
Visual Correspondence	NEG	~	POS	NEG	POS	~	~
Spearman Rank Correlation	NEG	~	POS	NEG	POS	~	~
	Wall tension versus cell density?						
Visual Correspondence	POS	POS	POS	~	POS	~	NEG
Spearman Rank Correlation	POS	~	POS	NEG	POS	NEG	NEG
	Von Mises stress versus wall thickness?						
Visual Correspondence	NEG	NEG	~	NEG	NEG	~	NEG
Spearman Rank Correlation	NEG	NEG	POS	NEG	NEG	POS	NEG
	Wall tension and wall thickness?						
Visual Correspondence	POS	POS	POS	POS	POS	NEG	POS
Spearman Rank Correlation	POS	POS	POS	POS	POS	NEG	POS

Table 4-22 also indicates there is no strong correspondence between von Mises stress and cell density. This is an important negative finding, since a fundamental hypothesis in this research is that intramural stresses stimulate inflammatory changes.

However maximal wall tension does exhibit a stronger positive correspondence to cell density. Although the pattern is not definitive for branch H7B, H7D or NA, the general trend is a positive correspondence among the hypertensive models and a negative correspondence among the normotensive cases. The one exception to this trend was branch H7D, which exhibited a strong negative correlation between wall tension and cell density. As discussed earlier this branch had a high wall tension on the opposite side of

the mother vessel from the branch point. Two lower peaks were in the branch transition region. The correlation was negative in large part because very low wall tension values were present in the smaller daughter vessel just downstream of the branch. So even the hypertensive branch that least conformed to the trend exhibited some features of a positive correlation.

Comparisons were also made between von Mises stress and wall thickness. These were generally negative. This is not surprising considering stress is generally inversely proportional to thickness, when curvature is unchanged. As an alternative to von Mises stress, maximal wall tension was considered. As a reminder, maximal wall tension is the maximum in-plane stress component multiplied by the wall thickness. This tends to emphasize the effects of curvature on intramural stresses. The drawback is that wall tension varies more significantly from large vessels to small vessels than midplane stress does, so there is more of a change in wall tension with vessel size. Given this caveat, maximal wall tension appears to be strongly correlated to wall thickness. The lone exception to this pattern is normotensive branch NA.

A few more anecdotal observations will be made, although there is insufficient data to draw firm conclusions. One case of particular interest was H21A, the branch subjected to 21 days of Angiotensin II hypertension. The distribution of wall thickness exhibited in H21A indicates three localized peaks corresponding closely to the three regions of negative Gaussian curvature. These are precisely the locations where midplane stresses would otherwise be high. It appears the geometry of H21A is becoming reoptimized for the new mechanical environment.

The question of mechanical adaptation can also be considered by looking at the normotensive vessels and assuming the geometry is already optimized for the mechanical environment. Figure 4-50 shows a constant thickness finite element model compared to the actual thickness distribution for branch NB. The average thickness is used in the finite element model on the left, yet there is a strong correspondence between the stress peaks and the wall thickness peaks. This suggests that this normotensive branch geometry is optimized for the stress environment and could help explain why elevating pressure and disturbing the mechanical homeostasis could lead to an inflammatory response that is localized at the branch.

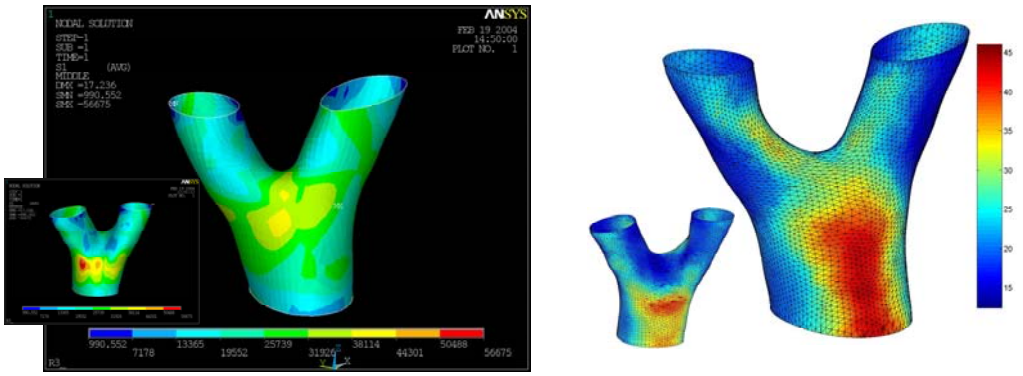

Figure 4-50: Stress distribution (in Pa) in a constant wall thickness finite element model versus the actual thickness distribution (in μm).

As previously mentioned, it is difficult to evaluate the time course of inflammation and adaptation in response to increased pressure since each harvest is a snapshot of the mechanical and biological environment at a given time.

CHAPTER 5:

CONCLUSIONS AND RECOMMENDATIONS

This research effort required the development of a unique set of methods to identify and compare morphological, mechanical, and inflammatory branch characteristics. The methods were implemented to compare the three-dimensional mechanical loads to the pattern of inflammation in small arterial branches.

Summary of Methods Developed

A histology-based reconstruction technique was developed that was suitable for small arterial branches. Embedding and sectioning procedures were optimized to reduce the distortions caused by microtomy. A pin alignment fixture produced an array of holes allowing for the correction of distortions and facilitated the reconstitution of section images into a three-dimensional stack. The mean square difference in intensities was used as an image similarity measure to align serial sections. The use of a point-cloud based reconstruction technique took full advantage of the high in-plane resolution afforded by microscopy while still making the reconstruction process computationally efficient.

The use of commercially available software (Geomagic Studio) after preprocessing made it possible to generate smooth representations of vessel surfaces that were suitable for importation into Ansys and subsequent finite element analysis. The

inner surface and outer surface were separately reconstructed and then Matlab code was created to accurately determine the local wall thickness and identify the midplane geometry.

Due to the small size of the mesenteric arteries, some unique problems were associated with section alignment, distortion correction, and surface reconstruction. Techniques developed to solve these problems have general utility in reconstructing other small structures from serial sections.

Finite element analysis played a unique role in this research because of the limitations in the types of mechanical experiments that could be conducted. The challenges associated with mechanical testing were further magnified by the interest in the local distribution of stress and strain at branch points. The use of a parametric finite element model based on idealized geometry provided insight into how variations in geometry, boundary conditions, and material properties affected the stress and strain distributions. The differences between the idealized models and the histology-based models were striking, emphasizing the importance of studying real geometries that are grounded in histology.

Variable thickness finite element models were created within Ansys based on the midplane geometry. Variable thickness shell elements were used that could account for large stress gradients through the wall with a single layer of elements. The shell element representation of the midplane also facilitated comparison with the pattern of inflammation.

In concert with the reconstruction and finite element work, a graphic user interface was developed to navigate the high magnification montages from microscopy.

Monocytes and macrophages were identified based on their cytoplasmic and nuclear morphology by a vascular biologist. The graphic user interface allowed an expert to load images, pan, zoom, and record the locations of a variety of markers. The centroid locations of monocytes and macrophages were recorded for each image. From a set of serial sections the inflammatory cell locations were compiled and aligned in three dimensions with the vessel reconstruction.

The distribution of inflammation through the branch was characterized by a series of local monocyte/macrophage density measurements within Matlab. The accurate determination of cell density in a region requires exclusion of the luminal volume and special considerations at the boundaries of the data.

The mechanical loads and inflammation were visually represented as a color-coded pattern on the surface reconstruction. This visualization technique proved useful in identifying relationships among data.

In addition, results were statistically compared by treating each point on the surface as a sampling point for a variety of branch characteristics. The distribution of most variables was not normal; therefore, non-parametric statistical methods were used to make comparisons. The Spearman rank correlation was used to identify possible correlations between variables, treating variables as paired observations. The Wilcoxon rank sum test was used to see if segregating the data based on one branch characteristic produced dissimilar samples of a second variable. In essence, this determines if some threshold value must be exceeded before a stimulus-response pattern is manifest. As the Wilcoxon rank sum test results were very sensitive to changes in threshold, they were not heavily relied on.

The branch characteristics studied included wall thickness, maximal in-plane wall tension, midplane von Mises stress, and cell density. The distance between each surface point and the nearest branch center was measured and treated as a separate characteristic. This distance is an inverse measure of branch proximity that proved useful in determining how other branch characteristics varied with respect to branch proximity.

The reconstruction technique, the finite element analysis, the cell density characterization, and the visual and statistical comparisons represent a considerable amount of the research effort. Collectively these techniques form a foundation for other three-dimensional studies where mechanical and biological phenomena may be interrelated.

While developing the methods has some inherent value, the purpose in doing so was to examine specific hypotheses about the character of stress and inflammation and their possible correlation. Of particular interest was the investigation of how mesenteric arterial branches in Sprague-Dawley rats were affected by the onset of hypertension.

Conclusions from Visual and Statistical Comparisons

Based upon the results and discussions in Chapter 4, the following research conclusions are drawn:

1. Characteristics such as branch angle, curvature and wall thickness are highly varied in the mesenteric arteries. These variations can be seen within a specific model as well as between models. While these variations make analysis and comparisons more challenging, they also emphasize the value of a histology-based approach.

2. For all hypertensive cases, wall thickness is positively correlated with branch proximity. By contrast, wall thickness is negatively correlated with branch proximity for both normotensive cases. This suggests the adaptive changes associated with the onset of hypertension may preferentially or uniquely affect the transition region of arterial branches.
3. The pattern of inflammation, as measured by monocyte/macrophage cell density, is highly concentrated near the branch for all hypertensive cases. The pattern is less clear for the normotensive cases, with one of the two branches exhibiting higher cell density measurements *away* from the branch center.
4. The magnitude of cell density, von Mises stress, and wall tension are all considerably lower for the normotensive cases. This is not surprising and readily seen by comparing the ranges and average values of various measurements. Most of the statistical comparisons are based on the relative magnitudes within a given geometry, although Appendix B provides same scale plots of all samples, grouped by branch characteristic.
5. Interestingly, wall thickness was negatively correlated to cell density for most cases. It was thought that the pattern of wall thickening might be evident by examining the net wall thickness, but the data suggests an opposite trend with cell density. Increased inflammation in the adventitia adjacent to locations where the media is comparatively thin is consistent with an adaptive response to elevated intramural stress.
6. Among the mechanical characteristics, both maximal wall tension and von Mises stresses were generally elevated in proximity to the branch center. Four

of the five hypertensive branches and one of two normotensive branches exhibited this pattern. The pattern corresponds to what was seen for cell density and suggests there might be a direct correspondence between mechanical loads and cell density.

7. The direct comparisons of von Mises stress with cell density did not indicate a consistent pattern. Branch H7D presented an unusual geometry and unusual challenges in the alignment and reconstruction process. This particular branch indicates a pattern where both cell density and stress are high in proximity to the branch, but the two branch characteristics are not colocalized as reflected by the direct visual and statistical comparisons.
8. The distribution of maximal wall tension was visually and statistically similar to the distribution of cell density. Four of the five hypertensive cases showed positive visual correspondence. Three of the five hypertensive cases exhibited a positive statistical correlation, with a fourth case (branch H7B) not exhibiting a statistically significant trend. A closer examination of branch H7B revealed that the peaks in wall tension and cell density were coincident with a tertiary branch. By contrast, the two normotensive branches indicated a negative correlation between wall tension and cell density.
9. Von Mises stress was negatively correlated with wall thickness for six of seven models while wall tension was strongly positively correlated to wall thickness for six of seven branches (including all five hypertensive cases). One might expect the stress distribution to be normalized due to variations in wall thickness under homeostatic conditions. However it is not reasonable to

assume that any of the hypertensive branches are in homeostasis. The presence of monocytes/macrophages in larger numbers at branch points suggests the branches are in the process of remodeling to accommodate the new mechanical environment.

10. Wall thickness tended to be high where a constant thickness model would have otherwise indicated large intramural stresses. This suggests that the mechanical environment may locally control the adaptive response within branches. But because wall thickness is related to both stress and inflammation, it is difficult to decouple the stress as a stimulus from inflammation as a response. The onset of hypertension is probably accompanied by an adaptive response, reducing the strength of correlations between stress and inflammation.

There are several possible explanations for the lack of a stronger positive correlation between intramural stress and inflammation:

1. The hypothesized stimulus and response are measured at the same time. It seems reasonable that the peak stimulus would in reality precede the peak response.
2. Because the experiments represent a snapshot, it is not possible to separate *changes* in stress and inflammation from the levels present before hypertension was induced.
3. If medial thickening and deposition of adventitia occur as part of the adaptive response there is no way to quantify these changes either. Such adaptive changes are expected and could affect the stress distribution.

4. Medial thickening reduces intramural stress but it is also indicative of an inflammatory response. Part of the problem is that medial thickening produced by smooth muscle cell hypertrophy does not produce a commensurate increase in the rigidity of the vessel wall. A finite element model accounting for local differences in material properties could address this problem.
5. Inflammation does not appear to affect all arteries and branches equally, so a lack of a positive trend in one branch may not be indicative of the pattern throughout the mesentery of an animal. Increasing the number of branches studied would help address such variability.
6. The inability to completely decouple potential stimuli is an inherent problem with animal studies. Elevated intramural stress is only one stimulus of inflammatory changes and other factors that were not studied may have influenced the pattern of inflammation. For example, endothelial dysfunction caused by fluid shear stress may play an important role even during the onset of hypertension.
7. Inflammation may be stimulated by some intramural stress quantity not considered. For example stress gradients through the wall or in the plane of the wall may be important. Stress gradients are a higher order phenomenon, which may be a more sensitive indicator of mechanical stimulus. As discussed, this sensitivity presents a problem since it makes a stress gradient more sensitive to local geometric changes and modeling assumptions.

Several of the items listed above might not completely mask a correlation between stress and inflammation, but could reduce the strength of the correlation. Some of the items represent limitations in this research effort that might be addressed by future studies or methodology enhancements.

Recommendations for Future Work

The role of fluid shear stress on the endothelium has not been addressed in this research. Studies have demonstrated that changes in fluid shear stress can alter endothelial cell function and can produce adaptive and maladaptive changes in vascular tissue (Ku, Giddens et al. 1985; Chappell, Varner et al. 1998; Cai and Harrison 2000). Therefore, endothelial dysfunction may be a critical element of an inflammatory response, even during the onset of hypertension. One possible avenue of further study would be to analyze the fluid mechanical environment of these arteries. The correspondence of inflammation with relevant fluid mechanical properties could be compared to the already documented pattern of inflammation for possible correlations. In addition the fluid and solid mechanical characteristics might be combined to determine if some synergy is necessary to produce an inflammatory response.

Variability in geometry, in the distribution of stress, and in the pattern of inflammation made it difficult to compare results from branch-to-branch. One solution would be to increase the sample size so outliers could be more readily identified. Another approach would be to consider an alternative to mesenteric branches. For example, future studies might focus on the carotid bifurcation and produce less sample-to-sample variability.

This research did not consider how microstructure affected mechanics, but the coupling of histology with finite element analysis lays the groundwork for others to investigate such matters. Nonhomogeneous models could be created using mixture theory and a histology-based identification of collagen and elastin content and organization. When microstructural modeling techniques have been further developed, it would be a relatively simple matter to use the section alignment, distortion correction, and surface reconstruction techniques to obtain a more physiologically grounded finite element model. The resulting models may help mechanistically link stresses and strains to cellular responses.

For structural analysis, the vessel was truncated at the external elastic lamina; hence the adventitia was not included in the finite element models. In a mechanical sense, the stiffness of the adventitia was included, since the model was benchmarked against pressure-diameter data from intact vessels. Incorporating the adventitia into the model presents difficulties, since the adventitia is irregular and its mechanical function is not well understood. Furthermore, the role and organization of adventitia near a branch point may be very different than elsewhere. The lack of data concerning the structure and function of the adventitia at branches can raise as many questions as it answers.

Clearly, the adventitia is a focal point for inflammatory changes in mesenteric arteries, so there is a great motivation to understand its mechanical role during hypertension. In a related research project, the sections used in this investigation are being re-stained with Trichrome stain to better evaluate the distribution and character of the adventitia.

Another interesting avenue for future studies is how angiogenesis may be affected by intramural stresses and inflammation. Researchers have found that intramural stresses appear to influence the development of collateral arterioles (Price, Less et al. 2002). During the course of this research, anecdotal evidence suggested that high intramural stress and high inflammation might be associated with angiogenesis. For example, branch H7B has a tertiary branch that corresponds to the peak in monocyte/macrophage density. Based on curvature considerations, this location would produce high stresses even in the absence of the tertiary branch. A more rigorous evaluation requires the use of immunological techniques that quantify cellular functions such as the expression of vascular endothelial growth factors.

Most of the recommendations for future work are natural extensions of this research and help underscore the value of the methods that were developed. It is hoped that this research will provide a framework for future studies, including additional exploration of these results, greater insight into the function of the adventitia during the onset of hypertension, and an investigation into the role of fluid shear stress in the inflammatory responses.

Appendix A:
Visualizations Grouped by Branch

The following visualizations are color-coded maps of cell density, wall thickness, maximal wall tension, and von Mises stress for all branches. The color map is scaled differently for each case to capture the full range of the data. The results are grouped by branch so comparisons can be more readily made between branch characteristics for a given branch.

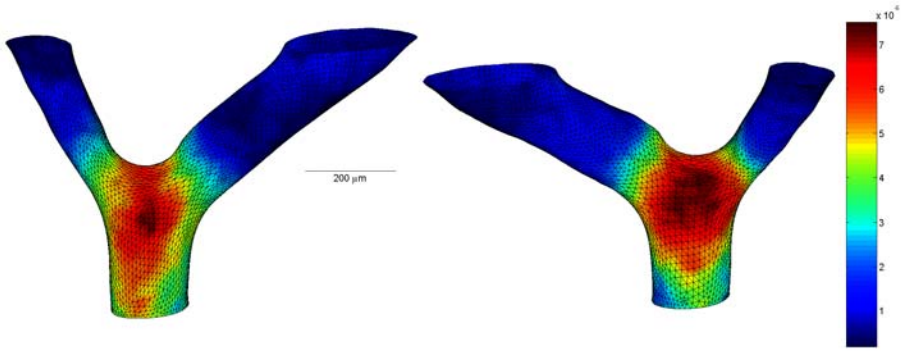

Figure A-1: Monocyte/macrophage cell density (cells/µm^3) for branch H7A.

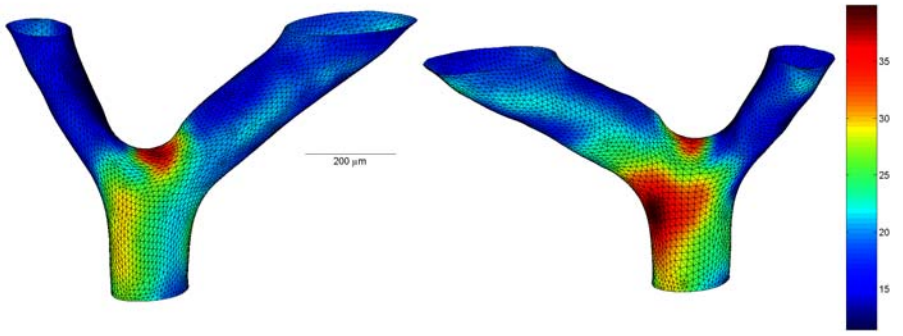

Figure A-2: Wall thickness in µm for branch H7A.

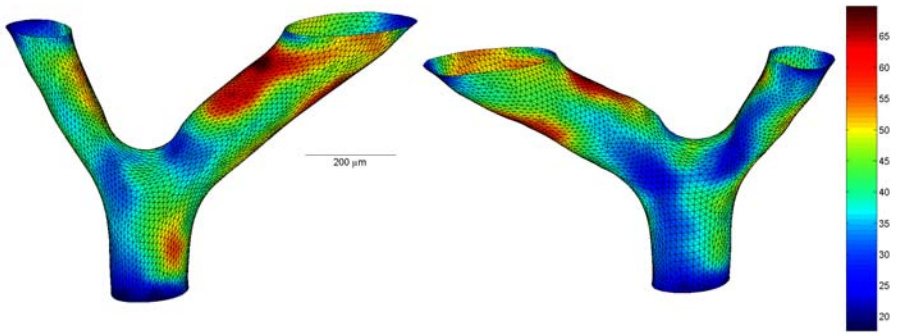

Figure A-3: Von Mises stress distribution in kPa for branch H7A.

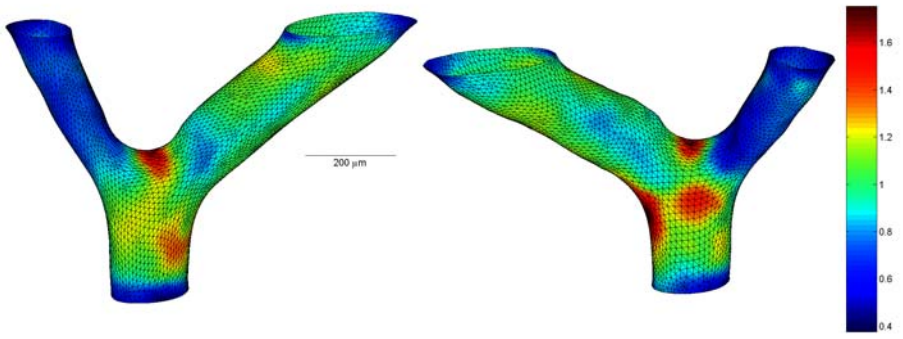

Figure A-4: Maximal wall tension in N/m for branch H7A.

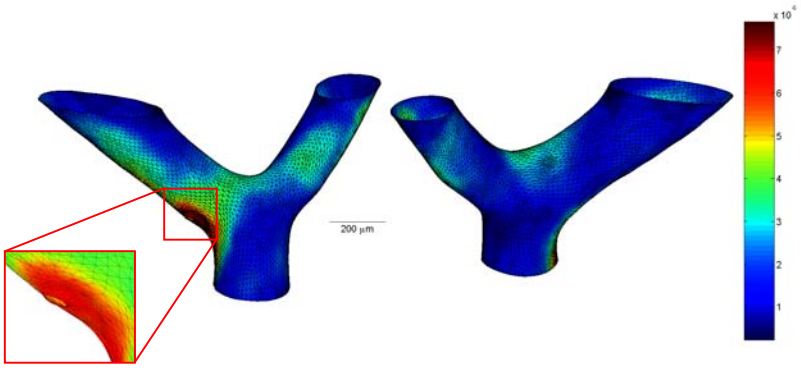

Figure A-5: Monocyte/macrophage cell density (cells/µm^3) for branchH7B.

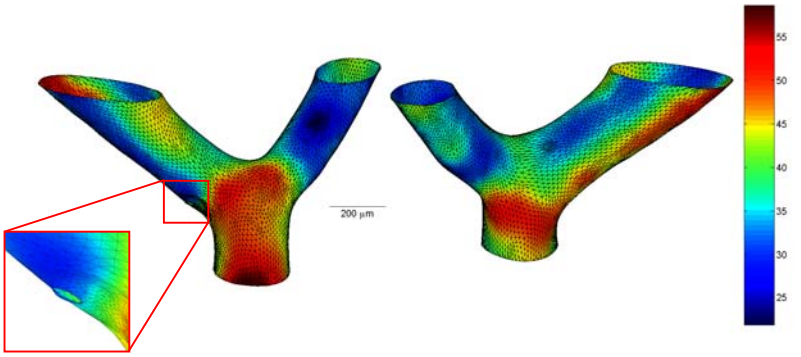

Figure A-6: Wall thickness in µm for branch H7B.

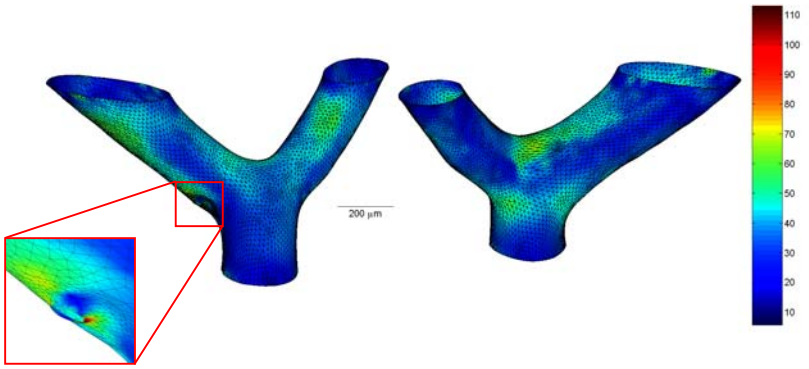

Figure A-7: Von Mises stress distribution in kPa for branch H7B.

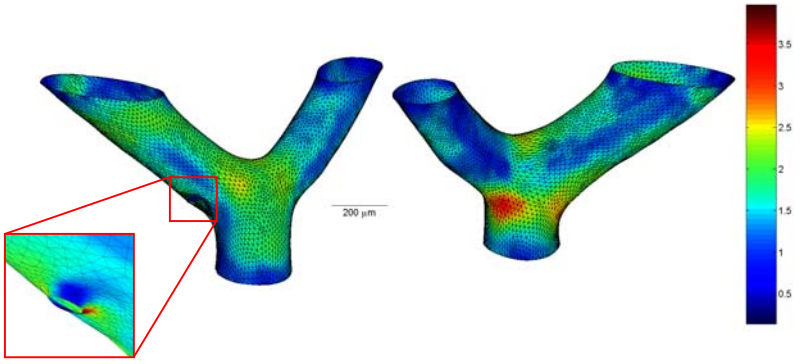

Figure A-8: Maximal wall tension in N/m for branch H7B.

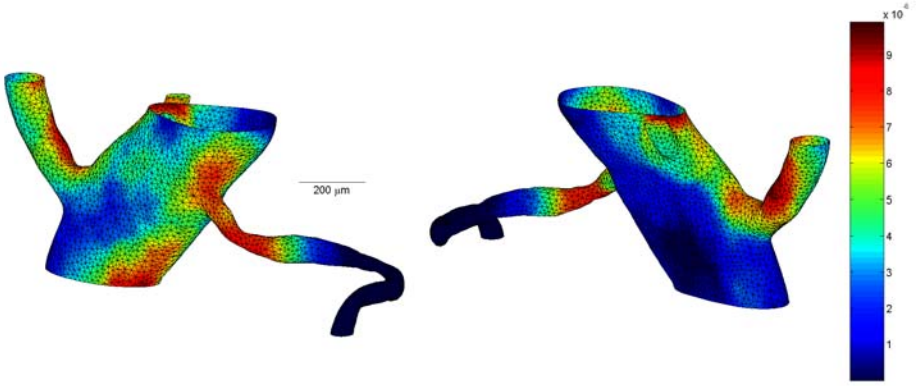

Figure A-9: Monocyte/macrophage cell density (cells/µm^3) for branch H7C.

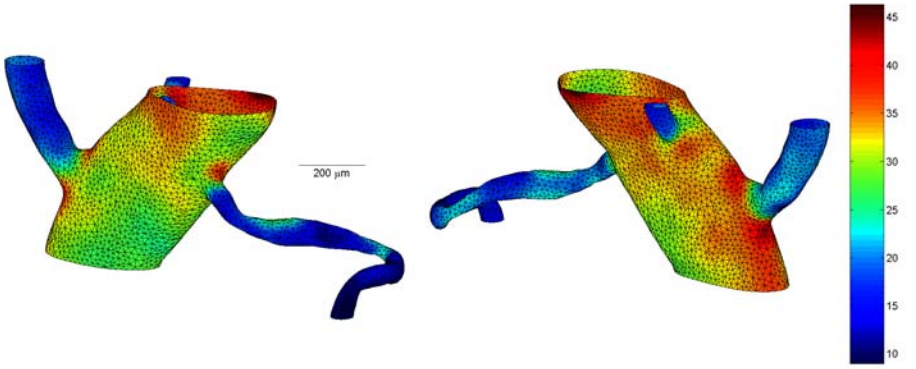

Figure A-10: Wall thickness in µm for branch H7C.

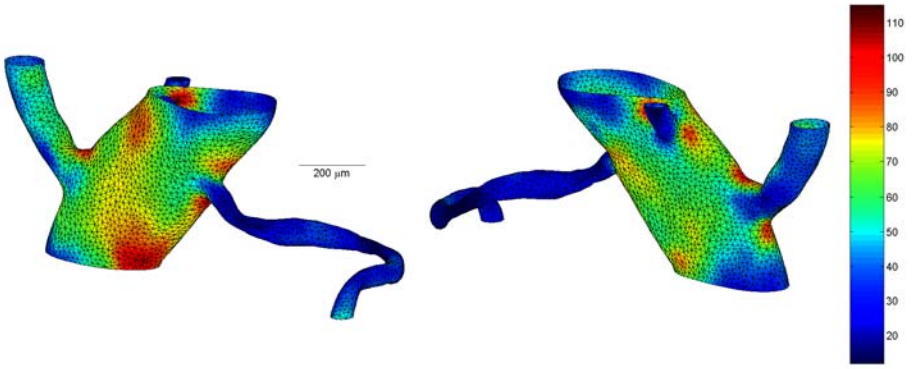

Figure A-11: Von Mises stress distribution in kPa for branch H7C.

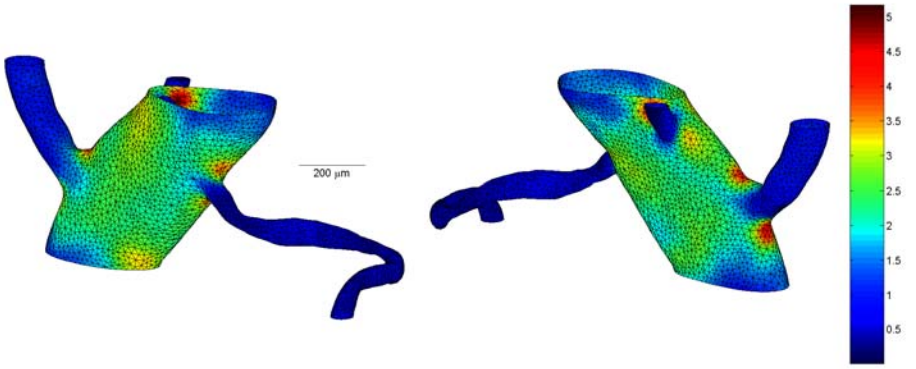

Figure A-12: Maximal wall tension in N/m for branch H7C.

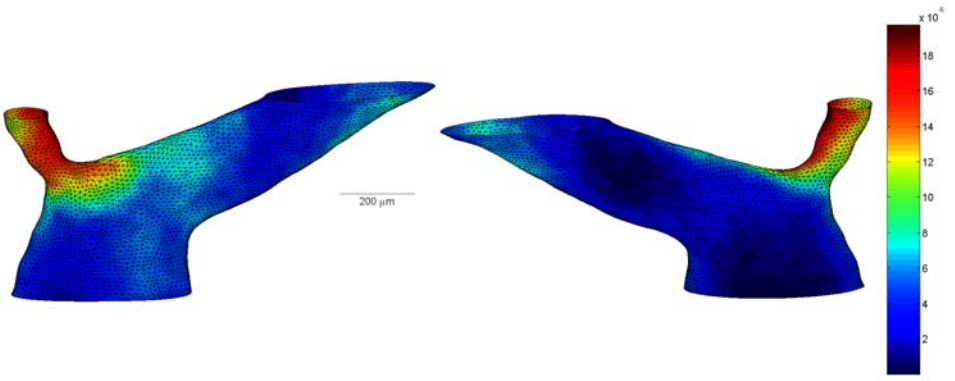

Figure A-13: Monocyte/macrophage cell density (cells/µm^3) for branch H7D.

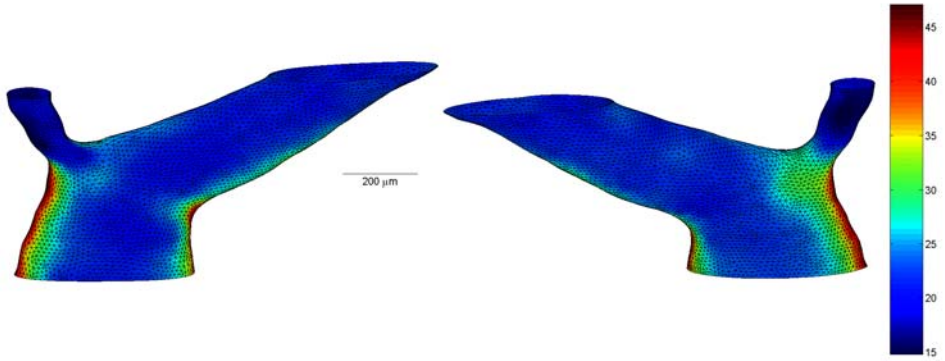

Figure A-14: Wall thickness in µm for branch H7D.

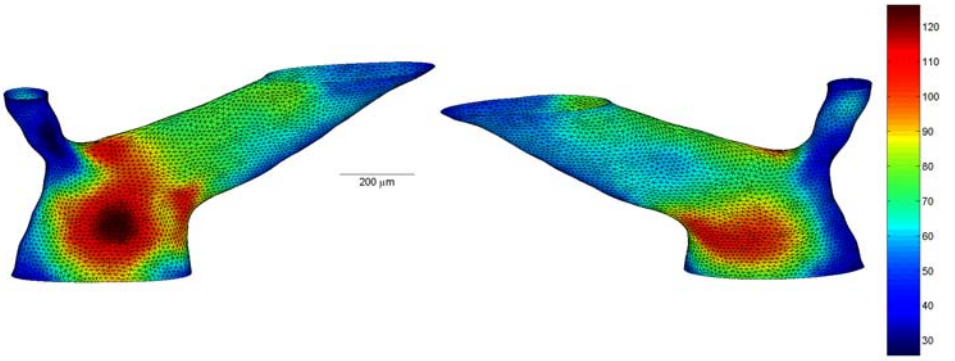

Figure A-15: Von Mises stress distribution in kPa for branch H7D.

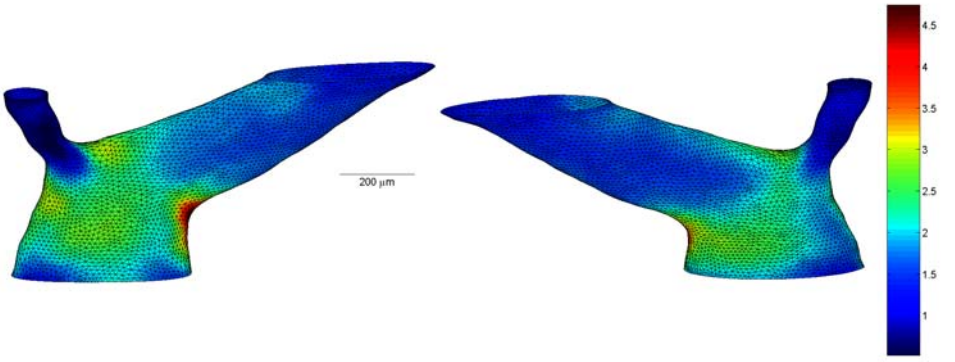

Figure A-16: Maximal wall tension in N/m for branch H7D.

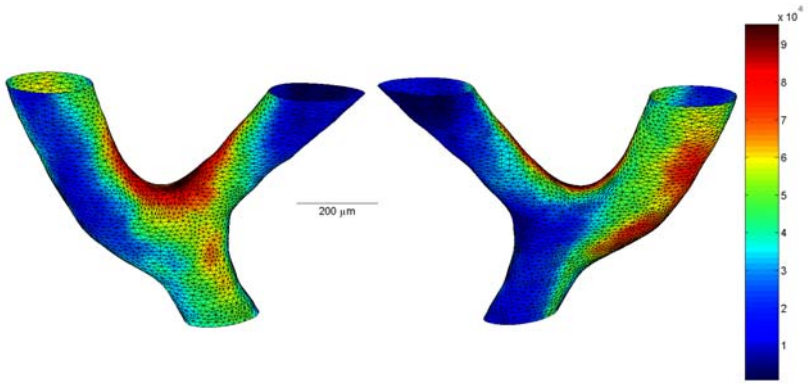

Figure A-17: Monocyte/macrophage cell density (cells/µm^3) for branch H21A.

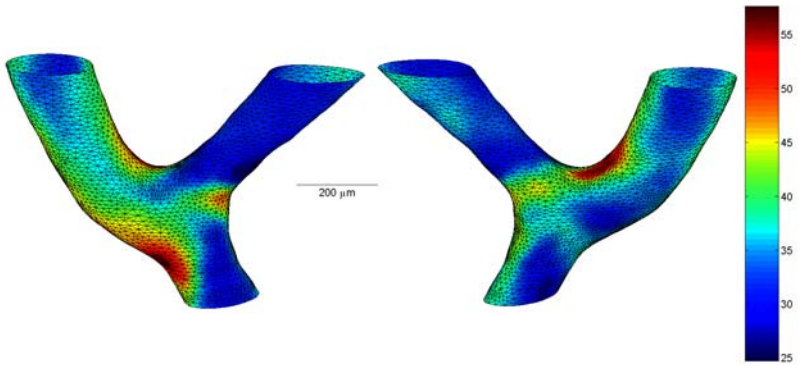

Figure A-18: Wall thickness in µm for branch H21A.

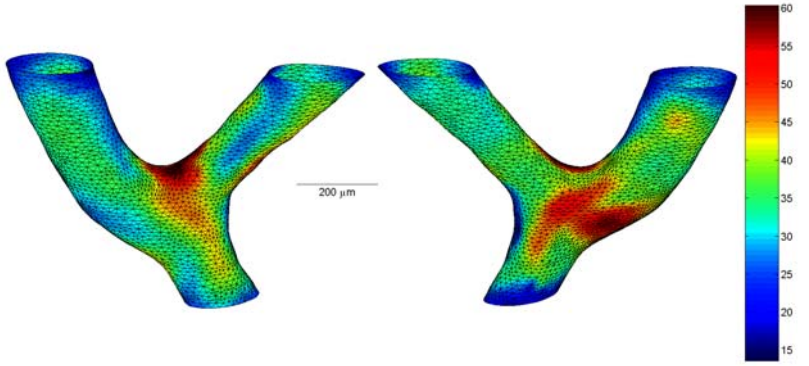

Figure A-19: Von Mises stress distribution in kPa for branch H21A.

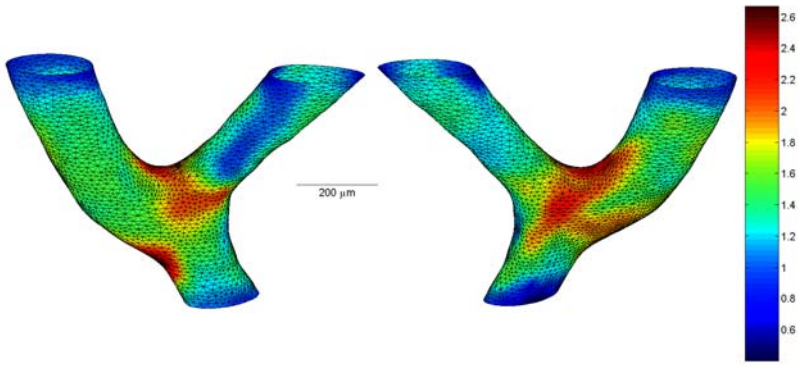

Figure A-20: Maximal wall tension in N/m for branch H21A.

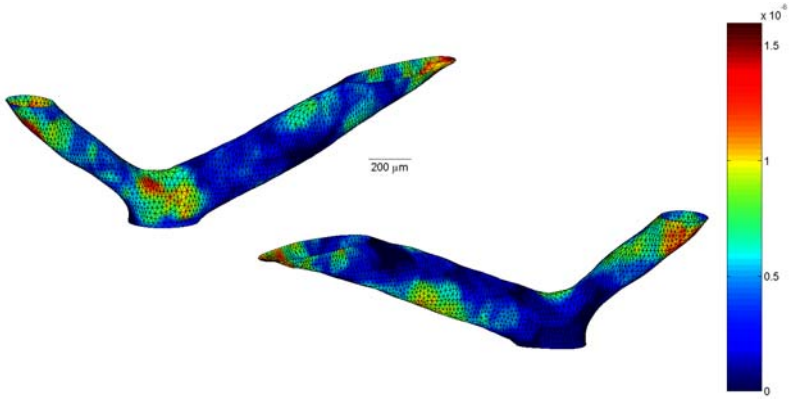

Figure A-21: Monocyte/macrophage cell density (cells/µm^3) for branch NA.

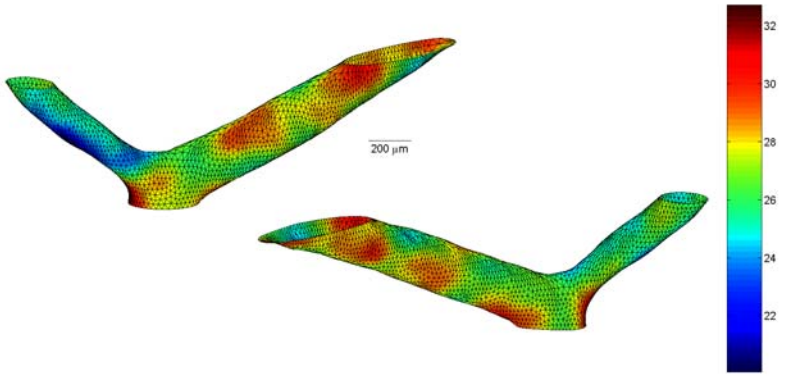

Figure A-22: Wall thickness in µm for branch NA.

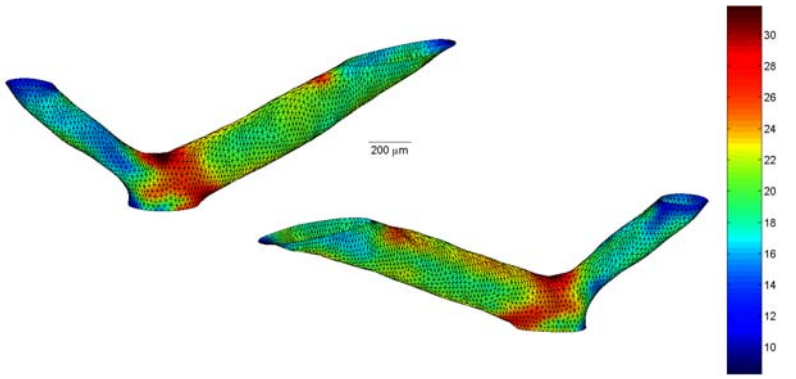

Figure A-23: Von Mises stress distribution in kPa for NA.

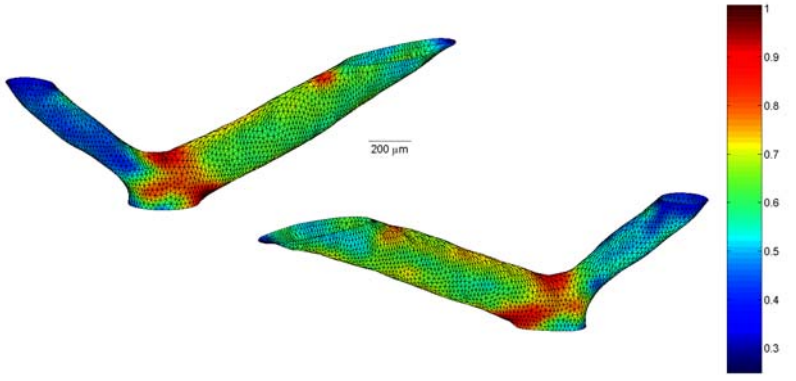

Figure A-24: Maximal wall tension in N/m for NA.

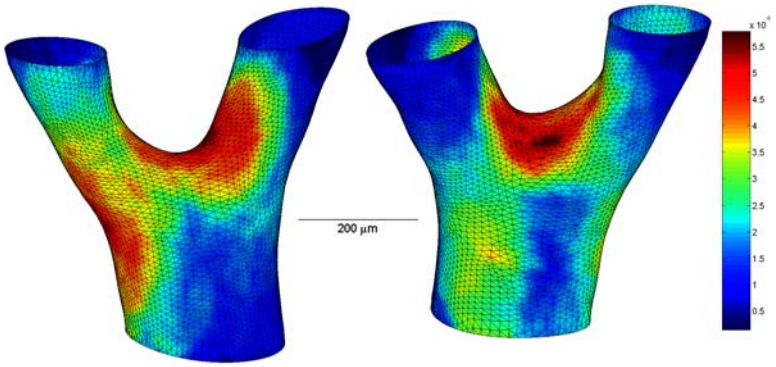

Figure A-25: Monocyte/macrophage cell density (cells/µm^3) for branch NB.

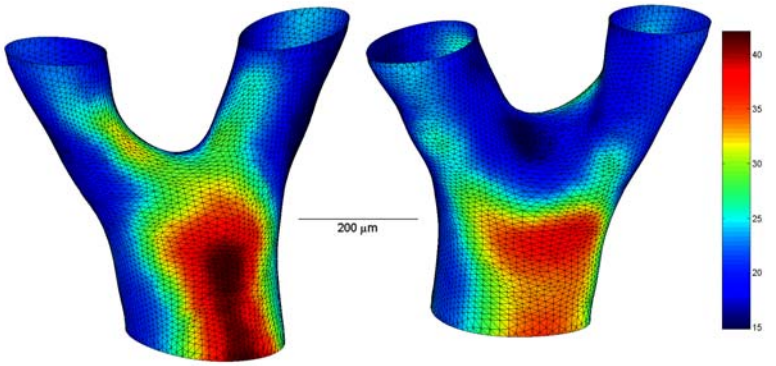

Figure A-26: Wall thickness in µm for branch NB.

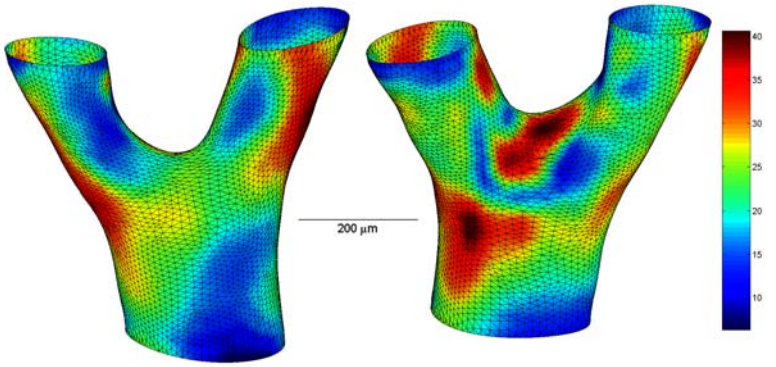

Figure A-27: Von Mises stress distribution in kPa for NB.

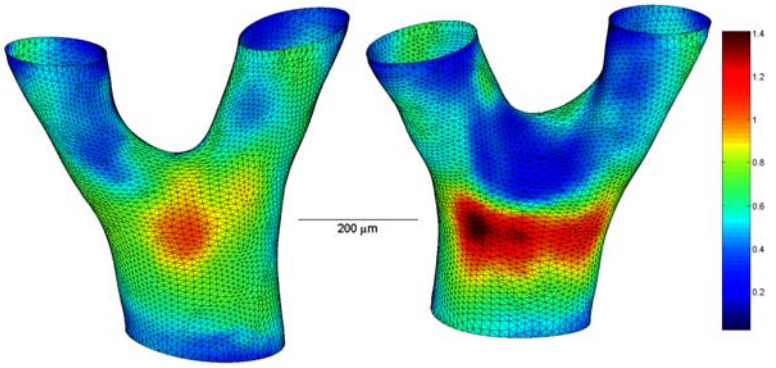

Figure A-28: Maximal wall tension in N/m for NB.

Appendix B:
Visualizations Grouped by Characteristic

The following visualizations are a second set of color-coded maps of cell density, wall thickness, maximal wall tension, and von Mises stress for all branches. The color maps share the same scale for each characteristic. The results are grouped by characteristic, so comparisons can be more readily made between branches for a given characteristic.

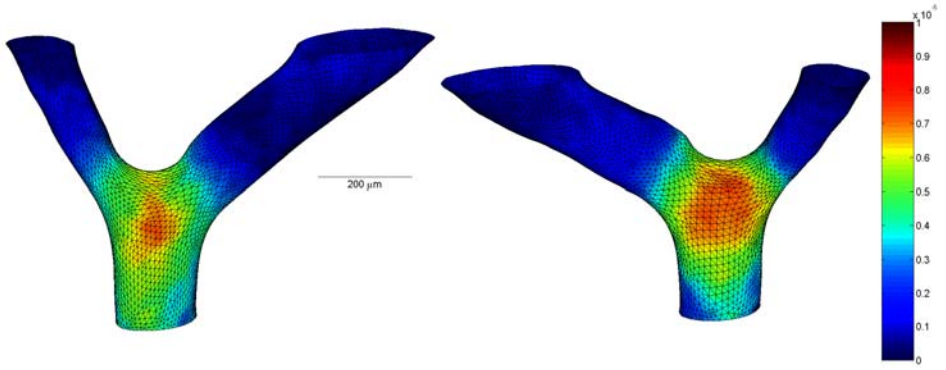

Figure B-29: Monocyte/macrophage cell density (cells/µm^3) for branch H7A.

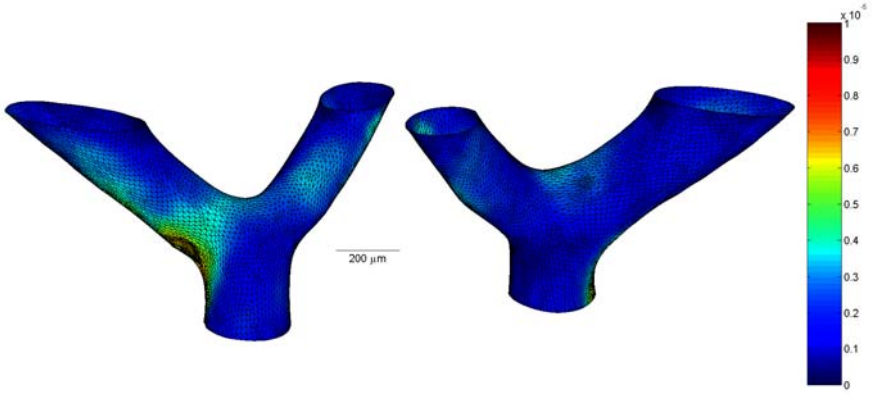

Figure B-30: Monocyte/macrophage cell density (cells/µm^3) for branch H7B.

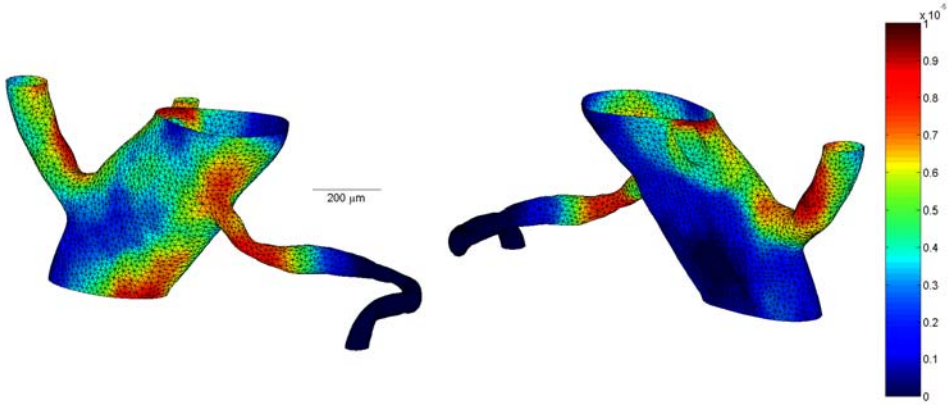

Figure B-31: Monocyte/macrophage cell density (cells/µm^3) for branch H7C.

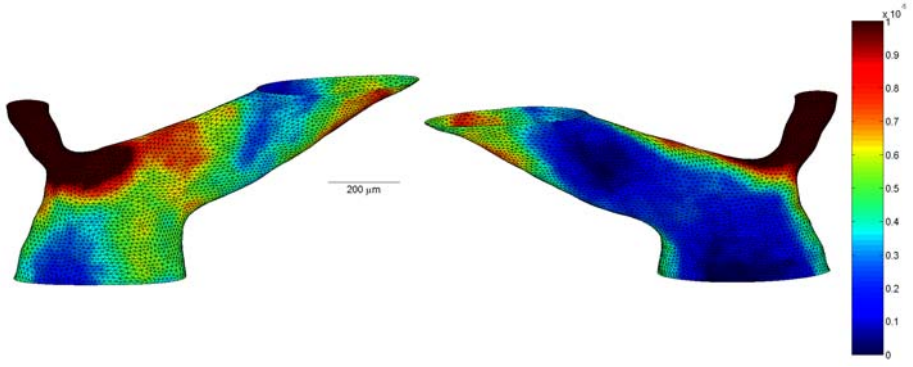

Figure B-32: Monocyte/macrophage cell density (cells/µm^3) for branch H7D.

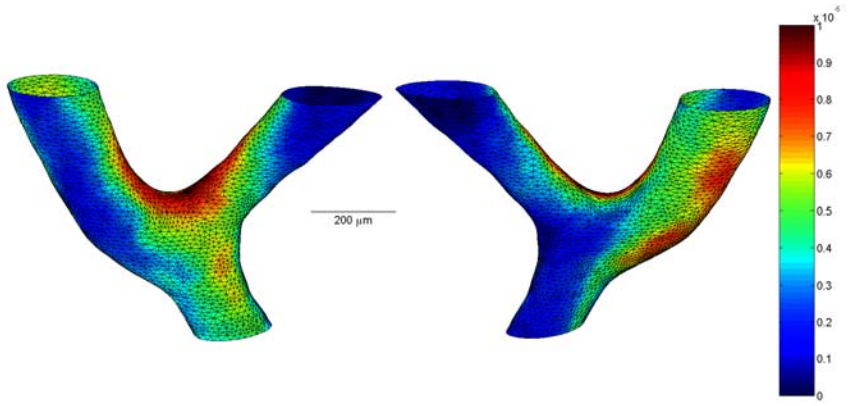

Figure B-33: Monocyte/macrophage cell density (cells/µm^3) for branch H21A.

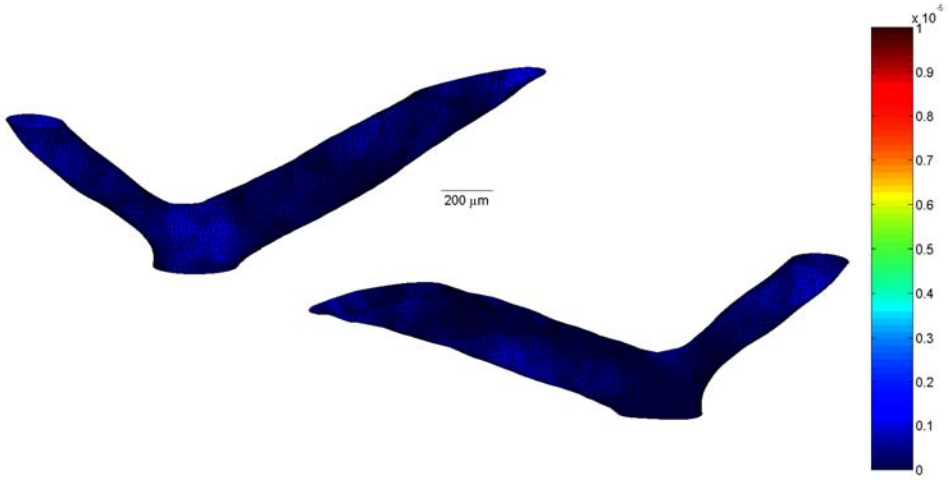

Figure B-34: Monocyte/macrophage cell density (cells/µm^3) for branch NA.

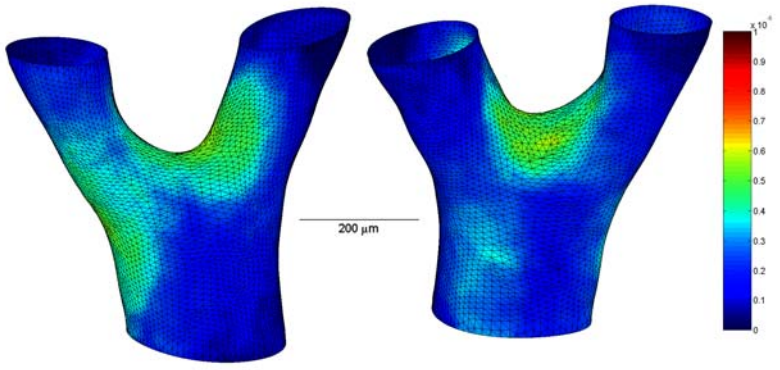

Figure B-35: Monocyte/macrophage cell density (cells/µm^3) for branch NB.

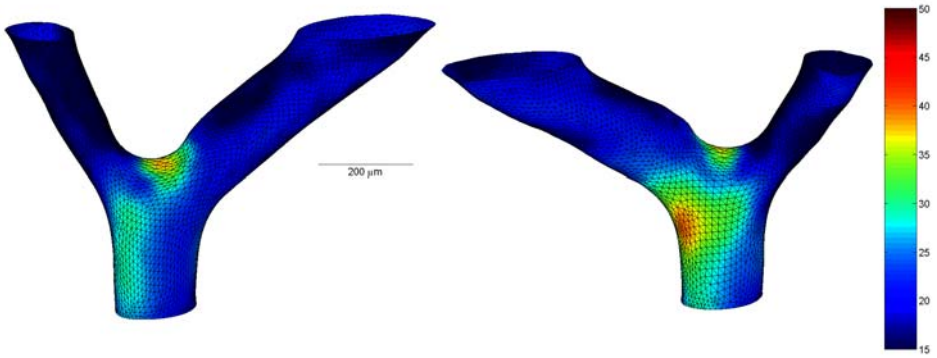

Figure B-36: Wall thickness in µm for branch H7A.

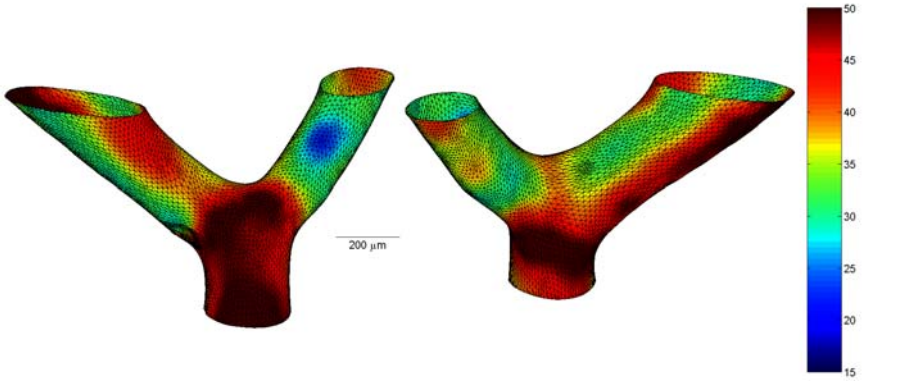

Figure B-37: Wall thickness in µm for branch H7B.

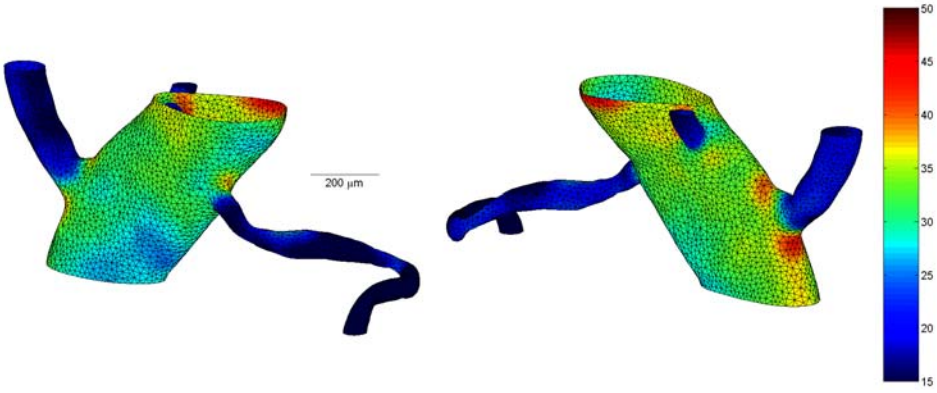

Figure B-38: Wall thickness in µm for branch H7C.

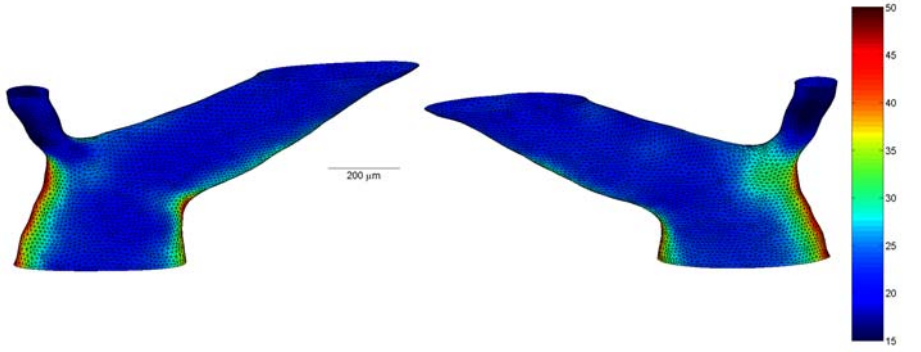

Figure B-39: Wall thickness in µm for branch H7D.

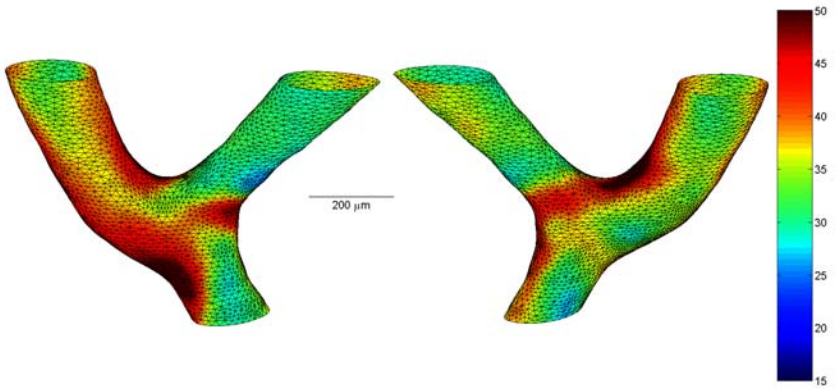

Figure B-40: Wall thickness in µm for branch H21A.

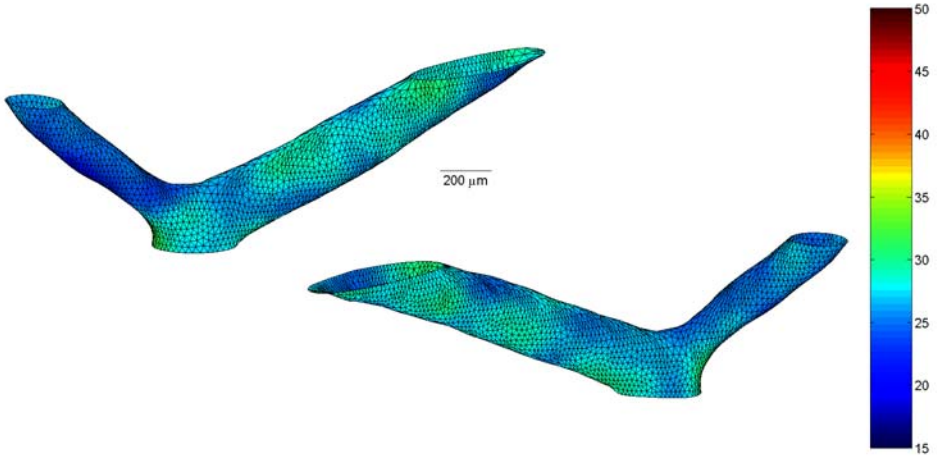

Figure B-41: Wall thickness in µm for branch NA.

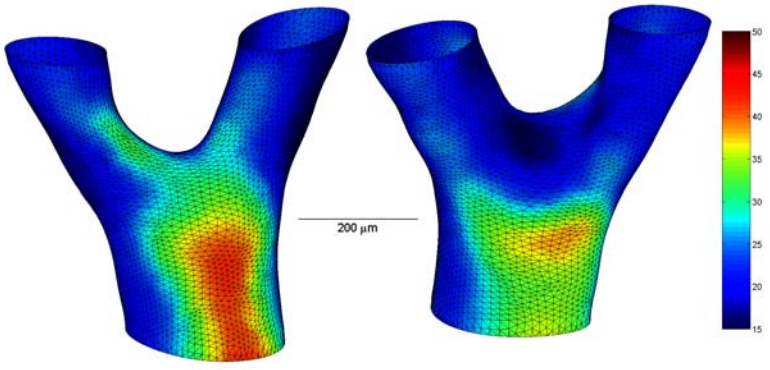

Figure B-42: Wall thickness in µm for branch NB.

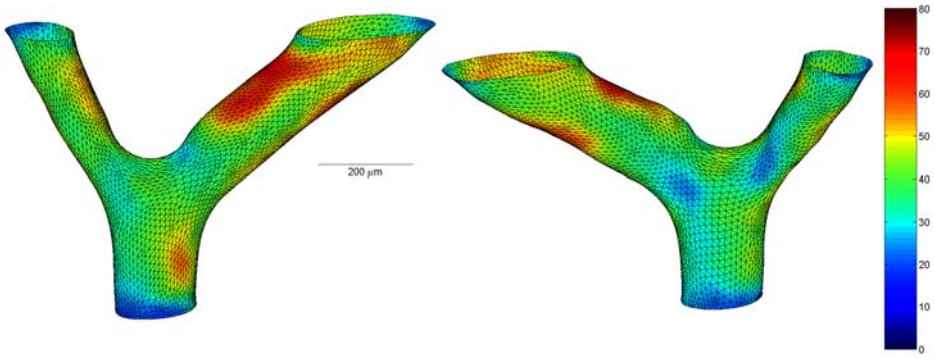

Figure B-43: Von Mises stress distribution in kPa for branch H7A.

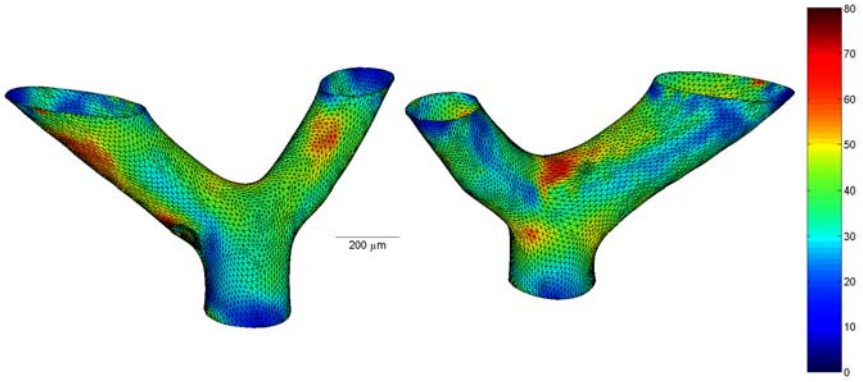

Figure B-44: Von Mises stress distribution in kPa for branch H7B.

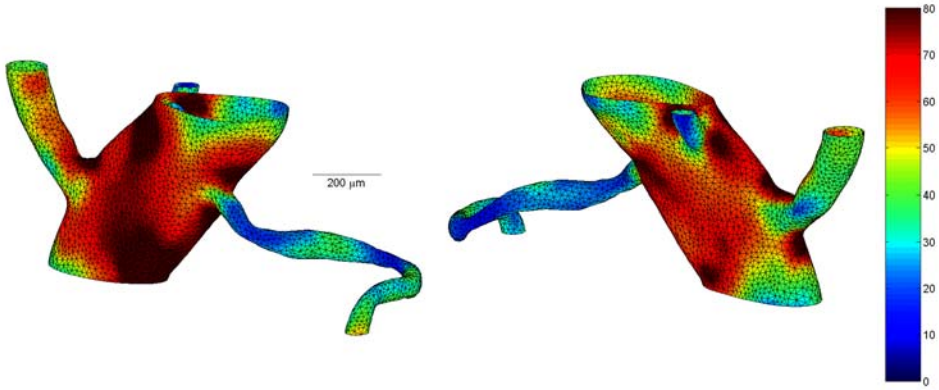

Figure B-45: Von Mises stress distribution in kPa for branch H7C.

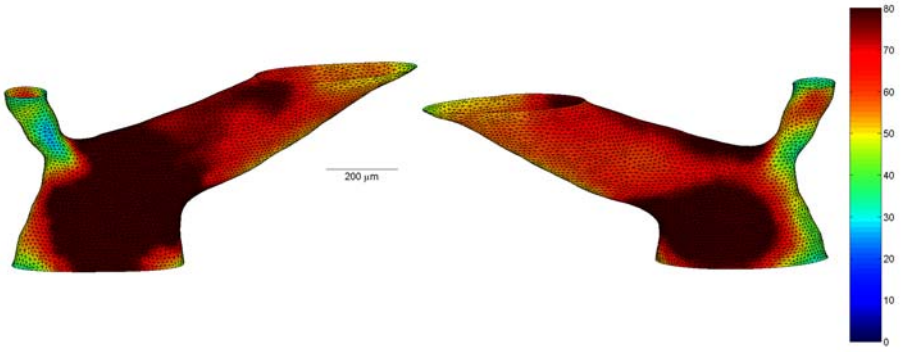

Figure B-46: Von Mises stress distribution in kPa for branch H7D.

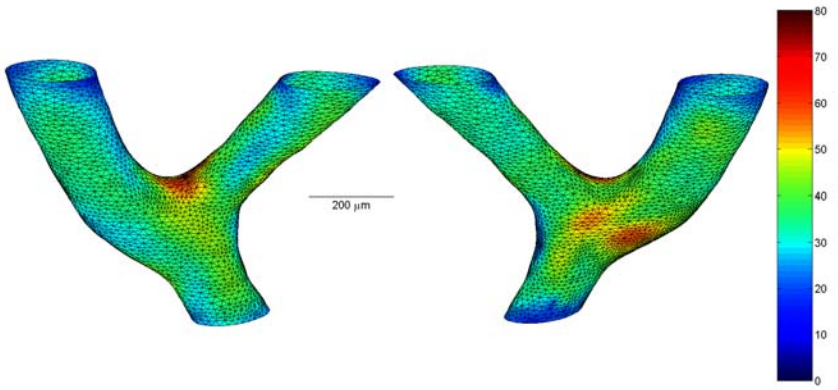

Figure B-47: Von Mises stress distribution in kPa for branch H21A.

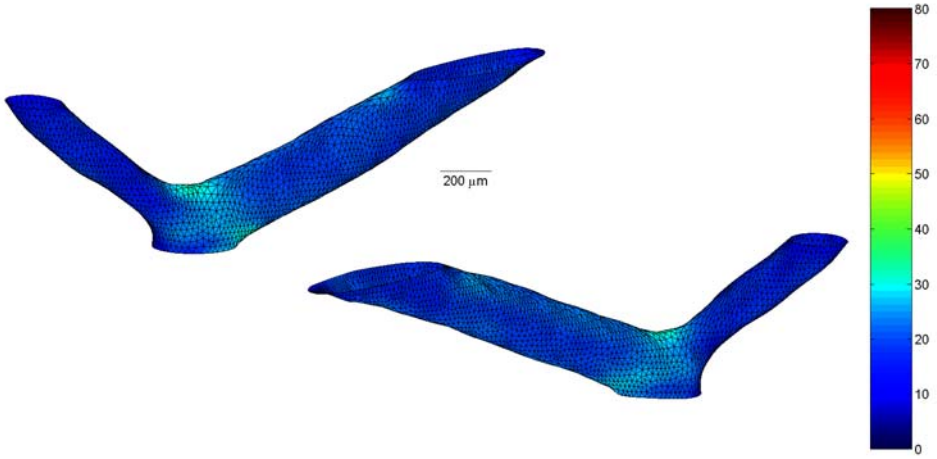

Figure B-48: Von Mises stress distribution in kPa for branch NA.

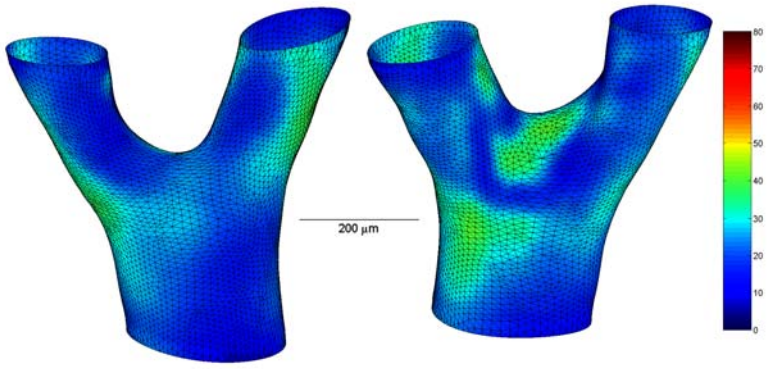

Figure B-49: Von Mises stress distribution in kPa for branch NB.

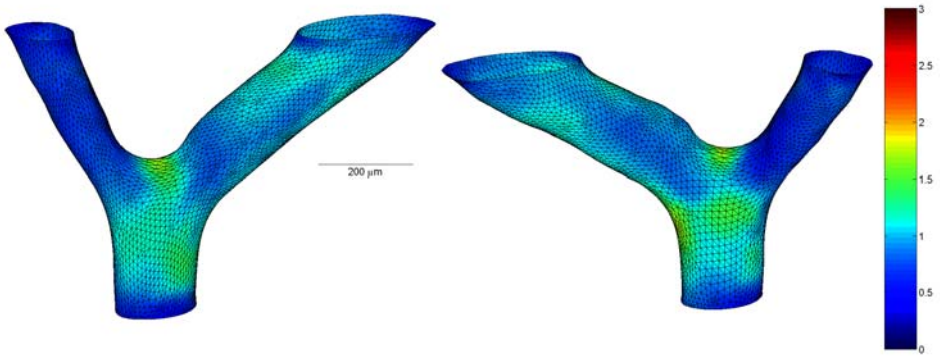

Figure B-50: Maximal wall tension in N/m for H7A.

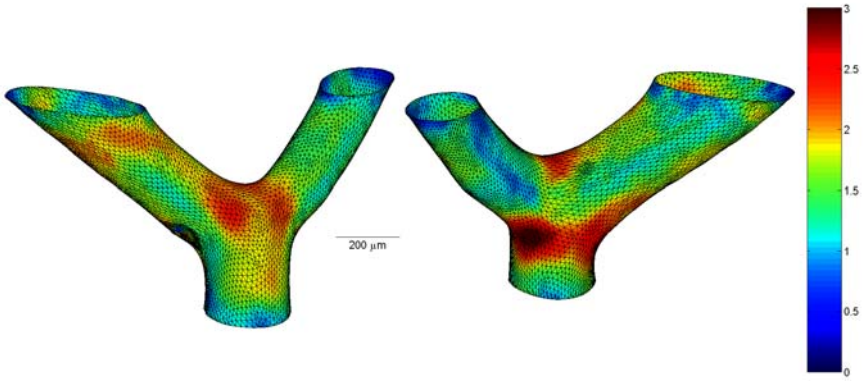

Figure B-51: Maximal wall tension in N/m for H7B.

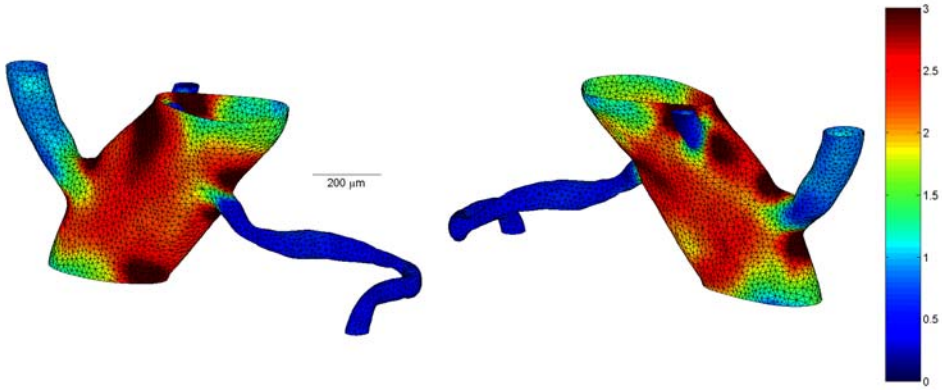

Figure B-52: Maximal wall tension in N/m for H7C.

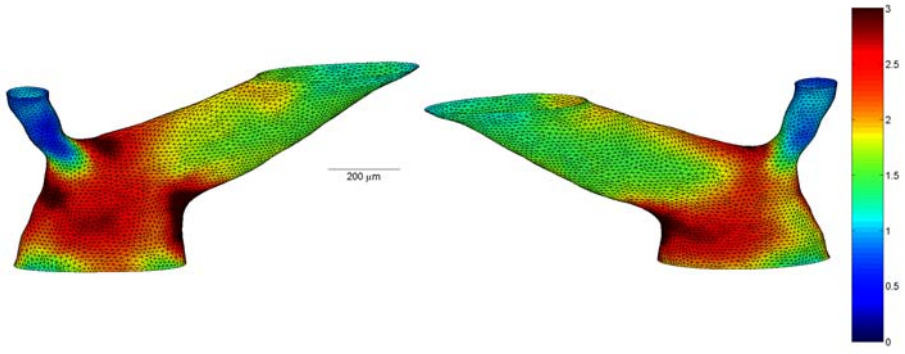

Figure B-53: Maximal wall tension in N/m for H7D.

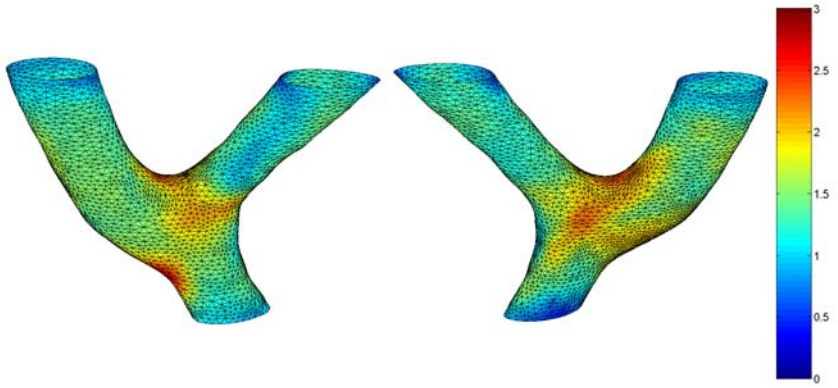

Figure B-54: Maximal wall tension in N/m for H21A.

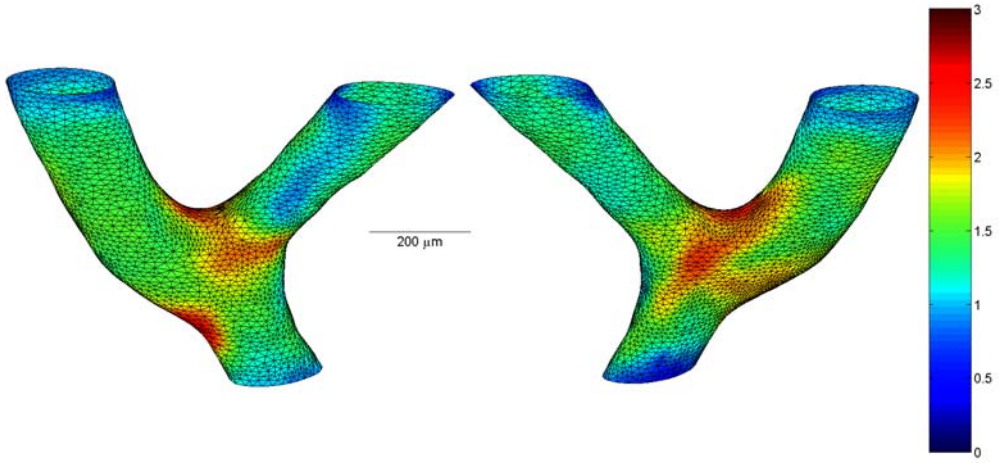

Figure B-55: Maximal wall tension in N/m for NA.

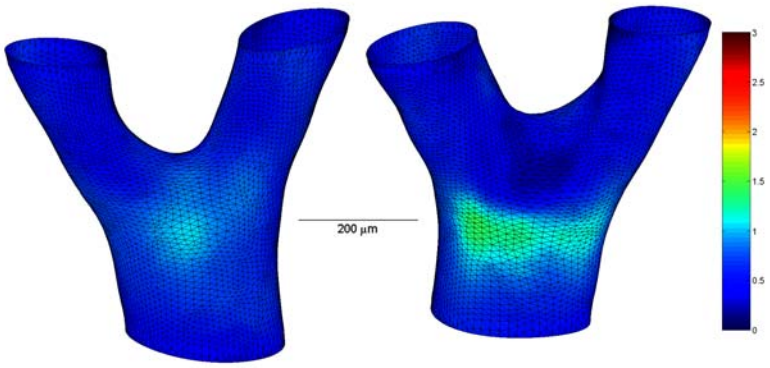

Figure B-56: Maximal wall tension in N/m for NB.

Appendix C:
Summary Tables of Animal Data

The initial focus was on a more extensive study of wild type mice involving a larger number of animals and a wider variety of conditions. Each sample consisted of about 200 serial sections, the samples were only embedded and sections after preliminary work indicated that a radio-isotopic *in situ* hybridization technique could be employed. The ISH results proved to be highly variable from section to section with significant background signal. The use of Polysciences ImmunoBed Kit proved problematic, with Polysciences revising their recommendations for this glycol methacrylate resin. Because the ISH protocol required a 6-8 week window between the initiation of studies and the first results, most of the slides were started in this process before the problems were identified.

The following tables summarize data for the Sprague-Dawley rat studies. Male Harlan Sprague-Dawley rats were used, the order specification was for rats between 239 grams and 250 grams. Typical blood pressure were 115-120 mmHg before hypertension and 150-160 mmHg after 7 days of Angiotensin II induced hypertension.

Table C-1: Raw data checks for coincident cells.

Coincident Cells - Raw Data Checks						
Branch Name	**Sample Name**	**Coincident**	**Aligned within 10 deg**	**Duplicate Cells Aligned**	**Three Cells Stacked**	**Total Number of Cells**
NA	R2 - Normo	0	0	0	0	222
NB	R3 - Normo	0	1	0	0	451
H7C	R1 - 7d	2	15	0	0	904
H7D	R4 - 7d	0	11	0	0	1091
H7A	R5 - 7d	0	4	1	0	492
H7B	R8 - 7d	0	7	0	0	1053
H21A	R10 - 21d	0	11	0	1	1124

Coincident: Multiple points represent the same cell
Aligned (10 deg): Two points in consecutive planes are within 10 degrees
Duplicate Aligned: Two points in two consecutive planes are within 10 degrees
Three Stacked: Three points in three consecutive planes are within 10 degrees

Table C-1 shows a series of raw data checks for coincident cells. The first check is for coincident cells. This involves checking to be sure that cells are counted twice. The earliest version of the program did not include any safeguard against double-clicking on cells and marking one cell multiple times. This problem was corrected as the program was developed and a check was employed on all the raw data. The check was performed after all the data sets where aligned, so that information could be also gathered about cell proximity in three-dimensions. Over 5300 monocytes and macrophages were identified, but only two were coincident and less than 0.1 percent were stacked by the criteria described below. The layers were 20 or 25 micrometers apart, so it is unlikely that a monocyte or macrophage nuclei would be counted twice on different layers.

Table C-2: Total cell density (cells/μm^3) for each branch.

Total Cell Density Measurements

Branch Name	Sample Name	Gross Volumetric Density	Average Density at Surface	Average Density on Cells
NA	R2 - Normo	1.50E-07	4.38E-07	4.83E-07
NB	R3 - Normo	6.42E-07	2.34E-06	1.84E-06
H7C	R1 - 7d	1.23E-06	3.32E-06	4.44E-06
H7D	R4 - 7d	1.31E-06	5.08E-06	5.63E-06
H7A	R5 - 7d	4.99E-07	3.40E-06	3.25E-06
H7B	R8 - 7d	7.18E-07	2.24E-06	2.32E-06
H21A	R10 - 21d	1.32E-06	4.02E-06	3.91E-06

Gross Volumetric Density: Cells divided by total volume
Average Density at Surface: Average subvolume value on branch surface
Average Density on Cells: Average subvolume value from all cells

Table C-2 shows three different cell density measures for each branch. The first measure is gross volumetric density that is simply the total number of cells divided by the total volume of the model, including lumen. The second measure is average cell density from the subvolume calculations centered on the lumen surface. The third measure is the average density of cells, from subvolume measurements centered on the cells.

Table C-3: Inlet/Outlet Cross-Sectional Dimensions (μm).

Inlet/Outlet Cross Sectional Dimensions

		in1					out1					out2					out3					out4
Sample Name	**Branch ID**	dmax	dmin	d_avg	t_avg	R/t	dmax	dmin	d_avg	t_avg	R/t	dmax	dmin	d_avg	t_avg	R/t	dmax	dmin	d_avg	t_avg	R/t	dmax
R2 - Normo	NA	325	185	255.0	27.0	4.72	234	212	223.0	26.4	4.22	182	175	178.5	28.4	3.14						
R3 - Normo	NB	362	250	306.0	26.2	5.84	308	158	233.0	18.2	6.40	208	168	188.0	18.6	5.05						
R1 - 7d	H7C	376	177	276.5	32.0	4.32	389	201	295.0	36.9	4.00	114	111	112.5	20.5	2.74	72	54	63.0	14.6	2.16	67
R4 - 7d	H7D	446	186	316.0	30.2	5.23	348	178	263.0	24.6	5.35	116	108	112.0	18.2	3.08						
R5 - 7d	H7A	168	134	151.0	24.9	3.03	138	133	135.5	17.4	3.89	110	91	100.5	14.5	3.47						
R8 - 7d	H7B	352	212	282.0	43.3	3.26	270	171	220.5	41.7	2.64	211	163	187.0	37.8	2.47	13.9	12.4	13.2	8.8	1.49	
R10 - 21d	H21A	270	180	225.0	44.8	2.51	220	206	213.0	37.6	2.83	202	186	194.0	36.6	2.65						
R8wbranch	H7B	352	212	282.0	43.3	3.26	270	171	220.5	41.7	2.64	211	163	187.0	37.8	2.47	13.9	12.4	13.2	8.8	0.75	

Table C-3 shows the inlet and outlet cross-sectional dimensions for each sample in the Sprague-Dawley rat series. This data was collected by transversely sectioning the models near the boundaries (away from the branch center) and measuring the cross sections. Note the decrease in radius to thickness ratios with hypertension and with decreasing vessel size. Note also the elliptical cross sectional character of some of the vessels.

Appendix D:
Histological Protocols

Appendix D contains the following protocols:

1. Harvest Procedure
2. Embedding Protocol
3. Modified Haematoxylin and Eosin Staining Protocol
4. Modified Haematoxylin Counterstain Protocol

Harvest Procedure

The rats were euthanized with carbon dioxide and then a centerline incision was made with scissors starting at the lower abdomen and moving through the thorax. The sternum was cut and the rib cage was opened to provide access to the heart. Saline was introduced into the vascular system by placing a needle into the right ventricle of the heart. The saline reservoir was elevated to produce a constant infusion pressure of approximately 80 mmHg. The vena cava was cut and the stopcock was opened so the saline could freely perfuse the vasculature. The perfusion was complete when the liver took on a blanched appearance, indicating blood has been flushed from the organ. This was an important step since the blood can cause clotting that results in incomplete perfusion of the small mesenteric arteries. For a limited number of cases, heparin was injected into the animals to help assure patency of the small arteries. Because there were no apparent differences in the results, this procedure was not continued for all cases.

After saline perfusion was complete Formalin was perfused through the vasculature in the same manner. Initial studies used a 10-minute perfusion, but all of the rats in the final study used a one-hour perfusion. The additional time for pressure fixation helped assure the mesentery was held in a pressure fixed state for subsequent processing.

GMA Embedding of Soft Tissues

Uses Polysciences ImmunoBed Kit, Optimized for Rat Mesentery

1. Harvest tissue from animal source. **Fix** the tissue in a conical tube with 20 x volume of acetone for two nights (48 hours) at 4°C. (Note: The original protocol called for overnight fixation in Formalin followed by transfer to 70% alcohol).

2. **Dehydrate** the tissue using a graded series of alcohol. Perform dehydration at 4ºC on a shaker. Use the following schedule:

1 x 2.0hr	70% alcohol
1 x 2.0hr	80% alcohol
2 x 2.0hr	95% alcohol
1 x 2.0hr	100% alcohol

Processed on automated system with vacuum until this point, then the follow steps are done by hand:

1 x overnight	1:1 100% alcohol:acetone
1 x 2.0hr	100% alcohol
1 x 2.0hr	100% alcohol

The acetone step serves to ensure complete removal of the lipid from the tissue prior to embedding. With mesentery tissue it is possible to view and evaluate whether there is still fat present and the acetone step should be extended. Post dehydration the tissue should appear slightly white.

3. Prepare the **infiltration** solution as described below.

Infiltration Solution:

Immuno-Bed solution A	50ml	25ml
Benzoyl peroxide, plasticized	0.625g	0.3125g

Mix well on a stirrer or shaker for 10-20 minutes.

Infiltration of the tissue is performed at 4ºC on a shaker. Avoid direct light or sources of heat during infiltration. Prepare solution A for the overnight step and again fresh the next morning for the remaining infiltration steps. Use the following schedule:

1 x overnight	1:1 100% alcohol:infiltration solution A
2 x 2hrs	Infiltration solution A (2 fresh changes)

Place the tissue (while in alcohol/infiltration) under vacuum when preparing the fresh infiltration solution.

4. The **embedding** procedure is an exothermic reaction, therefore it is necessary to limit the amount of heat generated in this step. Use fresh infiltration solution for the preparation of the embedding medium. Keep solution A on ice after preparation.

Immuno-Bed solution A	50ml	25ml	10ml
Benzoyl peroxide	0.625g	0.3125g	0.125g

Mix for a minimum of 20 minutes. Degas on ice while assembling jig.

Add Immuno-Bed solution B just before assembling jig/tissue and mold.

Immuno-Bed solution B	2.0ml	1.0ml	0.4ml

5. Begin **polymerization** process by cleaning a mold with 70% then 100% alcohol. Let mold dry completely. Remove tissue and solution A from the vacuum and place on ice. Add respective volume of Immuno-Bed solution B to solution A (see above for volumes). Mix well using a pipette being careful not to introduce bubbles. Return to ice. Quickly add about 1ml of embedding resin to the mold resting in an ice bath. Orientate tissue so that the bulk of the tissue is in the center of the. Remove any bubbles. Add additional resin to fill the mold. If necessary, top off the mold with additional. The resin contracts upon polymerization so ensure there is sufficient volume present. Polymerize in an ice bath or at 4ºC overnight. Polymerization should occur within 3 hours. Usually, the tissue is left overnight to ensure complete polymerization. Polymerization is optimized in anaerobic conditions.

7. Post polymerization, remove the tissue from the mold. Grind cured block to obtain plane surface for mounting. Superglue the cured block to an acrylic base. Let dry for 1 hour. The block is now ready for sectioning with a tungsten carbide blade on the rotary microtome.

Modified Haematoxylin and Eosin Stain for GMA Sections

Reagents & Solutions:

Acid Alcohol (70% alcohol, 0.5% hydrochloric acid)
199 ml 70% Alcohol
1 ml concentrated (12.1 M) HCl

Bluing Reagent (Thermo Shandon Product Number 6769001)

Active Ingredients:	Sodium bicarbonate	0.2%
	Lithium Carbonate	0.04%
	Methanol	37.0%

Aqueous Eosin

Active Ingredients:	Eosin Y	1.0% (10 g / l000 ml)
	Phloxine	0.1% (1 g / l000 ml)

Gill-3 Haematoxylin (Thermo Shandon Product Number 6765009)

Active Ingredients:	Aluminum sulfate	6.0%
	Haematoxylin	0.6%

Protocol used with a GMA resin produced by Polysciences (Immuno-Bed™ Kit, Cat.# 17324). This resin resembles JB-4 medium in tissue infiltrations, embedding, and cutting procedures.

Procedure:

1. Full strength Hematoxylin for 2 minutes.
2. Water rinse for 4 minutes.
3. Acid alcohol for 1 second.

   Note: Actual time is about 3 seconds due to slow dipping rate of autostainer. Use three dips if step done by hand.
4. Water rinse for 2 minutes.
5. Scott's Solution for 30 seconds.
6. Water rinse for 2 minutes.
7. Aqueous Eosin for 3 minutes.
8. Water rinse for 20 seconds.
9. Move to blank container at finish of autostain.
10. Air dry overnight on rack. Alternatively may blot and dry in oven at 37 °C for two hours or until dry. This may take longer if water has beaded on surface of

section. Beads of water can leach eosin out of section and produce uneven results.

11. For GMA sections, good section clarity can be achieved *without* Xylene. Use 1 or 2 drops of an aqueous mounting media on dry sections and let coverslip gradually spread the media. Allow several hours to dry.

Notes:

Use of aqueous Eosin is preferable since mixtures of alcohol and water have a deleterious effect on the glycol methacrylate resin. Channels form where the resin has dissolved or cracked and the sections can fully or partially detach from the slides. This is part of the rationale for the short time in acid alcohol.

The procedure was set up as program number 7 on the autostainer in the core histology lab. This program requires that the alcoholic eosin be replaced with aqueous eosin and two other modifications in the standard station layout. Therefore it is important to reserve the autostainer, monitor the staining process, and return the stations to their default contents. **Place a note on the stainer indicating the staner is unavailable for use by others during this program.**

Total program time is 14 minutes. Agitation is 10 dips per station if time permits.

Haematoxylin Counterstain for GMA Sections

Reagents & Solutions:

Acid Alcohol (70% alcohol, 0.5% hydrochloric acid)
199 ml 70% Alcohol
1 ml concentrated (12.1 M) HCl

Bluing Reagent (Thermo Shandon Product Number 6769001)

Active Ingredients:	Sodium bicarbonate	0.2%
	Lithium Carbonate	0.04%
	Methanol	37.0%

Gill-3 Haematoxylin (Thermo Shandon Product Number 6765009)

Active Ingredients:	Aluminum sulfate	6.0%
	Haematoxylin	0.6%

Protocol used with a GMA resin produced by Polysciences (Immuno-Bed™ Kit, Cat.# 17324). This resin resembles JB-4 medium in tissue infiltrations, embedding, and cutting procedures.

Procedure:

1. Full strength Hematoxylin for 10 seconds.
2. Water rinse for 1 minute.
3. Acid alcohol for 2 seconds.

   Note: Actual time is about 4 seconds due to slow dipping rate of autostainer. Use three dips if step done by hand.
4. Water rinse for 1 minute.
5. Scott's Solution for 30 seconds.
6. Water rinse for 1 minute.

Notes:

Used as a counterstain with IHC work. Time in acid alcohol is limited because it can damage the GMA sections. The procedure was set up as program number 9 on the autostainer in the core histology lab. Total program time is 4 minutes. Agitation is 10 dips per station if time permits.

Table D-4: Autostainer programs for H&E stain and haematoxylin counterstain.

Haematoxylin and Eosin Stain for GMA Sections

STEP	STATION	REAGENT	TIME(min:sec)	EXACT
1	8	Hematoxylin	2:00	N
2	wash 5	Water	4:00	N
3	9	Acid Alcohol	0:01	Y
4	wash 4	Water	2:00	N
5	10	Scott's Solution	0:30	N
6	wash 3	Water	2:00	N
7	12	Eosin, aqueous	3:00	N
8	wash 2	Water	0:20	N
9	wash 1	Blank	0:15	N

Notes: Total program time without draining is 14 minutes. Agitation rate is 10 dips per station. Aqueous eosin is used for this program. Make the appropriate reagent changes to the respective stations. **Place a note on the stainer indicating the stainer is unavailable for use by others during this program.**

Haematoxylin Counterstain for GMA Sections

STEP	STATION	REAGENT	TIME(min:sec)	EXACT
1	8	Hematoxylin	0:10	N
2	wash 5	Water	1:00	N
3	9	Acid Alcohol	0:02	N
4	wash 4	Water	1:00	N
5	10	Scott's Solution	0:30	N
6	wash 3	Water	1:00	N

Notes: Total program time without draining is 4 minutes. Agitation rate is 10 dips per station.

Appendix E:
Registration Fixture

The following pages show the registration fixture used to create an array of four holes in the GMA block. Figure E-57 and Figure E-58 are rendered three-dimensional views of the fixture with a mold and registration pins. Figure E-59 and Figure E-60 are engineering drawings describing the dimensions and tolerances of the fixture. The fixture consists of two discs cut from aluminum plates, held together by roll pins with two screws acting as handles. The two piece construction of the body allows the registration holes to be tapped with a larger diameter drill from the inside. The holes can then be completed using a smaller bit from the outside. This assures a snug fit near either outside surface and avoids the substantial challenges associated with trying to drill a long distance with a very small bit. Without this accommodation a much larger hole and pin combination would have been needed.

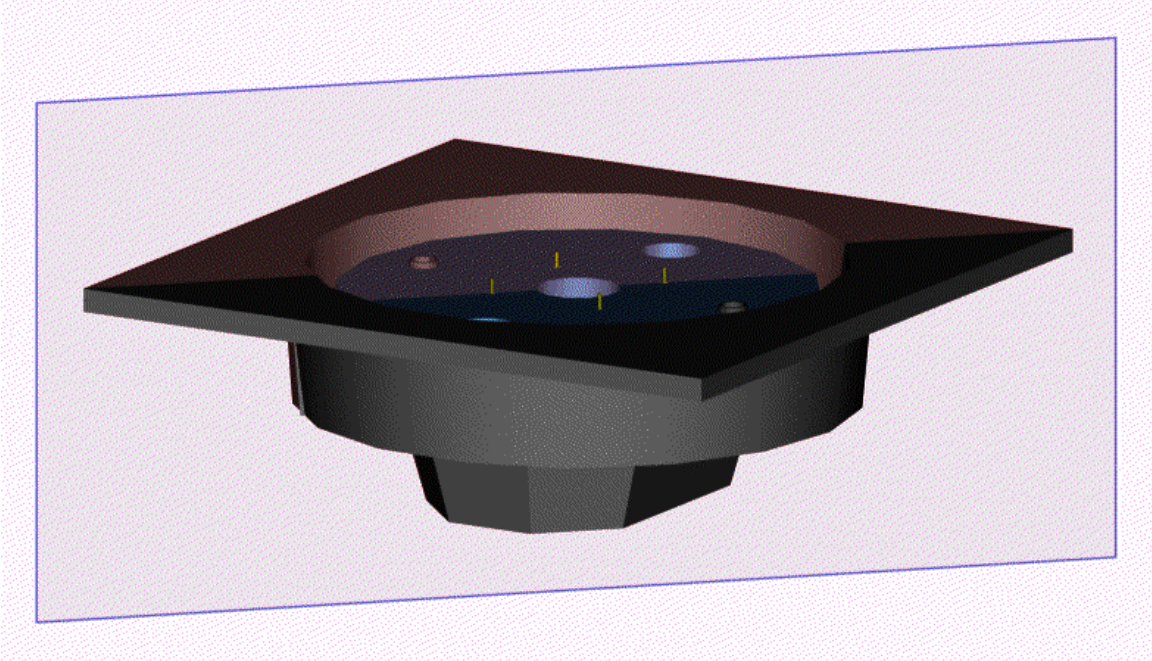

Figure E-57: Registration fixture and mold.

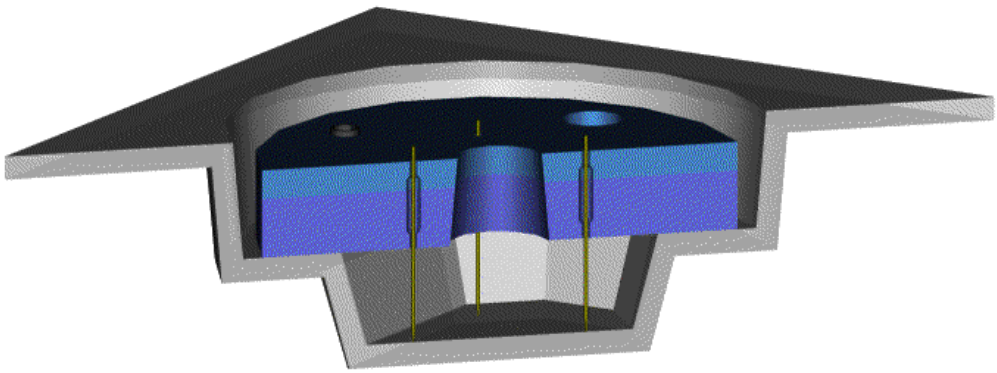

Figure E-58: Sectional view of registration fixture showing pins.

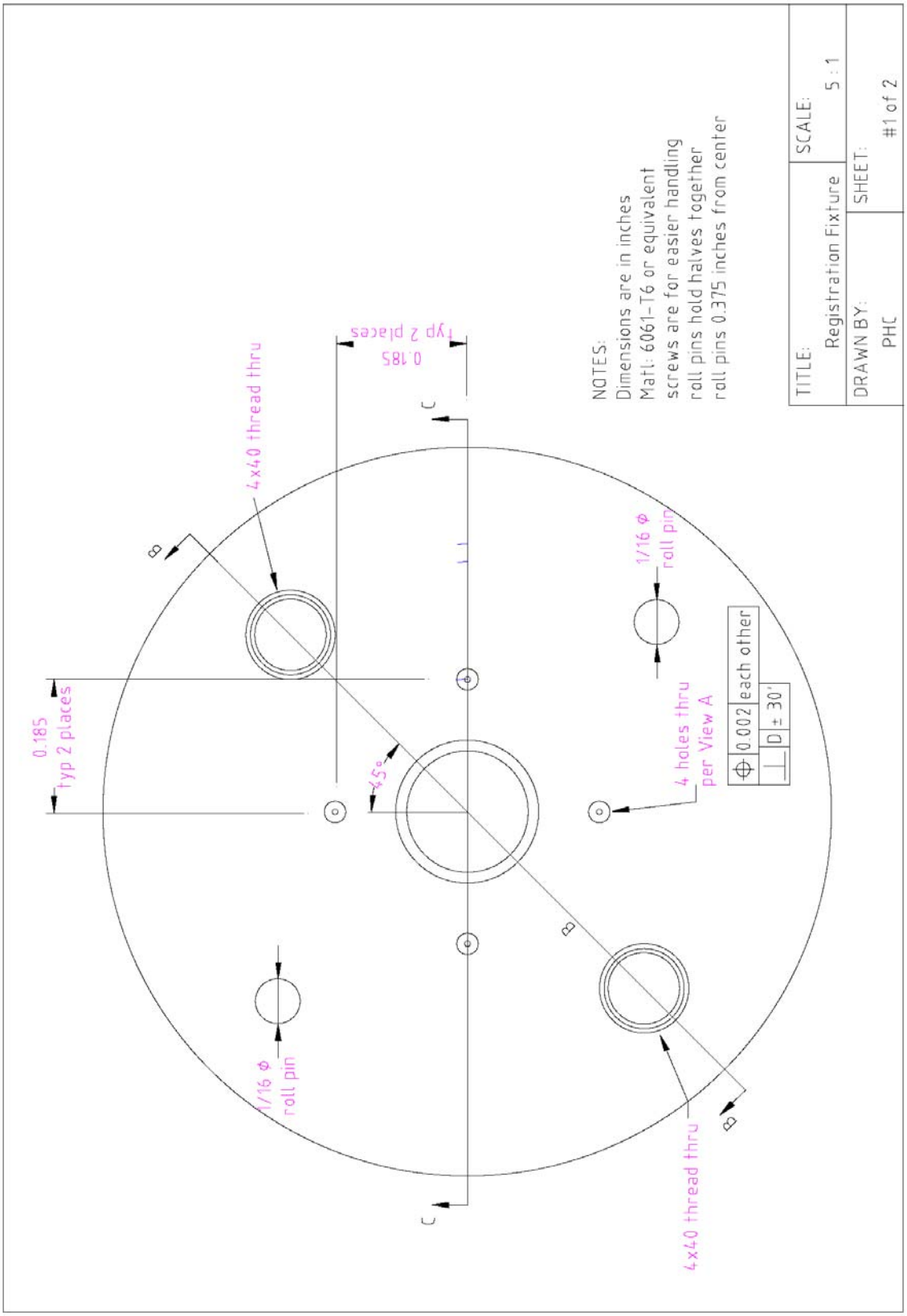

Figure E-59: Top view of registration fixture.

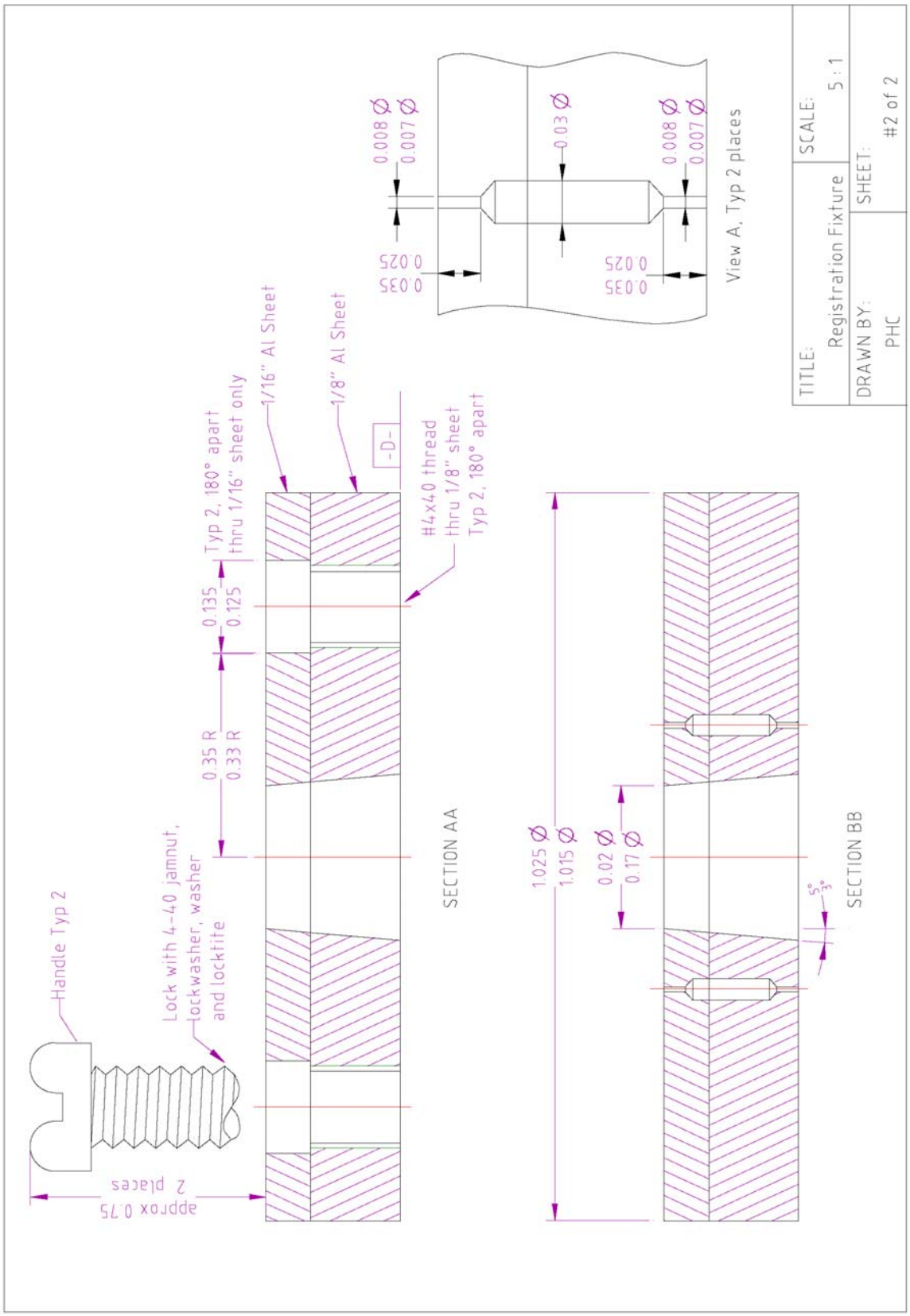

Figure E-60: Section views of registration fixture.

Appendix F:
Reconstruction Aids

Appendix F contains the topics related to reconstruction:

1. Aligning Sections with Pins
2. Sample Affine Registration
3. Wall Thickness and Midplane Geometry Determination
4. Gaussian Curvature

Aligning Sections with Pins

Ideally, alignment of any feature within the registration array can be done by applying the affine transformation to the deformed features. This sections will discuss how an attempt to validate this approach revealed large errors in alignment. For this reason, registration hole alignment was abandoned in favor of feature-based alignment (see Chapter 3 for details).

A fifth pin was introduced to evaluate the error associated with alignment. The fifth pin was placed in the central region of the block during embedding and serves as an arbitrary landmark that was easily identified from section to section. If the pin is aligned so that it is approximately normal to the cutting plane, then the locations of the fifth hole on serial sections have about the same x-y location. Based on the undeformed and deformed positions of the four alignment pins, the undeformed position of the fifth pin can be estimated. This position estimate includes the cumulative errors associated with measurement and with the assumption of uniform strains. For the case when the fifth pin is perfectly aligned and there is no error in position, the hole centroids would be coincident. So this approach provided a practical check of how accurately the registration method predicted the position of a given point.

A test case with a fifth pin produced the following results. The component strains from the affine transformation are shown in Figure J-61. This data is based on 16 sections over a depth of 220 micrometers. Like the previous example the pattern of strains was consistent and predictable from section to section. Even though the magnitude of deformations is dependent on cutting direction, the small standard deviation from section to section in these results suggests a high degree of predictability in the

strain pattern. The strains in the x-direction were consistently smaller than the strains in the y-direction. The error range in ε_x was +4.0% and –5.5% from the mean value. The error range in ε_y was +4.2% and –2.9% from the mean value. The error range in ε_{xy} was +250% and –307%, although this is based on a mean value that is nearly zero ($\varepsilon_{xy} \approx 0.0015$). The bar chart to the right in Figure J-61 illustrates that the cutting direction was approximately aligned with the principal strain direction. Together the schematic and bar chart more clearly show that shear strains are low because the cutting direction is approximately aligned with the direction of maximum principal strain.

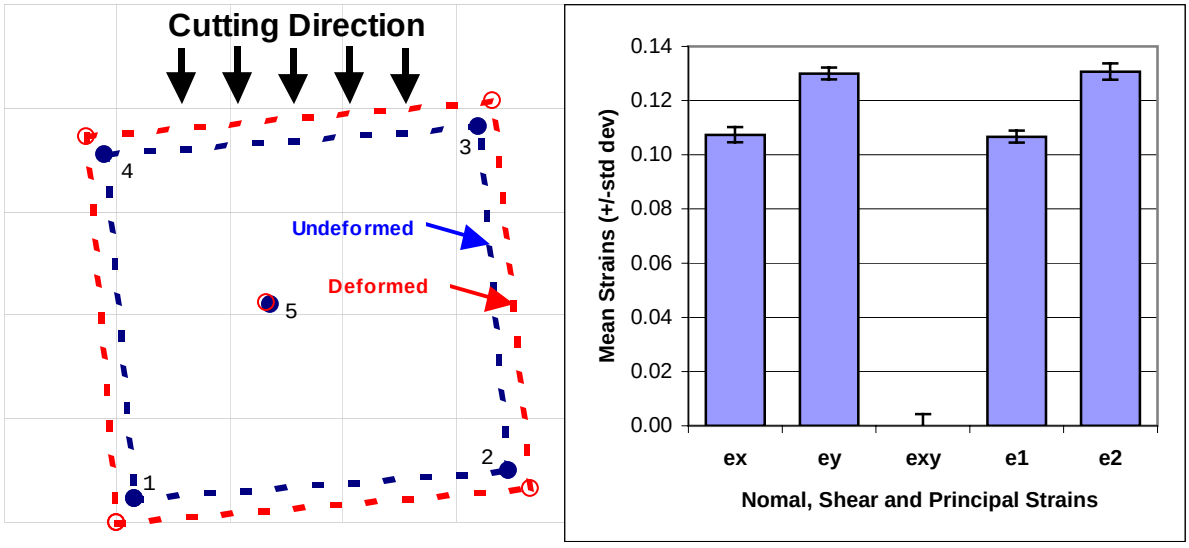

Figure J-61: Test case analysis that includes a fifth pin to evaluated the cumulative accuracy of the registration method.

Based on the affine transformation, Figure J-62 illustrates the variation associated with predicting the position of a hole on a series of 16 sections. Distances are expressed in micrometers and all four registration holes are used to align the sections in a least squares manner. The pin diameter is shown to help illustrate the net accuracy associated with predicting the undeformed position of a hole associated with a fifth pin. This fifth

pin was positioned transverse to the cutting plane, approximately in the middle of the registration array. The mean location of the fifth hole from all sections was treated as the true center of this feature, and the standard deviation from this mean was 4.3 μm in the x-direction and 3.0 μm in the y-direction.

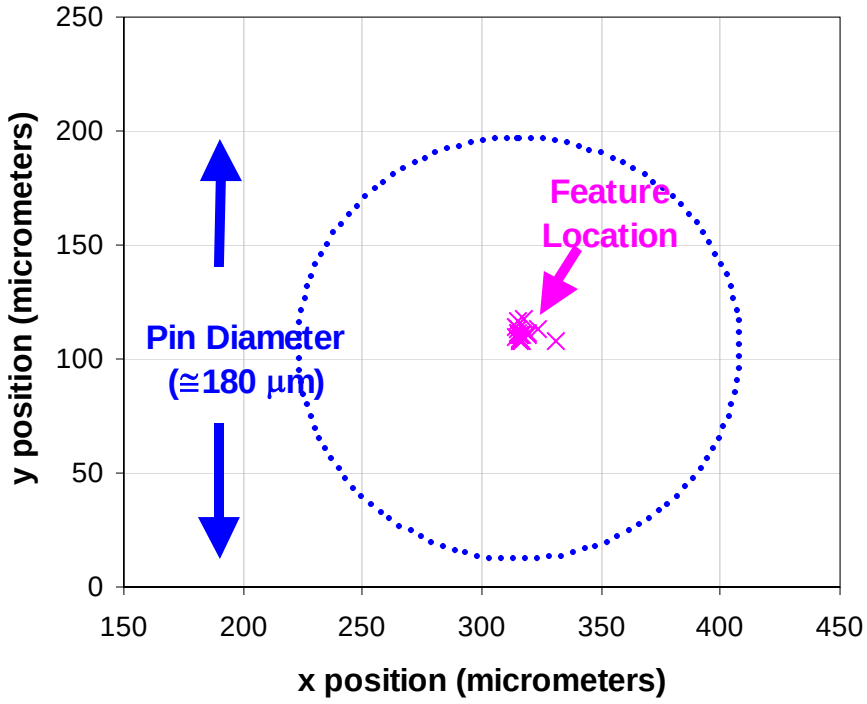

Figure J-62: Shows the alignment of a feature on a series of 16 sections that were part of a preliminary test case. Each point represents the position of a fifth pin hole for a single cross-section. Because the pin is transversely aligned with the cutting plane, the hole locations should be approximately coincident in the xy-plane.

While the average error in position was less than 5 μm, the section-to-section variation was somewhat larger. For this test case, the full range of variation was 18 μm in the x-direction and 10 μm in the y-direction. It might be possible to evaluate the residuals and identify outliers among the registration holes and improve the results, but

the overall accuracy of this approach would still be significant relative to the size of the vessels.

The original goal was to align the sections by using the registration holes with the least squares affine transformation method described in Chapter 3. However as work progressed it became clear that a significant amount of error was present. This was particularly evident when visually comparing the alignment of sequential sections. The most significant source of error appears to be the assumption of a uniform deformation pattern between the registration holes. This problem is exacerbated by the fact that the vessels are small and are not in close proximity to the registration holes (see Figure 3-2). It is recognized that a uniform deformation pattern is a first order correction of section deformations. It is not unreasonable to assume that soft tissue, when infused with GMA, would have relatively uniform cutting properties and therefore exhibit a relatively uniform pattern of deformations. But in reality, some sections exhibit splits and/or folds within the 6.7 x 6.7 mm array of holes. Such damage tends to introduce more significant alignment errors. A simple example of this can be illustrated by introducing a one percent error in the position of a single hole in the x-direction (67 μm). This produces a 33 μm error in position of the hole, which would translate to approximately an 8 μm shift in alignment after minimizing the residuals. It might be possible to eliminate holes that have been compromised by analyzing the residuals in greater detail, but an alternative approach was adopted that took full advantage of the information available and yielded more accurate alignment.

The greatest concern was that the section-to-section variation in alignment might introduce localized artifacts on the surface of the reconstruction. Part of the problem is

that the registration holes are several thousand micrometers away from the branch location (see Figure 3-2), so even small deviations from a uniform deformation pattern can be magnified and become significant. It seems preferable to use local features in proximity to the branch as landmarks for alignment. Such a method is described in Chapter 3.

Sample Affine Registration

```
%*************************************************************************
% R1_affine_registration.m
%*************************************************************************
% Description:
% This program loads a set of registration coordinates and determines the
% affine transformation based on a set of 4 registration points.  A fifth
% point represents the upper left hand corner of a captured image.  The
% transformation is done altogether and in stages to verify results and
% identify possible problems in the data set.
%
%*************************************************************************
% Created by: Peter Carnell
% Last Modified: 11-9-03
%*************************************************************************
%
clear all
close all

% sample cases affine reg  % could insert sample cases here

% load physical coords of 4 registration holes BR-BL-TL-TR
filename = 'R1';
nametype = [filename '_reg'];
load([nametype '.txt']);
Xu = double(eval(nametype))';

Z = Xu(3,:);
Xu = Xu(1:2,:);
[nr, npts] = size(Xu);
nsect = round(npts/4);
Xu = [Xu; ones(1,npts)];

% load physical coords of 4 image corners BR-BL-TL-TR
nametype2 = [filename '_corn_adj'];
load([nametype2 '.txt']);
Xc = double(eval(nametype2))';
Xc = Xc(1:2,:);
Xc = [Xc; ones(1,npts)];

% describe the undeformed registration array in a form that facilitates
% least squares analysis
% du = 6.735192091*1000/2; % measured value?
%du = 6.64538953*1000/2; % drawing spec value
% input coordinates of block face after sectioning
% R1 data:
dux = [1260.88; -5181.97; -4838.85; 1691.08];
duy = [737.19; 344.59; -6206.78; -5818.62];
```

```
dux = dux - mean(dux);
duy = duy - mean(duy);

D = [ dux(1),  duy(1),   1,    0,    0,   0;
       0,   0,   0,   dux(1),   duy(1),   1;
      dux(2),  duy(2),   1,    0,    0,   0;
       0,   0,   0,   dux(2),   duy(2),   1;
      dux(3),  duy(3),   1,    0,    0,   0;
       0,   0,   0,   dux(3),   duy(3),   1;
      dux(4),  duy(4),   1,    0,    0,   0;
       0,   0,   0,   dux(4),   duy(4),   1];

%
%   The measured positions on the sections are the data to be transformed.
%   The affine transformation is the matrix needed to transform the
%   coordinates into the undeformed coordinate system for a given section.
%
Xup = [];
Xcf = [];
for i = 1:nsect;
   Xup = [Xu(1,(4*i-3:4*i)); Xu(2,(4*i-3:4*i))];
   Xup = reshape(Xup,8,1);
   % Use the least squares difference in the residuals
   % to solve for the overconstrained affine transformation coefficients
   % problem (8 eqns in 6 unknowns)
   C = inv(transpose(D)*D)*transpose(D)*Xup;
   % place coefficients into a transformation matrix
   A(:,:,i) = [C(1), C(2), C(3);
               C(4), C(5), C(6);
                 0,    0,    1];
   Xcp = [Xc(1,(4*i-3:4*i)); Xc(2,(4*i-3:4*i)); ones(1,4)];
   Xcf = [Xcf inv(A(:,:,i))*Xcp];
end

% determine the affine transformation matrix and the planar strains
for i = 1:nsect;
   % Calculate Rotation - assumes counterclockwise from def to undef
   rot(i) = asin((A(1,2,i)-A(2,1,i))/2);
end

T = [];
R = [];
Adef = [];
Xu2 = [];
Xu3 = [];
Xu4 = [];
Xu5 = [];

for i = 1:nsect;
   T_temp = [1,  0,  -A(1,3,i);
             0,  1,  -A(2,3,i);
```

```
            0,  0,         1];
    R_temp = [cos(rot(i)),  -sin(rot(i)),  0;
            sin(rot(i)),   cos(rot(i)),  0;
                    0,             0,  1];
    T(:,:,i) = T_temp(:,:);
    R(:,:,i) = R_temp(:,:);
    Adef_temp = [inv(R_temp)*inv(T_temp)*inv(A(:,:,i))];
    Adef(:,:,i) = Adef_temp(:,:);
    Xu2_temp = T_temp*Xu(:,4*i-3:4*i);
    Xu2 = [Xu2 Xu2_temp];
    Xu3_temp = R_temp*Xu2(:,4*i-3:4*i);
    Xu3 = [Xu3 Xu3_temp];
    Xu4_temp = T_temp*R_temp*Adef_temp*Xu(:,4*i-3:4*i);
    Xu4 = [Xu4 Xu4_temp];
    Xu5_temp = inv(A(:,:,i))*Xu(:,4*i-3:4*i);
    Xu5 = [Xu5 Xu5_temp];
end
for i = 1:nsect;
    Xu5_temp = inv(A(:,:,i))*Xu(:,4*i-3:4*i);
    Xu5 = [Xu5 Xu5_temp];
end

% determine the transformation from the undeformed to deformed
% coordinates from the opposite transformation
for i = 1:nsect;
    Adef_inv(:,:,i) = inv(Adef(:,:,i));
end

% transformation required to correct sectioning artifact
% deconstruct the transformation matrix into meaningful components
for i = 1:nsect;
    % Calculate Cauchy Strains
    ex(i) = Adef_inv(1,1,i)-1;
    ey(i) = Adef_inv(2,2,i)-1;
    exy(i) = 0.5*(Adef_inv(1,2,i)+Adef_inv(2,1,i));
end

save([filename '.mat'])

figure
title([filename ' raw data'])
axis equal
axis ij
hold on
for i = 1:nsect;
    plot([Xu(1,4*i-3:4*i) Xu(1,4*i-3)],[Xu(2,4*i-3:4*i) Xu(2,4*i-3)],'b-')
    plot([Xu(1,4*i-3:4*i) Xu(1,4*i-3)],[Xu(2,4*i-3:4*i) Xu(2,4*i-3)],'rx')
end

figure
title([filename ' displaced data'])
```

```
axis equal
axis ij
hold on
for i = 1:nsect;
   plot([Xu2(1,4*i-3:4*i) Xu2(1,4*i-3)],[Xu2(2,4*i-3:4*i) Xu2(2,4*i-3)],'b-')
end
plot(D(1:2:end,1),D(1:2:end,2),'ro')
limits = axis;

figure
title([filename ' rotated data'])
axis equal
axis ij
axis(limits)
hold on
for i = 1:nsect;
   plot([Xu3(1,4*i-3:4*i) Xu3(1,4*i-3)],[Xu3(2,4*i-3:4*i) Xu3(2,4*i-3)],'b-')
end
plot(D(1:2:end,1),D(1:2:end,2),'ro')

figure
title([filename ' multi step corrected'])
axis equal
axis ij
axis(limits)
hold on
for i = 1:nsect;
   plot([Xu4(1,4*i-3:4*i) Xu4(1,4*i-3)],[Xu4(2,4*i-3:4*i) Xu4(2,4*i-3)],'b-')
end
plot(D(1:2:end,1),D(1:2:end,2),'ro')

figure
title([filename ' one step corrected'])
axis equal
axis ij
axis(limits)
hold on
for i = 1:nsect;
   plot([Xu5(1,4*i-3:4*i) Xu5(1,4*i-3)],[Xu5(2,4*i-3:4*i) Xu5(2,4*i-3)],'b-')
end
plot(D(1:2:end,1),D(1:2:end,2),'ro')

% statistics
sd_ex = std(ex,0);
sd_ey = std(ey,0);
sd_exy = std(exy,0);
sd_rot = std(rot,0);
se_ex = sd_ex/length(ex)^0.5;
se_ey = sd_ey/length(ey)^0.5;
se_exy = sd_exy/length(exy)^0.5;
se_rot = sd_rot/length(rot)^0.5;
```

```
m_ex = mean(ex);
m_ey = mean(ey);
m_exy = mean(exy);
m_rot = mean(rot);

figure
title([filename ' ex - Cauchy Strain in x-dir, m=' num2str(m_ex), ' sd=' num2str(sd_ex)]);
xlabel('section number');
ylabel('ex  ({\mum} / {\mum)}');
hold on;
bar(ex);

figure
title([filename ' ey - Cauchy Strain in y-dir, m=' num2str(m_ey), ' sd=' num2str(sd_ey)]);
xlabel('section number');
ylabel('ey  ({\mum} / {\mum)}');
hold on;
bar(ey);

figure
title([filename ' exy - shear strain, m=' num2str(m_exy), ' sd=' num2str(sd_exy)]);
xlabel('section number');
ylabel('exy  ({\mum} / {\mum)}');
hold on;
bar(exy);

figure
title([filename ' Theta - CCW Rotation, m=' num2str(m_rot), ' sd=' num2str(sd_rot)]);
xlabel('section number');
ylabel('rotations  (degrees)');
hold on;
bar(rot*180/pi);

saveas(1,[filename '_raw.fig'])
saveas(2,[filename '_raw_disp.fig'])
saveas(3,[filename '_raw_disp_rot.fig'])
saveas(4,[filename '_multistep_corrected.fig'])
saveas(5,[filename '_onestep_corrected.fig'])
saveas(6,'R7_ex.fig')
saveas(7,'R7_ey.fig')
saveas(8,'R7_exy.fig')
saveas(9,'R7_rot.fig')
%*************************************************************************
%*************************************************************************
```

Determining Wall Thickness and Midplane Geometry

```
%*************************************************************************
% midpoint_total.m
%*************************************************************************
% Description:
% This program determines the midpoint and distance for each polygon
% between two surfaces. It is used to determine the thickness and midplane
% geometry between an inner and outer vessel reconstruction from histology.
%
% Program Method:
% The program determines the normal for one polygon surface and then
% identifies the outer surface intersection using a ray tracing algorithm.
% A midplane point cloud is generated along with a local measure of the
% wall thickness at each surface point.
%
%*************************************************************************
% Subroutines Used:
% polygonplot_function.m - to confirm connectivity for both surfaces
% ray_triangle_intersect.m - function that determines whether intersection
%       is present and if so what the distance is between the two surfaces.
% plot_thick.m - plots line segment between two surfaces
% get_closest_int.m - find closest intersection if multiple intersections
%       exist.  Also includes a filter to avoid consideration of
%       intersections that are not between an inner and outer surface.
% interp_mid.m - use interpolation to estimate wall thickness where no
%       intersection occurs.
%*************************************************************************
% Created by: Peter Carnell
% Last Modified: 12-19-03
%*************************************************************************
close all
clear all
tic

setname = 'R1';
po = load([setname '_outer_vertices.txt']);

%load topology of the polygons
topo=load([setname '_outer_topo.txt']);
if(min(topo(:,1))==0)
   topo = topo + 1;
end

ni = load([setname '_inner_normals.txt']);
pi = load([setname '_inner_vertices.txt']);

%polygonplot_function(po,topo,ones(length(po),1));
%break
```

```
% indices of vertices to use for test
index=[];
int = [];
thick = [];
for j = 1:length(topo);
   % identify vertices of triangle and find normal
   vert0 = po(topo(j,1),:);
   vert1 = po(topo(j,2),:);
   vert2 = po(topo(j,3),:);
   n(j,:) = cross(vert1 - vert0, vert2 - vert0);
end

h = waitbar(0,'Please wait...');
inc_check = 1;
for i = 1:inc_check:length(pi);
   waitbar(i/length(pi),h)
   % origin of ray
   orig = pi(i,:);
   % direction of ray
   dir = ni(i,:);
   for j = 1:length(topo);
      % vertices of polygon
      vert = [po(topo(j,1),:); po(topo(j,2),:); po(topo(j,3),:)];
      % call function to determine ray triangle intersection
      [intersect,t] = ray_triangle_intersect(orig,dir,n(j,:),vert(1,:),vert(2,:),vert(3,:));
      if intersect == 1;
         index = [index; i j];
         int = [int intersect];
         thick = [thick; t];
         intersect = 0;
      end
   end
end
toc
close(h)

%save([setname '_thickness'])

% find the subset of vertices/normals that don't intersect outer surface
% This code subset code is repeated after get_closest_int (in interp_mid)
subset1=index(:,1);
subset2=(1:1:length(ni))';
for i = 1:length(subset1);
   for j = 1:length(subset2);
      if(subset1(i,1)==subset2(j,1))
         subset2(j,1)=0;
      end
   end
end
subset2=find(subset2~=0);
```

```
plot_thick

get_closest_int
plot_thick
save([setname '_thickness'])
%save([setname '_thickness_archive'])
interp_mid
figure
plot3(mid(:,1),mid(:,2),mid(:,3), 'g*')

%thick_total = [v_in; v_out];
%save([setname '_mid.txt'], 'mid', '-ascii')
%save([setname '_mid_thick.txt'], 'thick_total', '-ascii')

break
% Note: the following interpolation will produce a smoother model by
% using weighted averaging of the results.  Analysis indicates that these
% models have reduced accuracy near bounaries - so this approach is not
% taken
[v_out2] = dist_interp([pi(subset1,:); pi(subset2,:)], [v_in; v_out], [pi(subset1,:); pi(subset2,:)], 8);
pi_t = [pi(subset1,:); pi(subset2,:)];
ni_t = [ni(subset1,:); ni(subset2,:)];
for i = 1:length(v_out2);
   % origin of ray
   orig = pi_t(i,:);
   % direction of ray
   dir = ni_t(i,:);
   t = v_out2(i);
   plot_vector(orig,dir,t,'r-')
   mid_t(i,:) = orig+dir/norm(dir)*t/2;
end
hold on
plot3(mid_t(:,1),mid_t(:,2),mid_t(:,3), 'g*')
%*************************************************************************
%*************************************************************************
```

```
function [intersect,r] = ray_triangle_intersect(orig,dir,n,vert0,vert1,vert2);

%*************************************************************************
% function ray_triangle_intersect.m
%*************************************************************************
% Description:
% This program determines whether a ray intersects a triangle and
% returns a value for "intersect" that indicates if
% intersect = -1 => no intersection or degenerate triangle
% intersect =  0 => ray is parallel and out of the plane of the triangle
% intersect =  2 => ray is parallel and in the plane of the triangle
% intersect =  1 => intersection within the triangle
%
% Modelled after Moller & Trumbore (1997) and Dan Sunday, softsurfer
% Tomas Moller & Ben Trumbore, "Fast, Minimum Storage Ray-Triangle Intersection",
% J. Graphics Tools 2(1), 21-28 (1997)
% i1, i2 = indices of vertices to be used
% orig = origin of ray
% dir = direction of ray
% vert0 = vertex 0
% vert1 = vertex 1
% vert2 = vertex 2
%
%*************************************************************************
% Created by: Peter Carnell
% Last Modified: 12-19-03
%*************************************************************************

epsilon = 1E-6;
u = vert1 - vert0;
v = vert2 - vert0;
r = 0;
if (norm(n) < epsilon)  % triangle is degenerate (at least 2 points ~ coincident)
   intersect = -1;     % disp('degenerate case - 3 vertices do not form triangle')
   return
end
wo = orig - vert0;
a = -dot(n,wo);         % solve for constant in plane equation
b = dot(n,dir);
if(abs(b) < epsilon)    % ray is parallel to plane of triangle
   if(a == 0)          % ray is in plane of triangle
      intersect = 2;  % disp('ray is parallel & in plane of triangle')
      return
   else               % ray is not in plane of triangle
      intersect = 0;  % disp('ray is parallel & out-of-plane of triangle')
      return
   end
end

% get intersect point of ray with triangle
r = a / b;
```

```
if r < 0.0;             % ray goes away from triangle
   intersect = 0;     % no intersection % disp('ray pointed away from triangle')
   return
end
% also test if r > 1.0 => no intersect
I = orig + r*dir/norm(dir);    % intersect point %plot3(I(1),I(2),I(3),'y*')
% is I inside the triangle?
uu = dot(u,u);
uv = dot(u,v);
vv = dot(v,v);
w = I - vert0;
wu = dot(w,u);
wv = dot(w,v);
D = uv * uv - uu * vv;
% get & test parametric coords
s = (uv * wv - vv * wu)/D;
if (s < 0.0 | s > 1.0)
   intersect = 0;      % disp('s => ray intersects plane, but not triangle')
   return
end
t = (uv * wu - uu * wv) / D;
if(t < 0.0 | (s+t) > 1.0)
   intersect = 0;      % disp('t => ray intersects plane, but not triangle')
   return
end
% If all conditional tests are passed
intersect = 1;  % I is inside the triangle % disp('ray intesects triangle!')

%**************************************************************************
%**************************************************************************
```

```
%*************************************************************************
% plot_thick.m
%*************************************************************************
% Description:
% This program plots the line segments associated with each interior point.
% The lines are generated by projecting along an outward normal from each
% interior point and stopping at the intersection with the outer boundary
% blue lines show intersections with exterior surface
% red lines show intersections with longer than expected lengths
% green lines show outward normals that don't intersect an exterior surface.
%*************************************************************************
% Created by: Peter Carnell
% Last Modified: 12-19-03
%*************************************************************************
% find and plot the inner vertices and normals associated w/intersections
figure
hold on
for i = 1:length(thick);
   idx = index(i,1);
   % origin of ray - inner vertices
   orig = pi(idx,:);
   % direction of ray - outward normal
   dir = ni(idx,:);
   t = thick(i);
   plot_vector(orig,dir,t,'b-')
end
% find and plot thickness values greater than the specified value (red)
index2=find(abs(thick)>50);
for i = 1:length(index2);
   idx = index2(i);
   % origin of ray - inner vertices
   orig = pi(idx,:);
   % direction of ray - outward normal
   dir = ni(idx,:);
   t = thick(idx);
   plot_vector(orig,dir,t,'r-')
end
% plot the subset of vertices/normals that don't intersect outer (green)
for i = 1:length(subset2);
   idx = subset2(i,1);
   % origin of ray
   orig = pi(idx,:);
   % direction of ray
   dir = ni(idx,:);
   t = 50;
   plot_vector(orig,dir,t,'g-')
end
%*************************************************************************
%*************************************************************************
```

```
%*******************************************************************************
% interp_mid.m
%*******************************************************************************
% Description: This program identifies interior points that do not
% intersect the exterior surface and uses interpolation to estimate the
% thickness value at these locations.
%*******************************************************************************
% Created by: Peter Carnell
% Last Modified: 12-19-03
%*******************************************************************************
%close all
%clear all
%setname = 'R1';
%load([setname '_thickness_archive'])
%%%%coor_in = pi(subset1,:);
coor_in = pi(index(:,1),:);

% find the subset of vertices/normals that don't intersect outer surface
% note that there are boolean operations that could be used to replace the
% following lines of code (see union and intersect).  These were not
% discovered until after this code was written
subset1=index(:,1);
subset2=(1:1:length(ni))';
for i = 1:length(subset1);
   for j = 1:length(subset2);
      if(subset1(i,1)==subset2(j,1))
         subset2(j,1)=0;
      end
   end
end
subset2=find(subset2~=0);

coor_out = pi(subset2,:);
v_in = thick;
numclose = 8;

[v_out] = dist_interp(coor_in, v_in, coor_out, numclose);

figure
hold on
for i = 1:length(v_in);
   idx = subset1(i,1);
   % origin of ray
   orig = pi(idx,:);
   % direction of ray
   dir = ni(idx,:);
   t = v_in(i);
   plot_vector(orig,dir,t,'b-')
   mid1(i,:) = orig+dir/norm(dir)*v_in(i)/2;
end
```

```
for i = 1:length(v_out);
   idx = subset2(i,1);
   % origin of ray
   orig = pi(idx,:);
   % direction of ray
   dir = ni(idx,:);
   t = v_out(i);
   plot_vector(orig,dir,t,'r-')
   mid2(i,:) = orig+dir/norm(dir)*v_out(i)/2;
end

plot3(mid1(:,1),mid1(:,2),mid1(:,3), 'g*')
plot3(mid2(:,1),mid2(:,2),mid2(:,3), 'y*')

% for additional smoothing
%[v_out] = dist_interp(coor_out, v_out, coor_out, numclose);

mid = [mid1; mid2];
subset_total = [subset1; subset2];
[temp,sort_index]=sort(subset_total);
mid = mid(sort_index,:);
save([setname '_mid.txt'],'mid','-ASCII')

thick_total = [v_in; v_out];
thick_total = thick_total(sort_index);
save([setname '_mid_thick.txt'],'thick_total','-ASCII')

% use midpoint thickness with inner points & topology
% currently don't have topology of mid surface associated with mid points,
% therefore would have to generate new stl model and interpolate to generate
% pseudo-colored surface in Matlab
%*************************************************************************
%*************************************************************************
```

Gaussian Curvature

Early investigations indicated that the local curvature properties in the branch geometry could be treated as an important first order measure of intramural stress. As discussed earlier the Law of Laplace can be used to estimate the state of stress, provided the surface curvatures reflect the deformed geometry. Gaussian curvature is a mechanically relevant scalar quantity that is defined as follows:

$$C_{gaussian} = \frac{1}{R_1}\frac{1}{R_2}$$ Equation 5.1

Where R_1 and R_2 are the radii in the principal directions of curvature. If the two corresponding centers of curvature are on opposite sides of the surface then the Gaussian curvature is negative. By observation it can be shown that highly negative Gaussian curvature occurs in saddle regions where high stresses tend to occur. See Liao et al (Liao, Duch et al. 2004) for a recent example of how curvature can provide mechanically relevant information. In this research the finite element analysis of stresses limited the usefulness of such geometric measures.

Appendix G:
Image Processing and Segmentation

The image processing routines are divided into three groups: 1) basic image processing routines, 2) Canny edge detection and 3) Perona and Malik edge detection. The basic image processing routines include the determination of various derivatives of images and a routine to sort points into an ordered set of boundary points. The edge detection algorithms both include a subroutine and a main program where the subroutine is used.

Basic Image Processing Routines

gauss.m

```
function f = gauss(x,order,s)
% gauss calculates symbolic expression for gaussian derivatives
% Input arguments:
% x:        symbolic integration variable
% order:    order of gaussianderivative
% s:        sigma
% Output arguments:
% f:        gaussian derivative expression
% For example:
%   gauss(x,2,3)
%   calculates the second order gauss-derivative to x, with sigma = 3.
%
% Created by Martijn Cox, May 20th, 2003
   g0 = 1/(sqrt(2*pi)*s) * exp(-x.^2/(2*s.^2));
   f  = diff(g0,x,order) ;
```

gd.m

```
function [newimage,timeused] = gd(image,xorder,yorder,s)
% gd calculates gaussian derivatives of an image.
% Input arguments:
% image
% xorder:   order of x-derivative
% yorder:   order of y-derivative
% s:        sigma
% Output arguments:
% newimage: derivative image
% timeused: cpu-time used doing calculations
% For example:
%   gd(image,0,2,3)
% calculates the second order gaussion y-derivative with sigma = 3.
% Created by Martijn Cox, May 20th 2003
   t=cputime;
   syms x y
   xkernel=gauss(x,xorder,s);
   ykernel=gauss(y,yorder,s);
   xrow=-3*s:3*s;
   yrow=-3*s:3*s;
   xkernel=subs(xkernel,x,xrow);
   ykernel=subs(ykernel,y,yrow);
   newimage=conv2(xkernel,ykernel,image,'same');
   timeused=cputime-t;
```

gradmag.m

```
function [newimage,timeused] = gradmag(image,s)
% gradmag calculates gradient magnitude of an image: sqrt( (df/dx)^2 + (df/dy)^2 )
% Input arguments:
% image
% s:        sigma
% Output arguments:
```

```
% newimage: derivative image
% timeused: cpu-time used doing calculations
%
% For example:
%   gradmag(image,3)
%   calculates the gradient magnitude of image with sigma = 3.
%
% Created by Martijn Cox, May 20th, 2003
   t=cputime;
   f10=gd(image,1,0,s);
   f01=gd(image,0,1,s);
   newimage=(f01.^2+f10.^2).^0.5;
   newimage=(newimage-min(min(newimage))./(max(max(newimage))-min(min(newimage)));
   timeused=cputime-t;
```

Laplacian.m

```
function [newimage,timeused] = Laplacian(image,s)
% Laplacian calculates Laplacian of an image: d^2f/dx^2 + d^2f/dy^2
% Input arguments:
% image
% s:        sigma
% Output arguments:
% newimage: derivative image
% timeused: cpu-time used doing calculations
%
% For example:
%   Laplacian(image,3)
%   calculates the Laplacian of image with sigma = 3.
%
% Created by Martijn Cox, June 6th, 2003
   t=cputime;
   f20=gd(image,2,0,s);
   f02=gd(image,0,2,s);
   newimage=f02+f20;
   timeused=cputime-t;
```

sortdata.m

```
function sort_coords=sortdata(coords);
% coords=coordinates;
x=coords(1,1);
y=coords(1,2);
coords(1,:)=0;
sort_coords=[];
sort_coords=[sort_coords;[x,y]];

n=1;

while n==1
   new_pos=find( abs(coords(:,1)-x)<=1& abs(coords(:,2)-y)<=1 );
   if length(new_pos>=1)
      x=coords(new_pos(1),1);
      y=coords(new_pos(1),2);
      coords(new_pos(1),:)=0;
```

```
      sort_coords=[sort_coords;[x,y]];
   else
      i=find(coords(:,1)~=0&coords(:,2)~=0);
      coords=coords(i,:);
      if length(coords)>=1
         new_pos=1;
         x=coords(new_pos,1);
         y=coords(new_pos,2);
         coords(new_pos,:)=0;
         sort_coords=[sort_coords;[x,y]];
      else
         n=0;
      end
   end
end
```

Canny Edge Detection

blurcanny.m

```
function [wall,timeused]=blurcanny(image,s1,s2)
% blurcanny uses gaussian blurring combined with
% canny-edgedetection to find the edges in a histology image
% of a rat artery. It is called by the routine innerwall.m
% Input:
% image: an image of a rat artery
% s1: sigma for gaussian blurring
% s2: sigma for canny edgedetection
% Output:
% wall: detected edges
% timeused: cpu time used calling the routine
%
% Created by Martijn Cox, last changed on June 4th, 2003.
t_blurcanny=cputime;
disp('Blurring');
blur=gd(image,0,0,s1);
disp('Canny-edgedetection');
wall=edge(blur,[],'canny',s2);
cpu_blurcanny = cputime-t_blurcanny
% figure(1),imdisp((double(wall)==0).*double(blur))
% figure(2),imdisp((double(wall)==0).*double(image))
```

innerwall.m

```
function coords=innerwall(filename,s1,s2,slice)
% innerwall can be used to automatically detect the inner vessel wall,
% the most important method used for that is gaussian blurring, followed
% by canny-edgedetection.
% The function by itself can be called by another routine, vessel3d.m, which
% will call innerwall.m several times, to get the coordinates of the inner wall
% of a complete vessel.
% Input:
% filename: name of the imagefile to be loaded
% slice:    slicenumber, used as z-cooordinate
% Output:
```

```
% coords:   x-,y- and z-coordinates of the inner vessel wall
%
% Created by Martijn Cox, last changed on June 4th, 2003
%close all
%set path to image-directory -> NOT USED RIGHT NOW
% cd 'd:\bmt\trimester 4.3\image data\AB_ACGI_cropped';
% dir
% %type image filename
% filename=input('Image filename: ','s');
disp('Reading image');
image=imread(filename);

%downsample image
%image = image(1:10:end,1:10:end,:);
%select green image
[x,y,rgb]=size(image);
if rgb==3
   image=image(:,:,2);
end
%waldetect is another m-file, in this case blurs image with sigma = 5
%and then applies the canny edgedetector with sigma =1
canny=blurcanny(image,s1,s2);
%results of edgedetection is dilated to fill possible holes
bwdilate=imdilate(canny,ones(1));
%a mouseclick in the vessel fills the vessel(s)
disp('Click in one or more vessels to fill, enter to exit')
fill=bwfill(bwdilate);
bwerode=imerode(fill,ones(1));
%another mouseclick in the vessel selects the vessel object(s)
disp('Click in one or more vessels to get wall, enter to exit')
%vessel=bwselect(fill);
vessel=bwselect(bwerode);
%bwperim give the boundaries of the vessel
wall=bwperim(vessel);
%wall is displayed (black lines) in original image
imdisp(double(wall==0).*double(image));
pause
%selecting coords of wall
[ycoord,xcoord]=find(wall==1);

%a last check
wall2=zeros(size(wall));
for i=1:length(xcoord)
   wall2(ycoord(i),xcoord(i))=1;
end
%wall2 should be exactly the same as wall, so the result of this formula
%should be zero.
check=max(max((wall2-double(wall)).^2));
if check==0
   coords=[xcoord,ycoord];coords(:,3)=slice;
else
   disp('error!')
end
```

Perona and Malik Edge Detection

peronamalik5.m

```
function [newimage,timeused] = peronamalik5(f,dt,niter,kvalue)
% [imdiff,tgdf]=peronamalik5(f,0.2,20,0.9);
% peronamalik5 uses anisotropic diffusion equations for "edge-preserved smoothing" as first proposed
% by Perona and Malik (ref.).
% The equation to be solved is It = div( c(x,y,t)*nabla(I) ) In which I is the image, It, the (partial)
% time derivative of I, div the divergence operator, nabla the nabla operator and c(x,y,t) an arbitrary
% function.
% For edge-preserved smoothing c is chosen (for example) dependent of the gradient(magnitude) of an
image
% A large gradient(magnitude) will cause slow diffusion (less blurring/more edge enhancement).
% In this case c is made a function of the gaussian gradient magnitude, with a large sigma, so that only
% large edge-structures will be preserved, and small particles (nuclei) will be blurred away.
% A constant k defines the switchpoint between edge enhancement and blurring. k is defined as a
% percentage value of the integral of the histogram of the gradient magnitude of every iteration
% (of of of of of). Mostly to be 90%, as proposed by Canny (ref.)
% The diffusion equation is discretized in the most straightforward way possible:
% I(t+1) = I(t) + dt * div( c(x,y,t)*nabla(I) ).
% This expression is discretized by a 4-neighbours approximation, as proposed by Perona and Malik (ref.)
%
% Input:
% f: image to be computed
% dt: timestep, needs to be >0 and <0.25 to preserve stability
% niter: number of iterations
% kvalue: Used to calculate the constant k every iteration, mostly 90%
%
% Created by Martijn Cox, last changed on June 4th, 2003
t=cputime;
f=double(f(:,:,2));
[ymax xmax]=size(f);
f=(f-min(min(f)))./(max(max(f))-min(min(f)));
global k
newimage=[];
fnew=zeros(size(f));
   grad=gradmag(f,5);
   [counts,x]=imhist(grad);
   s=cumsum(counts)/sum(counts);
   a=find(s>kvalue);
   k=x(min(a));
disp('Solving anisotropic diffusion equations, timesteps:');
for n=1:niter

   i=1;j=1;
   fnew(i,j) = f(i,j) + dt * ( cs(i,j,grad).*( f(i+1,j)-f(i,j) ) + ce(i,j,grad).*( f(i,j+1) - f(i,j) ) );

   i=2:(ymax-1);j=1;
   fnew(i,j) = f(i,j) + dt * ( cs(i,j,grad).*( f(i+1,j)-f(i,j) ) + cn(i,j,grad).*( f(i-1,j) - f(i,j) )...
      + ce(i,j,grad).*( f(i,j+1) - f(i,j) ) );

   i=1;j=2:(xmax-1);
   fnew(i,j) = f(i,j) + dt * ( cs(i,j,grad).*( f(i+1,j)-f(i,j) ) + ce(i,j,grad).*( f(i,j+1) - f(i,j) )...
      + cw(i,j,grad).*( f(i,j-1)-f(i,j) ) );
```

```
    i=2:(ymax-1);j=2:(xmax-1);
    fnew(i,j) = f(i,j) + dt * ( cn(i,j,grad).*( f(i-1,j)-f(i,j) ) + cs(i,j,grad).*( f(i+1,j) - f(i,j) )...
       + ce(i,j,grad).*( f(i,j+1)-f(i,j) ) + cn(i,j,grad).*( f(i,j-1)-f(i,j) ) );

    i=ymax;j=2:(xmax-1);
    fnew(i,j) = f(i,j) + dt * ( cn(i,j,grad).*( f(i-1,j)-f(i,j) ) + ce(i,j,grad).*( f(i,j+1) - f(i,j) )...
       + cw(i,j,grad).*( f(i,j-1)-f(i,j) ) );

    i=2:(ymax-1);j=xmax;
    fnew(i,j) = f(i,j) + dt * ( cs(i,j,grad).*( f(i+1,j)-f(i,j) ) + cn(i,j,grad).*( f(i-1,j) - f(i,j) )...
       + cw(i,j,grad).*( f(i,j-1) - f(i,j) ) );

    i=ymax;j=xmax;
    fnew(i,j) = f(i,j) + dt * ( cn(i,j,grad).*( f(i-1,j)-f(i,j) ) + cw(i,j,grad).*( f(i,j-1) - f(i,j) ) );

    fprintf(1, '%3d', n);
    if (rem(n,20) == 0)
       fprintf(1, '\n');
    end
    f=fnew;
end
newimage=f;
timeused=cputime-t;
disp(strcat('timeused: ',num2str(timeused)));
function func=cn(i,j,grad)
global k
func=1 ./ (1 + grad(i-1,j)/k^2 );

function func=cs(i,j,grad)
global k
func=1 ./ (1 + grad(i+1,j)/k^2 );

function func=ce(i,j,grad)
global k
func=1 ./ (1 + grad(i,j+1)/k^2 );

function func=cw(i,j,grad)
global k
func=1 ./ (1 + grad(i,j-1)/k^2);
```

outerwall.m

```
function [coords,newimage,timeused]= outerwall(imdiff,thresh);
% Uses the result of peronamalik5.m to calculate the outer (and inner)
% vessel wall of a rat artery.
% The vessel is detected by thresholding.
% The function uses a number of dilation and erosion steps to get rid of
% some artefacts at the boundary or the interior of the vessel.
% After that it calculates the laplacian (d^2f/dx^2+d^2f/dy^2),
% which will be negative for the vessel.
% Mouse clicking selects the vessels, after which the walls are found
% and the coordinates saved.
%
% Input:
% imdiff: resulting image from perona malik anisotropic diffusion
% Output:
% coords: x and y coords of the outer and inner wall
```

```
% timeused: cpu time used during calculations
%
% Created by Martijn Cox, last changed on June 4th, 2003.
%close all
t=cputime;
disp('Click on vessel to select');
%thresholding and selecting vessel
newimage=bwselect((imdiff<thresh)&(imdiff>0.1));

%a series of erosion and dilation steps, or vice versa.
newimage=dilate(erode(newimage,ones(1,7)),ones(1,7));
% figure,imshow(newimage);
newimage=dilate(erode(newimage,ones(7,1)),ones(7,1));
% figure,imshow(newimage);
newimage=erode(dilate(newimage,ones(10,10)),ones(10,10));
% figure,imshow(newimage);
newimage=gd(double(newimage),0,2,7)+gd(double(newimage),2,0,7);
% figure,imdisp(newimage<0);
newimage=bwperim(newimage<0);
% figure,imshow(newimage);
% selecting coords of wall
[ycoord,xcoord]=find(newimage==1);

%%%%%%%%%%Sorting data-points along the path%%%%%%%%%%%%%%%%%%%%
t=cputime;
coords=[xcoord,ycoord];
x=coords(1,1);
y=coords(1,2);
%starting point is first point in coords
coords(1,:)=0;
%all points picked out of coords are deleted, in other words, set to zero.
sort_coords=[];
sort_coords=[sort_coords;[x,y]];
%new points are stored in sort_coords

n=1;

while n==1
   new_pos=find( abs(coords(:,1)-x)<=1& abs(coords(:,2)-y)<=1 );
   %find points connected to last point (x,y)
   if length(new_pos>=1)
      %when one or more neighbors are found, define the first one to be the
      %next point in line
      x=coords(new_pos(1),1);
      y=coords(new_pos(1),2);
      coords(new_pos(1),:)=0;
      sort_coords=[sort_coords;[x,y]];
      %as before, points are deleted from coords and stored into sort_coords
   else
      %when no neighbors are found, this means ending at a loose end, or completing
      % a circle. In that case, all the zero points are deleted from coords, after
      % which a new first point (new_pos) is again picked as the first point in coords.
      i=find(coords(:,1)~=0&coords(:,2)~=0);
      coords=coords(i,:);
      if length(coords)>=1
         new_pos=1;
```

```
            x=coords(new_pos,1);
            y=coords(new_pos,2);
            coords(new_pos,:)=0;
            sort_coords=[sort_coords;[x,y]];
        else
            %when all circles are completed, coords will be empty, and the program stops
            n=0;
        end
    end
end
cputime-t

%a last check
wall2=zeros(size(newimage));
for i=1:length(sort_coords)
    wall2(sort_coords(i,2),sort_coords(i,1))=1;
end
%wall2 should be exactly the same as newimage, so the result of this formula
%should be zero.
check=max(max((wall2-double(newimage)).^2));
if check==0
    coords=sort_coords;
else
    disp('error!')
end
close
timeused=cputime-t;
```

Appendix H:
Programs to Quantify Inflammation

Appendix H contains the following programs related to cell identification and cell density calculation:

1. Cell Selection Graphic User Interface
2. Cell Density Calculations
3. Volume Measurement Error
4. Branch Proximity Measurement

Other algorithms are not presented here. The method that color codes the cells rather than the surface is not presented, since it is conceptually similar to what has been presented. The polygon plotting function that is used is presented under Visualization Tools, although it is used here. Also the routine that directly determines the volume available for cells, since it is similar to Appendix H2, but less complicated.

Cell Selection Graphic User Interface

Figure H-63 and Figure H-64 are two screenshots of the cell selection graphic user interface (GUI). The program user can select multiple cell types, and navigate through each montaged image at high magnification.

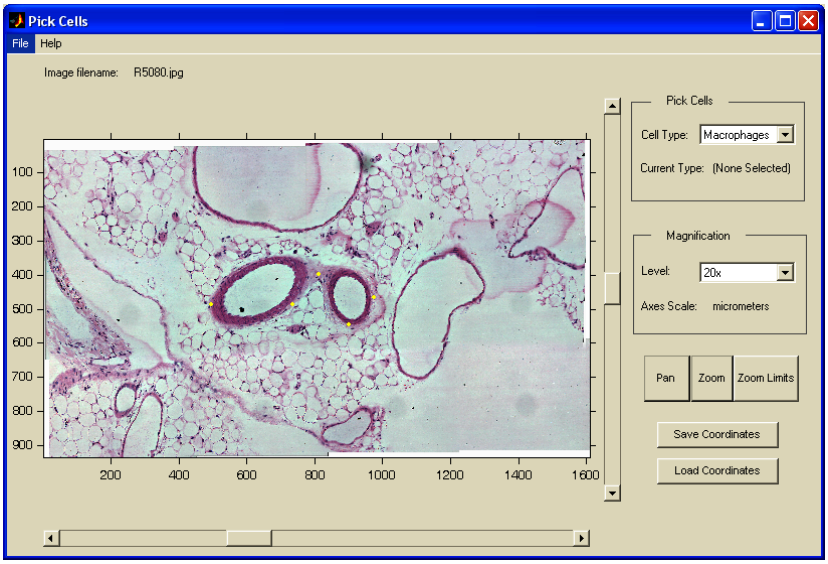

Figure H-63: Screenshot of cell selection graphic user interface.

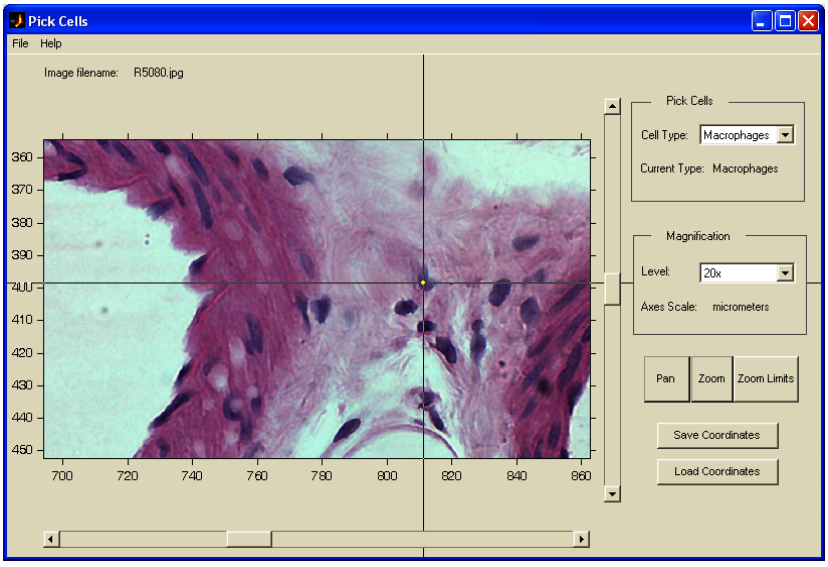

Figure H-64: Higher magnification screenshot of GUI.

```
function varargout = pickcells(varargin)

%***************************************************************************
% pickcells.m
%***************************************************************************
% Description:
% This program is the Matlab Graphic User Interface (GUI) that allows the
% user to load and navigate montaged images and manually identify
% inflammatory cells based on morphology.  The cell locations are visually
% shown and stored for later assembly into a three-dimensional view of
% inflammation.  The program could be generalized for any detection process
% that requires the judgement of an expert to identify discrete phenomena.
% The program is especially helpful when the detection process cannot be
% readily automated.
%***************************************************************************
% Functions/Other Programs:
% see callback contained within this code
% pickcells.fig - the figure associated with the GUI
% pan.m - pan function was implemented as an external function
%***************************************************************************
% Created by: Martijn Cox, Ben Spivey and Peter Carnell
% Last Modified: 3-25-04
%***************************************************************************
% Pickcells Application M-file for Pickcells.fig
%    FIG = Pickcells.fig
%    Pickcells('callback_name', ...) invoke the named callback.
%***************************************************************************

if nargin <= 1   % LAUNCH GUI
   addpath(pwd)
   initial_dir = pwd;
        fig = openfig(mfilename,'reuse');
        set(fig,'Menubar','none','Color',get(0,'defaultUicontrolBackgroundColor'));
% Generate a structure of handles to pass to callbacks, and store it.
        handles = guihandles(fig);
   handles = reset_coords(handles);%subroutine for initializing/resetting coords.
   handles.sound=wavread('laser.wav');
   handles.sound2=wavread('sound2.wav');
        guidata(fig, handles);

% Populate the listbox
   load_listbox(pwd,handles)%subroutine for file-selecting listbox.
        if nargout > 0
                varargout{1} = fig;
        end
%
elseif ischar(varargin{1}) % INVOKE NAMED SUBFUNCTION OR CALLBACK

        try
                if (nargout)
                        [varargout{1:nargout}] = feval(varargin(Alberts, Bray et al.)); % FEVAL
switchyard
                else
                        feval(varargin(Alberts, Bray et al.)); % FEVAL switchyard
                end
        catch
```

```
                disp(lasterr);
            end

end


%| ABOUT CALLBACKS:
%| GUIDE automatically appends subfunction prototypes to this file, and
%| sets objects' callback properties to call them through the FEVAL
%| switchyard above. This comment describes that mechanism.
%|
%| Each callback subfunction declaration has the following form:
%| <SUBFUNCTION_NAME>(H, EVENTDATA, HANDLES, VARARGIN)
%|
%| The subfunction name is composed using the object's Tag and the
%| callback type separated by '_', e.g. 'slider2_Callback',
%| 'figure1_CloseRequestFcn', 'axis1_ButtondownFcn'.
%|
%| H is the callback object's handle (obtained using GCBO).
%|
%| EVENTDATA is empty, but reserved for future use.
%|
%| HANDLES is a structure containing handles of components in GUI using
%| tags as fieldnames, e.g. handles.figure1, handles.slider2. This
%| structure is created at GUI startup using GUIHANDLES and stored in
%| the figure's application data using GUIDATA. A copy of the structure
%| is passed to each callback.  You can store additional information in
%| this structure at GUI startup, and you can change the structure
%| during callbacks.  Call guidata(h, handles) after changing your
%| copy to replace the stored original so that subsequent callbacks see
%| the updates. Type "help guihandles" and "help guidata" for more
%| information.
%|
%| VARARGIN contains any extra arguments you have passed to the
%| callback. Specify the extra arguments by editing the callback
%| property in the inspector. By default, GUIDE sets the property to:
%| <MFILENAME>('<SUBFUNCTION_NAME>', gcbo, [], guidata(gcbo))
%| Add any extra arguments after the last argument, before the final
%| closing parenthesis.

% ------------------------------------------------------------------- %
% ------------------------------------------------------------------- %
%         Functions of buttons in graphical user interface            %
% ------------------------------------------------------------------- %
% ------------------------------------------------------------------- %
% --------------------------------------------------------------------
function Open_Callback(h, eventdata, handles)
% hObject    handle to Open (see GCBO)
% eventdata  reserved - to be defined in a future version of MATLAB
% handles    structure with handles and user data (see GUIDATA)
[filename, pathname] = uigetfile( ...
{'*.bmp;*.jpg;*.jpeg;*.tiff','Image Files (*.bmp,*.jpg,*.jpeg,*.tiff)';
   '*.*',  'All Files (*.*)'}, ...
   'Open Image');
if filename ~= 0
   [path,name,ext,ver] = fileparts(filename);
```

```
    im=imread(filename);
    hold off
    iptsetpref('imshowaxesvisible','on')
    hold off
    imshow(im);
    hold on
    handles.im=im;
    convert_units(handles);
    handles.filename=name;
    handles = reset_coords(handles);
    set(handles.xslider,'Enable','on');
    set(handles.yslider,'Enable','on');
    set(handles.popupmenu1,'Enable','on');
    handles.init_xl=xlim;
    handles.init_yl=ylim;
    handles.xslider_initialized=0;
    handles.yslider_initialized=0;
    intro_mat=['Image filename:     ',filename];
    phrase=strcat(intro_mat);
    set(handles.txt_filename,'String',phrase)
    guidata(h,handles);
end

% ------------------------------------------------------------------- %
function varargout = popupmenu1_Callback(h, eventdata, handles, varargin)
% Choose cell type popupmenu.
% Calls subroutine pickcells
val = get(h,'Value');
if val==1
    celltype='Macrophages';
elseif val==2
    celltype='Mast Cells';
elseif val==3
    celltype='Leukocytes';
elseif val==4
    celltype='Neutrophils';
elseif val==5
    celltype='User Defined 1';
elseif val==6
    celltype='User Defined 2';
end
set(handles.txt_celltype,'String',celltype);
handles = pickcells(handles,val);
guidata(h,handles)

% ---------------------------------------------------------------------
function varargout = Save_button_Callback(h, eventdata, handles, varargin)
% Save button. Saves current cell coordinates in .mat file.
% x and y data is converted back into pixel coordinates before being saved
conversion_factor=.1699;
handles.coords.type1.xstore=handles.coords.type1.xstore/conversion_factor;
handles.coords.type1.ystore=handles.coords.type1.ystore/conversion_factor;
handles.coords.type2.xstore=handles.coords.type2.xstore/conversion_factor;
handles.coords.type2.ystore=handles.coords.type2.ystore/conversion_factor;
handles.coords.type3.xstore=handles.coords.type3.xstore/conversion_factor;
handles.coords.type3.ystore=handles.coords.type3.ystore/conversion_factor;
```

```
handles.coords.type4.xstore=handles.coords.type4.xstore/conversion_factor;
handles.coords.type4.ystore=handles.coords.type4.ystore/conversion_factor;
handles.coords.type5.xstore=handles.coords.type5.xstore/conversion_factor;
handles.coords.type5.ystore=handles.coords.type5.ystore/conversion_factor;
handles.coords.type6.xstore=handles.coords.type6.xstore/conversion_factor;
handles.coords.type6.ystore=handles.coords.type6.ystore/conversion_factor;
handles.coords.conversion_factor=conversion_factor;
handles.coords.xlimits=handles.init_xl/conversion_factor;
handles.coords.ylimits=handles.init_yl/conversion_factor;
coords=handles.coords;
filename=strcat(handles.filename,'coord');
save(filename,'coords');

% --------------------------------------------------------------------
function varargout = loadbutton_Callback(h, eventdata, handles, varargin)
% Load button. Tries to load saved coords, if exist.
try
   coordinates=strcat(handles.filename,'coord.mat');
   load(coordinates);
   handles.coords=coords;
   guidata(h,handles)
catch
   disp('No such filename found');
end

% --------------------------------------------------------------------
function varargout = yslider_Callback(h, eventdata, handles, varargin)
% Slider bar in y-direction.
% Value(val) varies between 0 and 1. Adjusts axis settings by sliding.
% Not allowed to set axis > ymax
val=get(h,'Value');
ymax=handles.init_yl(2);
yl=ylim;
pymin=yl(1);
pymax=yl(2);
percent=(pymax-pymin)/ymax;  % Percent height of current image compared to height of original image
if handles.yslider_initialized==0
   val=(ymax-pymax)/ymax;
   if val < 0
      val=0;
   end
   set(h,'Value',val);
end
handles.yslider_initialized=1;
newymin=ymax*(1-val-percent);
newymax=newymin+pymax-pymin;
if newymin<0
   newymin=0;
   newymax=ymax*percent;
end
ylim([newymin newymax]);
guidata(h,handles)

% --------------------------------------------------------------------
function varargout = xslider_Callback(h, eventdata, handles, varargin)
% Slider bar in x-direction.
```

```
% Value  (val) varies between 0 and 1. Adjusts axis settings by sliding.
% Not allowed to set axis > xmax
val=get(h,'Value');
xmax=handles.init_xl(2);
xl=xlim;
pxmin=xl(1);
pxmax=xl(2);
cur_obj=get(gco,'tag');
if handles.xslider_initialized==0
   val=pxmin/xmax;
   set(h,'Value',val);
end
handles.xslider_initialized=1;
newxmax=xmax*val+pxmax-pxmin;
if newxmax>xmax
   newxmax=xmax;
end
newxmin=newxmax-pxmax+pxmin;
xlim([newxmin newxmax]);
guidata(h,handles)

% --------------------------------------------------------------------
function varargout = Magnification_Callback(h, eventdata, handles, varargin)
% Defines the scale to be plotted by the convert_units routine.
% Calls subroutine convert_units
handles.axis=axis;
hold off
imshow(handles.im)
h_img=findobj(gcf,'Type','image');
xl=get(h_img,'XData');
yl=get(h_img,'YData');
xlim(xl);
ylim(yl);
convert_units(handles);
axis tight
handles.init_xl=xlim;
handles.init_yl=ylim;
hold on
plot(handles.coords.type1.xstore,handles.coords.type1.ystore,'y.')
plot(handles.coords.type2.xstore,handles.coords.type2.ystore,'r.')
plot(handles.coords.type3.xstore,handles.coords.type3.ystore,'b.')
plot(handles.coords.type4.xstore,handles.coords.type4.ystore,'g.')
plot(handles.coords.type5.xstore,handles.coords.type5.ystore,'w.')
plot(handles.coords.type6.xstore,handles.coords.type6.ystore,'c.')
guidata(h,handles)

% --------------------------------------------------------------------
function varargout = panbutton_Callback(h, eventdata, handles, varargin)
% hObject    handle to panButton (see GCBO)
% eventdata  reserved - to be defined in a future version of MATLAB
% handles    structure with handles and user data (see GUIDATA)
handles.xslider_initialized=0;
handles.yslider_initialized=0;
init_axes=[handles.init_xl;handles.init_yl];
% disp(init_axes)
button_state = get(h,'Value');
```

```
drawnow discard;
off = [handles.zoombutton];
set(off,'Value',0);
state=1;
while state==1
   pan(init_axes);
   k=waitforbuttonpress;
   type=get(gco,'Type');
   if k==1
      state=0;
      stringval='';
      tagval='';
      clear functions
   elseif ~strcmp(type,'image') & ~strcmp(type,'figure') & ~strcmp(type,'axes')
      tagval=get(gco,'Tag');
      stringval=get(gco,'String');
      if ~strcmp(stringval,'Pan')
         state=0;
      end
   end
end
set(handles.panbutton,'Value',0);
set(gcf,'windowbuttonupfcn','remove');
set(gcf,'windowbuttonmotionfcn','remove');
set(gcf,'pointer','arrow');
if k==1
   [h,handles]=keyboardPickcells(h,handles);
elseif strcmp(tagval,'zoomlimits')
   zoomlimits_func(h,handles);
elseif strcmp(stringval,'popupmenu1')
   set(handles.popupmenu1,'Enable','on');
elseif strcmp(tagval,'xslider') | strcmp(tagval,'yslider')
   set(handles.xslider,'Enable','on');
   set(handles.yslider,'Enable','on');
end
guidata(h,handles)

% --------------------------------------------------------------------
function zoombutton_Callback(h, eventdata, handles)
% Zoom button. Enables modzoom function. Disables pickcells popupmenu and sliderbars
% Mutually exclusive with sliderbutton and pickcells button.
handles.xslider_initialized=0;
handles.yslider_initialized=0;
state = 1;
k=waitforbuttonpress; % Prevent program from running until first point is selected
while state == 1
   % Act on whether the user pressed left or right mouse button
   selection_type=get(gcf,'SelectionType');
   if strcmp(selection_type,'normal')
      modzoom(handles,'leftclick');
   elseif strcmp(selection_type,'alt')
      modzoom(handles,'rightclick');
   end
   % Determine whether the user wants to continue zooming or select another action
   k=waitforbuttonpress;
   type=get(gco,'Type');
```

```
    if k==1
        state=0;
        stringval='';
        tagval='';
    elseif ~strcmp(type,'image') & ~strcmp(type,'figure') & ~strcmp(type,'axes')
        stringval=get(gco,'String');
        tagval=get(gco,'tag');
        if ~strcmp(stringval,'zoom')
            state=0;
        end
    end
end
set(handles.zoombutton,'Value',0)
% Acts on whether the user wants to change action to key board pick cells buttons,
% slider, or pick cells buttons
if k==1
    [h,handles]=keyboardPickcells(h,handles);
elseif strcmp(tagval,'zoomlimits')
    zoomlimits_func(h,handles);
elseif strcmp(tagval,'popupmenu1')
    set(handles.popupmenu1,'Enable','on');
    set(handles.popupmenu1,'Value',1);
elseif strcmp(tagval,'xslider') | strcmp(tagval,'yslider')
    set(handles.xslider,'Enable','on');
    set(handles.yslider,'Enable','on');
end
guidata(h,handles)

% --------------------------------------------------------------------
function zoomlimits_Callback(h, eventdata, handles)
% hObject    handle to zoomlimits (see GCBO)
% eventdata  reserved - to be defined in a future version of MATLAB
% handles    structure with handles and user data (see GUIDATA)
zoomlimits_func(h,handles);

% --------------------------------------------------------------------
function figure1_KeyPressFcn(h, eventdata, handles, varargin)
% Executes when user presses a number key between 1-5
% Allows the user to bypass the pop-up menu and select which cells to pick from the keyboard

[h,handles]=keyboardPickcells(h,handles);
guidata(h,handles);

% --------------------------------------------------------------------
function KeyboardShortcuts_Callback(hObject, eventdata, handles)
% Executes when user chooses Keyboard Shortcuts option under Help menu option.

line1='Choosing cells using the keyboard';
line2='------------------------------------------------------------------';
line3='Number key          Cell Type';
line4='       1              Macrophages (yellow)';
line5='       2              Mast Cells (red)';
line6='       3              Leukocytes (blue)';
line7='       4              Neutrophils (green)';
line8='       5              User Defined 1 (white)';
line9='       6              User Defined 2 (cyan)';
```

```
line10='-----------------------------------------------------------------';
shortcuts_message=strvcat(line1,line2, line3, line4, line5, line6,...
   line7, line8, line9, line10);
helpdlg(shortcuts_message,'Help  -  Keyboard Shortcuts');

% ------------------------------------------------------------------- %
% ------------------------------------------------------------------- %
%                  Subroutines used in the m-file                     %
% ------------------------------------------------------------------- %
% ------------------------------------------------------------------- %
% --------------------------------------------------------------------
function load_listbox(dir_path,handles)
% load_listbox populates the file selecting list box.
cd (dir_path)
dir_struct = dir(dir_path);
[sorted_names,sorted_index] = sortrows({dir_struct.name}');
handles.file_names = sorted_names;

% Filters out all files besides image files, directories, and parent folders
image_types={'jpeg';'jpg';'tiff';'bmp'};
dir_size=size(handles.file_names);
j=1;
for i=1:dir_size
   cur_file=strvcat(handles.file_names(i));
   [name,format]=strread(cur_file,'%s%s','delimiter','.');
   if isempty(format) | strcmp(format,'')
      new_files.names(j,:)=handles.file_names(i);
      new_files.isdir(j)=1;
      j=j+1;
   elseif ~isempty(format)
      for k=1:length(image_types)
         if strcmp(format,image_types(k))
            new_files.names(j,:)=handles.file_names(i);
            new_files.isdir(j)=0;
            j=j+1;
         end
      end
   end
end
handles.file_names = new_files.names;
[sorted_names,sorted_index] = sortrows(handles.file_names);
handles.file_names = sorted_names;

handles.is_dir = new_files.isdir;
handles.sorted_index = [sorted_index];
guidata(handles.figure1,handles)
%set(handles.openfile,'String',handles.file_names,'Value',1)
%set(handles.text1,'String',pwd)

function handles=reset_coords(handles)
% Initializes or resets the coordinates in the handle-structure.
handles.coords.type1.xstore=[];
handles.coords.type1.ystore=[];
handles.coords.type1.nstore=0;
handles.coords.type1.ID='macrophages';
handles.coords.type2=handles.coords.type1;
```

```
handles.coords.type2.ID='mast cells';
handles.coords.type3=handles.coords.type1;
handles.coords.type3.ID='leukocytes';
handles.coords.type4=handles.coords.type1;
handles.coords.type4.ID='neutrophils';
handles.coords.type5=handles.coords.type1;
handles.coords.type5.ID='user defined 1';
handles.coords.type6=handles.coords.type1;
handles.coords.type6.ID='user defined 2';

function handles=pickcells(handles,val);
% Main cell picking routine.
% Calls subroutines plot_coords
% Left click adds a dot. Right click deletes one.
% All other keyboard input exits cell picking mode.
button=0;
idelete=0;
xmax=handles.init_xl(2);
ymax=handles.init_yl(2);
nstop=0;
handles.axis=axis;

% Depending on case the coords are restored from handles structure.
switch val
case 1
   xstore=handles.coords.type1.xstore;
   ystore=handles.coords.type1.ystore;
   nstore=handles.coords.type1.nstore;
case 2
   xstore=handles.coords.type2.xstore;
   ystore=handles.coords.type2.ystore;
   nstore=handles.coords.type2.nstore;
case 3
   xstore=handles.coords.type3.xstore;
   ystore=handles.coords.type3.ystore;
   nstore=handles.coords.type3.nstore;
case 4
   xstore=handles.coords.type4.xstore;
   ystore=handles.coords.type4.ystore;
   nstore=handles.coords.type4.nstore;
case 5
   xstore=handles.coords.type5.xstore;
   ystore=handles.coords.type5.ystore;
   nstore=handles.coords.type5.nstore;
case 6
   xstore=handles.coords.type6.xstore;
   ystore=handles.coords.type6.ystore;
   nstore=handles.coords.type6.nstore;
end
handles=plot_coords(handles,val,xstore,ystore,nstore);
while(nstop~=1)
          [xpick, ypick, button] = ginput(1);
   type=get(gco,'Type'); % Only allows a user to select or remove a point if the cursor is over the image
   disp(type)
   if button==1 & strcmp(type,'image')
      xstore = [xstore, xpick];
```

```
      ystore = [ystore, ypick];
      nstore = nstore+1;
      %wavplay(handles.sound)
      handles = plot_coords(handles,val,xstore,ystore,nstore);
    elseif button==3
      for i=1:nstore;
        % Sensitivity of delete function is modified to be based upon
        % a measure of zoom level named avgdiff
        xl=xlim;
        yl=ylim;
        xldiff=1-abs(handles.init_xl(2)-xl(2))/handles.init_xl(2);
        yldiff=1-abs(handles.init_yl(2)-yl(2))/handles.init_yl(2);
        avgdiff=abs(xldiff+yldiff)/2;
        avgdiff=avgdiff/3;
        imsize_factor=handles.init_xl(2)/40;
        distance_from_marker=(((xpick-xstore(i))^2+(ypick-ystore(i))^2)^0.5);
        disp(distance_from_marker);
        if(distance_from_marker<=imsize_factor*avgdiff)
          idelete=i;
        end
      end
                    if(idelete~=0)
                xstore(:,[idelete])=[];
                                ystore(:,[idelete])=[];
        nstore=nstore-1;
        idelete=0;
        %wavplay(handles.sound2)
      end
      handles = plot_coords(handles,val,xstore,ystore,nstore);
    elseif(button~=1)&(button~=3)
      set(handles.txt_celltype,'String','(None Selected)')
    return
  end
end

function handles = plot_coords(handles,val,xstore,ystore,nstore)
% Coords are stored back again in handles structure to be able to
% plot all dots at the same time.
hold off
imshow(handles.im)
h_img=findobj(gcf,'Type','image');
xl=get(h_img,'XData');
yl=get(h_img,'YData');
xlim(xl);
ylim(yl);
convert_units(handles);
axis(handles.axis);
hold on
switch val
case 1
  handles.coords.type1.xstore=xstore;
  handles.coords.type1.ystore=ystore;
  handles.coords.type1.nstore=nstore;
case 2
  handles.coords.type2.xstore=xstore;
  handles.coords.type2.ystore=ystore;
```

```
   handles.coords.type2.nstore=nstore;
case 3
   handles.coords.type3.xstore=xstore;
   handles.coords.type3.ystore=ystore;
   handles.coords.type3.nstore=nstore;
case 4
   handles.coords.type4.xstore=xstore;
   handles.coords.type4.ystore=ystore;
   handles.coords.type4.nstore=nstore;
case 5
   handles.coords.type5.xstore=xstore;
   handles.coords.type5.ystore=ystore;
   handles.coords.type5.nstore=nstore;
case 6
   handles.coords.type6.xstore=xstore;
   handles.coords.type6.ystore=ystore;
   handles.coords.type6.nstore=nstore;
end
plot(handles.coords.type1.xstore,handles.coords.type1.ystore,'y.')
plot(handles.coords.type2.xstore,handles.coords.type2.ystore,'r.')
plot(handles.coords.type3.xstore,handles.coords.type3.ystore,'b.')
plot(handles.coords.type4.xstore,handles.coords.type4.ystore,'g.')
plot(handles.coords.type5.xstore,handles.coords.type5.ystore,'w.')
plot(handles.coords.type6.xstore,handles.coords.type6.ystore,'c.')

function handles = convert_units(handles)
% Converts image and axes units to micrometers from pixels
%%%%%%%%%%%%Right scale implemented, still need to check with
Peter%%%%%%%%%%%%%%%%
val=get(handles.Magnification,'Value');
switch val
case 1 %40x magnification
    mag_factor=.5;
case 2 %20x magnification
    mag_factor=1;
end

conversion_factor=.1699;     % Note: if this factor is changed, the panx_factor and pany_factor should also
be modified in pan.m
h_img=findobj(gcf,'Type','image');
im_xlimits=get(h_img,'XData')*conversion_factor*mag_factor;
im_ylimits=get(h_img,'YData')*conversion_factor*mag_factor;
set(h_img,'XData',im_xlimits);
set(h_img,'YData',im_ylimits);
h_axes=findobj(gcf,'Type','axes');
ax_xlimits=get(h_axes,'XLim')*conversion_factor*mag_factor;
ax_ylimits=get(h_axes,'YLim')*conversion_factor*mag_factor;
set(h_axes,'XLim',ax_xlimits);
set(h_axes,'YLim',ax_ylimits);
handles.init_xl=xlim;
handles.init_yl=ylim;

function [p_xlim, p_ylim]=modzoom(handles,input)
% Modzoom includes two features that are not available with the standard
% 'zoom' command:
% 1) retaining aspect ratio upon zooming in/out
```

```
% 2) retaining the same center point while zooming out

if strcmp(input,'leftclick')
   % Get original aspect ratio
   xl=xlim;
   yl=ylim;
   xdiff=xl(2)-xl(1);
   ydiff=yl(2)-yl(1);
   aspectr=xdiff/ydiff;
   % Draw zoom box and record points
   pointa = get(gca,'CurrentPoint');
   finalRect = rbbox;
   pointb = get(gca,'CurrentPoint');
   pointa = pointa(1,1:2);
   pointb = pointb(1,1:2);
   % Check whether user dragged box to bottom left or upper right
   if pointa(1) < pointb(1)
      xbot = pointa(1,1);
      xup = pointb(1,1);
   else
      x1ow = pointb(1,1);
      xup = pointa(1,1);
   end
   if pointa(2) < pointb(2)
      ybot=pointa(1,2);
      yup=pointb(1,2);
   else
      ybot=pointb(1,2);
      yup=pointa(1,2);
   end
   new_xdiff=abs(pointa(1)-pointb(1));
   new_ydiff=abs(pointa(2)-pointb(2));
   % Check for whether the zoom box is more vertical or horizontal and
   % zoom accordingly to hold the original aspect ratio
   if new_xdiff > new_ydiff
      xlim([xbot xup]);
      ydiff=new_xdiff/aspectr;
      margin=(ydiff-new_ydiff)/2;
      ybot=ybot-margin;
      yup=ybot+ydiff;
      ylim([ybot yup]);
   elseif new_ydiff > new_xdiff
      ylim([ybot yup]);
      xdiff=new_ydiff*aspectr;
      margin=(xdiff-new_xdiff)/2;
      xbot=xbot-margin;
      xup=xbot+xdiff;
      xlim([xbot xup]);
   end
elseif strcmp(input,'rightclick')
   % Get width and height of initial and current image in axis units
   init_xdiff=abs(handles.init_xl(1)-handles.init_xl(2));
   init_ydiff=abs(handles.init_yl(1)-handles.init_yl(2));
   xl=xlim;
   yl=ylim;
   xdiff=abs(xl(1)-xl(2));
```

```
    ydiff=abs(yl(1)-yl(2));
    % Set scale for zooming out in x and y directions
    new_xdiff=1.35*xdiff;
    new_ydiff=1.35*ydiff;
    % Calculate margin around current image within zoomed out image
    xmargin=(new_xdiff-xdiff)/2;
    ymargin=(new_ydiff-ydiff)/2;
    if new_xdiff > init_xdiff | new_ydiff > init_ydiff
        % Prevents zoomed out image from being larger than original pic
        axis tight % Sets the image to be fully zoomed out
        xslider=findobj('Tag','xslider');
        set(xslider,'Value',0);
        yslider=findobj('Tag','yslider');
        set(yslider,'Value',0);
    else
        % Set zoomed out limits for image
        new_xl_low=xl(1)-xmargin;
        new_xl_hi=xl(2)+xmargin;
        new_yl_low=yl(1)-ymargin;
        new_yl_hi=yl(2)+ymargin;
        xlim([new_xl_low new_xl_hi]);
        ylim([new_yl_low new_yl_hi]);
    end
end

function [h,handles]=keyboardPickcells(h,handles)
key=get(gcf,'CurrentCharacter');
if key=='1'
    val=1;
    celltype='Macrophages';
elseif key=='2'
    val=2;
    celltype='Mast Cells';
elseif key=='3'
    val=3;
    celltype='Leukocytes';
elseif key=='4'
    val=4;
    celltype='Neutrophils';
elseif key=='5'
    val=5;
    celltype='User Defined 1';
elseif key=='6'
    val=6;
    celltype='User Defined 2';
else
    celltype='';
end
set(handles.txt_celltype,'String',celltype)
handles = pickcells(handles,val);

function zoomlimits_func(h,handles)
state=1;
while state==1
    axis tight;
    k=waitforbuttonpress;
```

```
    type=get(gco,'Type');
    if ~strcmp(type,'image') & ~strcmp(type,'figure')
        stringval=get(gco,'String');
        tagval=get(gco,'tag');
        if ~strcmp(stringval,'zoomlimits')
            state=0;
        end
    elseif k==1
        state=0;
        stringval='';
        tagval='';
        clear functions
    end
end
set(handles.zoomlimits,'Value',0);
if strcmp(tagval,'popupmenu1')
    set(handles.popupmenu1,'Enable','on');
elseif strcmp(tagval,'xslider') | strcmp(tagval,'yslider')
    set(handles.xslider,'Enable','on');
    set(handles.yslider,'Enable','on');
end

function callbk
disp('hello world');
%*********************************************************************
%*********************************************************************

function pan(input)
%*********************************************************************
% pan.m
%*********************************************************************
% Description:
% Used with pickcells.m GUI. Updates picture position within axes to new
% position as the user pans across picture. Activated once user depresses
% the pan button, holds down the left-click button and drags the pointer
% within the axes.
%*********************************************************************
% Created by: Ben Spivey
% Last Modified: 2-26-04
%*********************************************************************

global CUR_OBJ_TYPE init_point_loc fin_point_loc cur_opposite cur_origin ratiox ratioy n_lengthx
n_lengthy
global xl yl initial_axes lengthx lengthy
if input~=zeros(2,2)
    initial_axes=input;
    lengthx=initial_axes(1,2)-initial_axes(1,1);
    lengthy=initial_axes(2,2)-initial_axes(2,1);
    input(:,:)=[];
    CUR_OBJ_TYPE = get(gco,'type');
    if strcmp(CUR_OBJ_TYPE,'image')
        set(gcf,'pointer','fleur');
        init_point_loc = get(gcf,'currentpoint');
        xl=xlim;
        yl=ylim;
        cur_origin = [xl(1) yl(1)];
```

```
      cur_opposite = [xl(2) yl(2)];
      n_lengthx=cur_opposite(1)-cur_origin(1);
      n_lengthy=cur_opposite(2)-cur_origin(2);
      ratiox = n_lengthx/lengthx;
      ratioy = n_lengthy/lengthy;
      set(gcf,'windowbuttonupfcn','pan(zeros(2,2))');
   end
else
   panx_factor=lengthx/114.7;
   pany_factor=lengthy/26.4;
   fin_point_loc=get(gcf,'currentpoint');
   delta = fin_point_loc - init_point_loc;
   delta(1) = -panx_factor*ratiox*delta(1);
   delta(2) = pany_factor*ratioy*delta(2);
   new_origin = cur_origin + delta;
   new_lim = cur_opposite + delta;
   if new_origin(1) < 0
      new_origin(1) = 0.01;
      new_lim(1) = new_origin(1) + n_lengthx;
   end
   if new_origin(2) < 0
      new_origin(2) = 0.01;
      new_lim(2) = new_origin(2) + n_lengthy;
   end
   if new_lim(1) > initial_axes(1,2)
      new_lim(1) = initial_axes(1,2);
      new_origin(1) = initial_axes(1,2) - n_lengthx;

   end
   if new_lim(2) > initial_axes(2,2)
      new_lim(2) = initial_axes(2,2);
      new_origin(2) = initial_axes(2,2) - n_lengthy;
   end
   xlim([new_origin(1) new_lim(1)]);
   ylim([new_origin(2) new_lim(2)]);
   set(gcf,'windowbuttonupfcn','remove');
   set(gcf,'windowbuttonmotionfcn','remove');
   set(gcf,'pointer','arrow');
end
%**************************************************************************
%**************************************************************************
```

Cell Density Calculations

The algorithm to determine cell density was divided into four programs:

StartProcedure.m - main program

mask2voxel.m - generates voxel mask from a series of binary images

calc_cell_bound3d - determines local cell density

polygonplot2.m - shows color-coded surface

(early incarnation of polygonplot_function.m)

Variations of this program are not presented here, but include:

1) A version of the program that calculates cell density and the cell locations and color codes the cells.
2) A version that does a weighted calculation where the proximity of cells to the center of the subvolume increases the cell density measure. It was observed that this did not significantly alter or enhance the pattern that was evident without weighting.
3) A version that solves the direct problem where the voxels available for cells is determined as opposed to the volume unavailable. This program was much slower, but presented nearly identical results and therefore helped validate the approach used.
4) An error analysis program that evaluates how the radius-to-voxel size affects the accuracy of the calculations.

```
%=========================================================================
%          StartProcedure.m
%=========================================================================
% Description:
% This is the main routine to start the procedure to determine the particle
% density for  each surface coordinate.  First of all the number of
% particles in a defined radius are calculated.  Second of all boundary
% issues are taken into account and the particle density is calculated.
%
% First order approximation of stresses can be calculated as well, there
% are commented now with '%%'.
%
% To accomplish this the m-files mask2voxel.m, calc_cells_bound3d.m are
% used. To visualize the obtained results the m-file polygonplot2.m is
% used.  To introduce a weighed function, use calc_cells_bound3d_weighed.m
%=========================================================================
% Created by: Tom Schroder and Peter Carnell
% Last Modified: 4/1/04
%=========================================================================

clear all
close all
warning off

tic

%define and initial global variables; step is the size of a voxel, Apng is the amount of
%.png files (necessary to create the voxel coordinates, see mask2voxel.m).
global stepX
global stepY
global stepZ
global radius
global Apng
stepX=10;
stepY=10;
stepZ=20;
radius=150;
Apng=26;
setname = 'R5';
surfname = '_inner';

%load the surface coordinates, the first column is unnecessary
coor = load([setname surfname '_vertices.txt']);

%load topology of the polygons
topo=load([setname surfname '_topo.txt']);
if(min(topo(:,1))==0)
   topo = topo + 1;
end

%load the particle coordinates, the first column is unnecessary
coor_p = load([setname '_cells.txt']);
```

```
%Images are read and processed to an array which consists of voxel
%coordinates
[voxel_coor]=mask2voxel;
save([setname surfname '_voxelmask_10x10x20.mat'], 'voxel_coor')

% In this file the number of inflammatory cells (particles) in a
% pre-defined radius of a surface coordinate of the model is calculated and
% stored. Later this number is converted  to the particle density. Also the
% volume ratio at surface boundary coordinates, in a sphere (3D), is
% determined.  Therefore a voxel-mask is needed.
% Every coordinate on the voxel-mask (a gridpoint) stands for a voxel and
% has a value 0 or 1.
% 1 stands for a voxel which is inside a lumen.
% 0 stands for a voxel which is outside the lumen.
% To make the computing time less only the voxels which have a voxel-value
% of 1 are  determined, the volume of these number of voxels is calculated
% and the volume the particles are found in is determined. Hence, surface
% coordinates which lie in the range of the model boundaries (physical
% boundary) have an adjusted sphere volume, the part of the sphere located
% beyond the boundary is calculated and subtracted from the total sphere
% volume.  The particle density can be calculated as follows:
% nrParticles/Vext, where Vext=volume where particles are located in.
[coor_visu]=calc_cells_bound3d(coor,coor_p,voxel_coor);

save([setname surfname '_coor_visu_10x10x20_R' num2str(radius) '.txt'], 'coor_visu', '-ASCII', '-
DOUBLE')

% this line is used to visuallize the branch at the top - like rotating
% 180 degrees - modified this approach in later code to conditionally
% invert the axes
coor_visu(:,2) = -coor_visu(:,2);
coor_visu(:,3) = -coor_visu(:,3);

%visualize the obtained data, with very efficient colorcoding by using polygons.
polygonplot2

toc
%==========================================================================
%==========================================================================

%==========================================================================
% mask2voxel.m
% 25 september 2003
%==========================================================================
%
% Images are read and processed to an array which consists of voxel coordinates
%
%==========================================================================

function [voxel_coor]=mask2voxel

%introduce global variables
global stepX
global stepY
global stepZ
global Apng;
```

```
%define path
dir=pwd;
c=strcat([dir '\R5_lumen_10x10x20_']);

voxel_coor=[];
for i=1:Apng
  %the images are read via imread
  I=logical(Imread([c num2str(i,'%04d') '.png']));

  %the pixels which have a value of 1 are located inside the lumen.
  [y x]=find(I==1);

  %the z-coordinate of a pixel, is determined, dependent of the image that is read.
  %Now it is a voxel. The height of a voxel is step.
  z=[];
  z(1:length(y),1)=(i-1);

  %the voxels are stored, with the right size (like the z-coor it is times step; a voxel has
  %dimensions: step*step*step.
  voxel_coor=[voxel_coor; (x(:,1)-0.5)*stepX (y(:,1)-0.5)*stepY z(:,1)*stepZ];

end
%=========================================================================
%=========================================================================

%=========================================================================
% calc_cells_bound3d.m
% 29 september 2003
%=========================================================================
% In this file the number of inflammatory cells (particles) in a
% pre-defined radius of a surface coordinate of the model is calculated
% and stored. Later this number is converted  to the particle density.
%=========================================================================
% Also the volume ratio at surface boundary coordinates, in a sphere
% (3D), is determined.  Therefore a voxel-mask is needed. Every
% coordinate on the voxel-mask (a gridpoint) stands for a voxel and has a
% value 0 or 1.  1 stands for a voxel which is inside a lumen.  0 stands
% for a voxel which is outside the lumen.  To make the computing time
% less only the voxels which have a voxel-value of 1 are  determined, the
% volume of these number of voxels is calculated and the volume
% the particles are found in is determined.
% Hence, surface coordinates which lie in the range of the model
% boundaries (physical  boundary) have an adjusted sphere volume, the
% part of the sphere located beyond the boundary is calculated and
% subtracted from the total sphere volume.  The particle density can be
% calculated as follows:  nrParticles/Vext, where Vext=volume where
% particles are located in.
%=========================================================================

function [coor_visu]=calc_cells_bound3d(coor,coor_p,voxel_coor)

%define global variables
global radius
global stepX
global stepY
```

```
global stepZ

%determine the minima of the model boundaries.
max_vox=max(voxel_coor(:,3));
min_vox=min(voxel_coor(:,3));

%determine the distances of a surface coordinate with all particle
%coordinates and find how many particles are within this radius for such a
%surface coordinate
for i=1:length(coor)
  distance=sqrt((coor(i,1)-coor_p(:,1)).^2+(coor(i,2)-coor_p(:,2)).^2+(coor(i,3)-coor_p(:,3)).^2);
  idist=find(distance<=radius);
  N(i,1)=length(idist);
  %the particles at the boundary are counted half.
  ibound = find(coor_p(idist,3)>max_vox-2*stepZ | coor_p(idist,3)<min_vox+2*stepZ);
  if ~isempty(ibound)
      N(i,1) = N(i,1) - 0.5*length(ibound);
  end
end

%the data is stored correctly, whereas the last column stands for the number
%of particles
coor_visu=[coor N];

%=========================================================================
% particle density calculation, determination of the volume where the
% particles are  situated in.
%=========================================================================

%calculate the total volume of a sphere
V_sphere=4/3*pi*radius^3;

%every coordinate of the surface model must be checked for boundary issues.
for i=1:length(coor_visu)
  temp=coor_visu(i,:);

  %if a surface coordinate is in range of the model boundary, not an
  %accurate volume calculation can be defined, because there is no
  %voxel-grid located outside the parameters of the model. Therefore the
  %volume of the sphere is adjusted. The sphere is not 'complete' in this
  %situation. The distance from the z-coordinate of the surface model
  %coordinate till the  maximum or minimum z-coordinate of the voxel-grid
  %(this distance is called d) is smaller than  the radius. The following
  %formula can be used to determine the volume of the sphere, V_cap,
  %outside the model boundaries:  Vcap=1/3*pi*h^2*(3*radius-h), where
  %h=radius-d-step/2; step/2 is added because V_cap would be calculated
  %differently. A voxel at the boundary has a height of step/2 which is
  %located outside the model but belongs to the model and not in the V_cap
  %calculation.

  %dmax and dmin are determined and compared to the radius for every
  %surface point.
  diff(1)=temp(3)-max_vox;, diff(2)=temp(3)-min_vox;
  dmax=abs(max_vox-temp(3));
  dmin=abs(min_vox-temp(3));
  d=min(dmax,dmin);
```

```
  if d<radius & diff(1)<0 & diff(2)>0
    h=radius-d-stepZ/2;
    Vcap=1/3*pi*h^2*(3*radius-h);
  elseif d<radius & diff(1)>0 | diff(2)<0
    h=radius+d-stepZ/2;
    Vcap=1/3*pi*h^2*(3*radius-h);
  else
    Vcap=0;
  end

  %the voxel_gridpoints in voxel_coor are located inside lumen.
  %The distance between a voxel gridpoint and the surface coordinate is
  %calculated,  and compared with the radius. The number of voxels that
  %doesn't comply are counted.
  distance=sqrt((voxel_coor(:,1)-temp(1)).^2+(voxel_coor(:,2)-temp(2)).^2+(voxel_coor(:,3)-temp(3)).^2);
  %a logical is made, it is quicker.
  amount_NOT_comply=sum(logical(distance<=radius));

  %determine the volume which corresponds with the number of voxels
  V_amount_NOT_comply=amount_NOT_comply*stepX*stepY*stepZ;

  %determine the cell density. The volume where the counted particles are
  %found is Vext and can be determined as follows:
  %Vext=V_sphere-Vcap-V_amount_not_comply.
        coor_visu(i,4)=coor_visu(i,4)/(V_sphere-Vcap-V_amount_NOT_comply);
end
%=========================================================================
%=========================================================================
```

A similar polygonplot function is presented in a separate appendix as a visualization tool and so polygonplot2.m is presented here.

Volume Measurement Error

The error associated with approximating the volume of a sphere with voxels was evaluated. The error is dependent on voxel size and sphere radius and this can be nondimensionalized by using voxel size divided by radius. Figure H-65 shows the volume error as indicated by the percent difference between the voxel approximation and exact volume of a sphere. The absolute value of the error is considered and the center of the sphere is randomly placed in a +/- one voxel distance from the center of the voxel array. The typical voxel size/radius was about 10/150 or 0.067. This results in a volume estimate error of much less than 1 percent.

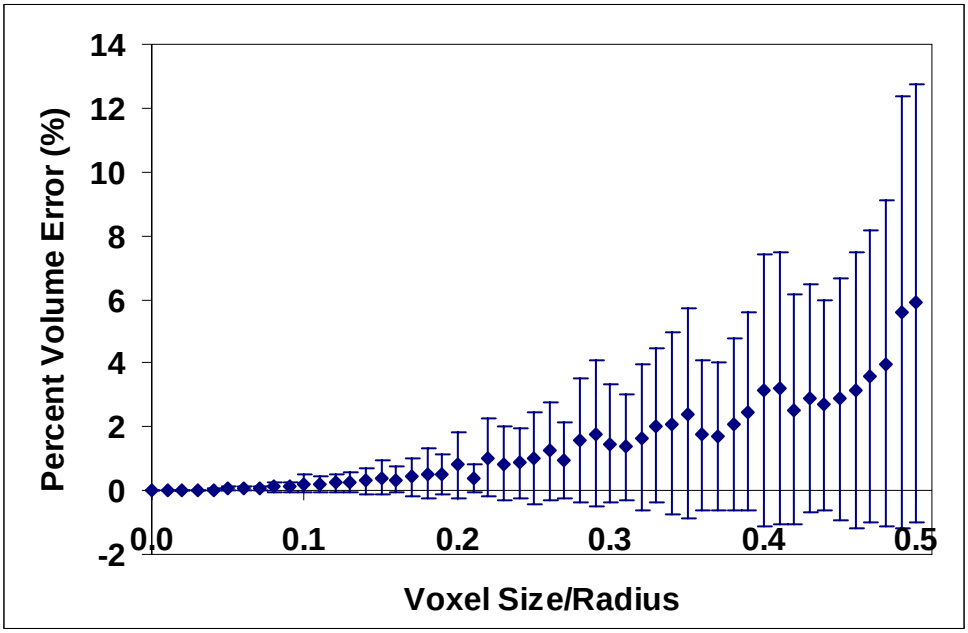

Figure H-65: Volume error estimates based on the relative voxel size.

The two programs used to generate this data follow.

```
%=========================================================================
%       error_voxelsize.m
%=========================================================================
%       determine the error involved with the used dimension of a voxel and the
%       radius; dx/Radius (dimensionless size of a voxel) vs Error
%       ((V_calc-V_actual)/V_actual)
%
%       To achieve this result the m-file error_voxel_mask.m is used.
%=========================================================================
% Created: Peter Carnell and Tom Schroder
% Last Modified: 5-30-04
%=========================================================================

clear all
close all
%introduce global variables
global radius
global step
radius=100;
step=10;

%determine actual volume of the sphere
V_actual=4/3*pi*(radius)^3;
nsamp = 100;
offset = 2*rand(3,nsamp)-1;
stats = [];
%for several voxel sizes (step) the error is calculated


h = waitbar(0,'Please wait...');
for voxel_size=1:1:50
   waitbar(voxel_size/25)
   err_array = [];
   for i = 1:nsamp;
      %rename to a better understanding variable
      dx=voxel_size;

      %calculate the number of voxels in the sphere, dependant on step and radius
      [amount]=error_voxel_mask2(radius,voxel_size,offset(:,i));

      %Determine the calculated volume.
      V_calc=amount*(voxel_size)^3;

      %determine the volume error in percentages
      err=((V_calc-V_actual)./V_actual)*100;

      %the voxel_size which is used in this calculation is visualized different
      if voxel_size==step
         r='bp';
      else
         r='k:+';
      end
      err_array = [err_array; err];
   end
   err_avg = mean(abs(err_array));
   err_std = std(err_array);
```

```
   stats = [stats; dx radius V_calc err_avg err_std];
end

figure(1)
xlabel('dx/Radius  [-]','fontsize',12)
ylabel('Volume error in percentages [-]','fontsize',12)
title('Error function of the voxel size','fontsize',14)
set(gca,'linewidth',1)
set(figure(1),'color',[1 1 1])
box off
hold on

plot(stats(:,1)./stats(:,2), stats(:,4), 'bx');
close(h)
break
for i = length(err);
   %plot the error results
   plot(dx/radius,err,r)
end
%=========================================================================
%=========================================================================

%=========================================================================
% Error_voxel_mask.m
%=========================================================================
% The number of voxel gridpoints is calculated, by calculating the distance
% of a voxel gridpoint with the origin. The distance is compared to  the
% radius and can be calculated as follows:
%
% d = sqrt((x-0)^2+(y-0)^2+(z-0)^2)
%=========================================================================
% Created: Peter Carnell and Tom Schroder
% Last Modified: 5-30-04
%=========================================================================

function [amount]=error_voxel_mask(radius,voxel_size,offset)
%make a voxel-mask
[x,y,z]=meshgrid(-radius-voxel_size:voxel_size:radius+voxel_size,-radius-
voxel_size:voxel_size:radius+voxel_size,-radius-voxel_size:voxel_size:radius+voxel_size);
x = x + offset(1)*voxel_size;
y = y + offset(2)*voxel_size;
z = z + offset(3)*voxel_size;
%reshape the x,y and z values to 1 array with voxels (coordinates)
r=length(x);
r1=length(y);
r2=length(z);
xt=reshape(x,r^3,1);
yt=reshape(y,r1^3,1);
zt=reshape(z,r2^3,1);
v_voxel_coor=[xt yt zt];
%determine the distance between each point in the voxel-mask, compare it
%with the  radius and find how many voxels are inside the sphere.
distance=sqrt(v_voxel_coor(:,1).^2+v_voxel_coor(:,2).^2+v_voxel_coor(:,3).^2);
amount=length(find(distance<=radius));
%=========================================================================
%=========================================================================
```

Branch Proximity Measurement

Figure H-66 shows a sample plot indicating the relationship between branch proximity and cell density. The program used to generate this data follows. Figure H-67 is a color coded representation of the minimum distance distribution for one case (Branch R1 or H7C).

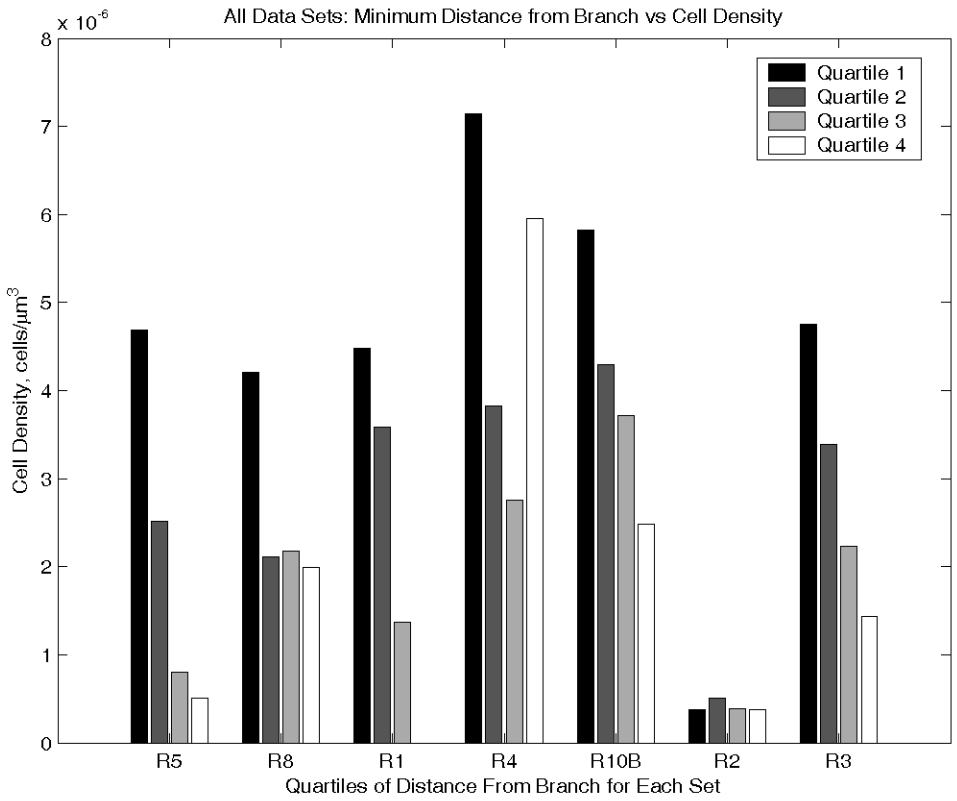

Figure H-66: Sample results from the branch proximity program. This program can be used to compare any two variables, but here it shows a strong relationship between cell density and branch proximity. Quartile 1 is the closest quartile of surface points to a branch and Quartile 4 is the farthest. Note the strong pattern for all cases except R4 (called H7D in the body of the report) and R2 (called NA in the body of the report).

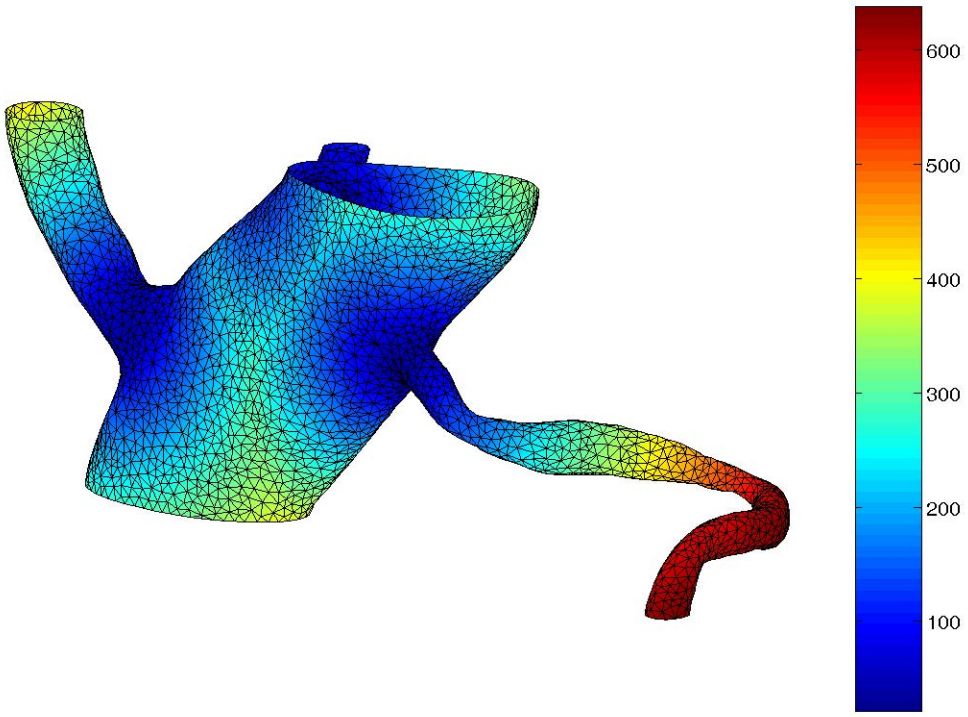

Figure H-67: Color-coded representation of the minimum distance from the nearest branch (distances μm). This is an inverse measure of branch proximity, as reflected by the low values near the branches (1 in ≈ 260 μm).

```
%=========================================================================
%       multiple_distance_only_dataset_new2.m
%=========================================================================
% Description:
% This is a modified routine for generating a proximity measure.  The
% proximity measure is based on the minimum distance between each surface
% point and the nearest branch center. Hence models that have multiple
% branches have multiple branch centers and the minimum distance to a
% branch is the minimum of the distance measurements from each center.
% This program also divides the data into quartiles based on one variable
% and then determines the average of a second variable within each
% quartile.  This visual approach complements the Wilcoxon rank sum test
% results.
% Note that this program was modified to include branch proximity
% calculations, but was never streamlined or cleaned up for this function.
%=========================================================================
% Created by: Peter Carnell
% Last Modified: 12-31-03
%=========================================================================

clear all
close all
```

```
random_noise = 0;
v_array = [];
std_array = [];

v2_name = 'inner_cell_density';
%v2_name = 'inner_wall_tension';
%v2_name = 'inner_seqv'; v2_name = 'inner_sint'; v2_name =
%'inner_invariant1'; v2_name = 'inner_invariant2'; v2_name =
%'inner_wall_thickness';

set_array = {'R5' 'R8' 'R1' 'R4' 'R10B' 'R2' 'R3'};
set_array = {'R1'};

v1_array = {'inner_wall_tension' ...
      'inner_seqv' ...
      'inner_sint' ...
      'inner_invariant1' ...
      'inner_invariant2' ...
      'inner_wall_thickness'};
v1_array = {'inner_wall_tension'};

for iset = 1:length(set_array);
   for jvalue = 1:length(v1_array);

      setname = set_array{iset};
      v1_name = v1_array{jvalue};

      if strcmp(setname,'R1')
         setlabel = ' - 7d';
         center = [1829.6311609447 1545.031205751  255.8148578727;
            1553.5209095106  1663.2768092677  471.3820281066;
            1459.1700164601          1944.293908309  293.7233075499];
      elseif strcmp(setname,'R4')
         setlabel = ' - 7d';
         center = [1252.03960437325          799.79613656175          197.4819276459];
      elseif strcmp(setname,'R5')
         setlabel = ' - 7d';
         center = [1060.187235  330.6016733  228.6537601]
      elseif strcmp(setname,'R8')
         setlabel = ' - 7d';
         center = [876.5785606 963.3715381 368.1694551; ...
               938.2410880 749.8838400 217.7375680];
      elseif strcmp(setname,'R10B')
         setlabel = ' - 21d';
         center = [583.7999051       607.700475       262.2018684];
      elseif strcmp(setname,'R2')
         setlabel = ' - Norm';
         center = [1724.543399       806.8681927       249.9689581];
      elseif strcmp(setname,'R3')
         setlabel = ' - Norm';
         center = [525.1430557       458.9273303       320.6900437];
      end

      if random_noise
         deltac = 50*rand(size(center)).*sign(randn(size(center)));
         center = center + deltac;
```

```
end

if strcmp(v1_name,'inner_wall_tension')
   xlabel_1 = 'Maximal Wall Tension, N/m';
   xlabel_2 = 'Quartiles of Wall Tension';
elseif strcmp(v1_name,'inner_seqv')
   xlabel_1 = 'Von Mises Stress, kPa';
   xlabel_2 = 'Quartiles of von Mises Stress';
elseif strcmp(v1_name,'inner_sint')
   xlabel_1 = 'Stress Intensity, kPa';
   xlabel_2 = 'Quartiles of Stress Intensity';
elseif strcmp(v1_name,'inner_invariant1')
   xlabel_1 = '1^{st} Stress Invariant, kPa';
   xlabel_2 = 'Quartiles of 1^{st} Stress Invariant';
elseif strcmp(v1_name,'inner_invariant2')
   xlabel_1 = '2^{nd} Stress Invariant, kPa^{2}';
   xlabel_2 = 'Quartiles of 2^{nd} Stress Invariant';
elseif strcmp(v1_name,'inner_wall_thickness')
   xlabel_1 = 'Wall Thickness, \mum';
   xlabel_2 = 'Quartiles of Wall Thickness';
end

if strcmp(v2_name,'inner_cell_density')
   ylabel_1 = 'Cell Density, cells/\mum^{3}';
elseif strcmp(v2_name,'inner_wall_thickness')
   ylabel_1 = 'Wall Thickness, \mum';
elseif strcmp(v2_name,'inner_wall_tension')
   ylabel_1 = 'Maximal Wall Tension, N/m';
elseif strcmp(v2_name,'inner_seqv')
   ylabel_1 = 'Von Mises Stress, kPa';
elseif strcmp(v2_name,'inner_sint')
   ylabel_1 = 'Stress Intensity, kPa';
elseif strcmp(v2_name,'inner_invariant1')
   ylabel_1 = '1^{st} Stress Invariant, kPa';
elseif strcmp(v2_name,'inner_invariant2')
   ylabel_1 = '2^{nd} Stress Invariant, kPa^{2}';
end

coor_in=load([setname '_inner_vertices.txt']);
if(exist([setname '_' v1_name '.txt']))
   disp(['...loading ' v1_name ' from memory.'])
   v1 = load([setname '_' v1_name '.txt']);
else
   disp(['File ' setname v1_name '.txt not found.']);
   break
end

%%%%Temporary Code to Generate Distance Files
dist = [];
for i = 1:size(center,1)
   dist_temp = ((coor_in(:,1) - center(i,1)).^2 + (coor_in(:,2) - center(i,2)).^2 + (coor_in(:,3) -
center(i,3)).^2).^0.5;
   dist = [dist dist_temp];
end
dist_min = min(dist,[],2);
save([setname '_inner_mindist.txt'], 'dist_min', '-ASCII');
```

```
%%%%%

if(exist([setname '_' v2_name '.txt']))
   disp(['...loading ' v2_name ' from memory.'])
   v2 = load([setname '_' v2_name '.txt']);
else
   disp(['File ' setname v2_name '.txt not found.']);
   break
end
maxz = max(coor_in(:,3));
minz = min(coor_in(:,3));
boundary_crop = 0.1*(maxz - minz);
maxz_crop = maxz - boundary_crop;
minz_crop = minz + boundary_crop;
icrop = find(coor_in(:,3) < maxz_crop & coor_in(:,3) > minz_crop);
coor_crop = coor_in(icrop,:);
v1_crop = v1(icrop);
v2_crop = v2(icrop);

% Separate v1_crop into quartiles & plot
ndiv = 4;

minv1_crop =  min(v1_crop);
maxv1_crop =  max(v1_crop);
for i = 1:ndiv;
   v_seg_top1 = maxv1_crop*i/ndiv + minv1_crop*(ndiv-i)/ndiv;
   v_seg_bot1 = maxv1_crop*(i-1)/ndiv + minv1_crop*(ndiv-i+1)/ndiv;
   ifind = find(v1_crop <= v_seg_top1 & v1_crop > v_seg_bot1);
   v_seg_mean1(i,1) = mean(v2_crop(ifind));
   v_std1(i,1) = std(v2_crop(ifind));
end

% calculate distance from center
%coor_crop = coor_in(icrop,:);
dist = [];
for i = 1:size(center,1)
   dist_temp = ((coor_in(:,1) - center(i,1)).^2 + (coor_in(:,2) - center(i,2)).^2 + (coor_in(:,3) -
center(i,3)).^2).^0.5;
   dist = [dist dist_temp];
end
dist_min = min(dist,[],2);
v3 = dist_min;
v3_crop = dist_min(icrop,:);


minv3_crop =  min(v3_crop);
maxv3_crop =  max(v3_crop);
for i = 1:ndiv;
   v_seg_top3 = maxv3_crop*i/ndiv + minv3_crop*(ndiv-i)/ndiv;
   v_seg_bot3 = maxv3_crop*(i-1)/ndiv + minv3_crop*(ndiv-i+1)/ndiv;
   ifind = find(v3_crop <= v_seg_top3 & v3_crop > v_seg_bot3);
   v_seg_mean31(i,1) = mean(v1_crop(ifind));
   v_std31(i,1) = std(v1_crop(ifind));
   v_seg_mean32(i,1) = mean(v2_crop(ifind));
   v_std32(i,1) = std(v2_crop(ifind));
end
```

```
        bdwidth = 5;
        topbdwidth = 30;
        sfract = 0.7;
        % %Ensure root units are pixels and get the size of the screen
        set(0,'Units','pixels')
        scnsize = get(0,'ScreenSize');
        %Define the size and location of the figures
        % [left bottom width heighth]
        pos1  = [bdwidth, (1-sfract)*scnsize(4)+bdwidth, scnsize(3)/2-2*bdwidth, sfract*scnsize(4)-
(topbdwidth+bdwidth)];
        pos2 = [pos1(1)+scnsize(3)/2, pos1(2), pos1(3), pos1(4)];

        comx = find(xlabel_1 == ',');
        comy = find(ylabel_1 == ',');

        v_array = [v_array; v_seg_mean32'];
        std_array = [std_array; v_std32'];
    end

end

figure
bar(v_array)
xlabel('Quartiles of Distance From Branch for Each Set')
ylabel(ylabel_1)
title(['All Data Sets: Minimum Distance from Branch vs ' ylabel_1(1:comy-1)])
set(gca,'XTickLabel', set_array)
legend('Quartile 1', 'Quartile 2', 'Quartile 3', 'Quartile 4', 0)
colormap(gray)

figure
plot3(coor_in(:,1),coor_in(:,2),coor_in(:,3),'b.')
hold on
plot3(center(:,1),center(:,2),center(:,3),'r*')

% Plot color coded distribution of min distance (v3)
figure
topo=load([setname '_inner_topo.txt']);
polygonplot_function(coor_in, topo, v3)
viewpoint = [172.5 16];
view(viewpoint)
colorbar
```

Appendix I:
Visualization Tools

In the previous appendix the cell density calculations were discussed and a polygon plotting program was mentioned. In this appendix the surface representation method will be presented with both color coding and shading.

1. Reading Surface Data
2. Shading Branch Surfaces
3. Color Coding and Scaling Branch Surfaces

Reading Surface Data

A variety of file formats may be used to represent surfaces, Amira uses a ".surf" format for which a Matlab conversion program was written. The key elements of a surface that are of interest are the vertices or points on the surface and the connectivity between those points. Sample code from such a file is contained in read_surf.m program that follows. In the visualizations in this research the vertices and topology are treated a coupled but separate files. The file names have unique prefixes that end in "_vertices" or "_topo" depending on data contained in the file.

```
%==========================================================================
% read_surf.m
%==========================================================================
% Description:
% This program reads an ASCII *.surf file exported from Amira and extracts
% the vertices and topology as separate files.  The files preserve the
% prefix name
%==========================================================================
% Created: Peter Carnell
% Last Modified: 11-20-03
%==========================================================================
%
% Sample format with column numbers:
%12345678901234567890123456789012345678901234567890123456789012345678901234567890
%# HyperSurface 0.1 ASCII
%
%Parameters {
%    Materials {
%        Inside {
%            id 0
%        }
%        Outside {
%            id 1
%        }
%    }
%    Filename "D:/Users/Peter Carnell/R5 - 7d/Variable Thickness/R5_mid.stl"
%}
%
%Vertices 5308
%"        1000.728210 255.218033 252.625443"
%"        997.597717 254.016663 262.250061"
%"        985.538208 254.928513 258.004181"
%NBranchingPoints 0
%NVerticesOnCurves 0
%BoundaryCurves 0
%Patches 1
%{
%InnerRegion Inside
```

```
%OuterRegion Outside
%BoundaryID 0
%BranchingPoints 0
%
%Triangles 10196
%  1 2 3
%  4 1 3
%  2 5 3
%12345678901234567890123456789012345678901234567890123456789012345678901234567890

clear all
close all hidden
tic
% open file
file_in = 'R5_mid.surf';
file_prefix = file_in(1:length(file_in)-5);

fid = fopen(file_in, 'r');
eofstat = 0;
% until end of file is reached...
while(eofstat==0)
   % read each line as character string
   tline = fgets(fid);
   % if character string meets data characteristics, extract data
   if(length(tline)) > 7 & tline(1:8) == 'Vertices';
      nvert = str2num(tline(9:end));
      for ivert = 1:nvert;
         tline = fgets(fid);
%           [x(nread,1) y(nread,1) z(nread,1)]= strread(tline,'%s %s %s');
         [vertices(ivert,1:3)]= strread(tline(2:end));
      end
   elseif(length(tline)) > 8 & tline(1:9) == 'Triangles';
      ntriangles = str2num(tline(10:end));
      for itriangles = 1:ntriangles;
         tline = fgets(fid);
         [topo(itriangles,1:3)]= strread(tline(2:end));
      end
   end
   eofstat = feof(fid);
end

fclose(fid);
save([file_prefix '_vertices_test.txt'], 'vertices', '-ASCII')
%save([file_prefix '_topo.txt'], 'topo', '-ASCII')

fid = fopen([file_prefix '_topo_test.txt'],'w');
fprintf(fid,'%i %i %i\n',topo');
fclose(fid);

toc
%=========================================================================
%=========================================================================
```

Shading Branch Surfaces

Branches were represented as shaded surfaces to provide more information about subtle nuances in the geometry that might not be as apparent in a wireframe or polygon representation. Shading was used for the grayscale reconstructions and also used in concert with the cell color-coding. But no shading was used with the color-coded surface visualizations, since it might cause confusion about the distribution of a given characteristic.

```
%=========================================================================
% surfaceplots_shaded_wcells.m
%=========================================================================
% Description:
% This program is a stripped-down version of the surfaceplot program.  It
% lights and shades the vessel surface and color codes the cells.  It can
% produce front and back views.  This version does not include the same
% dimensional scale control used elsewhere.% The options include:
%      inclusion colorbar (or not)
%      inclusion of rear view (or not)
%      inclusion of color-coded cells (or not)
%=========================================================================
% Created by: Peter Carnell
% Last Modified: 5-28-04
%=========================================================================

clear all
close all
colorbar_on = 1;
viewback = 1;
same_color_scale = 0;
v_array = [];
plotcells = 1;

% Define set of models to cycle through
set_array = {'R1' 'R4' 'R5' 'R8' 'R10B' 'R2' 'R3'};
set_array = {'R10B'};

% Define set of values to cycle through Note: For this version the only
% value in the value array is 'inner_shaded.'
v_array = {'inner_shaded'};
stat_v = [];
% Loop through each model
for iset = 1:length(set_array);
   % Loop through each value. Note that this option may yield unclear
   % results when shading is combined with surface values, if values other
   % than shading (constant) are used.
   for jvalue = 1:length(v_array);
      setname = set_array{iset};
```

```
        v_name = v_array{jvalue};
        coor_p = load([setname '_cells_v.txt']);
        if(size(coor_p,2)==5)
           coor_p=coor_p(:,2:5);
        end
        vc = coor_p(:,4);
        coor_p = coor_p(:,1:3);
        % Set view and scale parameters that are specific to each model.
        if strcmp(setname,'R1')
           setlabel = ' - 7d';
           viewpoint = [172.5 16];
           campoint = [-30,30];
           invert_coor = 0;
        elseif strcmp(setname,'R4')
           setlabel = ' - 7d';
           viewpoint = [172.5 16];
           campoint = [-30,30];
           invert_coor = 1;
        elseif strcmp(setname,'R5')
           setlabel = ' - 7d';
           viewpoint = [172.5 16];
           campoint = [-30,30];
           invert_coor = 1;
        elseif strcmp(setname,'R8')
           setlabel = ' - 7d';
           viewpoint = [105 16];
           campoint = [-30,30];
           invert_coor = 0;
        elseif strcmp(setname,'R10B')
           setlabel = ' - 21d';
           viewpoint = [-69 14];
           campoint = [-30,30];
           invert_coor = 1;
        elseif strcmp(setname,'R2')
           setlabel = ' - Norm';
           viewpoint = [172.5 16];
           campoint = [-30,30];
           invert_coor = 0;
        elseif strcmp(setname,'R3')
           setlabel = ' - Norm';
           viewpoint = [-69 14];
           campoint = [-30,30];
set           invert_coor = 0;
        end

        % Load the coordinates
        coor=load([setname '_inner_vertices.txt']);
        if strcmp(setname,'R1')
           coor=load([setname '_inner_vertices_moved.txt']);
        end
        % Load topo data and set all vertex values to one for shading.
        topo = load([setname '_inner_topo.txt']);
        if strcmp(v_name,'inner_shaded')
           v = 1e-9*ones(length(coor),1);
        elseif(exist([setname '_' v_name '.txt']))
           disp(['...loading ' v_name ' from memory.'])
```

```
   v = load([setname '_' v_name '.txt']);
else
   disp(['File ' setname '_' v_name '.txt not found.']);
   break
end

% Open new figure window and invert axes if appropriate for model.
figure
if invert_coor
   set(gca,'YDir','reverse')
   set(gca,'ZDir','reverse')
end
% Plot surface and determine initial viewpoint
polygonplot_function(coor,topo,v);
material([0.6 0.8 0.1 25 1.0])
camlight(campoint(1),campoint(2))
shading interp
minvc = min(vc);
minvc = 0;
maxvc = max(vc);
caxis([minvc maxvc])
view(viewpoint)
scale = 8;
[xs,ys,zs] = sphere(20);
xs = scale*xs;
ys = scale*ys;
zs = scale*zs;
cs = ones(size(zs));
for i = 1:length(coor_p)
   surf(xs+coor_p(i,1), ys+coor_p(i,2), zs+coor_p(i,3), vc(i)*cs)
end
material([0.8 0.8 0.1 25 1.0])
shading interp;
handle_cells = findobj('Type','surface');
%set(handle_cells,'FaceColor',[0.3 0.2 0.6]);
v_name = [v_name '_wcells'];
handle_vessel = findobj('Type','patch');
set(handle_vessel,'FaceLighting','phong')
set(handle_vessel,'FaceColor',[0.5, 0.5 0.5])
if colorbar_on
   colorbar
end
saveas(gcf,[setname '_' v_name '.png'])

if viewback
   % Determine view distance to be used for back view
   camera_pos = get(gca,'CameraPosition');
   camera_tar = get(gca,'CameraTarget');
   camera_dist = camera_pos - camera_tar;
   viewdist = (sum(camera_dist.^2))^0.5;

   % Rotate viewpoint azimuth angle
   viewpoint(1) = viewpoint(1) + 180;

   % Open new figure window and invert axes if appropriate for model.
   figure
```

```
        if invert_coor
           set(gca,'YDir','reverse')
           set(gca,'ZDir','reverse')
        end

        % Plot surface and determine initial viewpoint
        polygonplot_function(coor,topo,v);
        material([0.6 0.8 0.1 25 1.0])
        shading interp
        caxis([minvc maxvc])
        view(viewpoint)
        for i = 1:length(coor_p)
           surf(xs+coor_p(i,1), ys+coor_p(i,2), zs+coor_p(i,3), vc(i)*cs)
        end
        material([0.8 0.8 0.1 25 1.0])
        shading interp;
        handle_cells = findobj('Type','surface');
        %set(handle_cells,'FaceColor',[0.3 0.2 0.6]);
        handle_vessel = findobj('Type','patch');
        set(handle_vessel,'FaceLighting','phong')
        set(handle_vessel,'FaceColor',[0.5, 0.5 0.5])
        % Determine initial camera-target properties for back view and
        % then dolly camera along view axis to achieve same scale as
        % front view.
        camera_pos_back = get(gca,'CameraPosition');
        camera_tar_back = get(gca,'CameraTarget');
        camera_dist_back = camera_pos_back - camera_tar_back;
        viewdist_back = (sum(camera_dist_back.^2))^0.5;
        dolly_z = 1 - viewdist/viewdist_back;
        camdolly(0,0,dolly_z,'fixtarget');
        set(gca, 'CameraPosition', camera_pos_back);
        camera_pos_back = get(gca,'CameraPosition');
        camera_tar_back = get(gca,'CameraTarget');
        camera_dist_back = camera_pos_back - camera_tar_back;
        camlight(campoint(1),campoint(2))
        saveas(gcf,[setname '_' v_name '_back.png'])
      end
   end
   maxv = max(v);
   minv = min(v);
   meanv = mean(v);
   stdv = std(v);
   pdiffmax = (maxv - meanv)/meanv;
   pdiffmin = (minv - meanv)/meanv;
   temp_v = [meanv stdv maxv pdiffmax minv pdiffmin];
   stat_v = [stat_v; temp_v];
end
%=========================================================================
%=========================================================================
```

Color Coding and Scaling Branch Surfaces

As an alternative to shading the surfaces, color-coding the surfaces was a better approach for coupling the three dimensional pattern of a branch characteristic with the underlying geometry. The following program includes an option to scale the plots so that all the branches share a common spatial scale. A scale legend can also be included.

The basic approach is to adjust the camera distance so that it is constant for all branches. The furthest camera-to-branch distance must be used to keep the geometry completely within the figure window. The scale legend was plotted horizontally in the plane of projection. This involved some computation, but was an important step to assuring an accurate representation of scale.

```
%=========================================================================
% same_size_surfaceplots_shaded.m
%=========================================================================
% Description:
% This program generates shaded surface maps for any of the sets listed in
% set_array. This particular version can adjust the camera view so that the
% models share a common scale - this was accomplished by first cycling
% through and displaying all models with auto scaling, determining the
% distance between the camera position and the center of the geometry, and
% moving the camera position further away based on the ratio of
% viewdist_max/viewdist.  After the break at the end of the program the
% Matlab - generated distances between the camera position and the center
% of the geometry are shown.
% Back views can be generated and the scale can be adjusted using a camera
% dolly option - the camera is moved forward or back along the viewing axis
% to make the distance between the camera and target the same for both
% views.
% The options include:
%     use a common scale (or not)
%     inclusion of spatial scale (or not)
%     inclusion colorbar (or not)
%     inclusion of rear view (or not)
%     inclusion of color-coded cells (or not)
%=========================================================================
% Created by: Peter Carnell
% Last Modified: 5-14-04
%=========================================================================
% List of view distances for 7d, 21d, norm:
% R1:   viewdist = 10335.4280438042;
% R4:   viewdist = 8780.75968888954;
% R5:   viewdist = 6424.15385053687;
% R10B: viewdist = 10543.9580903059;
```

```
% R8:   viewdist = 8261.41991706657;
% R2:   viewdist = 16138.3561930909;
% R3:   viewdist = 4677.19229186058;
% This data is used to determine the maximum view distance (viewdist_max)
% to assure all branches are within the field of view
clear all
close all

viewdist_max = 16138.3561930909;
same_size = 0;
viewback = 0;
colorbar_on = 0;
v_array = [];
include_scale = 1;

% Define set of models to cycle through
set_array = {'R1' 'R4' 'R5' 'R8' 'R10B' 'R2' 'R3'};
set_array = {'R5'};

% Define set of values to cycle through
% Note: Recommend that one value at a time be used and that shading be kept
% separate from color-coding.  Color coding may require some other code
% adjustments.

% v_array = {'inner_wall_tension' ...
%         'inner_seqv' ...
%         'inner_wall_thickness' ...
%         'inner_cell_density'};
%v_array = {'inner_wall_thickness'};
%v_array = {'inner_shaded'};
stat_v = [];

% Loop through each model
for iset = 1:length(set_array);
   % Loop through each value. Note that this option may yield unclear
   % results when shading is combined with surface values, if values other
   % than shading (constant) are used.
   for jvalue = 1:length(v_array);
      setname = set_array{iset};
      v_name = v_array{jvalue};

      % Set view and scale parameters that are specific to each model.
      if strcmp(setname,'R1')
         setlabel = ' - 7d';
         viewpoint = [172.5 16];
         campoint = [-30,30];
         rscale = [-300 -500];
         invert_coor = 0;
      elseif strcmp(setname,'R4')
         setlabel = ' - 7d';
         viewpoint = [172.5 16];
         campoint = [-30,30];
         rscale = [300 500];
         invert_coor = 1;
      elseif strcmp(setname,'R5')
         setlabel = ' - 7d';
```

```
    viewpoint = [172.5 16];
    campoint = [-30,30];
    rscale = [200 400];
    invert_coor = 1;
elseif strcmp(setname,'R8')
    setlabel = ' - 7d';
    viewpoint = [105 16];
    campoint = [-30,30];
    rscale = [400 600];
    invert_coor = 0;
elseif strcmp(setname,'R10B')
    setlabel = ' - 21d';
    viewpoint = [-69 14];
    campoint = [-30,30];
    rscale = [200 400];
    invert_coor = 1;
elseif strcmp(setname,'R2')
    setlabel = ' - Norm';
    viewpoint = [172.5 16];
    campoint = [-30,30];
    rscale = [-600 -800];
    invert_coor = 0;
elseif strcmp(setname,'R3')
    setlabel = ' - Norm';
    viewpoint = [-69 14];
    campoint = [-30,30];
    rscale = [-250 -450];
    invert_coor = 0;
end

% Load the coordinates and adjust so that mean coordinate location
% is approximately zero.
coor=load([setname '_inner_vertices.txt']);
coor=coor - repmat(mean(coor),length(coor),1);

% Load topo data and set all vertex values to one for shading.
topo = load([setname '_inner_topo.txt']);
if strcmp(v_name,'inner_shaded')
    v = ones(length(coor),1);
elseif(exist([setname '_' v_name '.txt']))
    disp(['...loading ' v_name ' from memory.'])
    v = load([setname '_' v_name '.txt']);
else
    disp(['File ' setname '_' v_name '.txt not found.']);
    break
end

% Open new figure window and invert axes if appropriate for model.
figure
if invert_coor
    set(gca,'YDir','reverse')
    set(gca,'ZDir','reverse')
end

% Plot surface and determine initial viewpoint
polygonplot_function(coor,topo,v);
```

```
view(viewpoint)
if colorbar_on
   colorbar
end
% Include scale if this option is chosen.  The scale orientation is
% determined by taking the cross-product of the view direction and
% global z vector.  This cross-product represents the local
% x-direction (vperp) in the projected coordinate space.
if include_scale
   camera_tar = get(gca,'CameraTarget');
   camera_pos = get(gca,'CameraPosition');
   vcam = camera_tar - camera_pos;
   vcam = vcam/norm(vcam);
   vz = [0 0 1];
   vperp = cross(vz,vcam);
   vperp = vperp/norm(vperp);
   xp = [camera_tar(1)+vperp(1)*rscale(1) camera_tar(1)+vperp(1)*rscale(2)];
   yp = [camera_tar(2)+vperp(2)*rscale(1) camera_tar(2)+vperp(2)*rscale(2)];
   zp = [camera_tar(3)+vperp(3)*rscale(1) camera_tar(3)+vperp(3)*rscale(2)];
   hold on
   plot3(xp,yp,zp,'k-')

   % Create a long scale bar if rscale isn't already defined.
   % This helps determine where to put the scale so it doesn't
   % overlap the surface geometry.
   if ~exist('rscale', 'var')
      rscale = -500:100:500;
   end
   scale_length = max(rscale)-min(rscale);
   text(mean(xp), mean(yp), mean(zp), [num2str(scale_length) ' \mum'], ...
      'HorizontalAlignment', 'Center', 'VerticalAlignment', 'Top');
end

% Adjust viewpoint for same scale plots of all set names. Note that
% it is generally preferable to include a scale in the front view.
if same_size
   camera_pos = get(gca,'CameraPosition');
   camera_dist = camera_pos - mean(coor);
   viewdist = (sum(camera_dist.^2))^0.5;
   camera_pos = 0.77*viewdist_max/viewdist*camera_dist + mean(coor);
   set(gca,'CameraViewAngleMode','Manual')
   set(gca,'CameraPosition',camera_pos)
   v_name = [v_name '_samesize'];
end

% Adjust the surface material and lighting to achieve the desired
% shaded surface representation and save the file.
if strcmp(v_name(1:12),'inner_shaded')
   colormap('gray')
   material([0.8 0.8 0.1 25 1.0])
   camlight(campoint(1),campoint(2))
   shading faceted;
end
saveas(gcf,[setname '_' v_name '.png'])

if viewback
```

```
        % Determine view distance to be used for back view
        camera_pos = get(gca,'CameraPosition');
        camera_tar = get(gca,'CameraTarget');
        camera_dist = camera_pos - camera_tar;
        viewdist = (sum(camera_dist.^2))^0.5;

        % Rotate viewpoint azimuth angle
        viewpoint(1) = viewpoint(1) + 180;
        figure
        if invert_coor
           set(gca,'YDir','reverse')
           set(gca,'ZDir','reverse')
        end
        polygonplot_function(coor,topo,v);
        view(viewpoint)

        % Determine initial camera-target properties for back view and
        % then dolly camera along view axis to achieve same scale as
        % front view.
        camera_pos_back = get(gca,'CameraPosition');
        camera_tar_back = get(gca,'CameraTarget');
        camera_dist_back = camera_pos_back - camera_tar_back;
        viewdist_back = (sum(camera_dist_back.^2))^0.5;
        dolly_z = 1 - viewdist/viewdist_back;
        camdolly(0,0,dolly_z,'fixtarget');

        % Adjust the surface material and lighting to achieve the desired
        % shaded surface representation.
        if strcmp(v_name(1:12),'inner_shaded')
           colormap('gray')
           material([0.8 0.8 0.1 25 1.0])
           camlight(campoint(1),campoint(2))
           shading faceted;
        end
        saveas(gcf,[setname '_' v_name '_back.png'])
      end
   end
   maxv = max(v);
   minv = min(v);
   meanv = mean(v);
   stdv = std(v);
   pdiffmax = (maxv - meanv)/meanv;
   pdiffmin = (minv - meanv)/meanv;
   temp_v = [meanv stdv maxv pdiffmax minv pdiffmin];
   stat_v = [stat_v; temp_v];
end
%=========================================================================
%=========================================================================
```

Appendix J:
Finite Element Analysis Tools

To facilitate comparisons the finite element results were exported and read into Matlab using some data extraction programs.

1. Parametric Model Finite Element Model
2. Data Extraction Programs
3. Ansys APDL Code for a Parametric Model
4. Ansys APDL Code for a Histology-Based Model

Parametric Finite Element Model

Early in this research, a parametric finite element model was developed. Some sample Ansys batch files are presented later in this appendix. The main goal of these parameter studies was to investigate how gross changes in branch geometry affect the stress distribution. Initially it was thought that an idealized parametric model might be created as a surrogate for the real histological geometry. As the histological reconstructions were produced, it became clear that there was tremendous variability and great subtlety in real vessel geometry. The idealized parametric models could not capture such geometric variation. But the parametric models provided insights into how arterial branches respond and deform with pressure and influenced the final form of the finite element models.

A fully three dimensional finite element model is required to study the mechanical behavior of a branching blood vessel. The idealized geometry that will be described shortly permitted the use of quarter symmetry to evaluate stresses. This means a four-fold decrease in model size and about a sixteen-fold decrease in computational requirements. These size and computational benefits facilitated the study of a wide variety of parameters related to geometry, boundary conditions and material properties. The effect of geometric nonlinearities (large rotations, large displacements) was considered. Both linear elastic and nonlinear elastic models were developed and all models utilized quarter symmetry to reduce computational time and storage requirements.

The use of the quarter-symmetry, as described below, does not permit the study of the effects of branch angle or noncircular cross sections. It was concluded that the

additional complexity in parametric modeling did not warrant including branch angle and elliptical cross sections. Also the large localized variability in curvature and wall thickness that was seen among the histology-based reconstructions, suggested that it would be difficult to make meaningful comparisons between these histology-based reconstructions and idealized surrogates.

The branch geometry is similar in parametric form to that proposed by Thubrikar to study coronary arteries (Thubrikar, Roskelley et al. 1990). Figure J-68 shows a half-section of a daughter vessel branching from a main vessel. The quarter section that contains the mesh is representative of the finite element models used during these parameter studies.

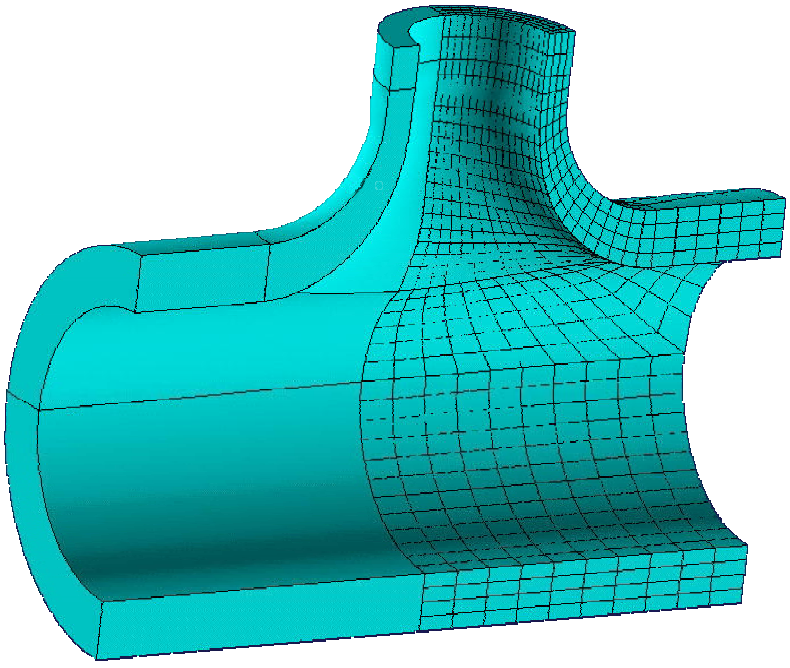

Figure J-68: Half-section of blood vessel. The meshed portion shows the quarter-symmetry of the finite element model.

For simplification, the daughter vessel was assumed to branch from the larger vessel at an angle of 90 degrees. This use of quarter-symmetry reduced the size of the model by about four-fold. Figure J-69 shows the geometric parameters that need to be defined to fully describe this geometry. R, T and L are the radius, thickness and length of the large vessel and small vessel. RXY and RYZ represent the curvatures in the XY and YZ planes, respectively. TXY and TYZ are wall thicknesses at the midpoint of the transition curve in the XY and YZ planes, respectively.

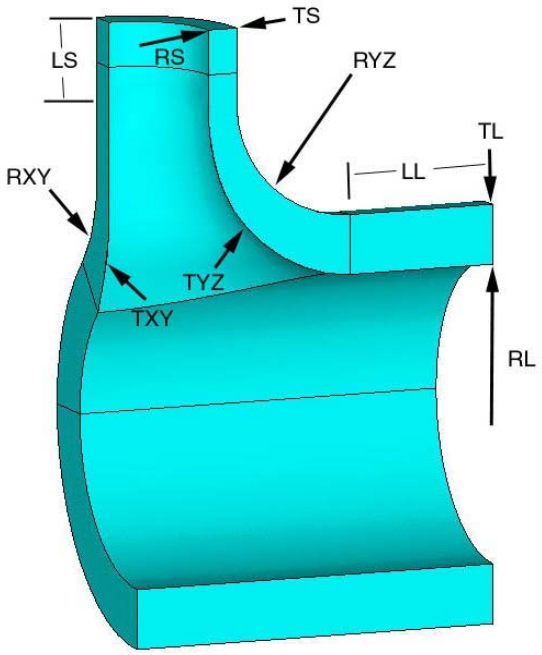

Figure J-69: Geometric parameters describing model.

This appears to be a minimum number of parameters necessary to define the geometry of a branch. This differs somewhat from Thubrikar's geometry, where the model has a prescribed transition length and a varying transition curvature that is difficult to characterize and dependent on mesh density. Thubrikar and his fellow researchers

chose this approach to avoid the abrupt transition in curvature, which might produce an artificial stress concentration, but such a problem was not seen in any of these models.

To study the effects of variations in geometry, a parametric model was developed using Ansys' parametric capabilities in batch mode. The geometry was defined algebraically and all geometric constructions were based on algebraic operations involving the geometric parameters previously identified. The model volume can be divided into three distinct sections; 1) the main vessel as represented by a quarter cylinder, 2) the daughter vessel also represented by a quarter cylinder and, 3) the transition region geometry which resembles a saddle by having radii of curvature located on opposite sides of the surfaces that define the inner and outer wall. Since the saddle is a complex geometric entity that cannot be described by volume or area primitives, the saddle volume had to built from the ground up by first creating key points, then lines, then areas, and finally the volume. The inner and outer surfaces of the saddle geometry were separately created by defining a series of splines upon which a surface was "skinned."

A hexahedral element with midside nodes was chosen to mesh the geometry (Ansys Element Reference Manual, SOLID95 element). The midside nodes make the element better suited for meshing curved surfaces. In addition the element supports large deflection, nonlinear material properties, orthotropic properties and it can tolerate irregular shapes with little loss in accuracy. The midside nodes increase the order of the element so that stresses and strains can vary linearly within the element and a lower mesh density is needed to capture stress gradients. This is particularly important since high stress gradients exist through the thickness in the transition geometry. Hexahedral

elements were chosen over tetrahedral elements because the hexahedral elements permitted greater control of mesh density, especially through the thickness of the wall.

One of the keys to efficiently/effectively modeling this branching blood vessel with brick elements is to make sure that there are a sufficient number of elements through the thickness to capture the bending behavior that occurs as the branch is pressurized.

To facilitate comparison between different models and different size vessels, the principal stresses were normalized by the mean circumferential stress:

$$\sigma_{normalized} = \frac{\sigma}{\left(\frac{PR}{h}\right)} \qquad \text{Equation J.2}$$

While there is a broad range of parameters that might be evaluated, in an effort to limit the scope and focus the parameter studies, a representative model was developed and key parameters were expressed in a nondimensionalized form. The ratio of radius to thickness is an important parameter that influences the magnitude of stress and percent variation through the thickness. The ratio of the radius divided by the thickness (R/T) was varied between 2.0 and 7.0 with the same ratio being used for both the large and small vessel (i.e. RL/TL = RS/TS).

Other parameters that were varied included the relative size of the vessels, the transition curvature and the length of the straight sections extending from the transition geometry. The ratio of the large radius to the small radius (RL/RS) was varied from 2.0 to 4.0. This range is representative of the majority of vessel branches within the mesentery of mice. The radius of curvatures associated with the XY and YZ planes were varied between 0.3*RL to 1.1*RL. Note that varying the curvatures as a function of the large vessel radius gives a more generalized solution. The lengths of the large vessel

(LL) and small vessel (LS) were varied between 0.25*RL to 3.0*RL. Once again, expressing the length as a function of the larger radius gives the results meaning for different size vessel models.

The thickness values associated with the saddle geometry, TXY and TYZ, were kept as functions of TS and TL respectively and were not varied independently. It was found that when these variables were treated independently of TS and TL that small changes would produce unnatural bulges in the transition region. These bulges are characterized by large differences in curvature from the inner surface to the outer surface of the vessel wall and do not represent the geometric patterns identified during histology.

A typical stress distribution is shown in Figure J-70. This figure is a contour plot of the maximum principal stress and it shows that the maximum stress is produced on the inner surface in a cross-section that is coincident with the longitudinal axes of both vessels. For branch angles other than 90 degrees, a greater stress occurs distal to the bifurcation, where the branch angle is acute. For this nonlinear, large deflection, large strain model, the magnitude of the maximum principal stress was about 6.7 times the average circumferential stress. The maximum principal stress was 4.4 times greater in the nonlinear model than in the linear model. The larger stress peaks in the nonlinear model can be attributed to three factors: 1) geometric changes due to large deformations (decreased wall thickness and increased curvature); 2) a less uniform distribution of stress through the thickness due to the nonlinear stress-strain behavior; and 3) more localized bending in the transition region because of large deformations. This highly localized stress peak demonstrates why real vessel branches can be ideal locations for determining if there is phenomenological connection between stress and inflammation.

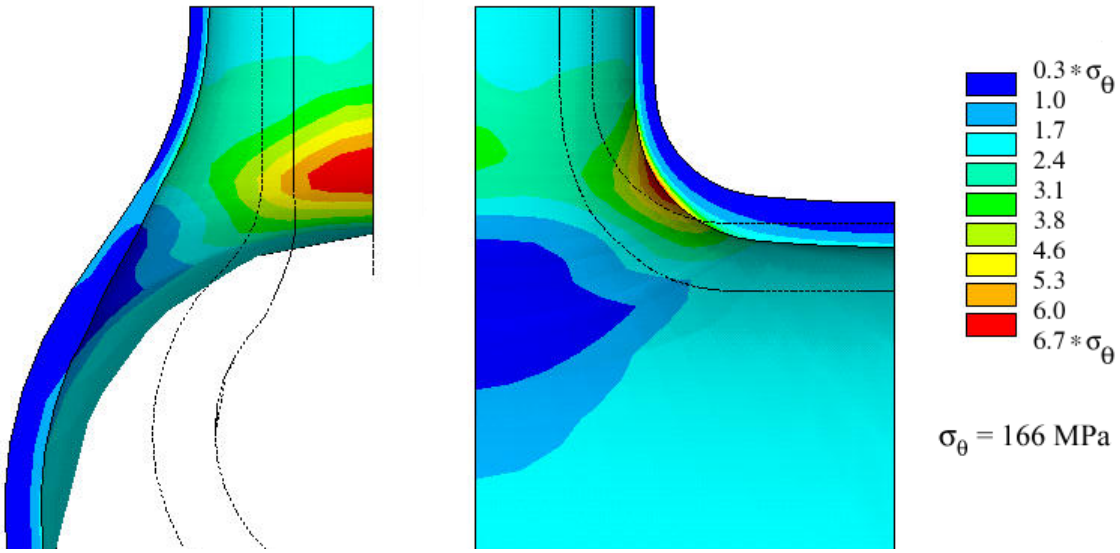

Figure J-70: Two views of the maximum principal stresses within a nonlinear model.

The stress concentration varied significantly with changes in curvature in the transition region. Figure J-71 shows that a three-fold increase in radius of curvature increased the stress concentration by 47%. Note that this behavior is opposite to what is seen in planar fillets in engineering design. This phenomenon is caused by the saddle geometry as described earlier and has been observed in pressure vessel design (Harvey 1974). This sensitivity to local changes in curvature underscores the importance of accurately representing branch architecture in the subsequent histological studies.

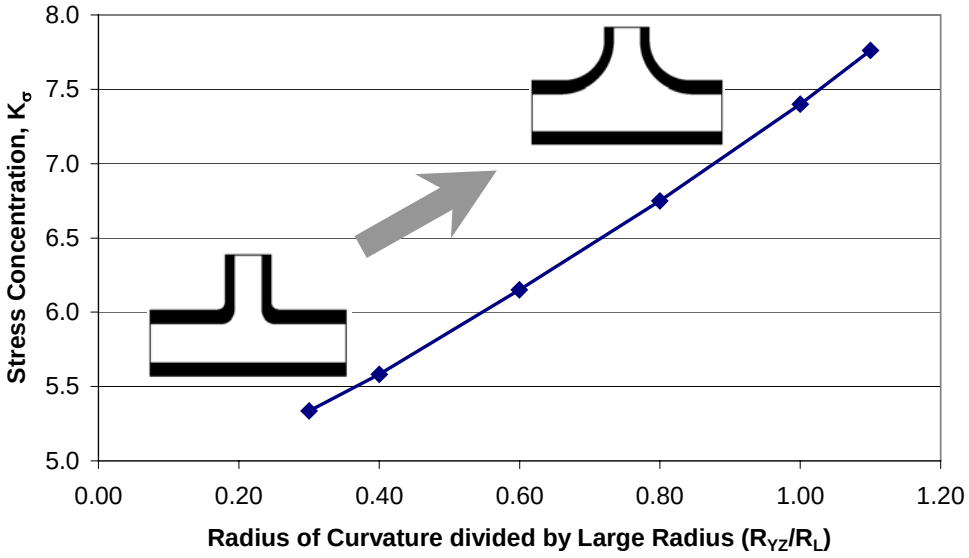

Figure J-71: Increasing radius of curvature in the transition region increases the magnitude of the stress concentration.

Convergence studies illustrate that, for hexahedral elements that permit linear variation of displacements, three layers of elements are sufficient to capture the stress variation through the thickness. A greater number of layers significantly increased the model size without a commensurate improvement in model convergence.

Data Extraction Programs

```
%*************************************************************************
% read_ansys_nlist.m
%*************************************************************************
% Description:
% This program reads a listing of nodal coordinates generated by Ansys
% nlist.lis.  The node listing is read line by line and identified as a
% line of data only if it begins with a number.  Test lines are ignored as
% are blank lines.
%*************************************************************************
% Author: Peter Carnell
% Last Modified: 2-29-04
%*************************************************************************
% Sample format with column numbers:
%12345678901234567890123456789012345678901234567890123456789012345678901234567890
%
% LIST ALL SELECTED NODES.   DSYS=  0
% SORT TABLE ON  NODE  NODE  NODE
%
%   NODE      X        Y        Z       THXY    THYZ    THZX
%      1   1015.2    254.32   351.93      0.00    0.00    0.00
%      2   978.36    276.74   343.81      0.00    0.00    0.00
%      3   1005.7    259.38   349.88      0.00    0.00    0.00
%      4   996.32    264.69   347.56      0.00    0.00    0.00
%
%12345678901234567890123456789012345678901234567890123456789012345678901234567890
clear all
close all hidden
% open file
file_in = 'nlist.lis';
file_out = [file_in(1:length(file_in)-4) '.txt'];
fid = fopen(file_in, 'r');
nread = 1;
eofstat = 0;
% until end of file is reached...
while(eofstat==0)
   % read each line as character string
   tline = fgets(fid);
   % if character string meets data characteristics, extract data
   if(length(tline)) > 7 & nread == str2num(tline(1:8));
      node(nread,1) = str2num(tline(1:9));
      x(nread,1) = str2num(tline(10:21));
      y(nread,1) = str2num(tline(22:33));
      z(nread,1) = str2num(tline(34:45));
      % could also read THXY THYZ & THZX if available
      nread = nread + 1;
   end
   eofstat = feof(fid);
end
fclose(fid);
save(file_out, 'x', 'y', 'z', '-ASCII')
%*************************************************************************
%*************************************************************************
```

```
%*************************************************************************
% read_ansys_scomp.m
%*************************************************************************
% Description:
% This program reads a listing of component stresses generated by Ansys
% prnsol_scomp.lis
%*************************************************************************
% Author: Peter Carnell
% Last Modified: 2-29-04
%*************************************************************************
% Sample format with column numbers:
%12345678901234567890123456789012345678901234567890123456789012345678901234567890
% PRINT S    NODAL SOLUTION PER NODE
%
%  ***** POST1 NODAL STRESS LISTING *****
%  PowerGraphics Is Currently Enabled
%
%  LOAD STEP=     1  SUBSTEP=     1
%   TIME=    1.0000      LOAD CASE=   0
%  SHELL NODAL RESULTS ARE AT MIDDLE FOR MATERIAL   1
%
%  THE FOLLOWING X,Y,Z VALUES ARE IN ROTATED GLOBAL COORDINATES,
%  WHICH INCLUDE RIGID BODY ROTATION EFFECTS
%
%   NODE    SX        SY        SZ        SXY       SYZ       SXZ
%      1   42684.     9229.3    35775.    -19263.    4149.6   -584.84
%      2   24350.     25007.    25414.    -22406.    13134.   -3323.3
%      3   39379.     12505.    33077.    -21390.    6000.4   -1717.2
%12345678901234567890123456789012345678901234567890123456789012345678901234567890
%*************************************************************************
clear all
close all
tic
% open file
file_in = 'prnsol_scomp.lis';
file_out = [file_in(1:length(file_in)-4) '.txt'];
fid = fopen(file_in, 'r');
nread = 1;
eofstat = 0;
% until end of file is reached...
while(eofstat==0)
   % read each line as character string
   tline = fgets(fid);
   % if character string meets data characteristics, extract data
   if(length(tline)) > 7 & nread == str2num(tline(1:9));
      node(nread,1) = str2num(tline(1:9));
      SX(nread,1) = str2num(tline(10:21));
      SY(nread,1) = str2num(tline(22:33));
      SZ(nread,1) = str2num(tline(34:45));
      SXY(nread,1) = str2num(tline(46:57));
      SYZ(nread,1) = str2num(tline(58:69));
      SXZ(nread,1) = str2num(tline(70:81));
      nread = nread + 1;
   end
   eofstat = feof(fid);
```

```
end
fclose(fid);
save(file_out, 'SX', 'SY', 'SZ', 'SXY', 'SYZ', 'SXZ', '-ASCII')
toc
%*************************************************************************
%*************************************************************************

%*************************************************************************
% read_ansys_sprinc.m
%*************************************************************************
% Description:
% This program reads a listing of principal stresses generated by Ansys
% prnsol.lis
%*************************************************************************
% Author: Peter Carnell
% Last Modified: 2-29-04
%*************************************************************************
% Sample format with column numbers:
%12345678901234567890123456789012345678901234567890123456789012345678901234567890
% PRINT S    NODAL SOLUTION PER NODE
%
%  ***** POST1 NODAL STRESS LISTING *****
%
%  LOAD STEP=     1  SUBSTEP=     1
%   TIME=    1.0000      LOAD CASE=   0
%  SHELL NODAL RESULTS ARE AT TOP
%
%    NODE    S1          S2          S3          SINT        SEQV
%       1   90528.      54002.      123.65      90404.      78771.
%       2   73399.      60476.      198.72      73200.      67671.
%       3   97831.      51581.      107.38      97724.      84672.
%       4  0.10094E+06  46976.      163.48     0.10078E+06  87350.
%    1033   26649.      3.7366     -9109.1      35759.      32185.
%12345678901234567890123456789012345678901234567890123456789012345678901234567890
clear all
close all hidden
tic
% open file
file_in = 'prnsol_sprinc.lis';
file_out = [file_in(1:length(file_in)-4) '.txt'];
fid = fopen(file_in, 'r');
nread = 1;
eofstat = 0;
% until end of file is reached...
while(eofstat==0)
   % read each line as character string
   tline = fgets(fid);
   % if character string meets data characteristics, extract data
   if(length(tline)) > 7 & nread == str2num(tline(1:8));
      node(nread,1) = str2num(tline(1:9));
      S1(nread,1) = str2num(tline(10:21));
      S2(nread,1) = str2num(tline(22:33));
      S3(nread,1) = str2num(tline(34:45));
      SINT(nread,1) = str2num(tline(46:57));
      SEQV(nread,1) = str2num(tline(58:69));
      nread = nread + 1;
```

```
   end
   eofstat = feof(fid);
end
fclose(fid);
save(file_out, 'S1', 'S2', 'S3', 'SINT', 'SEQV','-ASCII')
toc
%*************************************************************************
%*************************************************************************
```

Ansys APDL Code for a Parametric Model

Geometry Generation

```
/PREP7
/TITLE, Hypertension in a Mesenteric Artery
C*** Anaylsis type, element type, material properties
ANTYPE,STATIC
C*** Select 20-node brick element to better represent curvature and allow for easier
C*** alignment of orthotropic material properties. Note that KEYOPT(1)=1 aligns
C*** element coord system with specific midside nodes so that this coord system
C*** follows the curvature of the the blood vessel wall.
ET,1,SOLID95,1,,,,,
MP,EX,1,500
MP,NUXY,1,0.45

C*** Modify vector scaling to more easily visualize element coord systems
C*** /VSCALE,1,5,0
C*** /PSYMB,ESYS,1

/VIEW,,-1,0.2,-0.4
! /PNUM,LINE,1
/GRAPHICS,POWER
/DSCALE,1,1.0

C*** Create parameters to define geometry
RT_RATIO=2.5            ! Ratio of R/T
LS_RATIO=2.0            ! Ratio of RL/RS
PI=2*ASIN(1)            ! PI
RL=100                  ! radius of large vessel
TL=RL/RT_RATIO          ! thickness of large vessel
RS=RL/LS_RATIO          ! radius of small vessel
TS=RS/RT_RATIO          ! thickness of small vessel
RXY=TL+2*TS             ! radius of curvature in XY plane
RYZ=TL+2*TS             ! radius of curvature in YZ plane
TXY=0.4*TL+0.6*TS       ! thickness of wall at midpoint in XY plane
TYZ=0.5*TL+0.5*TS       ! thickness of wall at midpoint in YZ plane
THETAYZ=90/2/180*PI     ! angle at midpoint in YZ plane
LL=1.0*RL               ! straight length of large vessel (LL>=2*RL reduces BC effects)
LS=1.0*RS               ! straight length of small vessel (LL>=2*RL reduces BC effects)
LYZ=20                  ! extension of saddle in Y dir. (improves smoothness of skimming)

C*** Define internal pressure
P=120*0.133322          ! internal pressure (mmHg)*conversion=KPa

C*** Determine intermediate parameters
THETAXY=ACOS((RS+TS+RXY)/(RL+TL+RXY))! angle at midpoint in XY plane
X1=(RL+TL)*COS(THETAXY)              ! coordinates needed to specify the
Y1=(RL+TL)*SIN(THETAXY)              ! curves and thickness in the XY plane
X2=(RL+TL+RXY)*COS(THETAXY)          !
Y2=(RL+TL+RXY)*SIN(THETAXY)          !
X3=RS+TS                             !
Y3=(RL+TL+RXY)*SIN(THETAXY)          !
```

```
C*** Build up saddle geometry, from keypoints=>lines=>areas=>volumes

C*** Create cutting plane to trim larger vessel
K,1,0,0.95*RL,RS+TS+RYZ
K,2,0.95*RL*COS(THETAXY),0.95*RL*SIN(THETAXY),0
BSPLIN,1,2,,,,,-1,0,0,0,0,-1

K,3,0,1.05*(RL+TL),RS+TS+RYZ
K,4,1.05*(RL+TL)*COS(THETAXY),1.05*(RL+TL)*SIN(THETAXY),0
BSPLIN,3,4,,,,,-1,0,0,0,0,-1

LSTR,1,3
LSTR,2,4
AL,1,2,3,4

C*** Create upper quarter-section for larger vessel and trim w/cutting plane
CYLIND,RL,RL+TL,0,RS+TS+RYZ+LL,0,90,
VSBA,1,1,,DELETE,DELETE
VDELE,2,,,1

C*** Create lower quarter-section for larger vessel
CYLIND,RL,RL+TL,0,RS+TS+RYZ+LL,0,-90,

C*** Create quarter-section for smaller vessel in working plane
C*** WPCYS,-1,0
WPAVE,0,0,0
WPOFFS,0,RL+TL+RYZ,0
WPROTA,0,90,0
CYL4,0,0,RS,0,RS+TS,90,0
WPOFFS,0,0,-LS
CYL4,0,0,RS,0,RS+TS,90,LS-LYZ

C*** Create outer arc and inner spline and area in YZ plane
K,91,0,RL+TL+RYZ,RS+TS+RYZ,
LARC,16,20,91,RYZ,
KL,44,0.5,92,
LSTR,20,28
LCOMB,44,45,0
K,93,0,RL+TL+RYZ-(RYZ+TYZ)*COS(THETAYZ),RS+TS+RYZ-(RYZ+TYZ)*SIN(THETAYZ),
SPLINE,14,93,,,,21,0,0,1,0,1,0,
LSTR,21,29
LCOMB,47,48,0
LCOMB,47,49,0

C*** Create outer arc and inner spline and area in XY plane
/COM K,101,X1,Y1,0
K,102,X2,Y2,0
K,103,X3,Y3,0
K,104,X3-TS,Y3,0

LARC,15,103,102,RXY,
LSTR,103,19
LSTR,19,27
KL,50,0.5,105,
LCOMB,50,51,0
LCOMB,50,52,1
```

```
WPCSYS,-1,0,
KWPAVE,105
CSWPLA,11,0,1,1,
CSYS,11,
K,106,-TXY*COS(THETAXY/2),-TXY*SIN(THETAXY/2)
CSYS,0,
SPLINE,13,106,,,,104,cos(90-THETAXY),-sin(90-THETAXY),0,0,1,0,
LSTR,104,22
LSTR,22,30
LCOMB,53,54,0
LCOMB,53,55,0
LCOMB,53,56,1

C*** Create intermediate keypoints and splines to skin outer surface
NUMSTR,LINE,101
KL,44,0.15,201
KL,44,0.30,202
KL,44,0.45,203
KL,44,0.60,204
KL,44,0.75,205
KL,44,0.90,206
KL,50,0.15,211
KL,50,0.30,212
KL,50,0.45,213
KL,50,0.60,214
KL,50,0.75,215
KL,50,0.90,216
BSPLIN,201,211,,,,,-1,0,0,0,0,-1
BSPLIN,202,212,,,,,-1,0,0,0,0,-1
BSPLIN,203,213,,,,,-1,0,0,0,0,-1
BSPLIN,204,214,,,,,-1,0,0,0,0,-1
BSPLIN,205,215,,,,,-1,0,0,0,0,-1
BSPLIN,206,216,,,,,-1,0,0,0,0,-1
ASKIN,22,101,102,103,104,105,106,21,36

C*** Create intermediate keypoints and splines to skin inner surface
LFACT=0.96                ! Length factor to improve spline alignment
NUMSTR,LINE,201
KL,47,0.15,221
KL,47,0.30,222
KL,47,0.45,223
KL,47,0.60,224
KL,47,0.75,225
KL,47,0.90,226
KL,53,0.15*LFACT,231
KL,53,0.30*LFACT,232
KL,53,0.45*LFACT,233
KL,53,0.60*LFACT,234
KL,53,0.75*LFACT,235
KL,53,0.90*LFACT,236
BSPLIN,221,231,,,,,-1,0,0,0,0,-1
BSPLIN,222,232,,,,,-1,0,0,0,0,-1
BSPLIN,223,233,,,,,-1,0,0,0,0,-1
BSPLIN,224,234,,,,,-1,0,0,0,0,-1
BSPLIN,225,235,,,,,-1,0,0,0,0,-1
```

```
BSPLIN,226,236,,,,,-1,0,0,0,0,-1
ASKIN,19,201,202,203,204,205,206,30,38

AL,51,23,54,39
AL,24,46,37,48

C*** Create saddle volume from areas
VA,24,21,23,22,11,12

WPSTYLE,,,,,,,,0

C*** Connect upper and lower halves of the larger vessel
VGLUE,1,3
```

Boundary Condition Specification

```
C*** Specify pressure loading on internal surfaces
SFA,18,1,PRES,P
SFA,22,1,PRES,P
SFA,28,1,PRES,P
SFA,5,1,PRES,P

C*** Specify displacement BC's (symmetry BC's)
DA,7,SYMM      ! quarter symmetry - large vessel, lower area (UX=0)
DA,14,SYMM     ! quarter symmetry - large vessel, upper area (UX=0)
DA,24,SYMM     ! quarter symmetry - saddle area (UX=0)
DA,20,SYMM     ! quarter symmetry - small vessel, upper area (UX=0)

DA,1,SYMM      ! quarter symmetry - large vessel, lower area (UZ=0)
DA,25,SYMM     ! quarter symmetry - large vessel, upper area (UZ=0)
DA,23,SYMM     ! quarter symmetry - saddle area (UZ=0)
DA,19,SYMM     ! quarter symmetry - small vessel, upper area (UZ=0)

! DK,1,ALL      ! Fix point on axis of symmetry if necessary for model stability

C*** Specify displacement BC or no BC on cross-section of larger vessel
C*** symmetry displacement BC produces some bending resistence in YZ plane
C*** no displacement or pressure BC creates plane stress on outer surface
DA,2,SYMM      ! Lower end of large vessel (UZ=0) - comment out for plane stress
DA,26,SYMM     ! Upper end of large vessel (UZ=0) - comment out for plane stress

C*** Specify displacement BC -OR- pressure BC on cross-section of smaller vessel
C*** displacement BC implies symmetry, pressure BC is based on force equilibrium.
C*** Note that pressure and stress have opposite signs.
C*** Define normalized axial stress in smaller vessel based on
C*** equilibrium, for use as a BC.
C*** Note: The pressure-based BC is not appropriate for nonlinear/iterative
C*** models where geometry changes significantly due to deformations

! SPS=P*RS**2/(2*RS*TS+TS**2)
! SFA,10,1,PRES,-SPS     ! Pressure BC based on equilibrium

DA,10,SYMM     ! End of small vessel (UY=0)
```

Mesh Control and Generation

```
C*** Concatenate areas to obtain eight-sided volume for brick element mesh
ACCAT,26,8

C*** Specify number of divisions on lines that make up saddle volume
TDIV = 4
LDIV = 4*TDIV
CDIV = 4*TDIV
C*** Limit global size of elements to two times the element size on RYZ
SIZE=PI/2*(RYZ+LYZ)/LDIV*2
ESIZE,SIZE
C*** Specify number of divisions for lines through the thickness of saddle
TSPACE=1.0      ! Spacing ratio - negative=> denser mesh at midline
LESIZE,37,,,TDIV,SPACE
LESIZE,39,,,TDIV,SPACE
LESIZE,23,,,TDIV,SPACE
LESIZE,24,,,TDIV,SPACE
C*** Specify number of divisions for lines along length of saddle
LSPACE=-0.6     ! Spacing ratio - negative=> denser mesh at midline
LESIZE,46,,,LDIV,LSPACE
LESIZE,48,,,LDIV,LSPACE
LESIZE,51,,,LDIV,LSPACE
LESIZE,54,,,LDIV,LSPACE
C*** Specify number of divisions for lines around circumference of saddle
CSPACE=1.0      ! Spacing ratio - negative=> denser mesh at midline
LESIZE,19,,,CDIV,CSPACE
LESIZE,22,,,CDIV,CSPACE
LESIZE,36,,,CDIV,CSPACE
LESIZE,38,,,CDIV,CSPACE

VMESH,4,4,1
VMESH,2,2,1
VMESH,5,5,1
VMESH,1,1,1

FINISH

! /EXIT,NOSAV
```

Nonlinear Material Property Model

```
MP,EX,1,12000               ! INITIAL YOUNG'S MODULUS (KPa)
MP,NUXY,1,0.49              ! POISSON'S RATIO

TB,MELAS,1,1,31, ,          ! MULTILINEAR ELASTIC PROPERTY

TBPT,,1e-006,0.012          ! LOGARITHMIC STRAIN - TRUE STRESS TABLE
TBPT,,0.04879016,1.36395
TBPT,,0.09531018,2.8578
TBPT,,0.13976194,4.48155
TBPT,,0.18232156,6.2352
TBPT,,0.22314355,8.11875
```

```
TBPT,,0.26236426,10.1280915
TBPT,,0.30010459,12.54162644
TBPT,,0.33647224,15.50900575
TBPT,,0.37156356,19.15401188
TBPT,,0.40546511,23.62755801
TBPT,,0.43825493,29.11354605
TBPT,,0.47000363,35.83597454
TBPT,,0.50077529,44.06756053
TBPT,,0.53062825,54.140195
TBPT,,0.55961579,66.45761811
TBPT,,0.58778666,81.5107815
TBPT,,0.61518564,99.89646244
TBPT,,0.64185389,122.3398125
TBPT,,0.66782937,149.7216656
TBPT,,0.69314718,183.1116023
TBPT,,0.71783979,223.8079746
TBPT,,0.74193734,273.3863455
TBPT,,0.76546784,333.7580993
TBPT,,0.78845736,407.2413451
TBPT,,0.81093022,496.6466717
TBPT,,0.83290912,605.3808462
TBPT,,0.85441533,737.5721862
TBPT,,0.87546874,898.2221064
TBPT,,0.89608802,1093.388271
TBPT,,0.91629073,1330.405906

C*** SOLUTION SETTING

NLGEOM,ON          ! large deformation
AUTOTS,1
NSUBST,20,1000,1,1
```

Samples of Post-Processing Routines

```
C*** Path Definition through the thickness on YZ plane, midway along the saddle

PMAP,ACCURATE
PATH,TYZ,2,30,50,       ! Define path
PPATH,1,0,0,RL+TL,RS+TS,0,                          ! Define point 1 on path
PPATH,2,0,0,RL+TL+0.3*RYZ,RS+TS+0.3*RYZ,0,          ! Define point 2 on path
PDEF,SX,S,X,AVG       ! Longitudinal stress along curve (positive from large to small)
PDEF,SY,S,Y,AVG       ! Radial stress (positive outward)
PDEF,SZ,S,Z,AVG       ! Circumferential stress (positive by RH rule about small vessel)
PLPATH,SX,SY,SZ       ! Plot path item
PRPATH,SX,SY,SZ       ! Print/list path item

C*** Path Definition through the thickness on XY plane, midway along the saddle
PMAP,ACCURATE
PATH,TXY,2,30,50,       ! Define path
PPATH,1,0,RL*COS(THETAXY),RL*SIN(THETAXY),0,0            ! Define point 1 on path
PPATH,2,0,(RL+TL)*COS(THETAXY),(RL+TL)*SIN(THETAXY),0,0 ! Define point 2 on path
PDEF,SX,S,X,AVG       ! Longitudinal stress along curve (positive from large to small)
PDEF,SY,S,Y,AVG       ! Radial stress (positive outward)
PDEF,SZ,S,Z,AVG       ! Circumferential stress (positive by RH rule about small vessel)
PLPATH,SX,SY,SZ       ! Plot path item
PRPATH,SX,SY,SZ       ! Print/list path item
```

```
C*** Path Definition through the thickness on YZ plane, at large vessel end
PMAP,ACCURATE
PATH,TL,2,30,50,          ! Define path
PPATH,1,0,0,RL,RS+TS+RYZ+LL,0                ! Define point 1 on path
PPATH,2,0,0,RL+TL,RS+TS+RYZ+LL,0             ! Define point 2 on path
PDEF,SX,S,X,AVG         ! Longitudinal stress along curve (positive from large to small)
PDEF,SY,S,Y,AVG         ! Radial stress (positive outward)
PDEF,SZ,S,Z,AVG         ! Circumferential stress (positive by RH rule about small vessel)
PLPATH,SX,SY,SZ         ! Plot path item
PRPATH,SX,SY,SZ         ! Print/list path item

C*** Path Definition through the thickness on YZ plane, midway along the large vessel
PMAP,ACCURATE
PATH,TLH,2,30,50,         ! Define path
PPATH,1,0,0,RL,RS+TS+RYZ+0.5*LL,0            ! Define point 1 on path
PPATH,2,0,0,RL+TL,RS+TS+RYZ+0.5*LL,0         ! Define point 2 on path
PDEF,SX,S,X,AVG         ! Longitudinal stress along curve (positive from large to small)
PDEF,SY,S,Y,AVG         ! Radial stress (positive outward)
PDEF,SZ,S,Z,AVG         ! Circumferential stress (positive by RH rule about small vessel)
PLPATH,SX,SY,SZ         ! Plot path item
C*** PRPATH,SX,SY,SZ            ! Print/list path item

C*** Path Definition through the thickness on YZ plane, at the beginning of large vessel
PMAP,ACCURATE
PATH,TL0,2,30,50,         ! Define path
PPATH,1,0,0,RL,RS+TS+RYZ+0.0*LL,0            ! Define point 1 on path
PPATH,2,0,0,RL+TL,RS+TS+RYZ+0.0*LL,0         ! Define point 2 on path
PDEF,SX,S,X,AVG         ! Longitudinal stress along curve (positive from large to small)
PDEF,SY,S,Y,AVG         ! Radial stress (positive outward)
PDEF,SZ,S,Z,AVG         ! Circumferential stress (positive by RH rule about small vessel)
PLPATH,SX,SY,SZ         ! Plot path item
PRPATH,SX,SY,SZ         ! Print/list path item

C*** Path Definition along the inner surface on the YZ plane for 4 layer model
C*** this batch file is formed by picking nodes and only functions properly for a specific mesh
/REP,FAST
FLST,2,25,1
FITEM,2,5331
FITEM,2,5623
FITEM,2,42
FITEM,2,79
FITEM,2,77
FITEM,2,75
FITEM,2,73
FITEM,2,71
FITEM,2,69
FITEM,2,67
FITEM,2,65
FITEM,2,63
FITEM,2,61
FITEM,2,59
FITEM,2,57
FITEM,2,55
FITEM,2,53
FITEM,2,51
```

```
FITEM,2,1
FITEM,2,5980
FITEM,2,5978
FITEM,2,5976
FITEM,2,5974
FITEM,2,5972
FITEM,2,5970
PATH,PATH_IYZ,25,30,10,
PPATH,P51X,1
PDEF,STAT
AVPRIN,0,0,
PDEF,S1,S,1,AVG
/PBC,PATH, ,0
AVPRIN,0,0,
PDEF,Sx,S,X,AVG
/PBC,PATH, ,0
AVPRIN,0,0,
PDEF,SX,S,X,AVG
/PBC,PATH, ,0
AVPRIN,0,0,
PDEF,SY,S,Y,AVG
/PBC,PATH, ,0
AVPRIN,0,0,
PDEF,SZ,S,Z,AVG
/PBC,PATH, ,0
```

Ansys APDL Code for a Histology-Based Model

An example of an Ansys batch file is provided below. The general structure of the batch file was to have a master file that initialized a few items such as simulation name, and then called a series of scripts, followed by selected post-processing steps.

1. “init.txt” - variables initialized, options selected for later conditional checks
2. “import_geom.txt” – geometry imported
3. “mat_props.txt” – material model defined
4. “mest.txt” – geometry meshed
5. “constraints.txt” – boundary conditions defined
6. “solve.txt” – finite element model solved

Sample Master File for Histology Based FEA

```
!ANSYS APDL Code
/CLEAR,start
/CWD,'D:\Users\Peter Carnell\R1 - 7d\FEM'

/TRIAD,OFF
/EDGE,1,0,90
!Specify variable thickness as ANSYS array

/INPUT,'R1_load_varthick','txt'
!/INPUT,'R1_load_varthick_const','txt'

sim = 'R1_'
/FILENAME,%sim%,1      !Define filename.db

!Define title
/TITLE,%sim%

!Initializes constants to be used in other script routines
/INPUT,'init','txt'

!Import IGES surface into ANSYS
/INPUT,'import_geom_shell','txt'

!Generate material properties
/INPUT,'matprops','txt'

!Mesh model
```

```
/INPUT,'mesh_quad','txt'

!Specify constraints (displacements and pressure BC's)
/INPUT,'constraints','txt'

!Solve model
/INPUT,'solve','txt'

SAVE

!Selected postprocessing steps
! routine to calculate gradient of first principal stress through wall
!/INPUT,'gradient_calc','txt'

!/INPUT,'post_midprinc','txt'
/POST1          ! Enters the database results postprocessor.
/DSCALE,1,1.0   ! Sets the displacement multiplier for displacement displays

!Activate the global cartesion coordinate system
CSYS,0          ! activates a coordinate system (CSYS = 0 => global cartesian)
/EFACET,1       ! Specifies number of facets per element edge for PowerGraphics
AVPRIN,0, ,     ! Specifies how principal and vector sums are to be calculated

RSYS,0          ! activates coordinate system for results, unless LAYER = 0
SHELL,MID       ! Selects a shell element or shell layer location for results output
AVRES,2         ! Specifies how results will be averaged when PowerGraphics is enabled
LAYER,0         ! data are transformed into the element coordinate system
FORCE,TOTAL  ! static, damping and intertial forces

/GRESUME,'R1_viewfront','txt',' '
!/GRESUME,'R1_viewback','txt',' '

/AUTO, 1        ! Resets the focus and distance specs to "automatically calculated"

!/CONTOUR, ALL, 9, 10000, , 80000

!/AUTO,1
PLNSOL,S,1,0,1  ! plot first principal stress
/REP,FAST

!/INPUT,'gradient_calc','txt'

!FINISH

! Strain Energy Density
!/POST1
!/EFACET,1       ! Specifies number of facets per element edge for PowerGraphics
!AVPRIN,0, ,     ! Specifies how principal and vector sums are to be calculated
!PLNSOL,SEND,ELAS,0,1
```

Initialize Variables for Analysis

```
!Initializes constants to be used in other script routines
!/INPUT,'init','txt'
int_opt=0       !Reduced (0) or Full integration (2)
```

```
d_wall=28.3545476295627  !R1 thickness - Define (uniform)
thick_opt=1         !thick_opt=0:Uniform thickness
                    !thick_opt=1:Variable thickness

e1=1e6              !Define linear isotropic Young's modulus
nu=0.49             !Define Poisson's ratio

lin_opt=0           !linopt=0 --> Linear material
                    !linopt=1 --> Non-linear material

mooney_opt=5    !Define what Mooney-Rivlin material is to be used

layer_opt=1         !Define number of layers used
                    !Current options: 0, 1, 2, 4
intpoints=9         !Number of integration points per layer

pressure=1.33e4  !Define pressure to put on model.
!pressure=0.4*1.33e4        !Define pressure to put on model.
                    !100mmHg = 1.33e4Pa - hypertension
                    ! 40mmHg = 0.4*1.33e4Pa - normotension
                    ! 80mmHg = 0.8*1.33e4Pa - fixation pressure


nlgeom_opt=1    !0: Small displacement static analysis
                    !1: Large displacement static analysis
!kuse_opt=-1        !-1: Reformulate triangulated matrix every equilibrium iteration
                    ! 1: Reuse triangulated matrix every equilibrium
                    !iteration
kbc_opt=0           !Ramped(0) or Stepped(1) load
pred_opt=0          !Predictor (for substeps) off(0) or on(1)
autots_opt=1        !Automated timestepping off(0) or on(1)
nsubst_opt=2        !number of substeps (when autots_opt=0)
                    !Initial time step equals 1/nsubst_opt(when autots_opt=1)
!nsubstmin_opt=2            !Minimum number of substeps (when autots_opt=1)
!nsubstmax_opt=10 !Maximum number of substeps (when autots_opt=1)
!nsubstmax_opt=5 !Maximum number of substeps (when autots_opt=1)

!solver_opt=1       !1: Sparse direct solver. 2:PCG solver
                    !3:AMG   solver. 4: Frontal direct solver
```

Import Shell Geometry

```
!/INPUT,'import_geom_shell','txt'
/AUX15
IOPTN,IGES,NODEFEAT             !no defeaturing
IOPTN,MERGE,YES       !automatic merging of entities
IOPTN,SOLID,NO                  !no solid created - no for shell models, yes for solid models
IOPTN,SMALL,YES       !small areas are deleted
IOPTN,GTOLER, DEFA  !when merging use system default tolerance
IGESIN,'R1_mid_high_cropped','igs',' '        ! import iges
APLOT                                         ! area plot
FINISH
```

Define Material Properties/Wall Thickness/Section Characteristics

```
!/INPUT,'matprops','txt'
/PREP7

ET,1,SHELL181          !element type is SHELL 181
KEYOPT,1,3,int_opt     !0=default, 2=full integration
KEYOPT,1,8,1           !Store All Layers - average mid layer
KEYOPT,1,9,0           !avoid use of built-in UTHICK routine for user defined thickness
KEYOPT,1,10,0          !Default

!Real Constants, uniform thickness
!Alternatively can use the RTHICK command to specify variable thickness at each node
!Note: Variable thicknesses can only be implemented with midplane geometry
R,1,d_wall

!Linear material properties
MP,EX,1,e1
MP,PRXY,1,nu

!Nonlinear material properties
*IF,lin_opt,EQ,1,THEN
        TBFT,EADD,1,UNIA,'hyper_var','txt','.'
        TBFT,FADD,1,HYPER,MOON,mooney_opt
        TBFT,SOLVE,1,HYPER,MOON,mooney_opt,0
        TBFT,PLOT,1,UNIA,HYPER,MOON,mooney_opt
        TBFT,FSET,1,HYPER,MOON,mooney_opt
        ! Non-linear, hyperleastic mat props
        !5-parameter Mooney-Rivlin fitted to exp data
*ENDIF

!specify section description, based on number of layers
SECTYPE,1,shell
SECOFFSET,MID
*IF,thick_opt,EQ,0,THEN
  *IF,layer_opt,EQ,1,THEN
        SECDATA, d_wall,1,0.0,intpoints  !this will override variable thickness
  *ELSEIF,layer_opt,EQ,2
        SECDATA, d_wall/2,1,0.0,intpoints
        SECDATA, d_wall/2,1,0.0,intpoints
  *ELSEIF,layer_opt,EQ,4
        SECDATA, d_wall/4,1,0.0,intpoints
        SECDATA, d_wall/4,1,0.0,intpoints
        SECDATA, d_wall/4,1,0.0,intpoints
        SECDATA, d_wall/4,1,0.0,intpoints
  *ENDIF
*ENDIF

FINISH
```

Mesh Geometry

```
!/INPUT,'mesh_quad','txt'
/PREP7
```

```
!First meshing part, completely auto by ANSYS
MSHAPE,0,2D
MSHKEY,0

!Area Meshing, Manual meshing
ESIZE,0,7,
!MOPT,SPLIT,OFF
!mopt,qmesh,alte

CM,_Y,AREA
ASEL,ALL, , , ,

CM,_Y1,AREA
CHKMSH,'AREA'
CMSEL,S,_Y
AMESH,_Y1
CMDELE,_Y
CMDELE,_Y1
CMDELE,_Y2

NUMCMP,NODE

CM,_Y,AREA
ASEL,ALL, , , ,

CM,_Y1,AREA
CHKMSH,'AREA'
CMSEL,S,_Y
AMESH,_Y1
CMDELE,_Y
CMDELE,_Y1
CMDELE,_Y2

NUMCMP,NODE

*IF,thick_opt,EQ,1,THEN
        RTHICK,thick
*ELSEIF,thick_opt,EQ,0,THEN
        SECDATA, d_wall,1,0.0,intpoints
*ENDIF

FINISH
```

Specify Constraints (Displacement and Pressure Boundary Conditions)

```
/INPUT,'constraints','txt'
/PREP7
!CONSTRAINTS

FLST,2,12,4,ORDE,12
FITEM,2,18
FITEM,2,22
FITEM,2,45
FITEM,2,49
```

```
FITEM,2,392
FITEM,2,396
FITEM,2,409
FITEM,2,417
FITEM,2,542
FITEM,2,546
FITEM,2,677
FITEM,2,688
DL,P51X, ,ALL,0

FLST,2,10,4,ORDE,10
FITEM,2,179
FITEM,2,187
FITEM,2,251
FITEM,2,259
FITEM,2,269
FITEM,2,277
FITEM,2,299
FITEM,2,307
FITEM,2,315
FITEM,2,323
DL,P51X, ,ALL,0

FLST,2,12,4,ORDE,12
FITEM,2,72
FITEM,2,76
FITEM,2,104
FITEM,2,108
FITEM,2,218
FITEM,2,222
FITEM,2,338
FITEM,2,342
FITEM,2,365
FITEM,2,373
FITEM,2,724
FITEM,2,726
DL,P51X, ,ALL,0

SFA,ALL,1,PRES,pressure

FINISH
```

Solve Model

```
!/INPUT,'solve','txt'
/SOLU
ANTYPE,0
NLGEOM,ON
!PRED,OFF       ! ON-activates/OFF-dactivates a predictor in a nonlinear analysis
PRED,ON         ! ON-activates/OFF-dactivates a predictor in a nonlinear analysis
/STATUS,SOLU
NEQIT,50        ! max number of equilibrium iterations for nonlinear analyses
SOLVE
FINISH
```

Appendix K:
Statistical Tests

Because the data from these studies was generally not normally distributed, nonparametric statistical methods were employed. A uniform distribution of data can be achieved by replacing the values with the rankings of the values. The first step to nonparametric statistical analysis is to generate rankings, accounting for ties. This data is used to perform Spearman rank sum correlations or compare means of two samples based on a Wilcoxon rank sum.

1. Ranking Program, Accounting for Ties
2. Spearman Rank Sum Correlation Program
3. Spearman Rank Sum Correlation Results
4. Wilcoxon Rank Sum Test Program
5. Wilcoxon Rank Sum Test Results

Ranking Program, Accounting for Ties

```
function [v_rank, i_group_sort, i_sort] = rank_all(v, i_group)

%=========================================================================
%   rank_all.m
%=========================================================================
%   This program generates a numerical ranking from a row vector of values.
%   Ties are accounted for by averaging the ranking of the tied values. The
%   variable i_group allows the ranking of multiple samples from a single
%   population.  This is useful for the Wilcoxon rank sum statistical test,
%   as it was implemented in this research. permits the user to keep track
%   of multiple samples if the ranking requires that
%=========================================================================
%   Author:  Peter Carnell
%   Last Modified:  June 10, 2004
%=========================================================================

% sort values and rearrange i_group
[v_sort i_sort] = sort(v);
i_group_sort = i_group(i_sort);

nmax = length(v);
i = 1;

% move through sorted data, finding ties and assigning tied ranks to v_rank
while i <= nmax
   itie = find(v == v_sort(i))';
   ntie = length(itie) - 1;
   iavg = i + ntie/2;
   if ntie > 0
      v_rank(itie,1) = iavg;
   elseif ntie == 0
      v_rank(itie,1) = iavg;
   end
   i = i + ntie + 1;
end
```

Spearman Rank Correlation Program

```
%*************************************************************************
% spearman_rank_correlation.m
%*************************************************************************
% Description:
% This program performs a Spearman Rank Correlation test on paired
% observations. The values for each observation are ranked and the
% statistical test provides a quantitative measure of how closely the
% rankings are matched between the two sets of observations.  This is a
% non-parametric test that is suitable for identifying correlations even
% when the data exhibits a highly non-normal distribution.
%
% Program Method:
% The program can automatically runs through all branches and compares two
% variables.  First the surface points are filtered to remove points near
% the upper and lower boundaries.  Next the each variable is separately
% ranked using rank_all.m.  This function accounts for ties by averaging
% the rankings of the ties.
% The sum of the differences in the ranks is calculated.  This sum is
% normalized based on the number of observations to obtain a Spearman Rank
% Correlation Coefficient, r_s.  For a perfect postive correlation r_s =
% 1.0, while a perfect negative correlation would yield r_s = -1.0. Typical
% correlations are considerably less than 1.0, with the significance being
% dependent on the number of observations.
% For a small number of observations (30 or less), a table may be used to
% determine the critical values of r_s for a given confidence interval.
% For larger sample sizes the rankings can be normalized using a standard
% normal score (Z).  The null hypothesis is that there is no correlation
% and that differences in rankings are random. The data is exported to
% Excel where a probability can be assigned to rejecting the null
% hypothesis.
%
%*************************************************************************
% Uses rank_all.m function to rank values, accounting for ties.
% This function is also used in the Wilcoxon Rank Sum program.
%*************************************************************************
% Created by: Peter Carnell
% Last Modified: 6-9-04
%*************************************************************************
%

clear all
close all

stat_array = [];
stat_array2 = [];
test = 'none';
```

```
% test = 'test5';

% specify variables to compare
v1_name = '_inner_wall_thickness';
v2_name = '_inner_mindist';

% Define set of models to cycle through
set_array = {'R5' 'R8' 'R1' 'R4' 'R10B' 'R2' 'R3'};
%set_array = {'R5'};

% Loop through each model
for iset = 1:length(set_array);
   setname = set_array{iset};
   % Load the coordinates and variables
   coor_in = load([setname '_inner_vertices.txt']);
   v1 = load([setname v1_name '.txt']);

   % If test case is chosen, replace variables
   if strcmp(test,'none')
      v2 = load([setname v2_name '.txt']);
   elseif strcmp(test,'test1')
      v2 = rand(length(v1),1);
   elseif strcmp(test,'test2')
      v2 = rand(length(v1),1);
   elseif strcmp(test,'test3')
      % r_s = 1, r_s_para = 1
      v2 = v1;
   elseif strcmp(test,'test4')
      % r_s = -1, r_s_para = -1
      v2 = -v1;
   elseif strcmp(test,'test5')
      % r_s = -1, r_s_para = -1
      v1 = (1:length(v1))';
      v2 = v1+v1.*(-1).^v1;
   end

   % Apply spatial filtering
   maxz = max(coor_in(:,3));
   minz = min(coor_in(:,3));
   boundary_crop = 0.1*(maxz - minz);
   maxz_crop = maxz - boundary_crop;
   minz_crop = minz + boundary_crop;
   icrop = find(coor_in(:,3) < maxz_crop & coor_in(:,3) > minz_crop);
   coor_crop = coor_in(icrop,:);
   v1 = v1(icrop);
   v2 = v2(icrop);

   npts = length(v1);
   v1_mean = mean(v1);
   v2_mean = mean(v2);
   v1_std = std(v1);
```

```
    v2_std = std(v2);

    % Check to make sure v1 and v2 have same number of points
    if length(v1) ~= length(v2)
       disp('************************************************************')
       disp('   WARNING: Sample 1 and Sample 2 have different sizes,')
       disp('            cannot perform Spearman Rank Correlation.')
       disp('************************************************************')
    end

    % Rank v1 and v2 separately
    [v1_rank i1_group i1_rank] = rank_all(v1, ones(length(v1),1));
    [v2_rank i2_group i2_rank] = rank_all(v2, ones(length(v2),1));

    % Calculate sum of difference in ranks
    D = sum((v1_rank-v2_rank).^2);
    n = length(v1_rank);

    % Calculate Spearman Rank Correlation Coefficient
    r_s = 1-6.*D/(n^3-n);
    disp(['r_s = ' num2str(r_s)])

    % Calculate standard normal score and use in n is large
    z = r_s*(length(v1)-1)^0.5;

    % Store results in statistical table for export
    stat_array = [stat_array [npts v1_mean v1_std v2_mean v2_std r_s z]';

    stat_array2 = [stat_array2 [min(v1) max(v1) v1_mean v1_std]'];

end

break
%%%Diagnostic plots
figure
plot(v2,v1,'b.')

figure
plot(v2_rank,v1_rank,'b.')

figure
plot3(coor_in(:,1),coor_in(:,2),coor_in(:,3),'b.')
hold on
plot3(coor_crop(:,1),coor_crop(:,2),coor_crop(:,3),'g.')

figure
v1_full = load([setname v1_name '.txt']);
v2_full = load([setname v2_name '.txt']);
topo = load([setname '_inner_topo.txt']);
polygonplot_function(coor_in, topo, v1_full)
```

Spearman Rank Correlation Results

A sample set of results is presented here, although most results are presented in the body of this report. The correlations are generated by the Matlab program and the two-tailed test data is generated in Excel. Table K-5 and Table K-6 are sample results that illustrate that the order of the variables does not affect the correlation. The sum of the square of the difference in ranks is the same whether the difference is positive or negative.

Table K-5: Spearman rank correlations for wall tension versus cell density.

Wall Tension vs Cell Density

Spearman Rank Correlation:	H7A	H7B	H7C	H7D	H21A	NA	NB
Sample Size	3447	4661	3085	3808	3230	2055	4404
Mean Wall Tension (N/m)	0.981	1.669	1.686	1.944	1.552	0.623	0.627
Standard Deviation	0.205	0.381	0.908	0.575	0.289	0.102	0.182
Mean Cell Density (Cells/μm^3)	2.68E-06	2.59E-06	3.48E-06	5.15E-06	4.22E-06	4.27E-07	2.65E-06
Standard Deviation	2.03E-06	1.45E-06	2.43E-06	3.78E-06	1.98E-06	3.03E-07	1.18E-06
Correlation Coefficient (r_s)	0.1239	-0.0121	0.0952	-0.1463	0.2738	-0.2230	-0.0298
Standard Normal Score (Z)	7.28	-0.83	5.29	-9.03	15.56	-10.11	-1.98
Two-Tailed Test:							
Level of Significance (α)	0.05	0.05	0.05	0.05	0.05	0.05	0.05
Lower Critical Value	-1.960	-1.960	-1.960	-1.960	-1.960	-1.960	-1.960
Upper Critical Value	1.960	1.960	1.960	1.960	1.960	1.960	1.960
p-value	0.000000	0.407150	0.000000	0.000000	0.000000	0.000000	0.048223
Reject the null hypothesis?	YES	NO	YES	YES	YES	YES	YES

Table K-6: Spearman rank correlations for cell density versus wall tension.

Cell Density vs Wall Tension

Spearman Rank Correlation:	H7A	H7B	H7C	H7D	H21A	NA	NB
Sample Size	3447	4661	3085	3808	3230	2055	4404
Mean Cell Density (Cells/μm^3)	2.68E-06	2.59E-06	3.48E-06	5.15E-06	4.22E-06	4.27E-07	2.65E-06
Standard Deviation	2.03E-06	1.45E-06	2.43E-06	3.78E-06	1.98E-06	3.03E-07	1.18E-06
Mean Wall Tension (N/m)	0.981	1.669	1.686	1.944	1.552	0.623	0.627
Standard Deviation	0.205	0.381	0.908	0.575	0.289	0.102	0.182
Correlation Coefficient (r_s)	0.1239	-0.0121	0.0952	-0.1463	0.2738	-0.2230	-0.0298
Standard Normal Score (Z)	7.28	-0.83	5.29	-9.03	15.56	-10.11	-1.98
Two-Tailed Test:							
Level of Significance (α)	0.05	0.05	0.05	0.05	0.05	0.05	0.05
Lower Critical Value	-1.960	-1.960	-1.960	-1.960	-1.960	-1.960	-1.960
Upper Critical Value	1.960	1.960	1.960	1.960	1.960	1.960	1.960
p-value	0.000000	0.407150	0.000000	0.000000	0.000000	0.000000	0.048223
Reject the null hypothesis?	YES	NO	YES	YES	YES	YES	YES

Wilcoxon Rank Sum Test Program

```
%*************************************************************************
% wilcoxon_rank_sum.m
%*************************************************************************
% Description:
% This program performs a Wilcoxon rank sum statistical test.  This test
% compares the median ranks of two samples to determine the likelihood that
% the samples were randomnly selected from a given population.  Because the
% test substiutes the combined ranks of two samples for the values, it is a
% nonparametric statistical test.  The rankings are evenly distributed and
% therefore the test is well-suited to data that is not normally
% distributed.
%
% Program Method:
% The program can automatically runs through all branches and compare two
% variables.  First the surface points are filtered to remove points near
% the upper and lower boundaries.  The remaining surface points are
% segregated into two groups based on the magnitude of the first variable
% (v1).  Next the mean values of the second variable are ranked and the
% ranks are used in the place of the values to produce evenly distributed
% data.  The sums of the ranks of the two groups are compared and a Z
% statistic is generated.  The program cycles through each model and
% generates a summary table of data that can be imported into Excel where
% the statistical significance can be attached to the results.
%
% This program assumes that the first group is smaller than the second - a
% warning is issued if this is not the case.
%
%*************************************************************************
% Uses rank_all.m function to rank values, accounting for ties.
% This function is also used in the Spearman Rank Correlation program.
%*************************************************************************
% Created by: Peter Carnell
% Last Modified: 6-9-04
%*************************************************************************
%
clear all
close all

% Three simple tests are availabe to check the results
test = 0; % 0,1,2,3,4
fig_plot = 0;

div_value = 1;

v1_name = '_inner_invariant2';
v2_name = '_inner_cell_density';
```

```
ndiv = 4;
if div_value == 0
   ndiv = 10;
end

% Define set of models to cycle through
set_array = {'R5' 'R8' 'R1' 'R4' 'R10B' 'R2' 'R3'};
%set_array = {'R5'};

stat_v = [];

% Loop through each model
for iset = 1:length(set_array);
   setname = set_array{iset};
   % Load the coordinates and variables
   coor=load([setname '_inner_vertices.txt']);
   v1 = load([setname v1_name '.txt']);
   v2 = load([setname v2_name '.txt']);

   % If test case is chosen, replace variables
   if test == 1       % yields low Standard Normal Score Z
      v1 = (1:length(v1))';
      v2 = rand(length(v1),1);
   elseif test == 2    % yields high positive Standard Normal Score Z
      v2 = v1;
   elseif test == 3    % yields high positive Standard Normal Score Z
      v2 = -v1;
   end

   % Apply spatial filtering
   maxz = max(coor(:,3));
   minz = min(coor(:,3));
   boundary_crop = 0.1*(maxz - minz);
   maxz_crop = maxz - boundary_crop;
   minz_crop = minz + boundary_crop;
   icrop = find(coor(:,3) < maxz_crop & coor(:,3) > minz_crop);
   coor_crop = coor(icrop,:);
   v1_crop = v1(icrop);
   v2_crop = v2(icrop);
   if test == 4    %
      v1 = [-1; 1; 1; 2; 3; 4; 5];
      v2 = [-1; 1; 1; 2; 3; 4; 5];
      v1_crop = v1;
      v2_crop = v2;
      icrop = (1:length(v1))';
   end
   % Separate v1_crop into ndiv divisions (quartiles?)
   % div_value specifies if equal value or equal rank divisions are used
   if div_value
      % determine total range for v1
```

```
    minv1_crop =  min(v1_crop);
    maxv1_crop =  max(v1_crop);
    for i = 1:ndiv;
       % determine segment range for v1 and find corresponding v2
       v_seg_top1 = maxv1_crop*i/ndiv + minv1_crop*(ndiv-i)/ndiv;
       v_seg_bot1 = maxv1_crop*(i-1)/ndiv + minv1_crop*(ndiv-i+1)/ndiv;
       ifind1 = find(v1_crop <= v_seg_top1 & v1_crop > v_seg_bot1);
       v_seg_mean1(i,1) = mean(v2_crop(ifind1));
       v_std1(i,1) = std(v2_crop(ifind1));
    end
    coor_v1 = coor_crop(ifind1,:);
    minv2_crop =  min(v2_crop);
    maxv2_crop =  max(v2_crop);
    for i = 1:ndiv;
       v_seg_top2 = maxv2_crop*i/ndiv + minv2_crop*(ndiv-i)/ndiv;
       v_seg_bot2 = maxv2_crop*(i-1)/ndiv + minv2_crop*(ndiv-i+1)/ndiv;
       ifind2 = find(v2_crop <= v_seg_top2 & v2_crop > v_seg_bot2);
       v_seg_mean2(i,1) = mean(v1_crop(ifind2));
       v_std2(i,1) = std(v1_crop(ifind2));
    end
    coor_v2 = coor_crop(ifind2,:);
    ifind_c = intersect(ifind1,ifind2);
  elseif ~div_value
    % replace values with ranks of values and proceed as before
    [v1_rank i1_group i1_rank] = rank_all(v1_crop, ones(length(v1_crop),1));
    %%%%%%
    v1_crop = v1_rank;
    [v2_rank i2_group i2_rank] = rank_all(v2_crop, ones(length(v2_crop),1));
    %%%%%%
    v2_crop = v2_rank;
%      [v2_rank i2_group i2_rank] = rank_all(v2_crop, ones(length(v2_crop),1));

    minv1_crop =  min(v1_crop);
    maxv1_crop =  max(v1_crop);
    for i = 1:ndiv;
       v_seg_top1 = maxv1_crop*i/ndiv + minv1_crop*(ndiv-i)/ndiv;
       v_seg_bot1 = maxv1_crop*(i-1)/ndiv + minv1_crop*(ndiv-i+1)/ndiv;
       ifind1 = find(v1_crop <= v_seg_top1 & v1_crop > v_seg_bot1);
       v_seg_mean1(i,1) = mean(v2_crop(ifind1));
       v_std1(i,1) = std(v2_crop(ifind1));
    end
    coor_v1 = coor_crop(ifind1,:);
    minv2_crop =  min(v2_crop);
    maxv2_crop =  max(v2_crop);
    for i = 1:ndiv;
       v_seg_top2 = maxv2_crop*i/ndiv + minv2_crop*(ndiv-i)/ndiv;
       v_seg_bot2 = maxv2_crop*(i-1)/ndiv + minv2_crop*(ndiv-i+1)/ndiv;
       ifind2 = find(v2_crop <= v_seg_top2 & v2_crop > v_seg_bot2);
       v_seg_mean2(i,1) = mean(v1_crop(ifind2));
       v_std2(i,1) = std(v1_crop(ifind2));
    end
```

```
    coor_v2 = coor_crop(ifind2,:);
    ifind_c = intersect(ifind1,ifind2);
end

% Plot figures if fig_plot = 1
if fig_plot
    % Raw data - note labeling is case-specific
    figure
    set(gca,'FontSize',12)
    plot(v1_crop(:),v2_crop(:),'kx')
    xlabel('Maximal Wall Tension (N/m)');
    ylabel('Cell Density (cells/\mum^{3})');
    hold on
    plot(v1_crop(ifind1),v2_crop(ifind1),'bo')
    % Histogram of v1
    figure
    set(gca,'FontSize',12)
    hist(v1_crop, 50)
    xlabel('Maximal Wall Tension (N/m)');
    % Histogram of v1
    figure
    set(gca,'FontSize',12)
    hist(v2_crop, 50)
    xlabel('Cell Density (cells/\mum^{3})');
end

ifind_low = setdiff(1:length(v1_crop),ifind1)';

va = v2_crop(ifind1);
vb = v2_crop(ifind_low);

na = length(va);
nb = length(vb);

% Combine samples and define group identifier
v = [va; vb];
i_group = [ones(na,1); 2*ones(nb,1)];

% Generate rank and index
[v_rank i_group2 i_rank] = rank_all(v, i_group);
ia_group = find(i_group == 1);
ib_group = find(i_group == 2);
wa = sum(v_rank(ia_group));
wb = sum(v_rank(ib_group));
mu_a = na*(na+nb+1)/2;
mu_b = nb*(na+nb+1)/2;
ua = wa - na*(na+nb+1)/2;
ub = wb - nb*(na+nb+1)/2;
sd_pop = (na*nb*(na+nb+1)/12)^0.5;
Za = ua/sd_pop;
```

```
   alpha = 0.05;

   stat_v = [stat_v [alpha; na; wa; wa/na; nb; wb; wb/nb; na+nb; (wa+wb)/2; sd_pop; Za]];

   disp([setname v1_name ' vs ' setname v2_name ', div_value = ' num2str(div_value)])
   disp(['alpha = ' num2str(alpha)])
   disp(['Sample Size a:  ' num2str(na)])
   disp(['Sum of Ranks a:  ' num2str(wa)])
   disp(['Sample Size b:  ' num2str(nb)])
   disp(['Sum of Ranks b:  ' num2str(wb)])
   %%% conisder including check for na > nb
   disp(['Total Sample Size n:  ' num2str(na+nb)])
   disp(['Ta Test Statistic:  ' num2str(wa)])
   disp(['Ta Mean:  ' num2str(mu_a)])
   disp(['Ta Standard Error:  ' num2str(sd_pop)])
   disp(['Z Test Statistic  ' num2str(Za)])
   disp(' ')
   disp(' ')
end

if na > nb
   disp('************************************************************')
   disp('  WARNING: The groups must be reordered for accuracy and ')
   disp('           this program does not automatically do this.')
   disp('************************************************************')
end

%disp('     alpha; na; wa; wa/na; nb; wb; wb/nb; na+nb; (wa+wb); sd_pop; Za')
%stat_v'
```

Wilcoxon Rank Sum Test Results

Selected results of the Wilcoxon rank sum tests are presented in this appendix. While the general patterns are similar for these results as the Spearman rank sum correlation results, this approach appears to be more sensitive to changes in how the data is grouped. This approach is powerful and can be used in concert with bar charts to show trends, but in the end did not add significantly to the general conclusions. Part of the challenge is that natural variations in several of the characteristics occur between the larger mother vessel and smaller daughter vessels. These patterns are more apparent when the data is grouped by value or rank, as it is done here. For each comparison the data is grouped in four ways:

1) by range of values, upper quartile of variable 1 versus the rest;
2) by range of values, upper quartile of variable 2 versus the rest;
3) by number of values, upper 10% of variable 1 versus the rest; and,
4) by number of values, upper 10% of variable 2 versus the rest.

This is done for the following variable comparisons:

1) cell density versus wall thickness;
2) cell density versus von Mises stress;
3) cell density versus stress intensity;
4) cell density versus maximal wall tension;
5) cell density versus first stress invariant;
6) cell density versus second stress invariant;
7) wall thickness versus von Mises stress; and,
8) wall thickness versus maximal wall tension.

Table K-7: Wilcoxon rank sum test results for cell density versus wall thickness.

Wilcoxon Rank Sum Test

Cell Density grouped by Upper Quartile of Values for Wall Thickness

	H7A	H7B	H7C	H7D	H21A	NA	NB
Level of Significance (α):	0.05	0.05	0.05	0.05	0.05	0.05	0.05
Sample Size for Group A:	126	792	291	153	96	76	308
Sum of Ranks for Group A:	3.80E+05	1.21E+06	4.38E+05	3.67E+05	1.82E+05	4.36E+04	3.20E+05
Mean Rank for Group A:	3013	1523.5	1506.9	2400	1898	574.26	1040.3
Sample Size for Group B:	3321	3869	2794	3655	3134	1979	4096
Sum of Ranks for Group B:	5.56E+06	9.66E+06	4.32E+06	6.89E+06	5.04E+06	2.07E+06	9.38E+06
Mean Rank for Group B:	1675.1	2496.3	1546.8	1883.8	1606.8	1045.4	2289.9
Total Population Size:	3447.0	4661	3085	3808	3230	2055	4404
Total Sum of Ranks:	5.94E+06	1.09E+07	4.76E+06	7.25E+06	5.22E+06	2.11E+06	9.70E+06
Standard Deviation of Group A:	10965	34503	14460	13323	9000.4	5076.3	21520
Standard Normal Score of A:	14.81	-18.54	-0.73	5.69	3.01	-6.79	-16.63
Two-Tailed Test:							
Lower Critical Value:	-1.9600	-1.9600	-1.9600	-1.9600	-1.9600	-1.9600	-1.9600
Upper Critical Value:	1.9600	1.9600	1.9600	1.9600	1.9600	1.9600	1.9600
p-value:	0.0000	0.0000	0.4669	0.0000	0.0026	0.0000	0.0000
Reject the null hypothesis?	YES	YES	NO	YES	YES	YES	YES

Wilcoxon Rank Sum Test

Cell Density grouped by Upper 10% of Ranks for Wall Thickness

	H7A	H7B	H7C	H7D	H21A	NA	NB
Level of Significance (α):	0.05	0.05	0.05	0.05	0.05	0.05	0.05
Sample Size for Group A:	345	466	309	381	323	206	441
Sum of Ranks for Group A:	1.00E+06	7.02E+05	4.57E+05	8.51E+05	5.52E+05	1.68E+05	5.27E+05
Mean Rank for Group A:	2904.3	1507.3	1479.3	2233.6	1707.7	816.84	1194.6
Sample Size for Group B:	3102	4195	2776	3427	2907	1849	3963
Sum of Ranks for Group B:	4.94E+06	1.02E+07	4.30E+06	6.40E+06	4.67E+06	1.94E+06	9.17E+06
Mean Rank for Group B:	1592.7	2422.5	1550.1	1867.9	1605.3	1051.5	2314.7
Total Population Size:	3447.0	4661	3085	3808	3230	2055	4404
Total Sum of Ranks:	5.94E+06	1.09E+07	4.76E+06	7.25E+06	5.22E+06	2.11E+06	9.70E+06
Standard Deviation of Group A:	17536	27558	14852	20358	15900	8078.4	25329
Standard Normal Score of A:	23.22	-13.93	-1.33	6.16	1.87	-5.38	-17.55
Two-Tailed Test:							
Lower Critical Value:	-1.9600	-1.9600	-1.9600	-1.9600	-1.9600	-1.9600	-1.9600
Upper Critical Value:	1.9600	1.9600	1.9600	1.9600	1.9600	1.9600	1.9600
p-value:	0.0000	0.0000	0.1849	0.0000	0.0610	0.0000	0.0000
Reject the null hypothesis?	YES	YES	NO	YES	NO	YES	YES

Wilcoxon Rank Sum Test

Wall Thickness grouped by Upper Quartile of Values for Cell Density

	H7A	H7B	H7C	H7D	H21A	NA	NB
Level of Significance (α):	0.05	0.05	0.05	0.05	0.05	0.05	0.05
Sample Size for Group A:	364	329	214	198	233	48	388
Sum of Ranks for Group A:	1.06E+06	7.27E+05	1.80E+05	1.29E+05	3.19E+05	1.49E+04	6.53E+05
Mean Rank for Group A:	2899.2	2209.5	842.76	653.91	1370.5	310.98	1683.5
Sample Size for Group B:	3083	4332	2871	3610	2997	2007	4016
Sum of Ranks for Group B:	4.89E+06	1.01E+07	4.58E+06	7.12E+06	4.90E+06	2.10E+06	9.05E+06
Mean Rank for Group B:	1585.2	2340.2	1595.2	1973.1	1634.6	1045.1	2252.6
Total Population Size:	3447.0	4661	3085	3808	3230	2055	4404
Total Sum of Ranks:	5.94E+06	1.09E+07	4.76E+06	7.25E+06	5.22E+06	2.11E+06	9.70E+06
Standard Deviation of Group A:	17957	23531	12570	15063	13712	4062.7	23916
Standard Normal Score of A:	23.82	-1.70	-11.92	-16.44	-4.16	-8.47	-8.42
Two-Tailed Test:							
Lower Critical Value:	-1.9600	-1.9600	-1.9600	-1.9600	-1.9600	-1.9600	-1.9600
Upper Critical Value:	1.9600	1.9600	1.9600	1.9600	1.9600	1.9600	1.9600
p-value:	0.0000	0.0895	0.0000	0.0000	0.0000	0.0000	0.0000

Wilcoxon Rank Sum Test

Wall Thickness grouped by Upper 10% of Ranks for Cell Density

	H7A	H7B	H7C	H7D	H21A	NA	NB
Level of Significance (α):	0.05	0.05	0.05	0.05	0.05	0.05	0.05
Sample Size for Group A:	345	466	290	381	323	199	441
Sum of Ranks for Group A:	1.00E+06	1.01E+06	2.79E+05	3.34E+05	4.53E+05	1.69E+05	7.74E+05
Mean Rank for Group A:	2903.3	2164.7	962.87	877.48	1401.7	850.79	1756.1
Sample Size for Group B:	3102	4195	2795	3427	2907	1856	3963
Sum of Ranks for Group B:	4.94E+06	9.86E+06	4.48E+06	6.92E+06	4.77E+06	1.94E+06	8.93E+06
Mean Rank for Group B:	1592.8	2349.5	1603.2	2018.7	1639.3	1047	2252.2
Total Population Size:	3447.0	4661	3085	3808	3230	2055	4404
Total Sum of Ranks:	5.94E+06	1.09E+07	4.76E+06	7.25E+06	5.22E+06	2.11E+06	9.70E+06
Standard Deviation of Group A:	17536	27558	14438	20358	15900	7954.9	25329
Standard Normal Score of A:	23.20	-2.81	-11.65	-19.22	-4.34	-4.43	-7.77
Two-Tailed Test:							
Lower Critical Value:	-1.9600	-1.9600	-1.9600	-1.9600	-1.9600	-1.9600	-1.9600
Upper Critical Value:	1.9600	1.9600	1.9600	1.9600	1.9600	1.9600	1.9600
p-value:	0.0000	0.0049	0.0000	0.0000	0.0000	0.0000	0.0000

Table K-8: Wilcoxon rank sum test results for cell density versus von Mises stress.

Wilcoxon Rank Sum Test

Cell Density grouped by Upper Quartile of Values for Von Mises Stress

	H7A	H7B	H7C	H7D	H21A	NA	NB
Level of Significance (α):	0.05	0.05	0.05	0.05	0.05	0.05	0.05
Sample Size for Group A:	173	10	41	379	167	31	549
Sum of Ranks for Group A:	7.77E+04	4.59E+04	9.27E+04	6.50E+05	4.41E+05	4.80E+04	1.33E+06
Mean Rank for Group A:	449.14	4589.9	2260.9	1715.7	2637.9	1549.7	2418.5
Sample Size for Group B:	3274	4651	3044	3429	3063	2024	3855
Sum of Ranks for Group B:	5.86E+06	1.08E+07	4.67E+06	6.60E+06	4.78E+06	2.06E+06	8.37E+06
Mean Rank for Group B:	1791.4	2326.1	1533.3	1925.4	1559.8	1020	2171.7
Total Population Size:	3447.0	4661	3085	3808	3230	2055	4404
Total Sum of Ranks:	5.94E+06	1.09E+07	4.76E+06	7.25E+06	5.22E+06	2.11E+06	9.70E+06
Standard Deviation of Group A:	12757	4250.8	5665.3	20310	11736	3278.7	27873
Standard Normal Score of A:	-17.29	5.31	5.20	-3.52	14.55	4.93	4.25
Two-Tailed Test:							
Lower Critical Value:	-1.9600	-1.9600	-1.9600	-1.9600	-1.9600	-1.9600	-1.9600
Upper Critical Value:	1.9600	1.9600	1.9600	1.9600	1.9600	1.9600	1.9600
p -value:	0.0000	0.0000	0.0000	0.0004	0.0000	0.0000	0.0000
Reject the null hypothesis?	YES	YES	YES	YES	YES	YES	YES

Wilcoxon Rank Sum Test

Cell Density grouped by Upper 10% of Ranks for Von Mises Stress

	H7A	H7B	H7C	H7D	H21A	NA	NB
Level of Significance (α):	0.05	0.05	0.05	0.05	0.05	0.05	0.05
Sample Size for Group A:	345	466	309	381	323	206	441
Sum of Ranks for Group A:	1.89E+05	1.64E+06	6.03E+05	6.54E+05	7.63E+05	2.19E+05	1.06E+06
Mean Rank for Group A:	548.65	3519.7	1953	1717.6	2361.6	1065.3	2393.3
Sample Size for Group B:	3102	4195	2776	3427	2907	1849	3963
Sum of Ranks for Group B:	5.75E+06	9.22E+06	4.16E+06	6.60E+06	4.46E+06	1.89E+06	8.64E+06
Mean Rank for Group B:	1854.7	2199	1497.4	1925.3	1532.6	1023.8	2181.3
Total Population Size:	3447.0	4661	3085	3808	3230	2055	4404
Total Sum of Ranks:	5.94E+06	1.09E+07	4.76E+06	7.25E+06	5.22E+06	2.11E+06	9.70E+06
Standard Deviation of Group A:	17536	27558	14852	20358	15900	8078.4	25329
Standard Normal Score of A:	-23.12	20.10	8.53	-3.50	15.16	0.95	3.32
Two-Tailed Test:							
Lower Critical Value:	-1.9600	-1.9600	-1.9600	-1.9600	-1.9600	-1.9600	-1.9600
Upper Critical Value:	1.9600	1.9600	1.9600	1.9600	1.9600	1.9600	1.9600
p -value:	0.0000	0.0000	0.0000	0.0005	0.0000	0.3419	0.0009
Reject the null hypothesis?	YES	YES	YES	YES	YES	NO	YES

Wilcoxon Rank Sum Test

Von Mises Stress grouped by Upper Quartile of Values for Cell Density

	H7A	H7B	H7C	H7D	H21A	NA	NB
Level of Significance (α):	0.05	0.05	0.05	0.05	0.05	0.05	0.05
Sample Size for Group A:	364	329	214	198	233	48	388
Sum of Ranks for Group A:	3.77E+05	8.76E+05	1.92E+05	1.08E+05	5.67E+05	2.98E+04	9.54E+05
Mean Rank for Group A:	1036	2661.7	898.36	545.04	2434.4	620.64	2460
Sample Size for Group B:	3083	4332	2871	3610	2997	2007	4016
Sum of Ranks for Group B:	5.57E+06	9.99E+06	4.57E+06	7.14E+06	4.65E+06	2.08E+06	8.75E+06
Mean Rank for Group B:	1805.2	2305.9	1591.1	1979.1	1551.8	1037.7	2177.6
Total Population Size:	3447.0	4661	3085	3808	3230	2055	4404
Total Sum of Ranks:	5.94E+06	1.09E+07	4.76E+06	7.25E+06	5.22E+06	2.11E+06	9.70E+06
Standard Deviation of Group A:	17957	23531	12570	15063	13712	4062.7	23916
Standard Normal Score of A:	-13.95	4.62	-10.98	-17.87	13.92	-4.81	4.18
Two-Tailed Test:							
Lower Critical Value:	-1.9600	-1.9600	-1.9600	-1.9600	-1.9600	-1.9600	-1.9600
Upper Critical Value:	1.9600	1.9600	1.9600	1.9600	1.9600	1.9600	1.9600
p -value:	0.0000	0.0000	0.0000	0.0000	0.0000	0.0000	0.0000

Wilcoxon Rank Sum Test

Von Mises Stress grouped by Upper 10% of Ranks for Cell Density

	H7A	H7B	H7C	H7D	H21A	NA	NB
Level of Significance (α):	0.05	0.05	0.05	0.05	0.05	0.05	0.05
Sample Size for Group A:	345	466	290	381	323	199	441
Sum of Ranks for Group A:	3.58E+05	1.29E+06	3.03E+05	2.94E+05	7.49E+05	1.85E+05	1.08E+06
Mean Rank for Group A:	1036.4	2777.3	1044.9	771.7	2317.7	927.19	2452.4
Sample Size for Group B:	3102	4195	2795	3427	2907	1856	3963
Sum of Ranks for Group B:	5.59E+06	9.57E+06	4.46E+06	6.96E+06	4.47E+06	1.93E+06	8.62E+06
Mean Rank for Group B:	1800.5	2281.4	1594.7	2030.4	1537.5	1038.8	2174.7
Total Population Size:	3447.0	4661	3085	3808	3230	2055	4404
Total Sum of Ranks:	5.94E+06	1.09E+07	4.76E+06	7.25E+06	5.22E+06	2.11E+06	9.70E+06
Standard Deviation of Group A:	17536	27558	14438	20358	15900	7954.9	25329
Standard Normal Score of A:	-13.53	7.55	-10.01	-21.20	14.26	-2.52	4.35
Two-Tailed Test:							
Lower Critical Value:	-1.9600	-1.9600	-1.9600	-1.9600	-1.9600	-1.9600	-1.9600
Upper Critical Value:	1.9600	1.9600	1.9600	1.9600	1.9600	1.9600	1.9600
p -value:	0.0000	0.0000	0.0000	0.0000	0.0000	0.0117	0.0000

Table K-9: Wilcoxon rank sum test results for cell density versus maximum shear stress.

Wilcoxon Rank Sum Test

Cell Density grouped by Upper Quartile of Values for Max Shear Stress

	H7A	H7B	H7C	H7D	H21A	NA	NB
Level of Significance (α):	0.05	0.05	0.05	0.05	0.05	0.05	0.05
Sample Size for Group A:	223	11	114	414	192	40	422
Sum of Ranks for Group A:	1.07E+05	5.05E+04	2.44E+05	6.77E+05	4.67E+05	5.97E+04	1.08E+06
Mean Rank for Group A:	479.6	4592.4	2142.4	1636.2	2430.8	1491.5	2559.8
Sample Size for Group B:	3224	4650	2971	3394	3038	2015	3982
Sum of Ranks for Group B:	5.84E+06	1.08E+07	4.52E+06	6.57E+06	4.75E+06	2.05E+06	8.62E+06
Mean Rank for Group B:	1810.1	2325.7	1520	1937.2	1564	1018.8	2164.6
Total Population Size:	3447.0	4661	3085	3808	3230	2055	4404
Total Sum of Ranks:	5.94E+06	1.09E+07	4.76E+06	7.25E+06	5.22E+06	2.11E+06	9.70E+06
Standard Deviation of Group A:	14373	4457.8	9332.8	21119	12532	3716.1	24836
Standard Normal Score of A:	-19.31	5.58	7.32	-5.26	12.49	4.99	6.07
Two-Tailed Test:							
Lower Critical Value:	-1.9600	-1.9600	-1.9600	-1.9600	-1.9600	-1.9600	-1.9600
Upper Critical Value:	1.9600	1.9600	1.9600	1.9600	1.9600	1.9600	1.9600
p -value:	0.0000	0.0000	0.0000	0.0000	0.0000	0.0000	0.0000
Reject the null hypothesis?	YES	YES	YES	YES	YES	YES	YES

Wilcoxon Rank Sum Test

Cell Density grouped by Upper 10% of Ranks for Max Shear Stress

	H7A	H7B	H7C	H7D	H21A	NA	NB
Level of Significance (α):	0.05	0.05	0.05	0.05	0.05	0.05	0.05
Sample Size for Group A:	345	466	309	381	323	206	441
Sum of Ranks for Group A:	1.87E+05	1.59E+06	6.12E+05	6.13E+05	7.39E+05	2.15E+05	1.13E+06
Mean Rank for Group A:	543.21	3413.6	1980.8	1608.1	2287.7	1044.8	2558.4
Sample Size for Group B:	3102	4195	2776	3427	2907	1849	3963
Sum of Ranks for Group B:	5.76E+06	9.27E+06	4.15E+06	6.64E+06	4.48E+06	1.90E+06	8.57E+06
Mean Rank for Group B:	1855.3	2210.7	1494.3	1937.5	1540.8	1026.1	2162.9
Total Population Size:	3447.0	4661	3085	3808	3230	2055	4404
Total Sum of Ranks:	5.94E+06	1.09E+07	4.76E+06	7.25E+06	5.22E+06	2.11E+06	9.70E+06
Standard Deviation of Group A:	17536	27558	14852	20358	15900	8078.4	25329
Standard Normal Score of A:	-23.23	18.31	9.11	-5.55	13.66	0.43	6.20
Two-Tailed Test:							
Lower Critical Value:	-1.9600	-1.9600	-1.9600	-1.9600	-1.9600	-1.9600	-1.9600
Upper Critical Value:	1.9600	1.9600	1.9600	1.9600	1.9600	1.9600	1.9600
p -value:	0.0000	0.0000	0.0000	0.0000	0.0000	0.6692	0.0000
Reject the null hypothesis?	YES	YES	YES	YES	YES	NO	YES

Wilcoxon Rank Sum Test

Max Shear Stress grouped by Upper Quartile of Values for Cell Density

	H7A	H7B	H7C	H7D	H21A	NA	NB
Level of Significance (α):	0.05	0.05	0.05	0.05	0.05	0.05	0.05
Sample Size for Group A:	364	329	214	198	233	48	388
Sum of Ranks for Group A:	3.68E+05	7.88E+05	1.89E+05	1.04E+05	5.56E+05	2.96E+04	9.65E+05
Mean Rank for Group A:	1010.2	2395.7	881.71	526.32	2386.4	616.85	2486
Sample Size for Group B:	3083	4332	2871	3610	2997	2007	4016
Sum of Ranks for Group B:	5.57E+06	1.01E+07	4.57E+06	7.15E+06	4.66E+06	2.08E+06	8.74E+06
Mean Rank for Group B:	1808.3	2326.1	1592.3	1980.1	1555.6	1037.8	2175.1
Total Population Size:	3447.0	4661	3085	3808	3230	2055	4404
Total Sum of Ranks:	5.94E+06	1.09E+07	4.76E+06	7.25E+06	5.22E+06	2.11E+06	9.70E+06
Standard Deviation of Group A:	17957	23531	12570	15063	13712	4062.7	23916
Standard Normal Score of A:	-14.47	0.91	-11.26	-18.12	13.10	-4.86	4.60
Two-Tailed Test:							
Lower Critical Value:	-1.9600	-1.9600	-1.9600	-1.9600	-1.9600	-1.9600	-1.9600
Upper Critical Value:	1.9600	1.9600	1.9600	1.9600	1.9600	1.9600	1.9600
p -value:	0.0000	0.3654	0.0000	0.0000	0.0000	0.0000	0.0000

Wilcoxon Rank Sum Test

Max Shear Stress grouped by Upper 10% of Ranks for Cell Density

	H7A	H7B	H7C	H7D	H21A	NA	NB
Level of Significance (α):	0.05	0.05	0.05	0.05	0.05	0.05	0.05
Sample Size for Group A:	345	466	290	381	323	199	441
Sum of Ranks for Group A:	3.49E+05	1.18E+06	2.99E+05	2.84E+05	7.42E+05	1.84E+05	1.09E+06
Mean Rank for Group A:	1010.3	2531.1	1030.9	746.13	2296.7	923.74	2479.5
Sample Size for Group B:	3102	4195	2795	3427	2907	1856	3963
Sum of Ranks for Group B:	5.59E+06	9.69E+06	4.46E+06	6.97E+06	4.48E+06	1.93E+06	8.61E+06
Mean Rank for Group B:	1803.4	2308.8	1596.1	2033.3	1539.8	1039.2	2171.7
Total Population Size:	3447.0	4661	3085	3808	3230	2055	4404
Total Sum of Ranks:	5.94E+06	1.09E+07	4.76E+06	7.25E+06	5.22E+06	2.11E+06	9.70E+06
Standard Deviation of Group A:	17536	27558	14438	20358	15900	7954.9	25329
Standard Normal Score of A:	-14.04	3.38	-10.29	-21.68	13.84	-2.61	4.82
Two-Tailed Test:							
Lower Critical Value:	-1.9600	-1.9600	-1.9600	-1.9600	-1.9600	-1.9600	-1.9600
Upper Critical Value:	1.9600	1.9600	1.9600	1.9600	1.9600	1.9600	1.9600
p -value:	0.0000	0.0007	0.0000	0.0000	0.0000	0.0091	0.0000

Table K-10: Wilcoxon rank sum test results for cell density versus maximal wall tension.

Wilcoxon Rank Sum Test

Cell Density grouped by Upper Quartile of *Values* for Wall Tension

	H7A	H7B	H7C	H7D	H21A	NA	NB
Level of Significance (α):	0.05	0.05	0.05	0.05	0.05	0.05	0.05
Sample Size for Group A:	82	19	17	35	63	61	105
Sum of Ranks for Group A:	2.38E+05	5.08E+04	3.13E+04	8.18E+04	1.11E+05	6.62E+04	2.49E+05
Mean Rank for Group A:	2906	2671.9	1842.8	2336.7	1758.3	1084.6	2369
Sample Size for Group B:	3365	4642	3068	3773	3167	1994	4299
Sum of Ranks for Group B:	5.70E+06	1.08E+07	4.73E+06	7.17E+06	5.11E+06	2.05E+06	9.45E+06
Mean Rank for Group B:	1695.2	2329.6	1541.3	1900.5	1612.7	1026.3	2198.4
Total Population Size:	3447.0	4661	3085	3808	3230	2055	4404
Total Sum of Ranks:	5.94E+06	1.09E+07	4.76E+06	7.25E+06	5.22E+06	2.11E+06	9.70E+06
Standard Deviation of Group A:	8904.1	5853.6	3662.3	6474.3	7329.5	4565.1	12872
Standard Normal Score of A:	10.89	1.11	1.39	2.34	1.23	0.76	1.36
Two-Tailed Test:							
Lower Critical Value:	-1.9600	-1.9600	-1.9600	-1.9600	-1.9600	-1.9600	-1.9600
Upper Critical Value:	1.9600	1.9600	1.9600	1.9600	1.9600	1.9600	1.9600
p -value:	0.0000	0.2685	0.1641	0.0195	0.2197	0.4494	0.1745
Reject the null hypothesis?	YES	NO	NO	YES	NO	NO	NO

Wilcoxon Rank Sum Test

Cell Density grouped by Upper 10% of Ranks for Wall Tension

	H7A	H7B	H7C	H7D	H21A	NA	NB
Level of Significance (α):	0.05	0.05	0.05	0.05	0.05	0.05	0.05
Sample Size for Group A:	345	466	309	381	323	206	441
Sum of Ranks for Group A:	9.52E+05	1.02E+06	5.55E+05	7.40E+05	5.72E+05	2.22E+05	9.71E+05
Mean Rank for Group A:	2758.1	2179.6	1796.7	1941.5	1770.8	1079.2	2200.7
Sample Size for Group B:	3102	4195	2776	3427	2907	1849	3963
Sum of Ranks for Group B:	4.99E+06	9.85E+06	4.21E+06	6.51E+06	4.65E+06	1.89E+06	8.73E+06
Mean Rank for Group B:	1609	2347.8	1514.8	1900.4	1598.2	1022.3	2202.7
Total Population Size:	3447.0	4661	3085	3808	3230	2055	4404
Total Sum of Ranks:	5.94E+06	1.09E+07	4.76E+06	7.25E+06	5.22E+06	2.11E+06	9.70E+06
Standard Deviation of Group A:	17536	27558	14852	20358	15900	8078.4	25329
Standard Normal Score of A:	20.34	-2.56	5.28	0.69	3.15	1.31	-0.03
Two-Tailed Test:							
Lower Critical Value:	-1.9600	-1.9600	-1.9600	-1.9600	-1.9600	-1.9600	-1.9600
Upper Critical Value:	1.9600	1.9600	1.9600	1.9600	1.9600	1.9600	1.9600
p -value:	0.0000	0.0105	0.0000	0.4884	0.0016	0.1914	0.9750
Reject the null hypothesis?	YES	YES	YES	NO	YES	NO	NO

Wilcoxon Rank Sum Test

Wall Tension grouped by Upper Quartile of *Values* for Cell Density

	H7A	H7B	H7C	H7D	H21A	NA	NB
Level of Significance (α):	0.05	0.05	0.05	0.05	0.05	0.05	0.05
Sample Size for Group A:	364	329	214	198	233	48	388
Sum of Ranks for Group A:	9.29E+05	7.56E+05	1.87E+05	8.44E+04	5.16E+05	2.27E+04	6.67E+05
Mean Rank for Group A:	2553.5	2299.2	873.57	426.27	2216.6	472.92	1718.9
Sample Size for Group B:	3083	4332	2871	3610	2997	2007	4016
Sum of Ranks for Group B:	5.01E+06	1.01E+07	4.57E+06	7.17E+06	4.70E+06	2.09E+06	9.03E+06
Mean Rank for Group B:	1626.1	2333.4	1592.9	1985.6	1568.8	1041.3	2249.2
Total Population Size:	3447.0	4661	3085	3808	3230	2055	4404
Total Sum of Ranks:	5.94E+06	1.09E+07	4.76E+06	7.25E+06	5.22E+06	2.11E+06	9.70E+06
Standard Deviation of Group A:	17957	23531	12570	15063	13712	4062.7	23916
Standard Normal Score of A:	16.82	-0.44	-11.40	-19.43	10.21	-6.56	-7.85
Two-Tailed Test:							
Lower Critical Value:	-1.9600	-1.9600	-1.9600	-1.9600	-1.9600	-1.9600	-1.9600
Upper Critical Value:	1.9600	1.9600	1.9600	1.9600	1.9600	1.9600	1.9600
p -value:	0.0000	0.6566	0.0000	0.0000	0.0000	0.0000	0.0000

Wilcoxon Rank Sum Test

Wall Tension grouped by Upper 10% of Ranks for Cell Density

	H7A	H7B	H7C	H7D	H21A	NA	NB
Level of Significance (α):	0.05	0.05	0.05	0.05	0.05	0.05	0.05
Sample Size for Group A:	345	466	290	381	323	199	441
Sum of Ranks for Group A:	8.83E+05	1.10E+06	2.97E+05	2.55E+05	6.99E+05	1.82E+05	7.96E+05
Mean Rank for Group A:	2559.6	2366.5	1025.4	668.49	2163.6	914.13	1804.6
Sample Size for Group B:	3102	4195	2795	3427	2907	1856	3963
Sum of Ranks for Group B:	5.06E+06	9.76E+06	4.46E+06	7.00E+06	4.52E+06	1.93E+06	8.90E+06
Mean Rank for Group B:	1631.1	2327.1	1596.7	2041.9	1554.6	1040.2	2246.8
Total Population Size:	3447.0	4661	3085	3808	3230	2055	4404
Total Sum of Ranks:	5.94E+06	1.09E+07	4.76E+06	7.25E+06	5.22E+06	2.11E+06	9.70E+06
Standard Deviation of Group A:	17536	27558	14438	20358	15900	7954.9	25329
Standard Normal Score of A:	16.44	0.60	-10.40	-23.13	11.13	-2.85	-6.93
Two-Tailed Test:							
Lower Critical Value:	-1.9600	-1.9600	-1.9600	-1.9600	-1.9600	-1.9600	-1.9600
Upper Critical Value:	1.9600	1.9600	1.9600	1.9600	1.9600	1.9600	1.9600
p -value:	0.0000	0.5480	0.0000	0.0000	0.0000	0.0044	0.0000

Table K-11: Wilcoxon rank sum test results for cell density versus first stress invariant.

Wilcoxon Rank Sum Test

Cell Density grouped by Upper Quartile of Values for 1st Stress Invariant

	H7A	H7B	H7C	H7D	H21A	NA	NB
Level of Significance (α):	0.05	0.05	0.05	0.05	0.05	0.05	0.05
Sample Size for Group A:	552	164	728	245	338	161	793
Sum of Ranks for Group A:	3.72E+05	6.01E+05	1.24E+06	4.55E+05	7.09E+05	2.10E+05	1.59E+06
Mean Rank for Group A:	674.3	3666.7	1709.7	1858.5	2097.8	1305.4	2001.7
Sample Size for Group B:	2895	4497	2357	3563	2892	1894	3611
Sum of Ranks for Group B:	5.57E+06	1.03E+07	3.52E+06	6.80E+06	4.51E+06	1.90E+06	8.11E+06
Mean Rank for Group B:	1924.2	2282.3	1491.5	1907.7	1559.1	1004.4	2246.6
Total Population Size:	3447.0	4661	3085	3808	3230	2055	4404
Total Sum of Ranks:	5.94E+06	1.09E+07	4.76E+06	7.25E+06	5.22E+06	2.11E+06	9.70E+06
Standard Deviation of Group A:	21428	16927	21006	16646	16223	7228.1	32421
Standard Normal Score of A:	-27.04	12.94	5.78	-0.68	10.05	6.18	-4.91
Two-Tailed Test:							
Lower Critical Value:	-1.9600	-1.9600	-1.9600	-1.9600	-1.9600	-1.9600	-1.9600
Upper Critical Value:	1.9600	1.9600	1.9600	1.9600	1.9600	1.9600	1.9600
p -value:	0.0000	0.0000	0.0000	0.4986	0.0000	0.0000	0.0000
Reject the null hypothesis?	YES	YES	YES	NO	YES	YES	YES

Wilcoxon Rank Sum Test

Cell Density grouped by Upper 10% of Ranks for 1st Stress Invariant

	H7A	H7B	H7C	H7D	H21A	NA	NB
Level of Significance (α):	0.05	0.05	0.05	0.05	0.05	0.05	0.05
Sample Size for Group A:	345	466	309	381	323	206	441
Sum of Ranks for Group A:	1.86E+05	1.43E+06	5.70E+05	6.28E+05	6.75E+05	2.59E+05	7.83E+05
Mean Rank for Group A:	540.33	3061.9	1846	1648.8	2088.5	1256.5	1775
Sample Size for Group B:	3102	4195	2776	3427	2907	1849	3963
Sum of Ranks for Group B:	5.76E+06	9.44E+06	4.19E+06	6.62E+06	4.54E+06	1.85E+06	8.92E+06
Mean Rank for Group B:	1855.6	2249.8	1509.3	1932.9	1562.9	1002.5	2250.1
Total Population Size:	3447.0	4661	3085	3808	3230	2055	4404
Total Sum of Ranks:	5.94E+06	1.09E+07	4.76E+06	7.25E+06	5.22E+06	2.11E+06	9.70E+06
Standard Deviation of Group A:	17536	27558	14852	20358	15900	8078.4	25329
Standard Normal Score of A:	-23.29	12.36	6.30	-4.79	9.61	5.83	-7.44
Two-Tailed Test:							
Lower Critical Value:	-1.9600	-1.9600	-1.9600	-1.9600	-1.9600	-1.9600	-1.9600
Upper Critical Value:	1.9600	1.9600	1.9600	1.9600	1.9600	1.9600	1.9600
p -value:	0.0000	0.0000	0.0000	0.0000	0.0000	0.0000	0.0000
Reject the null hypothesis?	YES	YES	YES	YES	YES	YES	YES

Wilcoxon Rank Sum Test

1st Stress Invariant grouped by Upper Quartile of Values for Cell Density

	H7A	H7B	H7C	H7D	H21A	NA	NB
Level of Significance (α):	0.05	0.05	0.05	0.05	0.05	0.05	0.05
Sample Size for Group A:	364	329	214	198	233	48	388
Sum of Ranks for Group A:	3.43E+05	4.28E+05	2.20E+05	1.16E+05	3.08E+05	3.82E+04	6.31E+05
Mean Rank for Group A:	943.15	1300.4	1028.1	586.03	1320.5	796.42	1625.1
Sample Size for Group B:	3083	4332	2871	3610	2997	2007	4016
Sum of Ranks for Group B:	5.60E+06	1.04E+07	4.54E+06	7.14E+06	4.91E+06	2.07E+06	9.07E+06
Mean Rank for Group B:	1816.2	2409.3	1581.4	1976.8	1638.4	1033.5	2258.3
Total Population Size:	3447.0	4661	3085	3808	3230	2055	4404
Total Sum of Ranks:	5.94E+06	1.09E+07	4.76E+06	7.25E+06	5.22E+06	2.11E+06	9.70E+06
Standard Deviation of Group A:	17957	23531	12570	15063	13712	4062.7	23916
Standard Normal Score of A:	-15.83	-14.41	-8.77	-17.33	-5.01	-2.74	-9.37
Two-Tailed Test:							
Lower Critical Value:	-1.9600	-1.9600	-1.9600	-1.9600	-1.9600	-1.9600	-1.9600
Upper Critical Value:	1.9600	1.9600	1.9600	1.9600	1.9600	1.9600	1.9600
p -value:	0.0000	0.0000	0.0000	0.0000	0.0000	0.0062	0.0000

Wilcoxon Rank Sum Test

1st Stress Invariant grouped by Upper 10% of Ranks for Cell Density

	H7A	H7B	H7C	H7D	H21A	NA	NB
Level of Significance (α):	0.05	0.05	0.05	0.05	0.05	0.05	0.05
Sample Size for Group A:	345	466	290	381	323	199	441
Sum of Ranks for Group A:	3.21E+05	6.98E+05	3.30E+05	2.96E+05	4.85E+05	1.96E+05	7.43E+05
Mean Rank for Group A:	931.21	1498.2	1138.3	776.32	1502	986.03	1684.3
Sample Size for Group B:	3102	4195	2795	3427	2907	1856	3963
Sum of Ranks for Group B:	5.62E+06	1.02E+07	4.43E+06	6.96E+06	4.73E+06	1.92E+06	8.96E+06
Mean Rank for Group B:	1812.2	2423.5	1585	2029.9	1628.1	1032.5	2260.2
Total Population Size:	3447.0	4661	3085	3808	3230	2055	4404
Total Sum of Ranks:	5.94E+06	1.09E+07	4.76E+06	7.25E+06	5.22E+06	2.11E+06	9.70E+06
Standard Deviation of Group A:	17536	27558	14438	20358	15900	7954.9	25329
Standard Normal Score of A:	-15.60	-14.08	-8.13	-21.11	-2.31	-1.05	-9.02
Two-Tailed Test:							
Lower Critical Value:	-1.9600	-1.9600	-1.9600	-1.9600	-1.9600	-1.9600	-1.9600
Upper Critical Value:	1.9600	1.9600	1.9600	1.9600	1.9600	1.9600	1.9600
p -value:	0.0000	0.0000	0.0000	0.0000	0.0211	0.2937	0.0000

Table K-12: Wilcoxon rank sum test results for cell density second stress invariant.

Wilcoxon Rank Sum Test

Cell Density grouped by Upper Quartile of Values for 2nd Stress Invariant

	H7A	H7B	H7C	H7D	H21A	NA	NB
Level of Significance (α):	0.05	0.05	0.05	0.05	0.05	0.05	0.05
Sample Size for Group A:	502	9	164	125	350	103	315
Sum of Ranks for Group A:	3.37E+05	4.05E+04	2.88E+05	2.50E+05	7.15E+05	1.46E+05	4.86E+05
Mean Rank for Group A:	671.62	4497	1753.3	2003.9	2043.6	1420.4	1541.9
Sample Size for Group B:	2945	4652	2921	3683	2880	1952	4089
Sum of Ranks for Group B:	5.61E+06	1.08E+07	4.47E+06	7.00E+06	4.50E+06	1.97E+06	9.21E+06
Mean Rank for Group B:	1903.4	2326.8	1531.2	1901.1	1563.5	1007.3	2253.4
Total Population Size:	3447.0	4661	3085	3808	3230	2055	4404
Total Sum of Ranks:	5.94E+06	1.09E+07	4.76E+06	7.25E+06	5.22E+06	2.11E+06	9.70E+06
Standard Deviation of Group A:	20610	4033.1	11099	12088	16474	5869.2	21744
Standard Normal Score of A:	-25.63	4.83	3.11	1.03	9.10	6.89	-9.57
Two-Tailed Test:							
Lower Critical Value:	-1.9600	-1.9600	-1.9600	-1.9600	-1.9600	-1.9600	-1.9600
Upper Critical Value:	1.9600	1.9600	1.9600	1.9600	1.9600	1.9600	1.9600
p -value:	0.0000	0.0000	0.0019	0.3039	0.0000	0.0000	0.0000
Reject the null hypothesis?	YES	YES	YES	NO	YES	YES	YES

Wilcoxon Rank Sum Test

Cell Density grouped by Upper 10% of Ranks for 2nd Stress Invariant

	H7A	H7B	H7C	H7D	H21A	NA	NB
Level of Significance (α):	0.05	0.05	0.05	0.05	0.05	0.05	0.05
Sample Size for Group A:	345	466	309	381	323	206	441
Sum of Ranks for Group A:	1.95E+05	1.38E+06	5.67E+05	6.40E+05	6.56E+05	2.47E+05	7.56E+05
Mean Rank for Group A:	566.36	2959.8	1836.3	1678.7	2030.5	1200.1	1715.1
Sample Size for Group B:	3102	4195	2776	3427	2907	1849	3963
Sum of Ranks for Group B:	5.75E+06	9.49E+06	4.19E+06	6.61E+06	4.56E+06	1.87E+06	8.94E+06
Mean Rank for Group B:	1852.8	2261.2	1510.4	1929.6	1569.4	1008.8	2256.7
Total Population Size:	3447.0	4661	3085	3808	3230	2055	4404
Total Sum of Ranks:	5.94E+06	1.09E+07	4.76E+06	7.25E+06	5.22E+06	2.11E+06	9.70E+06
Standard Deviation of Group A:	17536	27558	14852	20358	15900	8078.4	25329
Standard Normal Score of A:	-22.78	10.63	6.10	-4.23	8.43	4.39	-8.49
Two-Tailed Test:							
Lower Critical Value:	-1.9600	-1.9600	-1.9600	-1.9600	-1.9600	-1.9600	-1.9600
Upper Critical Value:	1.9600	1.9600	1.9600	1.9600	1.9600	1.9600	1.9600
p -value:	0.0000	0.0000	0.0000	0.0000	0.0000	0.0000	0.0000
Reject the null hypothesis?	YES	YES	YES	YES	YES	YES	YES

Wilcoxon Rank Sum Test

2nd Stress Invariant grouped by Upper Quartile of Values for Cell Density

	H7A	H7B	H7C	H7D	H21A	NA	NB
Level of Significance (α):	0.05	0.05	0.05	0.05	0.05	0.05	0.05
Sample Size for Group A:	364	329	214	198	233	48	388
Sum of Ranks for Group A:	3.53E+05	2.82E+05	2.36E+05	1.17E+05	2.31E+05	4.34E+04	6.18E+05
Mean Rank for Group A:	968.44	856.32	1104.7	592.9	993.03	904.31	1594
Sample Size for Group B:	3083	4332	2871	3610	2997	2007	4016
Sum of Ranks for Group B:	5.59E+06	1.06E+07	4.52E+06	7.13E+06	4.99E+06	2.07E+06	9.08E+06
Mean Rank for Group B:	1813.2	2443	1575.7	1976.4	1663.9	1031	2261.3
Total Population Size:	3447.0	4661	3085	3808	3230	2055	4404
Total Sum of Ranks:	5.94E+06	1.09E+07	4.76E+06	7.25E+06	5.22E+06	2.11E+06	9.70E+06
Standard Deviation of Group A:	17957	23531	12570	15063	13712	4062.7	23916
Standard Normal Score of A:	-15.32	-20.62	-7.46	-17.24	-10.58	-1.46	-9.87
Two-Tailed Test:							
Lower Critical Value:	-1.9600	-1.9600	-1.9600	-1.9600	-1.9600	-1.9600	-1.9600
Upper Critical Value:	1.9600	1.9600	1.9600	1.9600	1.9600	1.9600	1.9600
p -value:	0.0000	0.0000	0.0000	0.0000	0.0000	0.1439	0.0000

Wilcoxon Rank Sum Test

2nd Stress Invariant grouped by Upper 10% of Ranks for Cell Density

	H7A	H7B	H7C	H7D	H21A	NA	NB
Level of Significance (α):	0.05	0.05	0.05	0.05	0.05	0.05	0.05
Sample Size for Group A:	345	466	290	381	323	199	441
Sum of Ranks for Group A:	3.29E+05	4.62E+05	3.44E+05	2.91E+05	4.05E+05	2.05E+05	7.30E+05
Mean Rank for Group A:	955	990.56	1185.9	763.48	1254.1	1032.4	1654.6
Sample Size for Group B:	3102	4195	2795	3427	2907	1856	3963
Sum of Ranks for Group B:	5.61E+06	1.04E+07	4.42E+06	6.96E+06	4.81E+06	1.91E+06	8.97E+06
Mean Rank for Group B:	1809.5	2479.9	1580.1	2031.4	1655.7	1027.5	2263.5
Total Population Size:	3447.0	4661	3085	3808	3230	2055	4404
Total Sum of Ranks:	5.94E+06	1.09E+07	4.76E+06	7.25E+06	5.22E+06	2.11E+06	9.70E+06
Standard Deviation of Group A:	17536	27558	14438	20358	15900	7954.9	25329
Standard Normal Score of A:	-15.13	-22.67	-7.17	-21.35	-7.34	0.11	-9.54
Two-Tailed Test:							
Lower Critical Value:	-1.9600	-1.9600	-1.9600	-1.9600	-1.9600	-1.9600	-1.9600
Upper Critical Value:	1.9600	1.9600	1.9600	1.9600	1.9600	1.9600	1.9600
p -value:	0.0000	0.0000	0.0000	0.0000	0.0000	0.9120	0.0000

Table K-13: Wilcoxon rank sum test results for wall thickness versus von Mises stress.

Wilcoxon Rank Sum Test

Wall Thickness grouped by Upper Quartile of Values for Von Mises Stress

	H7A	H7B	H7C	H7D	H21A	NA	NB
Level of Significance (α):	0.05	0.05	0.05	0.05	0.05	0.05	0.05
Sample Size for Group A:	126	792	291	153	96	76	308
Sum of Ranks for Group A:	7.67E+04	1.25E+06	5.17E+05	1.37E+05	1.91E+05	5.48E+04	3.32E+05
Mean Rank for Group A:	608.96	1573.2	1776.6	894.2	1985.9	721.57	1076.8
Sample Size for Group B:	3321	3869	2794	3655	3134	1979	4096
Sum of Ranks for Group B:	5.87E+06	9.62E+06	4.24E+06	7.12E+06	5.03E+06	2.06E+06	9.37E+06
Mean Rank for Group B:	1766.3	2486.1	1518.7	1946.8	1604.2	1039.8	2287.2
Total Population Size:	3447.0	4661	3085	3808	3230	2055	4404
Total Sum of Ranks:	5.94E+06	1.09E+07	4.76E+06	7.25E+06	5.22E+06	2.11E+06	9.70E+06
Standard Deviation of Group A:	10965	34503	14460	13323	9000.4	5076.3	21520
Standard Normal Score of A:	-12.81	-17.40	4.70	-11.60	3.95	-4.59	-16.11
Two-Tailed Test:							
Lower Critical Value:	-1.9600	-1.9600	-1.9600	-1.9600	-1.9600	-1.9600	-1.9600
Upper Critical Value:	1.9600	1.9600	1.9600	1.9600	1.9600	1.9600	1.9600
p -value:	0.0000	0.0000	0.0000	0.0000	0.0001	0.0000	0.0000
Reject the null hypothesis?	YES	YES	YES	YES	YES	YES	YES

Wilcoxon Rank Sum Test

Wall Thickness grouped by Upper 10% of Ranks for Von Mises Stress

	H7A	H7B	H7C	H7D	H21A	NA	NB
Level of Significance (α):	0.05	0.05	0.05	0.05	0.05	0.05	0.05
Sample Size for Group A:	345	466	309	381	323	206	441
Sum of Ranks for Group A:	2.22E+05	6.95E+05	5.44E+05	4.13E+05	4.13E+05	1.76E+05	5.59E+05
Mean Rank for Group A:	642.64	1492.3	1760.4	1084.9	1279.5	856	1268.1
Sample Size for Group B:	3102	4195	2776	3427	2907	1849	3963
Sum of Ranks for Group B:	5.72E+06	1.02E+07	4.22E+06	6.84E+06	4.80E+06	1.94E+06	9.14E+06
Mean Rank for Group B:	1844.3	2424.2	1518.8	1995.6	1652.8	1047.2	2306.5
Total Population Size:	3447.0	4661	3085	3808	3230	2055	4404
Total Sum of Ranks:	5.94E+06	1.09E+07	4.76E+06	7.25E+06	5.22E+06	2.11E+06	9.70E+06
Standard Deviation of Group A:	17536	27558	14852	20358	15900	8078.4	25329
Standard Normal Score of A:	-21.28	-14.18	4.52	-15.34	-6.83	-4.39	-16.27
Two-Tailed Test:							
Lower Critical Value:	-1.9600	-1.9600	-1.9600	-1.9600	-1.9600	-1.9600	-1.9600
Upper Critical Value:	1.9600	1.9600	1.9600	1.9600	1.9600	1.9600	1.9600
p -value:	0.0000	0.0000	0.0000	0.0000	0.0000	0.0000	0.0000
Reject the null hypothesis?	YES	YES	YES	YES	YES	YES	YES

Wilcoxon Rank Sum Test

Von Mises Stress grouped by Upper Quartile of Values for Wall Thickness

	H7A	H7B	H7C	H7D	H21A	NA	NB
Level of Significance (α):	0.05	0.05	0.05	0.05	0.05	0.05	0.05
Sample Size for Group A:	173	10	41	379	167	31	549
Sum of Ranks for Group A:	1.06E+05	1.69E+04	8.33E+04	4.95E+05	1.58E+05	2.52E+04	4.87E+05
Mean Rank for Group A:	613.32	1686.4	2030.8	1306.6	947.16	812.1	886.62
Sample Size for Group B:	3274	4651	3044	3429	3063	2024	3855
Sum of Ranks for Group B:	5.84E+06	1.08E+07	4.68E+06	6.76E+06	5.06E+06	2.09E+06	9.21E+06
Mean Rank for Group B:	1782.7	2332.4	1536.4	1970.6	1651.9	1031.3	2389.9
Total Population Size:	3447.0	4661	3085	3808	3230	2055	4404
Total Sum of Ranks:	5.94E+06	1.09E+07	4.76E+06	7.25E+06	5.22E+06	2.11E+06	9.70E+06
Standard Deviation of Group A:	12757	4250.8	5665.3	20310	11736	3278.7	27873
Standard Normal Score of A:	-15.06	-1.52	3.53	-11.16	-9.51	-2.04	-25.92
Two-Tailed Test:							
Lower Critical Value:	-1.9600	-1.9600	-1.9600	-1.9600	-1.9600	-1.9600	-1.9600
Upper Critical Value:	1.9600	1.9600	1.9600	1.9600	1.9600	1.9600	1.9600
p -value:	0.0000	0.1294	0.0004	0.0000	0.0000	0.0412	0.0000

Wilcoxon Rank Sum Test

Von Mises Stress grouped by Upper 10% of Ranks for Wall Thickness

	H7A	H7B	H7C	H7D	H21A	NA	NB
Level of Significance (α):	0.05	0.05	0.05	0.05	0.05	0.05	0.05
Sample Size for Group A:	345	466	309	381	323	206	441
Sum of Ranks for Group A:	2.68E+05	5.19E+05	5.97E+05	5.01E+05	3.40E+05	2.17E+05	3.74E+05
Mean Rank for Group A:	777.31	1113.4	1933.5	1314.6	1053	1055.4	849
Sample Size for Group B:	3102	4195	2776	3427	2907	1849	3963
Sum of Ranks for Group B:	5.67E+06	1.03E+07	4.16E+06	6.75E+06	4.88E+06	1.90E+06	9.33E+06
Mean Rank for Group B:	1829.3	2466.3	1499.5	1970.1	1678	1025	2353.1
Total Population Size:	3447.0	4661	3085	3808	3230	2055	4404
Total Sum of Ranks:	5.94E+06	1.09E+07	4.76E+06	7.25E+06	5.22E+06	2.11E+06	9.70E+06
Standard Deviation of Group A:	17536	27558	14852	20358	15900	8078.4	25329
Standard Normal Score of A:	-18.63	-20.59	8.13	-11.04	-11.43	0.70	-23.57
Two-Tailed Test:							
Lower Critical Value:	-1.9600	-1.9600	-1.9600	-1.9600	-1.9600	-1.9600	-1.9600
Upper Critical Value:	1.9600	1.9600	1.9600	1.9600	1.9600	1.9600	1.9600
p -value:	0.0000	0.0000	0.0000	0.0000	0.0000	0.4853	0.0000

Table K-14: Wilcoxon rank sum test results for wall thickness versus maximal wall tension.

Wilcoxon Rank Sum Test

Wall Thickness grouped by Upper Quartile of Values for Wall Tension

	H7A	H7B	H7C	H7D	H21A	NA	NB
Level of Significance (α):	0.05	0.05	0.05	0.05	0.05	0.05	0.05
Sample Size for Group A:	126	792	291	153	96	76	308
Sum of Ranks for Group A:	4.03E+05	2.54E+06	6.20E+05	4.51E+05	2.95E+05	8.99E+04	1.10E+06
Mean Rank for Group A:	3197.6	3203.5	2131.9	2947.7	3075.3	1182.4	3574.5
Sample Size for Group B:	3321	3869	2794	3655	3134	1979	4096
Sum of Ranks for Group B:	5.54E+06	8.33E+06	4.14E+06	6.80E+06	4.92E+06	2.02E+06	8.60E+06
Mean Rank for Group B:	1668.1	2152.4	1481.7	1860.8	1570.8	1022.1	2099.3
Total Population Size:	3447.0	4661	3085	3808	3230	2055	4404
Total Sum of Ranks:	5.94E+06	1.09E+07	4.76E+06	7.25E+06	5.22E+06	2.11E+06	9.70E+06
Standard Deviation of Group A:	10965	34503	14460	13323	9000.4	5076.3	21520
Standard Normal Score of A:	16.93	20.03	11.85	11.98	15.57	2.31	19.64
Two-Tailed Test:							
Lower Critical Value:	-1.9600	-1.9600	-1.9600	-1.9600	-1.9600	-1.9600	-1.9600
Upper Critical Value:	1.9600	1.9600	1.9600	1.9600	1.9600	1.9600	1.9600
p -value:	0.0000	0.0000	0.0000	0.0000	0.0000	0.0208	0.0000
Reject the null hypothesis?	YES	YES	YES	YES	YES	YES	YES

Wilcoxon Rank Sum Test

Wall Thickness grouped by Upper 10% of Ranks for Wall Tension

	H7A	H7B	H7C	H7D	H21A	NA	NB
Level of Significance (α):	0.05	0.05	0.05	0.05	0.05	0.05	0.05
Sample Size for Group A:	345	466	309	381	323	206	441
Sum of Ranks for Group A:	1.01E+06	1.48E+06	6.53E+05	1.03E+06	7.82E+05	2.50E+05	1.60E+06
Mean Rank for Group A:	2916.7	3173.1	2112.4	2708.3	2421.4	1213.8	3628.4
Sample Size for Group B:	3102	4195	2776	3427	2907	1849	3963
Sum of Ranks for Group B:	4.94E+06	9.39E+06	4.11E+06	6.22E+06	4.44E+06	1.86E+06	8.10E+06
Mean Rank for Group B:	1591.4	2237.5	1479.6	1815.1	1526	1007.3	2043.8
Total Population Size:	3447.0	4661	3085	3808	3230	2055	4404
Total Sum of Ranks:	5.94E+06	1.09E+07	4.76E+06	7.25E+06	5.22E+06	2.11E+06	9.70E+06
Standard Deviation of Group A:	17536	27558	14852	20358	15900	8078.4	25329
Standard Normal Score of A:	23.47	14.24	11.85	15.04	16.37	4.74	24.83
Two-Tailed Test:							
Lower Critical Value:	-1.9600	-1.9600	-1.9600	-1.9600	-1.9600	-1.9600	-1.9600
Upper Critical Value:	1.9600	1.9600	1.9600	1.9600	1.9600	1.9600	1.9600
p -value:	0.0000	0.0000	0.0000	0.0000	0.0000	0.0000	0.0000
Reject the null hypothesis?	YES	YES	YES	YES	YES	YES	YES

Wilcoxon Rank Sum Test

Wall Tension grouped by Upper Quartile of Values for Wall Thickness

	H7A	H7B	H7C	H7D	H21A	NA	NB
Level of Significance (α):	0.05	0.05	0.05	0.05	0.05	0.05	0.05
Sample Size for Group A:	82	19	17	35	63	61	105
Sum of Ranks for Group A:	2.75E+05	5.49E+04	5.21E+04	1.28E+05	1.91E+05	7.79E+04	4.13E+05
Mean Rank for Group A:	3359.5	2889.1	3064.2	3652.3	3038.1	1277.8	3934.7
Sample Size for Group B:	3365	4642	3068	3773	3167	1994	4299
Sum of Ranks for Group B:	5.67E+06	1.08E+07	4.71E+06	7.12E+06	5.03E+06	2.03E+06	9.29E+06
Mean Rank for Group B:	1684.1	2328.7	1534.6	1888.3	1587.2	1020.4	2160.2
Total Population Size:	3447.0	4661	3085	3808	3230	2055	4404
Total Sum of Ranks:	5.94E+06	1.09E+07	4.76E+06	7.25E+06	5.22E+06	2.11E+06	9.70E+06
Standard Deviation of Group A:	8904.1	5853.6	3662.3	6474.3	7329.5	4565.1	12872
Standard Normal Score of A:	15.06	1.81	7.06	9.45	12.23	3.34	14.13
Two-Tailed Test:							
Lower Critical Value:	-1.9600	-1.9600	-1.9600	-1.9600	-1.9600	-1.9600	-1.9600
Upper Critical Value:	1.9600	1.9600	1.9600	1.9600	1.9600	1.9600	1.9600
p -value:	0.0000	0.0701	0.0000	0.0000	0.0000	0.0008	0.0000

Wilcoxon Rank Sum Test

Wall Tension grouped by Upper 10% of Ranks for Wall Thickness

	H7A	H7B	H7C	H7D	H21A	NA	NB
Level of Significance (α):	0.05	0.05	0.05	0.05	0.05	0.05	0.05
Sample Size for Group A:	345	466	309	381	323	206	441
Sum of Ranks for Group A:	1.02E+06	1.69E+06	7.36E+05	1.03E+06	8.04E+05	2.52E+05	1.67E+06
Mean Rank for Group A:	2953.8	3622.5	2382.2	2692.3	2490.1	1220.9	3779.5
Sample Size for Group B:	3102	4195	2776	3427	2907	1849	3963
Sum of Ranks for Group B:	4.92E+06	9.18E+06	4.02E+06	6.23E+06	4.41E+06	1.86E+06	8.03E+06
Mean Rank for Group B:	1587.2	2187.5	1449.6	1816.9	1518.3	1006.5	2027
Total Population Size:	3447.0	4661	3085	3808	3230	2055	4404
Total Sum of Ranks:	5.94E+06	1.09E+07	4.76E+06	7.25E+06	5.22E+06	2.11E+06	9.70E+06
Standard Deviation of Group A:	17536	27558	14852	20358	15900	8078.4	25329
Standard Normal Score of A:	24.20	21.84	17.46	14.74	17.77	4.92	27.46
Two-Tailed Test:							
Lower Critical Value:	-1.9600	-1.9600	-1.9600	-1.9600	-1.9600	-1.9600	-1.9600
Upper Critical Value:	1.9600	1.9600	1.9600	1.9600	1.9600	1.9600	1.9600
p -value:	0.0000	0.0000	0.0000	0.0000	0.0000	0.0000	0.0000

REFERENCES

Abovsky, M., Y. Lanir, et al. (1996). "Tethering affects the mechanics of coronary capillaries." J. Biomechanics 29(5): 597-607.

Accorsi, M. L. (1988). "A method for modelling microstructural material discontinuities in a finite element analysis." International Journal for Numerical Methods in Engineering 26: 2187-2197.

Accorsi, M. L. (1993). "Mechanics of adaptive materials using the eigenstrain finite element method." Adaptive Structures and Material Systems 35: 203-207.

Accorsi, M. L. and R. Chamarajanagar (1991). "Numerical validation of a hybrid finite element method using eigenstrain." Computers and Structures 41(5): 1065-1071.

Alberts, B., D. Bray, et al. (1998). Essential Cell Biology: An Introduction to the Molecular Biology of the Cell. New York, Garland Publishing.

Alexander, R. W. (1995). "Hypertension and the pathogenesis of atherosclerosis - oxidative stress and the mediation of arterial inflammatory response: A new perspective." Hypertension 25: 155-161.

Anayiotos, A. S., S. A. Jones, et al. (1994). "Shear stress at a compliant model of the human carotid bifurcation." J Biomechanical Engineering 116: 98-106.

Archimbaud, E., A. Islam, et al. (1987). "Immunoperoxidase detection of myeloid antigens in glycolmethacrylate-embedded human bone marrow." Journal of Histochemistry and Cytochemistry 35(5): 595-599.

Armentano, R. L., J. G. Barra, et al. (1995). "Arterial wall mechanics in conscious dogs. Assessment of viscous, inertial, and elastic moduli to characterize aortic wall behavior." Circ Res 76: 468-478.

Atkinson, T., R. Haut, et al. (1997). "A microstructural poroelastic model for patellar tendon." BED - 1997 Bioengineering Conference 35: 573-574.

Badouel, D. (1990). An Efficient Ray-Polygon Intersection. Graphics Gems.

Baheerathan, S., F. Albregtsen, et al. (1998). "Registration of serial sections of mouse liver cell nuclei." Journal of Microscopy 192(October): 37-53.

Baldwin, A. L. (1999). "Modified hemoglobins produce venular interendothelial gaps and albumin leakage in the rat mesentery." American Journal of Phsiology 277: H650-H659.

Ballyk, P. D., M. Ojha, et al. (1996). "The importance of large strain in blood vessel mechanics." Advances in Bioengineering, ASME-BED 33: 331-332.

Bancroft, J. D. and A. Stevens (1996). Theory and Practice of Histological Techniques, Churchill Livingstone.

Bankman, I. N., Ed. (2000). Handbook of Medical Imaging: Processing and Analysis. Academic Press Series in Biomedical Engineering. San Diego, Academic Press.

Barber, C. b., D. P. Dobkin, et al. (1996). "The quickhull algorithm for convex hulls." ACM Transactions on Mathematical Software (TOMS) 22(4): 469-483.

Beattie, D., Xu C, Vito RP, Glagov S, Whang MC (1998). "Mechanical analysis of heterogeneous, atherosclerotic human aorta." J Biomechanical Engineering 120(5): 602-607.

Beattie, D. K., R. P. Vito, et al. (1996). "Measurement of the strain field in heterogeneous, diseased human aorta."

Benetos, A., M. Safar, et al. (1997). "Pulse pressure: A predictor of long-term cardiovascular mortality in a French male population." Hypertension 30: 1410-1415.

Bensaid, A. M., L. O. Hall, et al. (1991). "MRI segmentation using supervised and unsupervised methods." Annual International Conference of the IEEE Engineering in MEdicine and Biology Society 13(1): 60-61.

Bergel, D. H. (1960). "The static elastic properties of the arterial wall." Journal of Physiology 156: 445-457.

Bergel, D. H. (1961). "The dynamic elastic properties of the arterial wall." J Physiol 156: 458-469.

Berry, J., A. Rachev, et al. (1992). Analysis of the effects of a non-circular two layer stress-free state on arterial wall stresses. Proc. 14th Intl. Conference IEEE Engineering Medicine Biology.

Breslow, J. L. (1996). "Mouse models of atherosclerosis." Science 272(May 3): 685-8.

Bronzino, J. D. (1995). The Biomedical Engineering Handbook. Boca Raton, CRC Press.

Brossollet, L. (1992). "Mechanical issues in vascular grafting: a review." Intl. J. of Artificial Organs 15: 579-584.

Brossollet, L. and R. Vito (1996). "A new approach to mechanical testing and modeling of biological tissues, with application to blood vessels." Journal of Biomechanical Engineering 118: 433-439.

Brossollet, L. J. and R. P. Vito (1995). "An alternate formulation of blood vessel mechanics and the meaning of the in vivo property." J Biomechanics 28(6): 679-687.

Bund, S. J. (2001). "Spontaneously Hypertensive Rat Resistance Artery Structure Related to Myogenic and Mechanical Properties." Clinical Science 101: 385-393.

Buntin, C. and F. Silver (1990). "Noninvasive assessment of mechanical properties of peripheral arteries." Annals of Biomedical Engineering 18: 549-566.

Burston, W. R. and K. Thurley (1957). "A technique for the orientation of serial histological sections." Journal of Anatomy 91: 409-412.

Bush, E., N. Maeda, et al. (2000). "CC chemokine receptor 2 is required for macrophage infiltration and vascular hypertrophy in angiotensin II-induced hypertension." Hypertension 36: 360-363.

Cai, H. and D. G. Harrison (2000). "Endothelial Dysfunction in Cardiovascular Diseases: The Role of Oxidant Stress." Circulation Research 87: 840-844.

Camacho, D. L. A., R. H. Hopper, et al. (1997). "An improved method for finite element mesh generation of geometrically comlex structures with applications to the skullbase." J Biomechanics 30(10): 1067-1070.

Canfield, T. and P. Dobrin (1987). Static elastic properties of blood vessels. Handbook of Bioengineering, McGraw Hill.

Canny (1986). "A Computational Apporach to Edge Detection." IEEE Transactions on Pattern Analysis and Machine Intelligence PAMI-8(6): 679-698.

Cantini, C., P. Kieffer, et al. (2001). "Aminoguanidine and Aortic Wall Mechanics, Structure, and Composition in Aged Rats." Hypertension 38: 943-948.
Capers, Q., R. W. Alexander, et al. (1997). "Monocyte chemoattractant protein-1 expression in aortic tissues of hypertensive rats." Hypertension(30): 1397-1402.
Caps, M. T., T. S. Hatsukami, et al. (1996). "A clinical marker for arterial wall healing: The double line." Journal of Vascular Surgery 23: 87-94.
Carmeliet, P. and D. Collen (1997). "Molecular analysis of blood vessel formation and disease." Am J Physiol 273: H2091-H2104.
Carmines, D., J. McElhaney, et al. (1991). "A piece-wise nonlinear elastic stress expression of human and pig coronary arteries tested in vitro." J. Biomechanics 24: 899-906.
Carson, F. L. (1997). Histotechnology: A Self-Instructional Text. Chicago, ASCP Press.
Ceiler, D. L. and J. G. R. D. Mey (2000). "Chronic NG-Nitro-L-Arginine Methyl Ester Treatment Does Not Prevent Flow-Induced Remodeling in Mesenteric Feed Arteries and Arcading Arterioles." Arteriosclerosis, Thrombosis, and Vascular Biology 20: 2057-2063.
Chapin, R. E., M. D. Ross, et al. (1984). "Immersion fixation methods for glycol methacrylate-embedded testes." Toxicol Pathol 12(3): 221-227.
Chappell, D. C., S. E. Varner, et al. (1998). "Oscillatory shear stress stimulates adhesion molecule expression in cultured human endothelium." Circ Res 82: 532-539.
Chaudhry, H. R., B. Bukiet, et al. (1997). "Residual stresses in oscillating thoracic arteries reduce circumferential stresses and stress gradients." Journal of Biomechanics 30(1): 57-62.
Chen, J., S. Yoon, et al. (1997). Finite element procedures for large deformation analysis of arterial segments. ASME Bioengineering Conference, Sun River, OR.
Chen, W. W. S. (1999). On Computing Gaussian Curvature of Some Well Know Distributions. Joint Statistical Meetings of the American Statistical Association, Baltimore, MD.
Cheng, G., H. Loree, et al. (1993). "Distribution of circumferential stress in ruptured and stable atherosclerotic lesions: A structural analysis with histopathological correlation." Circulation 87: 1179-1187.
Cheng, G. C., W. H. Briggs, et al. (1997). "Mechanical strain tightly controls fibroblast growth factor-2 release from cultured human vascular smooth muscle cells." Circ Res 80: 28-36.
Chobanian, A. V. (1990). "1989 Corcoran Lecture: Adaptive and maladaptive responses of the arterial wall to hypertension." Hypertension 15: 666-674.
Christensen, K. L. (1991). "Reducing pulse pressure in hypertension may normalize small artery structure." Hypertension 18: 722-727.
Chuong, C. J. and Y. C. Fung (1983). "Three-dimensional stress distribution in arteries." Journal of Biomechanical Engineering 105(August): 268-274.
Clark, J. M. and S. Glagov (1985). "Transmural organization of the arterial media - the lamellar unit revisited." Arteriosclerosis 5(January/February): 19-34.
Coatrieux, J. L., M. Garreau, et al. (1994). "Computer vision approaches for three-dimensional reconstruction of coronary arteries: review and prospects." Critical Reviews in Biomedical Engineering 22(1): 1-38.

Cowin, S. (1996). "Strain or deformation rate dependent finite growth in soft tissues." J. Biomechanics 29(5): 647-649.
Cowin, S. C. (2000). "How is a Tissue Built?" Journal of Biomechanical Engineering 122(December): 553-569.
Dalager-Pedersen, S., E. Falk, et al. (1999). "Effects of Temperature and Histopathologic Preparation on the Size and Morphology of Atherosclerotic Carotid Arteries as Imaged by MRI." Journal of Magnetic Resonance Imaging(10): 876-885.
Davies, M. J. (1998). "Reactive oxygen species, metalloproteinases, and plaque stability." Circulation 97: 2382-2383.
Davies, P. F. (1997). "Mechanisms involved in endothelial responses to hemodynamic forces." Atherosclerosis 131 Suppl: S15-S17.
Delfino, A., N. Stergiopulos, et al. (1997). "Residual strain effects on the stress field in a thick wall finite element model of the human carotid bifurcation." Journal of Biomechanics 30(8): 777-786.
Delfino, A., N. Stergiopulos, et al. (1996). "Residual strain effects on the stress field in a thick finite element model of the human carotid bifurcation." ASME Bioeng DIV PUBL BED 33: 327-328.
Demiray, H. (1996). "A quasilinear constitutive relation for arterial wall materials." J. Biomechanics 29(8): 1011-1014.
Deverell, M. H., N. Bailey, et al. (1989A). "Tissue distortion in three-dimensional reconstruction of wax or plastic embedded microscopic structures." Pathology Research Practices 185: 598-601.
Deverell, M. H. and W. F. Whimster (1989B). "A method of image registration for three-dimensional reconstruction of microscopic structures using an IBAS 2000 image analysis system." Pathogy Research Practices 185: 602-605.
Dhar, P., G. Jayaraman, et al. (1996). "Effect of pressure on transmural fluid flow in different de-endothelialised arteries." Medical & Biological Egineering & Computing 34: 155-159.
Dickhout, J. G. and R. M. Lee (2000). "Increased medial smooth muscle cell length is responsible for vascular hypertrophy in young hypertensive rats." Am J Physiol Heart Circ Physiol 279(5): H2085-H2094.
Dixon, A. D. and P. Howarth (1957). "A photographic method of graphic reconstruction." Journal of Anatomy, London 91: 162-166.
Dollery, C. M., J. R. McEwan, et al. (1995). "Matrix metalloproteinase and cardiovascular disease." Circ Res 77: 863-868.
Dowling, N. E. (1999). Mechanical Behavior of Materials: Engineering Methods for Deformation, Fracture, and Fatigue. Upper Saddle River, New Jersey, Prentice-Hall Inc.
Edelsbrunner, H. (1995). "Algebraic Decomposition of Non-convex Polyhedra." IEEE: 248-257.
Edelsbrunner, H. and P. Fu (1998). Apparatus and Method for Geometric Morphing. USA, Raindrop Geomagic, Inc.
Edelsbrunner, H. and P. Fu (2002). Methods of Generating Three-Dimensional Digital Models of Objects by Wrapping Point Cloud Data Points. USA, Raindrop Geomagic, Inc.

Edelsbrunner, H., D. G. Kirkpatrick, et al. (1983). "On the Shape of a Set of Points in the Plane." IEEE Transactions on Information Theory IT-29(4): 551-559.
Edelsbrunner, H., D. Letscher, et al. (2000). "Topological Persistence and Simplification." IEEE: 454-463.
Edelsbrunner, H. and E. P. Mucke (1994). "Three-Dimensional Alpha Shapes." ACM Transactions on Graphics 13(1): 43-72.
Elad, D., A. Foux, et al. (1988). "A model for the nonlinear elastic response of large arteries." J. Biomechanical Engineering.
Ellis, S. and K. Burg (2003). Plastic Resins - Limitations and Opportunities for Histology (Workshop #26). NSH 2003.
Erickson, R. P. (1996). "Mouse models of human genetic disease: which mouse is more like a man?" BioEssays 18(12): 993-998.
Faux, I. D. and M. J. Pratt (1987). Computational Geometry for Design and Manufacture. Chichester, Ellis Horwood Limited.
Finlay, H. M., P. Whittaker, et al. (1998). "Collagen Organization in the Branching Region of Human Brain Arteries." Stroke(29): 1595-1601.
Frakes, D. H., C. P. Conrad, et al. (2003). "Application of an Adaptive Control Grid Interpolation Technique to Morphological Vascular Reconstruction." IEEE Transactions on Biomedical Engineering 50: 197-206.
Franklin, S. S., M. J. Jacobs, et al. (2001). "Predominance of isolated systolic hypertension among middle-aged and elderly U.S. hypertensives: analysis based on National Health and Nutrition Examination Survey (NHANES) III." Hypertension 37: 869-874.
Fridez, P., M. Zulliger, et al. (2003). "Geometrical, Functional, and Histomorphometric Adaptation of Rat Carotid Artery in Induced Hypertension." Journal of Biomechanics(36): 671-680.
Friedman, M. H., B. D. Kuban, et al. (1995). "Fabrication of vascular replicas from magnetic resonance images." Journal of Biomechanical engineering 117: 364-366.
Fronek, K. and Y. C. Fung (1980). "Mechanical properties of arteries as a function of topography and age." Biorheology 17: 227-234.
Fry, D. (1987). "Mass transport, atherogenesis, and risk." Arteriosclerosis 7: 88-100.
Fukui, T., N. Ishizaka, et al. (1997). "p22phox mRNA expression and NADPH oxidase activity are increased in aortas from hypertensive rats." Circulation Research 80: 45-51.
Fung, Y. (1987). Mechanics of soft tissues. Handbook of Bioengineering, McGraw Hill: 1.1-1.11.
Fung, Y., S. Liu, et al. (1993A). Remodeling of the constitutive equation while a tissue remodels itself under stress. ASME Bioengineering Conference.
Fung, Y. C. (1993B). Biomechanics: Mechanical Properties of Living Tissues. New York, Springer-Verlag.
Fung, Y. C. (1997). Biodynamics: Circulation. New York, Springer-Verlag.
Fung, Y. C. and S. Q. Liu (1992). "Strain distribution in small blood vessels with zero-stress state taken into consideration." Am J Physiol 262: H544-H552.

Gaballa, M., T. Raya, et al. (1992). "Arterial mechanics in spontaneously hypertensive rats-mechanical properties, hydraulic conductivity, amd two-phase finite element models." Circulation Research 71: 145-158.

Galis, Z., G. Sukhova, et al. (1994). "Increased expression of matrix metalloproteinases and matrix degrading activity in vulnerable regions of human atherosclerotic plaques." J. Clinical Investigation 94: 2493-2503.

Galis, Z. S., K. Asanuma, et al. (1998). "N-Acetyl-Cysteine decreases the matrix-degrading capacity of macrophage-derived foam cells." Circulation 97: 2445-2453.

Gentile, A. N. and E. Harth (1978). "The alignment of serial sections by spatial filtering." Computers and Biomedical Research 11: 537-551.

Gere, J. M. and S. P. Timoshenko (1997). Mechanics of Materials. Boston, PWS Publishing Company.

Gerrity, R. G. (1981A). "The role of the monocyte in atherogenesis: I. Transition of blood-borne monocytes into foam cells in fatty lesions." American Journal of Pathology 103: 181-190.

Gerrity, R. G. (1981B). "The role of the monocyte in atherogenesis: II. Migration of foam cells from atherosclerotic lesions." American Journal of Pathology 103: 191-200.

Giddens, D. P. and D. N. Ku (1987). "A note on the relationship between input flow waveform and wall shear rate in pulsatile, separating flows." Journal of Biomechanical Engineering 109: 175-176.

Glagov, S. (1994). "Intimal hyperplasia, vascular modeling, and the restenosis problem." Circulation 89(6): 2888-2891.

Glagov, S., H. S. Bassiouny, et al. (1995). "Intimal thickening: morphogenesis, functional significance and detection." Journal of Vascular Investigation 1(1): 2-14.

Glagov, S., H. S. Bassiouny, et al. (1997). "Mechanical determinats of plaque modeling, remodeling and disruption." Atherosclerosis 131 Suppl: S13-S14.

Glagov, S., D. P. Giddens, et al. (1992). "Tissue reactions to mechanical stresses in relation to artery wall stability." BED-Vol. 22, Advances in Bioengineering: 135-137.

Glagov, S., I. William P. Newman, et al. (1990). Pathobiology of the human atherosclerotic plaque. New York, Springer-Verlag.

Glagov, S., C. Zarins, et al. (1988). "Hemodynamics and Atherosclerosis: Insights and perspectives gained from studies of human arteries." Archives of Pathology and Laboratory Medicine 112: 1018-1031.

Gleason, R. L., L. A. Taber, et al. (2004). "A 2-D Model of Flow-Induced Alterations in the Geometry, Structure, and Properties of Carotid Arteries." Journal of Biomechanical Engineering 126(3): 371-381.

Goldschmidt, M. E., K. J. McLeod, et al. (2001). "Integrin-mediated mechanotransduction in vascular smooth muscle cells: Frequency and force response characteristics." Circulation Research 88: 674-680.

Goshtasby, A., L. Staib, et al. (2003). "Nonrigid Image Registration: Guest Editors' Introduction." Computer Vision and Image Understanding 89: 109-113.

Gray, H. (1973). Gray's Anatomy, Descriptive and Surgical. Philadelphia, Running Press.

Greenwald, S., A. Rachev, et al. (1994). The contribution of the structural components of the arterial wall to residual strains. Proc. 13th Southern Biomedical Engineering Conference.

Griendling, K. K. and R. W. Alexander (1998). Chapter 4: Cellular Biology of Blood Vessels. The Heart. R. W. Alexander, R. Schlant and V. Fuster. New York, McGraw-Hill: 125-141.

Griffith, L. G. and A. J. Grodzinsky (2001). "Advances in biomedical engineering." JAMA 285(5): 556-561.

Guilak, F. (1995). "Compression-induced changes in the shape and volume of the chondrocyte nucleus." Journal of Biomechanics 28(12): 1529-1541.

Guo, X. and G. S. Kassab (2004). "Distribution of stress and strain along the porcine aorta and coronary arterial tree." American Journal of Physiology: Heart and Circulatory Physiology 286(6): H2361-H2368.

Guzman, L. A., m. J. Mick, et al. (1996). "Role of intimal hyperplasia and arterial remodeling after baloon angioplasty. An experimental study in the atherosclerotic rabbit model." Arterioscler Thromb Vasc Biol 16: 479-487.

Hajinal, J. V., D. L. G. Hill, et al. (2001). Medical Image Registration. New York, CRC Press.

Halpern, W., G. Osol, et al. (1984). "Mechanical behavior of pressurized in vitro prearteriolar vessels determined with a video system." Annals of Biomedical Engineering 12: 463-479.

Han, H. and Y. Fung (1995). "Longitudinal strain of canine and porcine aortas." J. Biomechanics 28(5): 637-641.

Han, H. C. and Y. C. Fung (1991). "Species dependence of the zero stress state of aorta: pig versus rat." Journal of Biomechanical Engineering 113: 446-451.

Harvey, I. F. (1974). Theory and design of modern pressure vessels. New York, Van Nostrand Reinhold.

Hawkins, E. P., S. C. Heffelflinger, et al. (1992). "Leukocyte adhesion deficiency: clinical and postmortem observations." Pediatr. Pathol. 12: 119-130.

Hayashi, K. (1993). "Experimental approaches on measuring the mechanical properties and constitutive laws of arterial walls." Journal of Biomechanical Engineering 115(November): 481-488.

Hayashi, K., A. Makino, et al. (2001). "Remodeling of arterial wall in response to blood pressure and blood flow changes." ASME: 819-820.

Heard, O. O. (1953). "The influence of surface forces in microtomy." Anatomical Research 117: 725-737.

Heath, C. A. and S. R. Magari (1996). "Mini-Review: mechanical factors affecting cartilage regeneration in vitro." Biotechnology and Bioengineering 50: 430-437.

Heyndrickx, G. R., D. H. Boettcher, et al. (1976). "Effects of angiotensin, vasopressin, and methoxamine on cardiac function and blood flow distribution in concious dogs." American Journal of Physiology 231(5): 1579-1587.

Hibbard, L. S. and R. A. Hawkins (1988). "Objective image alignment for three-dimensional reconstruction of digital autoradiograms." Journal of Neuroscience Methods 26: 55-74.

Hironaka, K., M. Yano, et al. (1997). "In vivo aortic wall characteristics at the early stage of atherosclerosis in rabbits." Am J Physiol 273: H1142-H1147.

Hishikawa, K., T. Nakaki, et al. (1995). "Pressure enhances endothelin-1 release from cultured human endothelial cells." Hypertension 25: 449-452.

Hofer, M., G. Rappitsch, et al. (1996). "Numerical study of wall mechanics and fluid dynamics in end-to-side anastomoses and correlation to intimal hyperplasia." J Biomechanics 29(10): 1297-1308.

Holden, M., D. L. G. Hill, et al. (2000). "Voxel Similarity Measures for 3-D Serial MR Brain Image Registration." IEEE Transactions on Medical Imaging 19(Number 2): 94-102.

Hollister, S., J. Brennan, et al. (1994B). "A homogenization sampling procedure for calculating trabecular bone effective stiffness and tissue level stress." J. Biomechanics 27(4): 433-444.

Hollister, S. J. and N. Kikuchi (1994A). "Homogenization theory and digital imaging: a basis for studying the mechanics and design principles of bone tissue." Biotechnology and Bioengineering 43: 586-596.

Holzapfel, g. A., R. Eberlein, et al. (1996). "Large strain analysis of soft biological membranes: formulation and finite element analysis." Comput methods Appl Mech Engrg 132: 45-61.

Holzapfel, G. A., T. C. Gasser, et al. (2000). "A new constitutive framework for arterial wall mechanics and a comparative study of material models." Journal of Elasticity 61: 1-48.

Holzapfel, G. A., M. Stadler, et al. (2002). "A layer-specific three-dimensional model for the simulation of balloon angioplasty using magnetic resonance imaging and mechanical testing." Annals of Biomedical Engineering 30: 753-767.

Hong, J. H. and T.-H. Lim (1996). "Poroelastic model of vertebral trabecular bone in the uniaxial stress condition and experimental validation." BED - 1996 Advances in Bioengineering 33: 129-130.

Howard, A. B., R. W. Alexander, et al. (1997). "Cyclic strain induces an oxidative stress in endothelial cells." American Journal of Physiology 272: C421-C427.

Imura, T., K. Yamamoto, et al. (1990). "In vivo viscoelastic behavior in the human aorta." Circulation Research 66: 1413-1419.

Ingber, D. E. (1998). "The architecture of life." Scientific American(January): 49-57.

Jansson, T., T. Gustavsson, et al. (1995). "Automated correction of linear deformation due to sectioning in serial micrographs." Journal of Microscopy 177(February): 119-127.

Javois, L. C. (1999). Immunocytomchemical Methods and Protocols. Totowa, New Jersey, Humana Press.

Johnson, M. and J. M. Tarbell (2001). "A biphasic, anisotropic model of the aortic wall." Journal of Biomechanical Engineering 123(February): 52-57.

Jones, A. S., B. K. Milthorpe, et al. (1994). "Measurement of microtomy induced section distortion and its correction for 3-dimensional histological reconstructions." Cytometry 15: 95-105.

Jovinge, S., M. Crisby, et al. (1997). "DNA fragmentation and ultrastructural changes of degenerating cells in atherosclerotic lesions and smooth muscle cells exposed to oxidized LDL in vitro." Arteriscler Thromb Vasc Biol 17: 2225-2231.

Kaazempur-Mofrad, M. R., A. G. Isasi, et al. (2004). "Characterization of the Atherosclerotic Carotid Bifurcation Using MRI, Finite Element Modeling, and Histology." Annals of Biomedical Engineering 32(7): 932-946.

Kent, A., J. G. Williams, et al. (1993). Encyclopedia of Computer Science and Technology: 3-D Imaging in Medicine. New York, Marcel Dekker. 28: 341-370.

Keren, G. and M. B. Leon (1994). "Intravascular ultrasound of atherosclerotic vessels: changes observed during interventional procedures." American Jounral of Cardiac Imaging 8(2 (April)): 129-139.

Kim, Y.-J., L. J. Bonassar, et al. (1995). "The role of cartilage streaming potential, fluid flow and pressure in the stimulation of chondrocyte biosynthesis during dynamic compression." Journal of Biomechanics 28(9): 1055-1066.

Koyama, H. and M. A. Reidy (1997). "Reinjury of arterial lesions induces intimal smooth muscle cell replication that is not controlled by fibroblast growth factor 2." Cic Res 80: 408-417.

Ku, D., D. Giddens, et al. (1985). "Pulsatile flow and atherosclerosis in the human carotid bifurcation." Atherosclerosis 5: 293-302.

Ku, D. N. (1997). "Blood flow in arteries." Annual Review of Fluid Mechanics(29): 399-434.

Kwan, M. K., W. M. Lai, et al. (1990). "A finite deformation theory for cartilage and other soft hydrated connective tissues - I. equilibrium results." Journal of Biomechanics 23(2): 145-155.

Laible, J. P., D. Pflaster, et al. (1994). "A dynamic material parameter estimation procedure for soft tissue using a poroelastic finite element model." Journal of Biomechanical Engineering 116(February): 19-29.

Lanir, Y. (1996). "Plausibility of structural constitutive equations for swelling tissues - implications of the C-N and S-E conditions." Journal of Biomechanical Engineering 118: 10-16.

Lee, E., A. J. Grodzinsky, et al. (1995A). "Human vascular smooth muscle cell-monocyte interactions and metalloproteinase secretion in culture." Arterioscler Thromb Vasc Biol 15: 2284-2289.

Lee, R. T., F. Berditchevski, et al. (1995B). "Integrin-mediated collagen matrix reorganization by cultured human vascular smooth muscle cells." Circ Res 76: 209-214.

LeVeen, R. R., G. L. Wolf, et al. (1983). "Morphometric changes in normal arteries and those undergoing transluminal angioplasty." Investigative Radiology 18(1): 63-67.

Levenston, M. E., E. H. Frank, et al. (1996). "Variationally derived 3-field lagrange multiplier and augmented lagrangian poroelastic finite elements for soft tissues." Advances in Bioengineering, ASME BED 33: 145-146.

Liao, D., B. U. Duch, et al. (2004). "Tension and stress calculations in a 3-D fourier model of gall bladder geometry obtained from MR images." Annals of Biomedical Engineering 32(5): 744-755.

Likar, B. and F. Pernus (1999). "Registation of serial transverse sections of muscle fibers." Cytometry 37: 93-106.

Liu, S. Q. (1998). "Influence of tensile strain on smooth muscle cell orientation in rat blood vessels." Journal of Biomechanical Engineering 120(June 1998): 313-320.

Liu, S. Q. and Y. C. Fung (1998). "Changes in the organization of smooth muscle cells in rat vein grafts." Annals of Biomedical Engineering 26: 86-95.

Lorensen, W. E. and H. E. Cline (1987). "Marching cubes: a high resolution 3D surface construction algorithm." Computer Graphics 21(4): 38-44.

Mackay, A. J., C. A. Hamilton, et al. (2001). "Radial artery hypertrophy occurs in coronary atherosclerosis and is independent of blood pressure." Clinical Science(100): 509-516.

Mak, A. F. (1986). "The apparent viscoeleastic behavior of articular cartilage - the contributions from the intrinsic matrix viscoelasticity and interstitial fluid flows." Journal of Biomechanical Engineering 108(May): 123-130.

Mak, A. F. T., L. Huang, et al. (1994). "A biphasic poroelastic analysis of the flow dependent subcutaneous tissue pressure and compaction due to epdermal loadings: issues in pressure sore." Journal of Biomechanical Engineering 116(November): 421-429.

Masuda, H., H. Bassiouny, et al. (1989). "Artery wall restructuring in response to increased flow." Surgical Forum 40: 258-286.

Mathieu-Costello, O. and K. Fronek (1985). "Morphometry of the amount of smooth muscle cells in the media of various rabbit arteries." Journal of Ultrastructural Research 91: 1-12.

Matsumoto, T. and K. Hayashi (1993). "Mechanical and dimensional adaptation of rat aorta to hypertension." ASME Journal of Biomechanical Engineering.

Matsumoto, T., K. Hayashi, et al. (1995). "Residual strain and local strain distributions in the rabbit atherosclerotic aorta." Journal of Biomechanics 28(10): 1207-1217.

Moller, T. and B. Trumbore (1997). "Fast, minimum storage ray-traingle intersection." Journal of Graphics Tools 2(1): 21-28.

Mow, V. C., M. H. Holmes, et al. (1984). "Fluid transport and mechanical properties of articular cartilage: a review." Journal of Biomechanics 17(5): 377-394.

Mow, V. C., S. C. Kuei, et al. (1980). "Biphasic creep and stress relaxation of articular cartilage in compression: theory and experiments." Journal of Biomechanical Engineering 102: 73-84.

Mow, V. C., A. Ratcliffe, et al. (1992). "Cartilage and diarthrodial joints as paradigms for hierarchical materials and structures." Biomaterials 13(2): 67-97.

Mulvany, M. J. (2002). "Small artery remodeling and significance in the development of hypertension." News Physiol Sci 17: 105-109.

Niklason, L. E. and R. Langer (2001). "Prospects for organ and tissue replacement." JAMA 285(5): 573-576.

Ogden, R. W. and C. A. J. Schulze-Bauer (2000). "Phenomenological and structural aspects of the mechanical response of arteries." Mechanics in Biology BED-Vol. 46: 125-140.

Ollerenshaw, J. D., A. M. Heagerty, et al. (1988). "The effects of coarctation hypertension upon vascular inositol phospholipid hydrolysis in Wistar rats." Journal of Hypertension 6: 733-738.

Passerini, A. G., D. C. Polacek, et al. (2004). "Coexisting proinflammatory and antioxidative endothelial transcription profiles in a distrurbed flow region of the adult porcine aorta." Proceedings of the National Academy of Science 101(8): 2482-2487.

Peifer, J. W., L. Klein, et al. (1995). "Sensitivity of 3D coronary reconstruction to acquisition calibration errors." (October): 1.

Pentland, A. and S. Sclaroff (1991). "Closed-form solutions for physically based shape modeling and recognition." IEE Transactions on Pattern Analysis and Machine Intelligence 13(7): 715.

Perona, P. and J. Malik (1990). "Scale-space and edge detection using anisotropic diffusion." IEEE Transactions on Pattern Analysis and Machine Intelligence 12(7): 629-639.

Piedrahita, J. A., S. H. Zhang, et al. (1992). "Generation of mice carrying a mutant apolipoprotein E gene inactivated by gene targeting in embryonic stem cells." Proceedings of the National Academy of Science 89: 4471-4475.

Prabha, P. S., U. N. Das, et al. (1990). "Free radical generation, lipid peroxidation and essential fatty acids in uncontrolled essential hypertension." Prostaglandins Leukotrienes and Essential Fatty Acids 41: 27-33.

Prendergast, P. J., W. D. v. Driel, et al. (1996). "A comparison of finite element codes for the solution of biphasic poroelastic problems." Proc Instn Mech Engrs 210: 131-136.

Press, W. H., B. P. Flannery, et al. (1992). Numerical Recipes in FORTRAN: The Art of Scientific Computing. Cambridge, England, Cambridge University Press.

Price, R. J., J. R. Less, et al. (2002). "Hemodynamic Stresses and Structural Remodeling of Anastomosing Arteriolar Networks: Design Principles of Collateral Arterioles." Microcirculation 9(2): 111-124.

Pries, A. R., T. W. Secomb, et al. (1995). "Structure and hemodynamics of microvascular networks: heterogeneity and correlations." American Journal of Physiology 269: H1713-H1722.

Pries, A. R., T. W. Secomb, et al. (1996). "Relationship between structural and hemodynamic heterogeneity in microvascular networks." American Journal of Physiology 270: H545-H553.

Pries, A. R., T. W. Secomb, et al. (1998). "Structural adaptation and stability of microvascular networks: theory and simulations." American Journal of Physiology 275: H349-H360.

Pries, A. R., T. W. Secomb, et al. (1999). "Structural autoregulation of terminal vascular beds: vascular adaptation and development of hypertension." Hypertension 33: 153-161.

Pries, A. R., T. W. Secomb, et al. (1994). "Resistance to blood flow in microvessels in vivo." Circulation Research 75: 904-915.

Reddy, J. N. (1993). An Introduction to the Finite Element Method. Boston, McGraw-Hill.

Romeu, J. L. (2003). "Anderson-Darling: A Goodness of Fit Test for Small Sample Assumptions." Selected Topics in Assurance Related Technologies 10(5).

Ryan, B. F. and B. L. Joiner (2001). Minitab Handbook. Pacific Grove, CA, Duxbury.

Sakamoto, H., M. Aikawa, et al. (2001). "Biomechanical Strain Induces Class A Scavenger Receptor Expression in Human Monocyte/Macrophages and THP-1 Cells: A Potential Mechanism of Increased Atherosclerosis in Hypertension." Circulation(104(1)): 109-114.

Salam, T. A., A. B. Lumsden, et al. (1996). "Low shear stress promotes intimal hyperplasia thickening." Journal of Vascular Investigation 2(1): 12-22.
Salazar, R. S., M. J. Thubrikar, et al. (1995). "Pressure-induced mechanical stress in the carotid artery bifurcation: a possible correlation to atherosclerosis." Journal of Biomechanics 28(11): 1333-1340.
Schneck, D. J. (1995). Chapter 1: An Outline of Cardiovascular Structure and Function. Physiologic Systems, CRC Press: 3-14.
Schroeder, W., K. Martin, et al. (1998). The Visualization Toolkit. Upper Saddle River, Prentice Hall PTR.
Schulze-Bauer, C. A. J., C. Morth, et al. (2003). "Passive Biaxial Mechanical Response of Aged Human Iliac Arteries." Journal of Biomechanical Engineering 125(3): 395-406.
Siegel, R. J., K. Swan, et al. (1985). "Limitations of postmortem assessment of human coronary artery size and luminal narrowing: differential effects of tissue fixation and processing on vessels with different degrees of atherosclerosis." Journal of the American College of Cardiology 5(2): 342-346.
Simon, B. R. (1992). "Multiphase poroelastic finite element models for soft tissue strucures." Applied Mechanics Review 45(6): 191-218.
Simon, B. R., M. V. Kaufman, et al. (1998A). "Porohyperelastic-transport-swelling theory, material properties and finite element models from large arteries." International Journal of Solids Structures 35(34-35): 5021-5031.
Simon, B. R., M. V. Kaufmann, et al. (1993). "Finite element models for arterial wall mechanics." Journal of Biomechanical Engineering 115(November): 489-496.
Simon, B. R., M. V. Kaufmann, et al. (1998B). "Porohyperelastic finite element analysis of large arteries using ABAQUS." Journal of Biomechanical Engineering 120(April): 296-298.
Simon, B. R., J. P. Liable, et al. (1996). "A poroelastic finite element formulation including transport and swelling in soft tissue structures." Journal of Biomechanical Engineering 118(February): 1-9.
Simon, B. R., J. Liu, et al. (1997). "Data reduction methods for determination of material properties for porohyperelastic-transport-swelling (PHETS) finite element models of large arteries." BED - 1997 Bioengineering Conference 35: 35-36.
Skrinjar, O. (2003). Discussions and notes on image alignment techniques.
Sokolnikoff, I. S. (1983). Mathematical Theory of Elasticity. Malabar, Robert E. Krieger Publishing Company.
Springer, T. A. (1994). "Review: Traffic signals for lymphocyte recirculation and leukocyte emigration: the multistep paradigm." Cell 76: 301-314.
Studholme, C., D. L. G. Hill, et al. (1996). "Automated 3-D Registration of MR and CT Images of the Head." Medial Image Analysis 1(2): 163-175.
Studholme, C., D. L. G. Hill, et al. (1997). "Automated Three-Dimensional Registration of Magnetic Resonance and Positron Emission Tomography Brain Images by Multiresolution Optimization of Voxel Similarity Measures." Medical Physics 24(1): 25-35.
Sunday, D. (2003). Intersections of Rays and Segments with Triangles in 3D. 2003.
Taber, L. A. (1998). "A Model for Aortic Growth Based on Fluid Shear and Fiber Stresses." Journal of Biomechanical Engineering 120(June 1998): 348-354.

Taddei, S., A. Virdis, et al. (2001). "Restoration of nitric oxide availability after calcium antagonist treatement in essential hypertension." Hypertension 37: 943-948.

Tang, D., C. Yang, et al. (2004). "Effect of a Lipid Pool on Stress/Strain Distributions in Stenotic Arteries 3-D Fluid-Structure Interactions (FSI) Models." Journal of Biomechanical Engineering 126(3): 363-370.

Tang, D., C. Yang, et al. (2004). "3D MRI-Based Multicomponent FSI Models for Atherosclerotic Plaques." Annals of Biomedical Engineering 32(7): 947-960.

Taylor, W. R. (1998). "Mechanical deformation of the arterial wall in hypertension: A mechanism for vascular pathology." The American Journal of the Medical Sciences 316(3): 156-161.

Thompson, P. and A. W. Toga (2000). Warping Strategies for Intersubject Registration. Handbook of Medical Imaging. I. N. Bankman. San Diego, Academic Press: 569-601.

Thubrikar, M. J. and F. Robicsek (1995). "Current Review: Press-induced arterial wall stress and atherosclerosis." Annals of Thoracic Surgery 59: 1594-1603.

Thubrikar, M. J., S. K. Roskelley, et al. (1990). "Study of stress concentration in the walls of the bovine coronary arterial branch." J. Biomechanics 23(1): 15-26.

Thurston, G. and A. L. Baldwin (1994). "Endotheilial actin cytoskeleton in rat mesentery microvasculature." American Journal of Physiology 266: H1896-H1909.

Timoshenko, S. P. and J. N. Goodier (1987). Theory of Elasticity. New York, McGraw-Hill Book Company.

Tropea, B. I., S. Glagov, et al. (1997). Chapter 4: Hemodynamics and Atherosclerosis. The Basic Science of Vascular Disease. A. N. Sidawy, B. E. Sumpio and R. G. DePalma. Armonk, Futura Publishing: 107-126.

Udupa, J. and G. Herman (1991). 3D Imaging in Medicine. New York, CRC Press: 3-27.

Vacek, L. and P. Braveny (1978). "Effect of angiotensin II on blood pressure and on microvascular beds in mesentery, skin, and skeletal muscle of the rat." Microvascular Research 16: 43-50.

Vito, R. P. and S. A. Dixon (2003). "Blood Vessel Constitutive Models - 1995-2002." Annual Review of Biomedical Engineering(5): 413-439.

von der Thusen, J. H., T. J. C. van Berkel, et al. (2001). "Induction of rapid atherogenesis by perivascular carotid collar placement in apolipoprotein E-deficient and low-density lipoprotein receptor-deficient mice." Circulation 103: 1164-1170.

Walpole, R. E. and R. H. Myers (1993). Probability and Statistics for Engineers and Scientists. New York, Macmillan Publishing Company.

Walzog, B. and P. Gaehtgens (2000). "Adhesion molecules: The path to a new understanding of acute inflammation." News in Physiological Sciences 15(June): 107-113.

Watanabe, T., H. Yaegashi, et al. (1997). "The lobular architecture of the normal human pancreas: A computer-assisted three-dimensional reconstruction study." Pancreas 15(1): 48-55.

Watanabe, T., H. Yaegashi, et al. (1999). "Changing distribution of islets in the developing human pancreas: A computer-assisted three-dimensional reconstruction study." Pancreas 18(4): 349-354.

Weiss, D., J. J. Kools, et al. (2001A). "Angotensin II-induced hypertension accelerates the development of atherosclerosis in apoE-deficient mice." Circulation(103): 448-454.
Weiss, D., D. Sorescu, et al. (2001B). "Angiotensin II and Atherosclerosis." American Journal of Cardiology 87(8A): 25C-32C.
Weiss, J. A., B. N. Maker, et al. (1996). "Finite element implementation of incompressible, transversely isotropic hyperelasticity." Computer Methods in Applied Mechanics and Engineering(135): 107-128.
Werner, M., A. Chott, et al. (2000). "Effect of formalin tissue fixation and processing on immunohistochemistry." American Journal of Surgical Pathology 24(7): 1016-1019.
White, F. M. (1986). Fluid Mechanics. New York, McGraw-Hill Book Company.
White, S. S., C. K. Zarins, et al. (1993). "Hemodynamic patterns in two models of end-to-side vascular graft anastomoses: effects of pulsatility, flow division, reynolds number, and hood length." Transactions of the ASME 115: 104-111.
Wilhjelm, J. E., K. Vogt, et al. (1997). "Influence of tissue ppreservation methods on arterial geometry and chogenicity." Ultrasound Med Biol 23(7): 1071-1082.
Willis, G. C. (1954). "Localizing factors in atherosclerosis." The Canadian Medical Association Journal 70(1): 1-9.
Wilson, P. W. (1994). "Established risk factors and coronary artery disease: the Framingham Study." American Journal of Hypertension 7: 7s-12s.
Wolf, S. and N. T. Werthessen (1976). Anatomical and physiological characteristics of arteries. Dynamics of arterial flow. New York, Plenum. 115: 48.
Wolinsky, H. and S. Glagov (1964). "Structural basis for the static mechanical properties of the aortic media." Circulation Research 14: 400-413.
Wolinsky, H. and S. Glagov (1967). "A lamellar unit of aortic medial structure and function in mammals." Circulation Research 20: 99-111.
Wong, R. K., A. L. Baldwin, et al. (1999). "Cadherin-5 redistribution at sites of TNF-a and IFN-g induced permeability in mesenteric venules." American Journal of Physiology 276: H736-H748.
Woods, R. P. (2000). Spatial Transformation Models. Handbook of Medical Imaging. I. N. Bankman. San Diego, Academic Press: 465-490.
Xu, C., C. K. Zarins, et al. (2000). "Differential transmural distribution of gene expression for collagen types I and III proximal to aortic coarctation in the rabbit." Journal of Vascular Research 37(3): 170-182.
Xu, C., C. K. Zarins, et al. (2000). "Hypercholesterolemia superimposed by experimental hypertension induces differential distribution of collagen and elastin." Arterioscler Thromb Vasc Biol. 20: 2566-2572.
Yaegashi, H. (2001). Personal Communications with Dr. Hiroshi Yaegashi. P. Carnell. Miyamachi, Japan: Section alignment and reconstruction techniques.
Yaegashi, H., T. Takahashi, et al. (1987). "Microcomputer-aided reconstruction: a system designed for the study of 3-D microstructure in histology and histopathology." Journal of Microscopy 146: 55-65.
Yaegashi, H., Y. Zhang, et al. (2000). "Computer-assisted 3D mapping and morphometry of dysplastic zones in endoscopically resected colonic adenomas." Journal of Pathology 191: 143-149.

Yamada, H. (1973). Strength of Biological Materials. Huntington, Robert E. Krieger Publishing Company.
Zervoudaki, A. I. and P. K. Toutouzas (2003). "Remodeling of Resistance Vessels in Essential Hypertension." Hellenic Journal of Cardiology 44: 116-124.
Zhang, S. H., R. L. Reddick, et al. (1992). "Spontaneous hypercholesterolemia and arterial lesions in mice lacking apolipoprotein E." Science(258): 468-471.
Zhou, J. and Y. C. Fung (1997). "The Degree of Nonlinearity and Anisotropy of Blood Vessel Elasticity." Proceedings of the National Academy of Science 94: 14255-14260.
Zienkiewicz, O. C. (1977). The Finite Element Method. London, McGraw-Hill.